FINITE ELEMENT INVESTIGATION INTO THE PERFORMANCE OF EMBEDDED PLATE ANCHORS IN SAND

A Dissertation

by

NABIL M. ALI HAMEED AL HAKEEM

Submitted to the Office of Graduate and Professional Studies of
Texas A&M University
in partial fulfillment of the requirements for the degree of

DOCTOR OF PHILOSOPHY

Chair of Committee,	Charles P. Aubeny
Committee Members,	Robert Lytton
	Marcelo Sanchez
	Jerome J. Schubert
Head of Department,	Robin Autenrieth

August 2019

Major Subject: Civil Engineering

ABSTRACT

As offshore energy and other development extend to deeper waters, conventional platforms are increasingly being replaced by floating facilities. Also, up to 60% of wind power development is anticipated to be in deeper waters that require floating platforms moored to the seabed by anchors. Seabed soils at sites often contain sandy soil strata; therefore, practical development of offshore wind power requires anchor systems that are suitable for deployment in sands, such as piles, suction caissons and direct embedment plate anchors. Of these options, plate anchors are particularly attractive due to their compact size, light weight, variety of installation techniques, and highly efficient and suitable for a wide range of soil conditions. However, more reliable predictive models for plate anchor performance in cohesionless soils are needed for mooring systems to be securely designed.

The limited research focus on plate anchor performance in cohesionless soil, particularly for deep embedment, has triggered a strong motivation for this research. Therefore, extensive small and large deformation finite element simulations were conducted to study the effects of anchor embedment depth, with special emphasis on characterizing the transition in the anchor behavior from a shallow to a deep failure, considering elastic soil behavior (in terms of Rigidity Index I_r) in evaluating anchor performance. Additionally, there is a significant gap in knowledge concerning the keying behavior of direct embedment plate anchors in sand after installation, and the corresponding irrecoverable loss of embedment. Finally, most previous plate anchors

research have focused on either horizontal or vertical anchor orientations while the effect of inclined orientations has received limited attention.

The predictions showed that at shallow anchor embedment depths, rigidity index I_r has negligible influence on anchor capacity while the performance of deeply embedded anchors is strongly influenced by rigidity index I_r. This study developed an empirical model for predicting anchor pullout capacity as function N_q (D_r, γ', z/D), describing the transition in the breakout factor N_q from the shallow mode to its maximum value N_{qmax}. In regard to the keying process behavior, the large deformation finite element analyses showed that the angle of orientation α at which the maximum pullout capacity occurs increases with increasing e/B ratio, ranging between 75º and 85º. Also, the predictions revealed that as the loading eccentricity ratio e/B increases, the loss in anchor embedment δ_z/B during rotation decreases. However, once the eccentricity $e \geq B$, a minimal loss in anchor embedment can be achieved regardless of the plate thickness. A linear relationship was observed between the maximum loss in anchor embedment and anchor pullout angle θ at any e/B ratio. In regard to the pullout capacities of inclined plate anchors in cohesionless soil. An empirical equation was proposed to estimate the breakout factor of an inclined anchor at any inclination angle θ between 0º and 90º. Also, the observations showed a significant sensitivity of the breakout factor N_q to the plate width B.

ACKNOWLEDGEMENTS

This research would not have been possible without the assistance of some precious and wonderful people. I would first like to thank my advisor and committee chair, Dr. Charles Aubeny, for his guidance, advice and continual support throughout the course of this research. Dr. Charles Aubeny made himself available to answer any questions even though his schedule was always busy. His courses that I took with him at the beginning of my research offered me very good tools to investigate my research.

I would like to extend my gratitude to Dr. Marcelo Sanchez who enhanced my knowledge in soil mechanics and plasticity theory. My other committee members, Dr. Robert Lytton and Dr. Jerome Schubert also deserve thanks for their support and guidance. I also want to express my gratitude to Iraqi Ministry of Higher Education and Scientific Research / Wasit University for the financial support during my PhD study.

Thanks also go to my friends, colleagues and the department faculty and staff for making my time at Texas A&M University a great experience. I am very grateful for everyone who has been a part of my research and contributed to it in any way. I would like to share my achievements with all people who supported me throughout my PhD journey and I forgot to mention them here.

Finally, special thanks to my wife Riyam Alzuabidi for her patience and love also to my great mother for her encouragement.

CONTRIBUTORS AND FUNDING SOURCES

Contributors

This work was supervised by a dissertation committee consisting of Professor Charles P. Aubeny [Advisor] and Professors Robert Lytton, Marcelo Sanchez [Civil Engineering Department] and Jerome J. Schubert [Petroleum Engineering Department].

All other work conducted for the dissertation was completed by the student independently. This dissertation contains no material which has been accepted for the award of any other degree or diploma in any university.

Funding Sources

This study was supported by a scholarship from Iraqi Ministry of Higher Education and Scientific Research / Wasit University.

TABLE OF CONTENTS

Page

LIST OF FIGURES

Page

LIST OF TABLES

Page

CHAPTER I

INTRODUCTION

1.1 Background

Soil anchors are primarily designed and constructed to serve as a foundation system for resisting uplift and lateral forces in onshore and offshore applications. In onshore applications, plate anchors are made from steel plate, precast concrete slabs, poured concrete slabs, or timber sheets. They are installed by excavating the ground to the desired depth and then using good-quality soil for backfilling and compacting (Das, 1990). Plate anchors subjected to uplift and lateral forces can be found in many geotechnical onshore applications such as transmission towers, tunnels, submerged pipelines, aircraft moorings, and the tieback resistance of earth retention structures, as well as in the underpinnings of settling structures.

Generally, anchors in offshore applications (see Figure 1.1) serve to secure moorings in a fixed position on the seabed. Floating structures are often the system of choice in offshore energy development. For instance, in oil and gas applications in water depths greater than 500 m, conventional platforms are generally replaced by floating facilities (Song et al., 2009). Offshore wind energy is in an early stage of development, and promising as an economical and clean energy solution. Currently, offshore wind development is largely taking place in shallow water depths, where fixed supporting structures are feasible. However, most wind power development is anticipated to be located in deeper waters, at depths greater than 40 m; this would require floating platforms

moored to the seabed by anchors. Seabed soils at these sites often contain sandy soil strata. Therefore, practical development of offshore wind power requires anchor systems that are suitable for deployment in sand. Anchors in offshore applications are available in many types, depending on how they obtain the ability to maintain their position. The oil - gas and renewable energy industries have regularly moored different sizes of floating facilities, anchoring them to the seabed by a variety of anchor alternatives, including piles, suction caissons, dynamically installed anchors, drag embedded anchors, and an assortment of direct embedment plate anchors, as shown in Figure 1.2.

(a) Future floating wind turbine technology (Laurie Carol, NREL 2017).

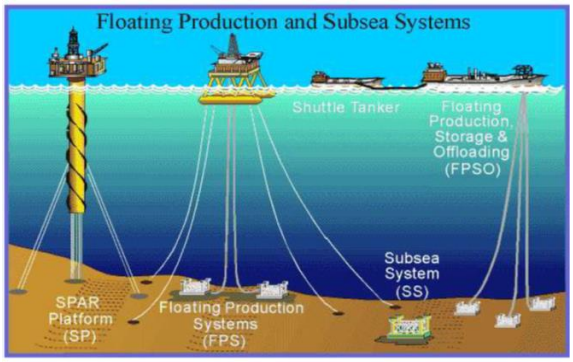

(b) Offshore production facilities (courtesy of Mineral Management Services).

(c) Pelamis wave energy converter (courtesy of Sounds & Sea Technology).

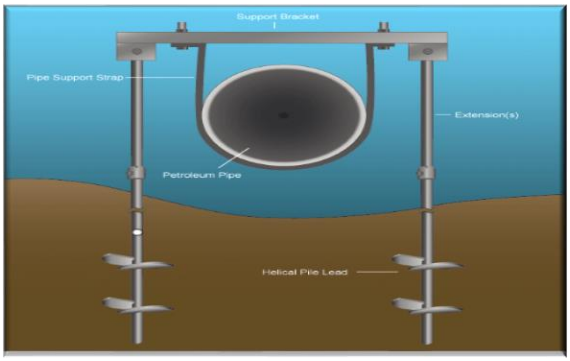

(d) Helical plate anchor (for underwater pipelines). http://www.macleandixie.com/

Figure 1.1 Offshore applications.

(a) Driven piles (courtesy of JD Murff).

(b) Typical drag anchor (courtesy of Sounds & Sea Technology).

(c) Suction caisson (courtesy of E Clukey).

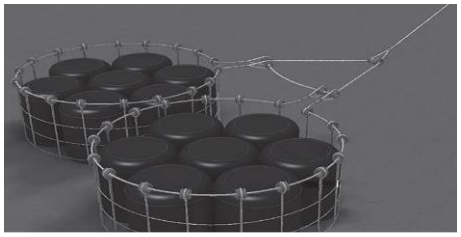

(d) Dead weight anchors (courtesy of C. Aubeny).

(e) Vertically-loaded anchor (courtesy of C. Aubeny).

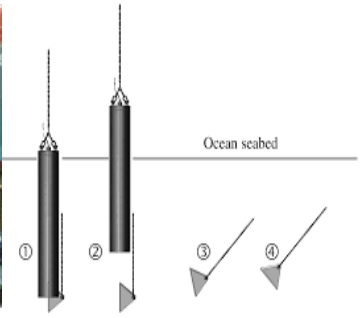

(f) Suction-embedded plate anchor (courtesy R Wilde, Intermoor).

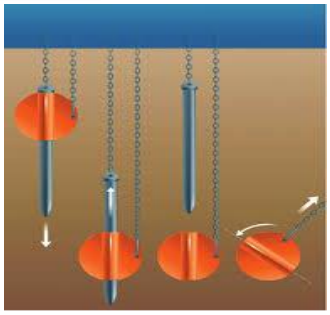

(g) Dynamically-embedded plate anchor (O' Loughlin et al., 2014).

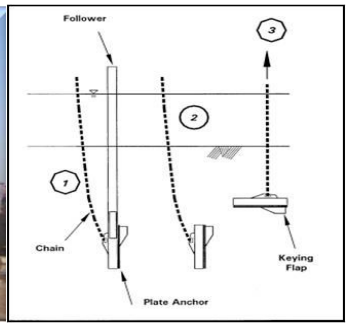

(h) Pile-driven PDPA (NAVFAC, 2011).

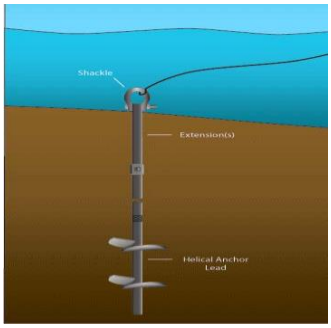

(i) Helical anchor (courtesy of MacLean Dixie HFS).

Figure 1.2 Offshore anchors.

Over the last five decades, various types of anchors have been developed to meet the growing needs of anchorage systems in floating facilities for oil and gas and wind energy structures. In the last thirty years, embedded plate anchors have served as a practical and efficient option for mooring such floating facilities (see Figures 1.2f to 1.2k), due to their:

- Compact size,
- Low weight,
- Variety of installation techniques,
- Suitability for a wide range of soil conditions, and
- High efficiency (i.e., the holding capacity-to-dry-weight ratio of the plate). Figure 1.3 shows the high level of efficiency offered by the plate anchor option for certain anchor geometries and soil profiles, as compared to the caisson option.

All contribute to greatly reduced costs in terms of manufacture, transport, and installation. Although direct embedment anchor installation is typically more costly than drag installation, it permits relatively precise positioning both vertically and horizontally. Additionally, deep embedment is possible in sandy and stratified soil profiles in which deep penetration is not possible by drag embedment (Aubeny, 2017). Figure 1.4 shows the main geometric shapes of plate anchors investigated in the present research.

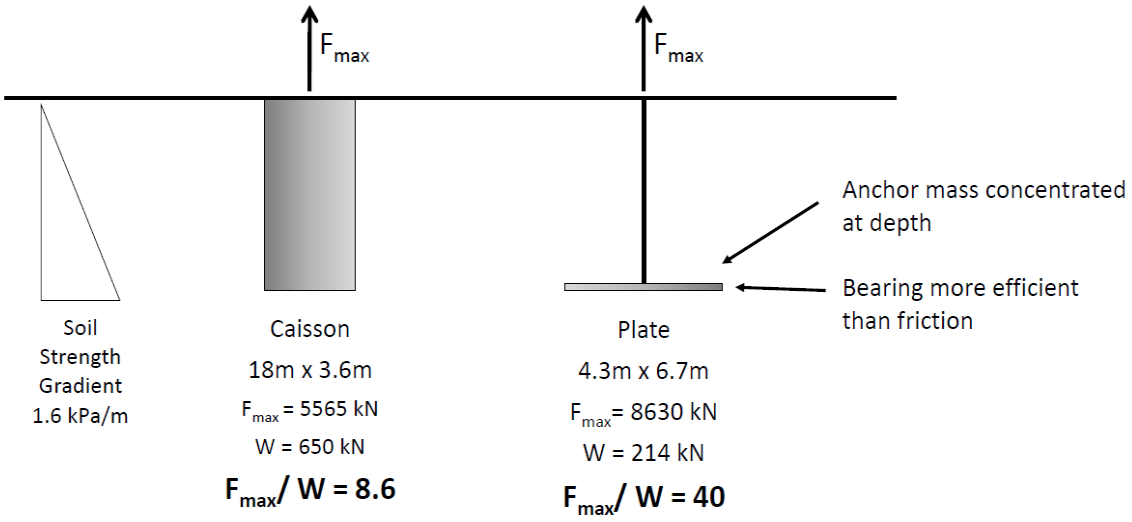

Figure 1.3 Plate anchor efficiency (Aubeny, 2016).

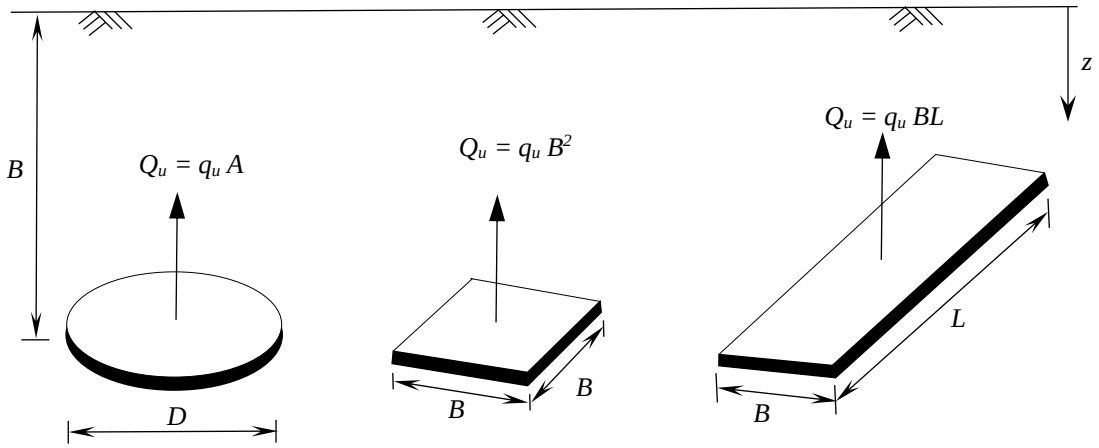

Figure 1.4 Different geometric shapes of plate anchors.

1.2 Installation of Offshore Plate Anchors

Directly embedded plate anchors can be installed through a variety of means, as outlined below.

1.2.1 Suction Embedded Plate Anchors (SEPLA)

Suction-embedded plate anchors (SEPLAs) comprise one alternative approach that can be used to embed a plate anchor at a target depth. This is accomplished by locating a vertical plate at the base of a suction caisson (see Figure 1.2f). A SEPLA is primarily intended for use in soft clay (Aubeny, 2017). This installation technique offers the advantages of known location and embedment depth, and avoids the issue of interference with other seabed infrastructure (Barron, 2014). The installation and keying processes are summarized schematically in Figure 1.5. A SEPLA undergoes the following main steps during its installation.

Step 1: Suction self-weight penetration

The plate anchor is inserted vertically into the base of the suction caisson and lowered to the seabed. Then, the suction caisson penetrates the seabed under its own weight, until the end-bearing and skin friction resistances equal the caisson's weight.

Step 2: Suction caisson penetration

Closing the vent valve on the top of the caisson causes differential pressure that is created by pumping water from the interior of the caisson. This generates the driving force necessary to overcome the frictional resistance along the caisson wall, until the caisson is fully embedded and the plate anchor reaches its target depth.

Step 3: Suction caisson retraction

The plate anchor is released and the water is pumped back into the interior of the caisson, causing upward movement of the suction caisson and leaving the plate anchor

embedded in the seabed at a vertical orientation. When the bottom of the suction caisson reaches the seabed, the caisson is retrieved and prepared for use in the next installation.

Step 4: Plate anchor keying and steady pullout

In this step, the connected anchor chain is tensioned in the design direction of the applied loading. As the chain cuts into the soil, the plate anchor rotates or "keys" into its target orientation. Unrecoverable embedment loss occurs during the plate anchor's keying process. Afterwards, the plate anchor is approximately perpendicular to the direction of loading at the anchor's pad eye, such that the ultimate capacity is mobilized when the maximum projected area is presented to the direction of loading.

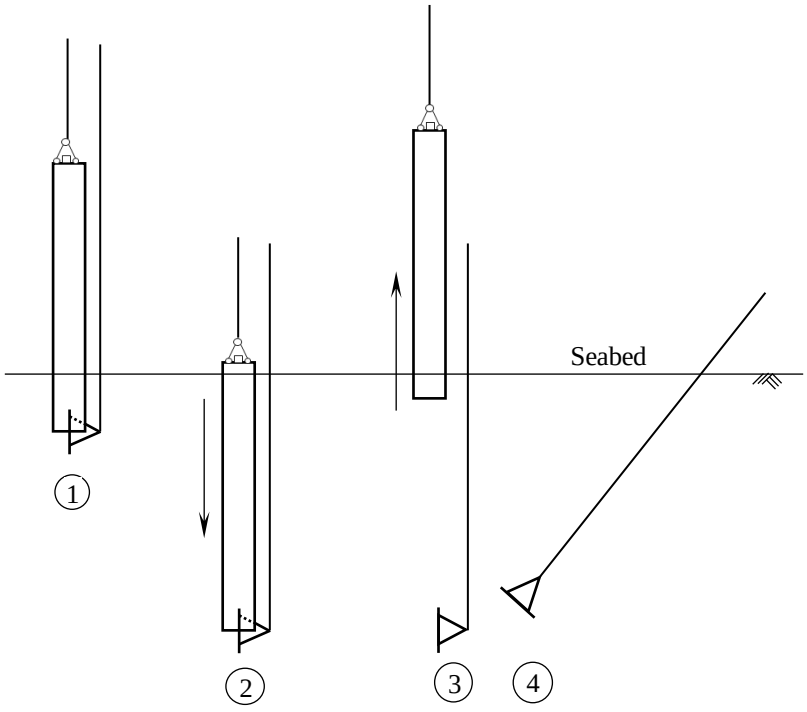

Figure 1.5 Suction-embedded plate anchor concept.

1.2.2 Pile Driven Plate Anchors (PDPA)

Conventional pile driving, rather than the suction caisson technique, can be used to drive the plate anchor vertically to the required depth and then key or rotate it to an orientation approximately perpendicular to the direction of the applied mooring line load (see Figure 1.2h). This is a common approach used by the US Navy when installing plate anchors. In this process, the plate anchor is attached to the tip of a pile, termed a "follower," which can be installed by hammer driving, vibration, or jetting. Then the pile is extracted for the next installation (Aubeny, 2017). Pile driven plate anchors (PDPAs) can be installed in a wide range of soil profiles, including soft and over-consolidated clays and all types of sand (Forrest et al., 1995). The type of hammer depends on the soil type and anchoring requirements. Impact or hammer equipment is used in stiff clays and dense sands; vibratory hammers may be considered for loose sands soil and soft mud. Jetting may be used to assist penetration into dense sand when vibratory hammers are used (NAVFAC, 2012). PDPAs have no particular limitations with regards to installation depths in either sand, clay, or stratified soil profiles.

1.2.3 Dynamically Embedded Plate Anchors (DEPLA)

The most recently developed plate anchor installation technique is dynamic-embedded plate anchors (DEPLAs). A DEPLA consists of a rocket-shaped anchor comprised of a removable central shaft named a "follower," and a set of four flukes (see Figure 1.2g). This new, dynamically installed anchor combines the installation benefits of other dynamically installed anchors with the capacity benefit of plate anchors (O'Loughlin et al., 2013). Dynamically embedded plate anchors penetrate the seabed to a target depth

via the kinetic energy obtained through a freefall in the water. The follower is retrieved after the anchor penetrates to the required depth, and then re-used for the next installation, leaving the anchor flukes vertically embedded in the seabed. Then, the anchor flukes rotate or "key" into the target orientation (see Figure 1.2g). This technique is economically attractive due to the advantage of relatively quick and easy installation. However, their capacity-to-weight ratio is low, meaning that they need to be very large to provide the required anchor capacity. Both the experimental and numerical investigations performed by O'Loughlin et al. (2013) demonstrate that the capacity of a DEPLA is much higher than that of other dynamically installed anchors with capacities up to 40 times the dry weight of the plate and a plate-bearing capacity factor of about 15.

1.2.4 Helical Anchors

In the energy industry, helical anchors have received relatively little attention with regards to offshore floating structures, although they have long been in use for anchoring vessels and submarine pipelines. They offer the advantage of relatively rapid, easy, and inexpensive installation, and are composed of one or more helical plates fixed to a central shaft (see Figure 1.2k). Helical anchors are installed in both sand and clay by applying torque and axial force to the shaft using hydraulic torque motors that are transmitted to the helical plate (Aubeny, 2017). Due to the pitch of the helical plate, these elements produce no spoils and create minimal disturbance in the area surrounding the anchor installation (Young, 2012).

All of the abovementioned methods of installation are effective in normally consolidated clay profiles. In contrast, only limited installation depths are possible through

suction or dynamic installation in sand, stiff clay, and stratified soil profiles. PDPAs and helical anchors have no particular limitations with regards to installation depths in either sand, clay, or stratified soil profiles. The plate anchors in all of the above-mentioned techniques except helical anchors are installed vertically and then reoriented to achieve a large projected area to maximize ultimate uplift anchor capacity. However, these anchors attached to floating structures by using two major types of mooring systems, i.e. catenary or taut-wire moorings system as shown in Figure 1.6. The main difference between taut and catenary moorings for the geotechnical anchor system is the angle at which the mooring enters the seafloor (Randolph and Gourvenec, 2011). It is noted that even catenary mooring lines, which are horizontal at the seabed, are inclined (by about 15° from horizontal) due to the curvature in the reverse catenary (Figure 1.6a). In taut or semi-taut systems (Figure 1.6b), the inclination angle is substantially larger and arrives an angle up to 50° relative to the horizontal at the seabed, and the anchor has to resist horizontal and vertical forces. Additionally, tension-leg platforms are usually anchored with vertical moorings that arrive at an angle close to 90° and will result in mainly vertical forces. The steeper the angle between mudline and floating platform is, the shorter and lighter the anchor line will be (Randolph and Gourvenec, 2011).

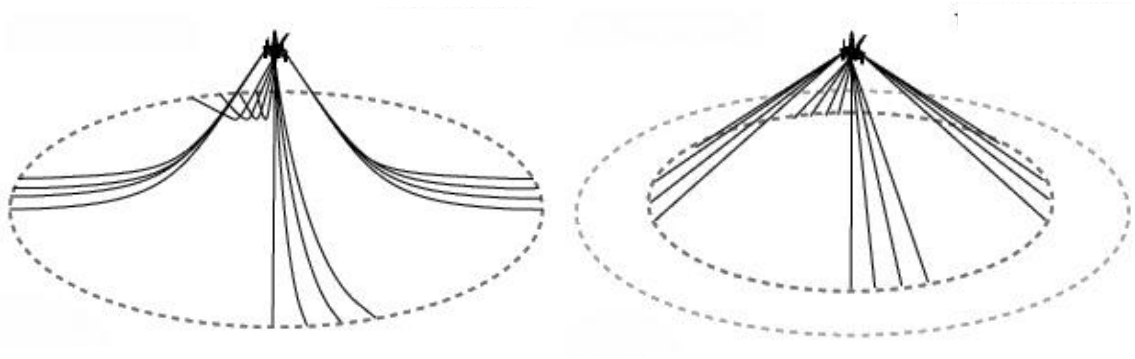

(a) Catenary system (b) Taut-leg system

Figure 1.6 Mooring Systems
http://www.dredgingengineering.com.

1.3 Research Objectives

Cohesionless soil strata are common in nearshore deposits. Such a condition is particularly relevant to floating renewable energy systems, which are often situated relatively close to shore. Therefore, practical development of offshore wind power requires anchor systems suitable for deployment in sand, such as piles, caissons, and direct embedment plate anchors. The present study investigates the performance of directly-embedded plate anchors in sand, from an offshore rather than onshore point of view. A primary measure of anchor performance is its pullout capacity, which increases as the embedment depth grows due to improved soil strength and the diminishing effect of the free surface. However, irrespective of the plate anchor installation method, reliable prediction of anchor pullout capacity is required. To achieve a reliable assessment of the pullout capacity of plate anchors in cohesionless soil, the following main points must be considered.

1.3.1 The Effects of Anchor Embedment Depth

Most previous studies on embedded plate anchor capacity problems in sand have covered relatively shallow anchor embedment ranges (approximately 8 to 10 plate widths or diameters), which is insufficiently deep to characterize the transition of the anchor behavior from shallow to deep embedment. The main objectives of this part of the research are to:

- Improve the general understanding of deep plate anchor behavior in sand, with a focus on describing the transition from shallow to deep failure mechanisms; and
- Identify the need for considering elastic soil behavior (in terms of the rigidity index, I_r) in evaluating anchor performance, especially for deep anchors.

1.3.2 Effects of the Plate Keying Process

Irrespective of the plate anchor installation method except helical anchor, an embedded plate anchor always has a vertical orientation after penetration of the seabed to the required depth. Installation usually involves a "keying" process, where the anchor rotates to an orientation that is nearly perpendicular to the direction of the mooring line load. During keying, the anchor moves both horizontally and vertically as it rotates to its target orientation. The upward vertical displacement is of particular concern, since a loss of anchor embedment leads to a reduction in pullout capacity. Very limited experimental data are available for plate anchor keying in sand, and to the author's knowledge, no analytical or numerical studies have been performed. However, the primary objective of this section of the research focuses on a significant gap in numerical knowledge concerning the keying behavior of direct embedment plate anchors in sand.

1.3.3 Effects of Anchor Inclination/Load Angle

The majority of the reported experimental, analytical, and numerical studies have been concerned with evaluating the pullout resistance of either horizontal or vertical plate anchors. The mooring systems of offshore floating structures usually involve inclined load orientations, where the plate anchor does not have a horizontal orientation. For shallowly embedded anchors, where free surface effects are dominant, plate orientation is likely to be particularly important. In this part of the research, the effects of anchor inclination will receive considerable attention.

1.4 Dissertation Structure

The dissertation is divided into seven chapters. The content of each chapter is described below.

Chapter 2 provides an overview of main previous theoretical/numerical and experimental studies relevant to the pullout capacity of plate anchors embedded in sand. The anchor keying process and post-anchor pullout capacity are also summarized. Installation aspects of the problem are not addressed.

Chapter 3 provides details regarding the following points:

- Description of the Mohr Coulomb yielding criterion, plastic flow rule, and significance of dilatancy in plate anchor performance;
- Numerical techniques used in this research to handle the issue of excessive distortion of the finite element mesh where large deformations are required to mobilize the pullout capacity, especially for deeply embedded plate anchors; and
- Soil anchor interface modeling and the collapse criterion adopted in this research

Chapter 4 presents a parametric finite element study of the pullout capacity of circular, horizontally oriented anchors in sand subjected to centric loading, using conventional small strain and large deformation finite element (i.e., Arbitrary Lagrangian Eulerian) analyses to characterize the transition of the anchor behavior from a shallow to deep failure mechanism, depending on the soil properties friction angle ϕ', dilation angle ψ and rigidity index I_r. Also, this part of the research investigates the influence of elastic behavior (in terms of the rigidity index I_r) of the soil on the pullout capacity of deeply embedded plate anchors.

Chapter 5 focuses on a numerical investigation of the behavior of vertically installed strip plate anchors during rotation and prediction of the irrecoverable loss of embedment that accompanies that rotation, since such loss can lead to significant reductions in the uplift capacity of plate anchors. Therefore, the keying process of plate anchors embedded in uniform sand was simulated using the large deformation finite element analysis made possible by the RITSS technique.

Chapter 6 presents a finite element study investigating the pullout capacity of strip plate anchors in sand at various embedment depths and with inclination angles ranging from 0^o to 90^o, where the pullout direction is centrically perpendicular to the anchor plate face. Parametric finite element analyses are used to introduce simple design charts relating the breakout capacity to the embedment depth and relative density.

Chapter 7 presents the conclusions and recommendations for further work related to this research.

CHAPTER II

LITERATURE REVIEW

2.1 Introduction

A number of previous investigations have been performed to predict the pullout capacity of horizontally and vertically embedded plate anchors in sand, including conventional small-scale laboratory models, centrifuge modeling, limit equilibrium analysis, upper and lower bound limit analysis, and elasto-plastic finite element analyses. The performance of embedded plate anchors in clay have received unlimited coverage in the research literature while attention to plate anchors in sand has been relatively limited, particularly for deeply embedded plates. This chapter presents a brief overview of the main published theoretical, numerical, and experimental research into quantifying of uplift plate anchor capacities in sand, and the anchor keying behavior and post- pullout anchor capacity in sand and clay, estimating the loss of anchor embedment during keying process.

2.2 Uplift Plate Anchor Capacity

The resistance of soil to compression is reasonably well understood while the resistance to uplift is uncertain and there are a number of competing theories reported in the literature (Meyerhof and Adams, 1968). An accurate prediction of the pullout capacity of plate anchor is important for an economical design and stability of the supported structure. Since early of 1960s', a number of previous studies have been performed to determine the uplift capacity of embedded plates anchors in cohesionless soil. The

following sections provide a summary of studies into uplift plate anchor capacities in sand, which is divided into analytical, numerical, and experimental investigations.

2.2.1 Limit Equilibrium Analysis

Several theories have been developed based on limit equilibrium approach to predict the breakout capacity of shallow horizontal plate anchors embedded in different types of soil. The limit equilibrium solution is guided by the deformation mechanisms observed in model tests (Cheuk et al., 2007). This approach assumes a failure surface condition and then the forces acting on that surface are determined. Therefore, the breakout capacity is determined by considering the weight of soil within the failure zone and the friction developed along the failure surface. The limit equilibrium approach assumes that the sliding block at the ultimate load inclined at an angle α to the vertical. The greater the angle α, the more soil to be displaced during pullout, thereby increasing the pullout capacity. Also, a reasonable estimate of lateral earth pressures is needed to quantify the friction forces that acting on the failure surface, therefore contribute to possible increase in pullout capacity. Thus, the shape of the failure zone and the lateral earth pressure estimates were the two main assumptions among the limit equilibrium models that proposed by different researchers. This section presents some limit equilibrium models for the pullout resistance of plate anchors embedded in sand. Generally, for shallow embedment depths, the commonly observed and assumed failure slip surfaces appearing in the literature are shown in Figure 2.1. Some early theories were presented to predict the uplift resistance for embedded circular plate anchors. For all the three failure modes shown in the figure, the failure slip surface at ultimate load starts from

the corner of the plate anchor and extend to the free surface. A critical feature of the failure mode is the angle β (Figure 2.1) at which the failure surface intersects the ground surface. For loose sand and soft clay, β may equals 90º while for dense sand and stiff clay β may be close to 45 – ϕ/2, where ϕ is the friction angle of soil (Das, 1990) and that observed by Dickin (1988) as well.

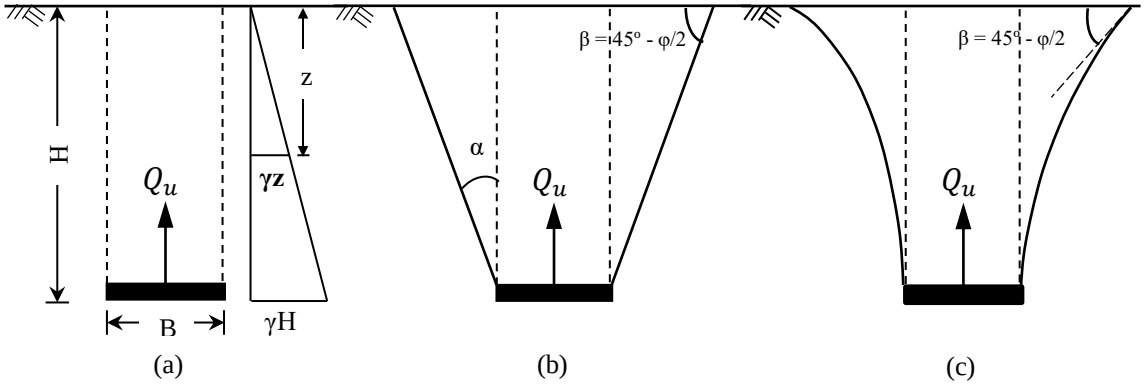

Figure 2.1 Three different failure modes of shallow embedded plate anchors in sand: (a) frictional cylinder; (b) truncated cone; (c) circular failure surface.

However, for relatively deep anchors conditions at ultimate load, local shear failure will be localized around the plate and does not extend to the ground surface. The gross uplift resistance for the given plate anchor in Figure 2.1 can be defined as:

$$Q_{u(gross)} = Q_u + W_{Anchor} \tag{2.1}$$

where Q_u is net uplift anchor capacity, while W_{Anchor} is effective self-weight of the anchor. The net uplift resistance Q_u is a combination of the effective soil weight over the plate anchor and shearing resistance mobilized with a defined failure surface. The first type of failure modes (Figure 2.1a, as indicated by Das 1990) was first proposed by Majer (1955)

to estimate the uplift resistance of shallowly embedded circular plate anchors. He assumed a cylindrical failure surface having a diameter equal to the anchor diameter to predict the uplift capacity. For frictional soils, Q_u is the summation of the weight of the soil mass inside the failure cylindrical surface plus the frictional resistance mobilized along the failure surface.

$$Q_u = \gamma V = \gamma \pi H \frac{B^2}{4} + \int_0^H (\sigma_o' tan\phi) d_z \qquad (2.2)$$

where V is the volume of the soil mass in the truncated cone, γ is the unit weight of soil, H is the embedment depth of anchor, σ_o' is the effective stress at a depth z measured from the ground surface [$\sigma'_o = (\pi B)(\gamma z)$] (Figure 2.1a), and ϕ is the soil friction angle. Simplifying and integration of Eq. 2.2 gives Eq. 2.3

$$Q_u = \gamma \pi H \frac{B^2}{4} + (\gamma \pi B \frac{H^2}{2}) tan\phi \qquad (2.3)$$

When assuming this type of failure mode, the uplift capacity tends to be underestimated because the failure mass mobilized by an anchor is normally larger than the cylinder above the anchor. (Ilamparuthy et al. 2002). Mors (1959) proposed the second type of failure mode at ultimate uplift load Figure 2.1b. He proposed that the failure surface may be approximated as a truncated cone having an apex angle of $\beta = 45^o - \phi/2$. The net uplift resistance Q_u is calculated to be only the weight of soil mass inside the failure surface. The shearing resistance mobilized along the failure surface has been neglected as obvious in Eq. 2.4.

$$Q_u = \gamma V = \gamma\pi \frac{H}{3}\left\{3B^2 + 4H^2 + cot^2(45 - \frac{\phi}{2}) + 6HBcot(45 - \frac{\phi}{2})\right\} \quad (2.4)$$

A similar theory was proposed by Downs and Chieurzzi (1966) but they proposed that the apex angle β equals to 60º. Therefore, the net uplift capacity Q_u becomes as in Eq. 2.5.

$$Q_u = \gamma\pi \frac{H^3}{3}\left\{3B^2 + 1.33H^2 + 3.46H\right\} \quad (2.5)$$

The Mors method is usually too conservative for shallow anchors because it ignores the frictional force along the failure surface. However, it overestimates the pullout capacity for deep anchors where the failure surface normally does not extend to the ground surface and will be smaller than the assumed truncated cone (Liu et al. 2012).

A more complicated failure surface (Figure 2.1c) or Figure 2.2 was first observed by Balla (1961), based on several model field test results in dense sand for shallow circular anchors, and Baker and Kondner (1966). The failure surface in this type is a circular that extends from the edge of the plate and intersects the free surface at an angle of approximately 45º - ϕ/2. The radius of the circle aa' equals to:

$$r = \frac{H}{\sin(45 + \frac{\phi}{2})} \quad (2.6)$$

The net uplift capacity Q_u of an anchor embedded at shallow depth is the sum of the weight of mobilized soil within the failure zone plus the shearing resistance developed along the failure surface and can take the following expression:

$$Q_u = H^3\gamma\left\{F_1(\phi, \frac{H}{D}) + F_3(\phi, \frac{H}{D})\right\} \quad (2.7)$$

where $F_1 + F_3 = Q_u / (H^3\gamma)$; $F_1(\phi, \frac{H}{D}) + F_3(\phi, \frac{H}{D})$ are non-dimensional factors that can be determined using Figure 2.3.

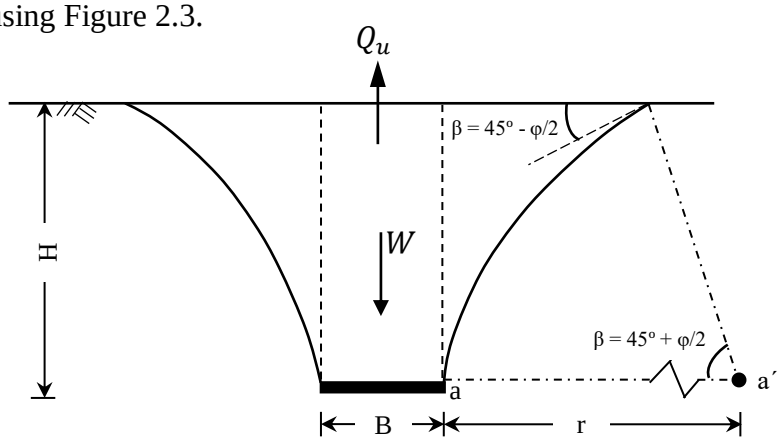

Figure 2.2 Circular arc failure surface (after Bella, 1961).

Das (1990) indicated that Balla's theory is in good agreement for anchors embedded in dense sand at an embedment ratio of $H/D \leq 5$. However, for anchors located in loose to medium sand and with embedment ratio $H/D > 5$, Balla's theory overestimates the net ultimate uplift capacity Q_u. The main reason that the theory is overestimates Q_u for $H/D >$ about 5, even in dense sand, is that it is essentially a deeply embedded anchor and the failure surface does not extend to the soil surface. Based on the experiments that performed by Baker and Kondner (1966) on circular plate anchors embedded in Ottawa dense sand ($\phi = 42^o$), they observed the distinct circular failure surface that was observed by Balla (1961) for $H/D < 6$, while the failure surface was different for $H/D > 6$. They concluded that the analysis of Balla (1961) could be used for anchors of $H/D < 6$.

Several studies developed limit equilibrium models for shallowly embedded, horizontal strip and circular anchors based on observed failure mechanisms from small

scale tests. The following paragraphs summarize the main proposed models by several researchers to predict the vertical uplift capacity of square, rectangular, circular and strip plate anchors in dry sand. It would appear that the lack of agreement on uplift-capacity theory lies in the difficulty of predicting the geometry of the failure zone (Meyerhof and Adams, 1968).

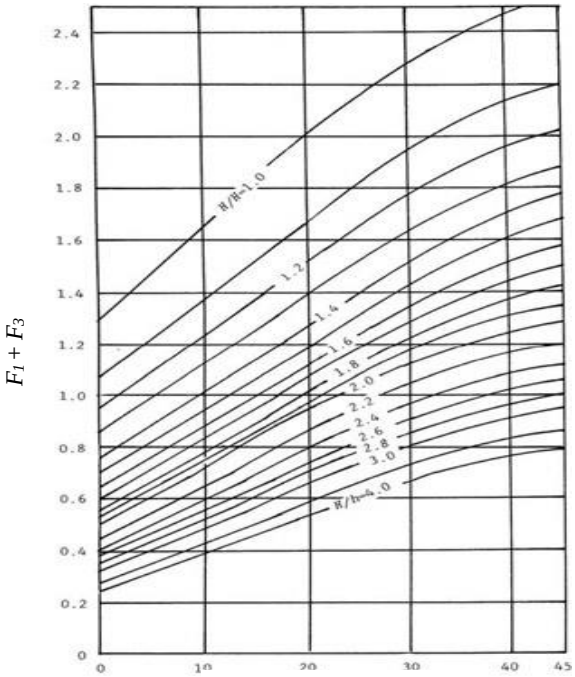

Figure 2.3 Variation of $F_1 + F_3$ based on Balla's theory (1961).

2.2.1.1 Meyerhof and Adams

An approximate general theory of uplift resistance in soil has been developed by Meyerhof and Adams, 1968, which is based on the observations and test data presented by a series of model uplift tests in sand (loose and dense) and clay for strip and rectangular anchors. The study has considered the ultimate uplift capacity of soils under centric

vertical loading relative to the plane of the plate. They found that the uplift resistance is a combination of the soil weight over the foundation and soil shearing resistance mobilized with a defined failure surface. The failure slip surface varies in shape and extent depending on the embedment depth/width ratio, and the rigidity or soil relative density. The theory is derived for a strip and is then modified for circular and rectangular footings and also for group action. A theoretical shape factors are applied to the general expression to account for the three- dimensional effect of individual square or circular footings. The theory is simplified by considering the forces acting on a cylindrical surface above the plate anchor. Also, the actual failure surfaces are simplified because of the complex form of the failure surfaces. Figure 2.4 shows the two distinct failure modes depending on the embedment depth, namely shallow and deep embedment.

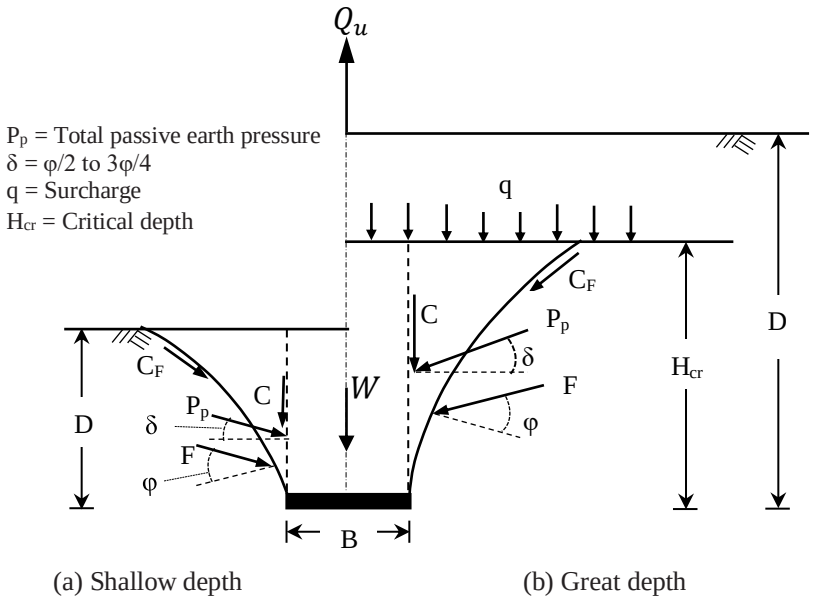

Figure 2.4 Failure of soil above a strip plate anchor under uplift loading based on Meyerhof and Adams (1968).

In bearing-capacity theory the stresses are distributed below the footing in a continuous medium which is assumed to be homogeneous and isotropic: consequently, the geometry of the failure zone is predictable, and consistent with conventional soil mechanics theory. In uplift capacity the stresses are distributed above the footing, and their distribution appears to be uniquely influenced by the surface boundary (Meyerhof and Adams, 1968). In loose sands the increase in uplift capacity with depth is approximately linear and much less than that in dense sand (Meyerhof and Adams, 1968).

2.2.1.1.1 Strip anchor

(a) Shallow embedment

As can be noticed from Figure 2.4, at the net ultimate uplift load Q_u, the failure surface is curved and extends from the corner of the anchor to the free surface. Unit shearing resistance t_f along the failure slip surface includes mobilized a cohesive force C_f and friction force F can be expressed as:

$$t_f = c + \sigma \tan \phi \tag{2.8}$$

where c is unit cohesion, σ is normal stress, and ϕ is the angle of shearing resistance. Form equilibrium, the

$$Q_u = 2C_f \cos\alpha + 2F \cos\beta + W \tag{2.9}$$

W is the total weight of lifted soil mass plus plate anchor, α and β are average inclination with vertical of forces C_f and F respectively. Meyerhof and Adams, 1968 assumed that in the absence of a rigorous solution for the stress on the curved pyramidal failure surface, Q_u can be expressed by:

$$Q_u = 2C + 2P_p \sin\delta + W \tag{2.10}$$

where $C = cD$ = cohesion along vertical plane through footing edge and P_p is the total passive earth pressure inclined at average angle δ acting downward on vertical plane through footing edge. Normal component of total passive earth pressure P_p can be expressed by:

$$P_p \cos\delta = \gamma(D^2/2)K_p \tag{2.11}$$

where K_p coefficient of passive earth pressure. Substituting K_p into Eq. 2.10

$$Q_u = 2cD + \gamma D^2 K_{pv} + W \tag{2.12}$$

where $K_{pv} = K_p \tan\phi$ Test results on model strip plate anchor indicate that, for sands, the average angle of the failure surface with the vertical varies between about $\phi/3$ and $2\phi/3$. For an average value of about $\phi/2$ for this angle, trial calculations have shown that δ is approximately $2\phi/3$. From the corresponding passive earth pressure coefficients K_p, based on curved failure surfaces (Caquot and Kerisel 1949), the vertical component K_{pv} governing the uplift resistance has been evaluated and is shown in Figure 2.5. It is of interest to note that for a given value of ϕ, the value of K_{pv} is not very sensitive to changes of δ in the range of about $\phi/2$ and $3\phi/4$, and the corresponding theoretical failure surface has roughly the observed shape.

For convenience of the analysis and comparison with test results the value of K_{pv}, may be expressed by:

$$K_{pv} = K_u \tan\phi \tag{2.13}$$

where K_u is nominal uplift coefficient of earth pressure on vertical plane through plate anchor edge. Thus Eq. 2.12 becomes

$$Q_u = 2cD + \gamma D^2 K_u \tan\phi + W \tag{2.14}$$

For sands $c = 0$, thus Eq. 2.12 will be:

$$Q_u = \gamma D^2 K_u \tan\phi + W \tag{2.15}$$

The corresponding theoretical values of K_u, are shown in Figure 2.5 and are found to vary from about 0.7 to nearly 1.

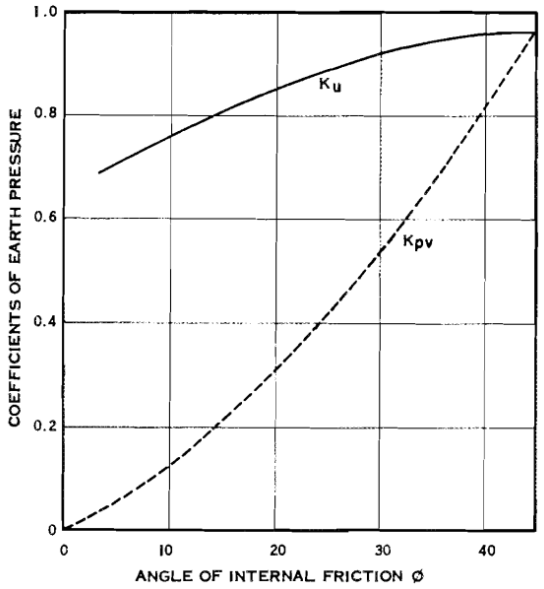

Figure 2.5 Theoretical uplift coefficients of earth pressure for strip footing (after Meyerhof and Adams, 1968).

(b) Deep embedment

For deeper plate anchors, the failure surface in Figure 2.4 does not extend to the ground surface. The extent of this local shear failure may be incorporated in the analysis by limiting the vertical extent H of the failure surface and using the surcharge pressure q

above the level of the failure surface is $q = \gamma(D - H)$. Accordingly, Eq. 2.15 may be modified for great plate anchor depths in sand and written as in Eq. 2.16.

$$Q_u = \gamma H(2D - H)K_u \tan\phi + W \tag{2.16}$$

The magnitude of H can be determined from the observed extent of the failure surface and an analyses of test results is given in Table 2.1.

Table 2.1 The value of *H/B* from test results (after Meyerhof and Adams, 1968).

Friction Angle ϕ (°)	20	25	30	35	40	45	48
Depth *H/B*	2.5	3	4	5	7	9	11

2.2.1.1.2 Circular anchor:

The analysis for strip plate anchor can be modified to circular plate anchor by determining the shearing resistance from cohesion and passive earth pressure inclined at δ on a vertical cylindrical surface through the plate edge (Figure 2.4). Thus, for shallow anchor depths ($D \leq H$), Eqs. 2.10 and 2.14 become:

$$Q_u = \pi BC + s\pi BP_p \sin\delta + W \tag{2.17}$$

or

$$Q_u = \pi cBD + s(\pi/2)\gamma BD^2 K_u \tan\phi + W \tag{2.18}$$

where s = shape factor governing the passive earth pressure on a convex cylindrical wall. Similarly, for great depths ($D > H$), Eq. 2.18 becomes:

$$Q_u = \pi cBH + s(\pi/2)\gamma BH(2D - H)K_u \tan\phi + W \tag{2.19}$$

Test results on model circular plate anchor reviewed below have shown that for sands the average angle of the failure surface with the vertical varies between about $\phi/4$ and $\phi/2$. For an average value of about $\phi/3$, the angle δ is approximately $2\phi/3$ and the

corresponding values of the shape factor *s* can be estimated from approximate earth pressure theories based on plane failure surfaces (Berezantzev 1952 and MacKay 1986). For shallow embedment depths the theoretical results are approximately represented by:

$$s = 1 + mD/B \tag{2.20}$$

where *s* has a maximum value

$$s = 1 + mH/B \tag{2.21}$$

and *H/B* is given in Table 2.1 and the coefficient *m* has the values given in Table 2.2 The corresponding earth pressure coefficients, designated as sK_u are shown in Figure 2.6 for circular plate anchors at shallow and great depths in sands.

Table 2.2 Values of shape factor *s* and coefficient *m* against friction angle. (after Meyerhof and Adams, 1968).

Friction Angle ϕ(°)	20	25	30	35	40	45	48
Coefficient *m*	0.05	0.1	0.15	0.25	0.35	0.5	0.6
Max factor *s*	1.12	1.30	1.60	2.25	3.45	5.50	7.60

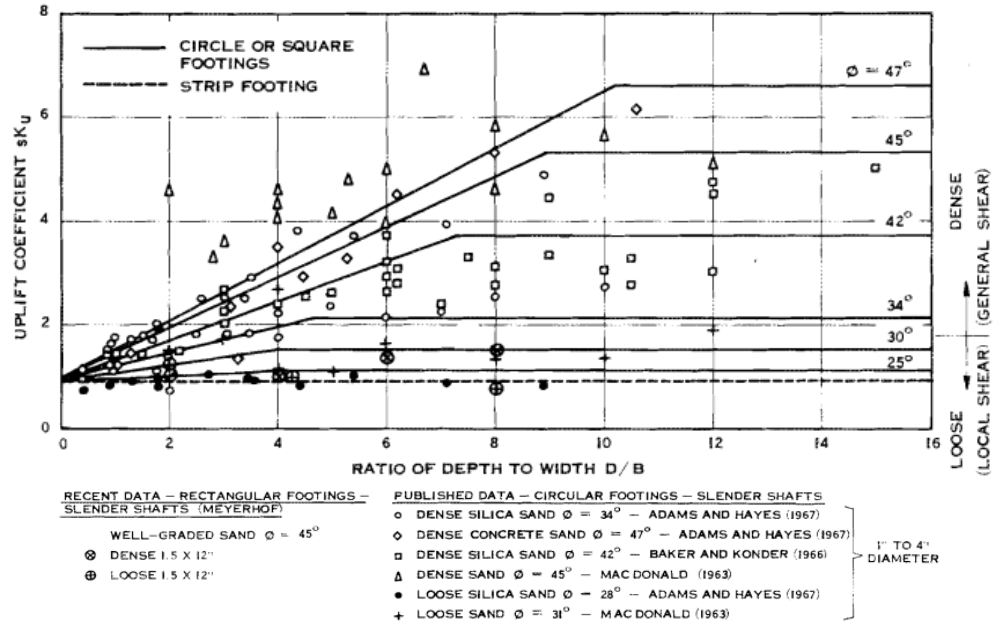

Figure 2.6 Comparison of theory and model tests for plate anchors in sands (after Meyerhof and Adams, 1968).

2.2.1.1.3 Rectangular anchor:

An approximate analysis for the ultimate uplift load of a rectangular footing of width *B* and length *L* can be obtained by assuming that the earth pressure along the perimeter of the two end portions of length *B/2* is governed by the shape factor *s* as for circular anchor, while the passive earth pressure along the central portion of length *L– B* is the same as for a strip footing. On this basis it can be shown that for shallow depths:

$$Q_u = 2c(B+L)D + \gamma D^2(2sB + L - B)K_u \tan\phi + W \tag{2.22}$$

For great depths the following equation applies:

$$Q_u = 2cH(B+L) + \gamma H(2D - H)(2sB + L - B)K_u \tan\phi + W \tag{2.23}$$

For square footings $B = L$ in the above expressions.

Meyerhof (1973) developed the theory of Meyerhof and Adams (1968) to estimate the pullout capacity of shallow inclined strip plate anchors subjected to an axial pullout force (Figure 2.7) by using active and passive earth pressure theory. The following relationship was proposed by Meyerhof to estimate the breakout factor for inclined plate anchor at inclination angle θ between angles 0° and 90° for embedment depth ratios ranging from 1 to 10. (Das, 1990).

$$N_\gamma = \frac{1}{2}K_b\left(\frac{H_c}{B}\right)\left(1 + \frac{1}{2H_c/B}sin\theta\right)^2 + \left(1 + \frac{1}{2H_c/B}sin\theta\right)cos^2\theta \tag{2.24}$$

K_b is an uplift coefficient that is determined from the earth pressure coefficients for an inclined wall (Caquot and Kerisel 1949) as shown in Figure 2.8 for the values of θ = 0°, 45°, 75° and 90°, and θ is the inclination angle of plate anchor with respect to horizontal.

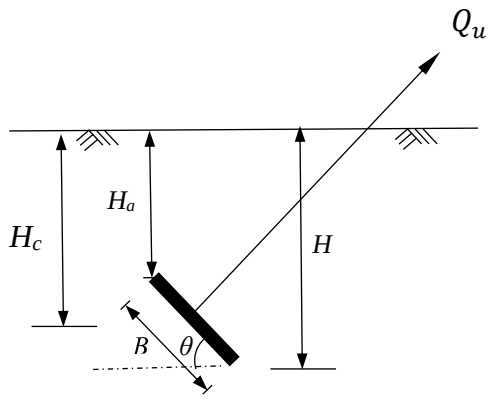

Figure 2.7 Inclined shallow strip anchor plate.

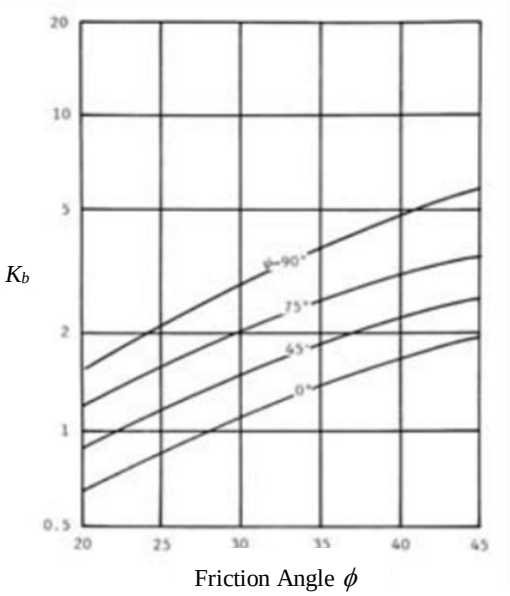

Figure 2.8 Variation of Meyerhof's earth pressure coefficient K_b(after Das 1990)

2.2.1.2 Murray and Geddes 1987

Murray and Geddes (1987) developed a limit equilibrium model for the vertical uplift of shallow strip and circular anchors in dense and medium sand. Figure 2.9 illustrates the failure mechanism considered for the limit equilibrium method. Figure 2.9 shows that the failure surface starts vertical at the edge of the plate anchor and then curves as it reaches to the soil surface. The failure surface meets the vertical at an angle of $\phi/2$. The net ultimate uplift resistance is then determined by the weight of soil vertically above the plate (W_{bd}) added to twice the sum of the weight of soil contained in wedge abc (W_w) and the vertical component of the shearing resistance force (F). Murray and Geddes (1987) developed the following dimensionless form of the ultimate uplift resistance for strip and circular anchors:

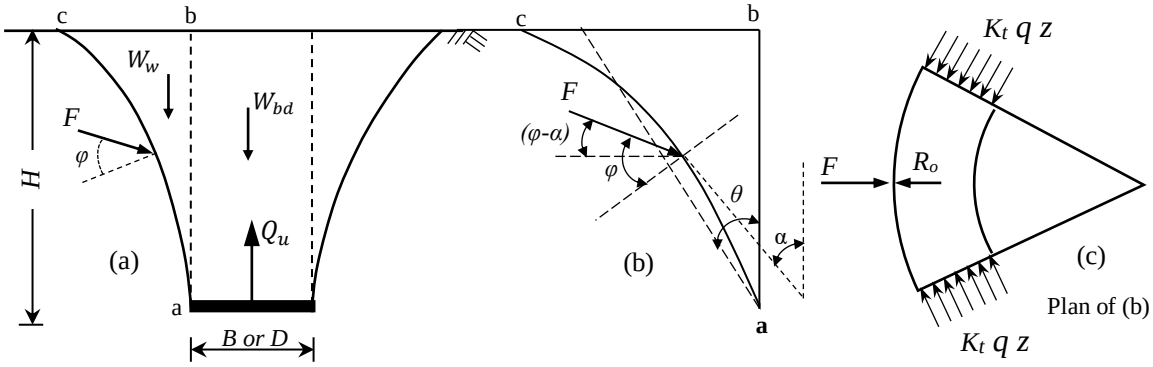

Figure 2.9 Definition of parameters in equilibrium analysis (after Murray and Geddes, 1987).

(a) Strip anchor

$$\frac{P}{\gamma BH} = 1 + \left(\frac{H}{B}\right)\left[\frac{\tan\phi \tan\delta_w}{\tan\delta_w - \tan(\phi - \alpha)}\right] \tag{2.25}$$

where $\phi \geq \delta_w \geq (\phi - \alpha) \geq 0$. If the $\alpha = \theta$ is adopted and this requires a straight- line failure configuration, the analysis is simplified and $\phi \geq \theta \geq 0$. Thus, limits can be placed on the uplift capacity.

$$1 \leq \frac{P}{\gamma BH} \leq 1 + \left(\frac{H}{B}\right)\tan\phi \tag{2.26}$$

The lower limit of the ultimate uplift resistance is obviously unrealistic and implies that it is equal to the weight of soil vertically above the plate. A practical approach would be to take an average value of $\alpha = \theta = \phi/2$ and a mid-range value of $\delta_w = 3\phi/4$. Therefore Eq. 2.25 may be rewritten:

$$\frac{P}{\gamma BH} = 1 + \left(\frac{H}{B}\right)\left[\sin\phi + \sin\frac{\phi}{2}\right] \tag{2.27}$$

(b) Circular anchor

The ultimate uplift resistance may be written in dimensionless form as:

$$\frac{P}{\gamma BH} = 1 + \left(\frac{2H}{D}\right)\left[\frac{\tan\phi \tan\delta_w}{\tan\delta_w - \tan(\phi - \alpha)}\right]\left[1 + \frac{2H}{3D}\left\{\tan\theta + K_t \tan(\phi - \alpha)\right\}\right] \quad (2.28)$$

where $\phi \geq \delta_w \geq (\phi - \alpha) \geq 0$. If the $\alpha = \theta$ is adopted this requires a straight- line failure configuration, and the analysis is simplified and $\phi \geq \theta \geq 0$. Thus, limits can be placed on the uplift capacity.

$$1 \leq \frac{P}{\gamma BH} \leq 1 + \left(\frac{2H}{D}\right)\tan\phi\left[1 + \frac{2H}{3D}\tan\phi\right] \quad (2.29)$$

The lower limit of the ultimate uplift resistance is obviously unrealistic and implies that it is merely equal to the weight of soil vertically above the plate. A practical approach would be to adopt Eq. 2.28 and take an average value of $\alpha = \theta = \phi/2$ and a mid-range value of $\delta_w = 3\phi/4$ as for strip anchor case. They assumed the lateral earth pressure coefficient K_t equals to at rest condition $K_o = 1 - \sin\phi$ to estimate the lateral earth pressure that acting along the failure surface at the ultimate load. Thus

$$\frac{P}{\gamma AH} = 1 + 2\left(\frac{H}{D}\right)\left[\sin\phi + \sin\frac{\phi}{2}\right]\left[1 + \frac{2H}{3D}\tan\frac{\phi}{2}(2 - \sin\phi)\right] \quad (2.30)$$

where P is the ultimate uplift resistance of circular anchor or ultimate uplift resistance per unit length of strip anchor, A is the plan area of circular anchor, B is the width strip anchor, D is the diameter of circular anchor, H is the depth of embedment, ϕ is the angle of shearing resistance, γ is the unit weight of soil α is the angle made by the tangent to the vertical, and δ_w is the inclination of the resultant forces W_w and F to the horizontal in Figure 2.9a.

2.2.1.3 White et al., 2008

A limit equilibrium solution was adopted by White et al., 2008 for the prediction of ultimate uplift resistance of pipe and horizontal plate anchor embedded in sand. This solution assumes that an inverted trapezoidal block (Figure 2.10) is lifted above the anchor. The shear planes on each side of the block are inclined at the angle of dilation ψ, which is consistent with experimental observation by Cheuk et al. (2007) and Lui et al, 2012. The uplift resistance is simply the weight of the lifted soil. Hence, from the area of the trapezium of soil above the plate anchor, the uplift resistance is given by Eq. 2.31, which is the upper limit of the ultimate uplift resistance for Murray and Geddes (1987) as in Eq. 2.26.

$$\frac{P}{\gamma' BH} = 1 + \left(\frac{H}{B}\right)\tan\phi_p \tag{2.31}$$

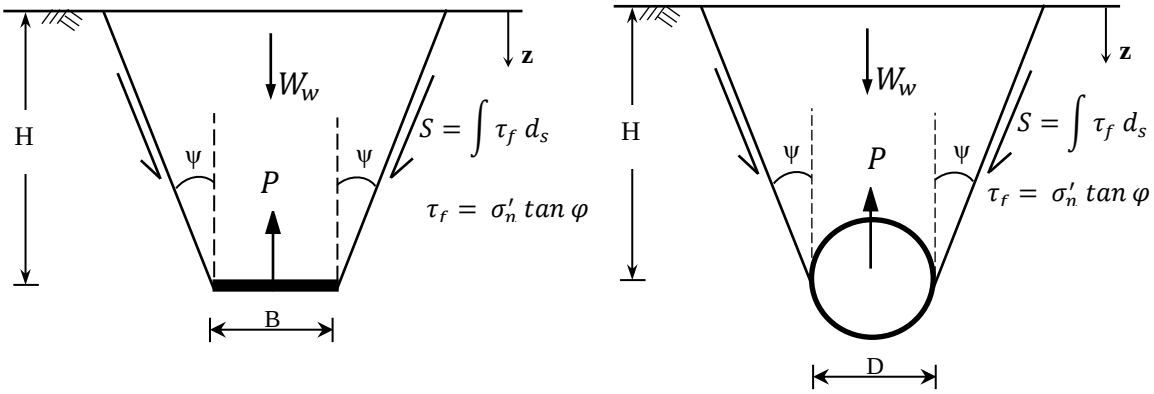

Figure 2.10 Sliding block mechanism with shear planes at ψ with vertical for strip plate and pipe geometry (after White et al. 2008).

The limit equilibrium approach has the advantage that normality can be neglected, and the assumed failure mechanism can be tuned to match experimental observations. The limit equilibrium solution adopted by White et al., 2008 assumes that shear planes on each side

of the failure block are inclined at the angle of dilation ψ. The uplift resistance was computed by considering the weight of soil within the trapezoidal failure zone and the shear resistance along the two inclined sliding planes. Determining of the weight of the mobilized soil block is straightforward while an assumption regarding the distribution of normal stress (and hence shear resistance) along the slip planes must be proposed. White et al., 2008 assumed that the normal stress on the sliding planes is equal to the values at K_o conditions using Mohr's circle shown in Figure 2.11, implying that the normal stress on the failure surface does not change throughout deformation.

An increase in vertical stress in the sliding planes is permitted, as shown by the larger Mohr's circle representing the conditions at peak resistance. From the geometry of these two Mohr's circles, the peak mobilized shear stress along the slip surface can be calculated as in Eq. 2.32.

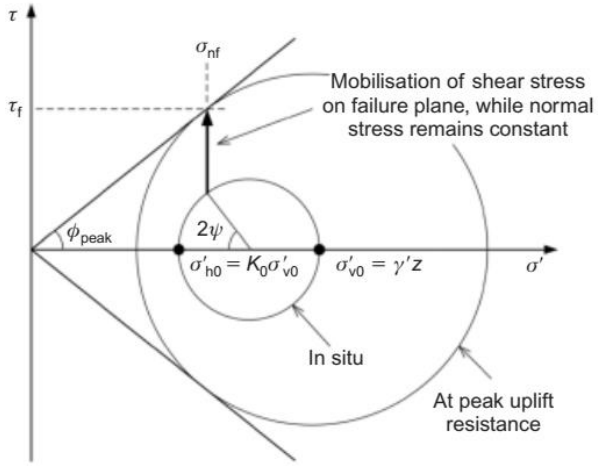

Figure 2.11 Assumed Mohr's circles in situ and at peak uplift

$$\tau_f = \gamma' z \tan\phi_p \left\{ \frac{(1+K_o)}{2} - \frac{(1-K_o)}{2} cos2\psi_p \right\} \quad (2.32)$$

By integrating τ_f in Eq. 2.32 above along the failure surface and equating the vertical forces acting on the sliding block, the peak uplift force per unit length, *P*, is calculated as:

$$P = \gamma' HB + \gamma' H^2 \tan\psi_p + \gamma' H^2 (\tan\phi_p - \tan\psi_p)\left\{\frac{(1+K_o)}{2} - \frac{(1-K_o)}{2} cos2\psi_p\right\} \quad (2.33)$$

Eq. 2.33 can be normalized to obtain a dimensionless breakout factor, N_γ, which is a function of the embedment depth *H/B* and an uplift factor F_{ps}:

$$N_\gamma = \frac{P}{\gamma' BH} = 1 + F_{ps}\left(\frac{H}{B}\right) \quad (2.34)$$

$$F_{ps} = \tan\psi_p + (\tan\phi_p - \tan\psi_p) \times \left\{\frac{(1+K_o)}{2} - \frac{(1-K_o)}{2} cos2\psi_p\right\} \quad (2.35)$$

The limit equilibrium solution includes three independent variables: (a) the peak friction angle ϕ_p (b) the peak dilation angle ψ_p, and (c) the effective unit weight γ'. If we assume the normality condition ($\phi_p = \psi_p$), Eq. 2.33 reduces to the simple upper-bound solution given by Eq. 2.31.

2.2.1.4 Giampa 2014 and Giampa et al., 2017

Giampa, 2014 proposed a new axisymmetric (as) model for helical anchors using non-associated flow limit equilibrium model adapted by White et al. (2008), which it is assumed that the sliding planes is inclined at an angle equal to the dilation angle ψ. Therefore, the weight of the soil wedge W_w plus the resistance along the failure surface will represent the breakout capacity of circular plate anchor. The weight of the truncated cone of the soil wedge is defined by Eq. 2.36. Giampa, 2017 also assumed (as White el., 2008) that the normal stress on the sliding planes is equal to the values at K_o conditions

and does not change during uplift loading. Consistent with the assumptions made by White et al., 2008, only frictional energy dissipation is considered on the failure surface. Thus the peak-mobilized shear stress (τ_f) can be determined by Eq. 2.37:

$$W_w = \frac{1}{3}\gamma'\pi H\left\{\left(\frac{D}{2}+H\tan\psi_p\right)^2+\frac{1}{2}D^2+\frac{1}{2}DH\tan\psi_p\right\} \tag{2.36}$$

$$\tau_f = \gamma' z\tan\phi'_p\left\{\frac{(1+K_o)}{2}-\frac{(1-K_o)}{2}cos2\psi_p\right\} \tag{2.37}$$

Through integration of τ_f in Eq. 2.37 along the failure surface and equating the vertical forces acting on the sliding block, the peak uplift resistance, *P*, is defined as:

$$\begin{aligned} P = {} & \frac{1}{3}\gamma'\pi H\left\{\left(\frac{D}{2}+H\tan\psi_p\right)^2+\frac{1}{2}H^2+\frac{1}{2}DH\tan\psi_p\right\}+ \\ & \gamma'\pi H^2\tan\phi_p\left\{\frac{(1+K_o)}{2}-\frac{(1-K_o)}{2}cos2\psi_p\right\}\left\{\frac{D}{2}+H\tan\psi_p-\frac{2}{3}H\tan\psi_p\right\} \end{aligned} \tag{2.38}$$

Normalized form of Eq. (2.38), N_γ, for circular plate anchor is expressed by Eq. 2.39 to be as a function of embedment ratio (*D/B*) and uplift factors (F_{as1}, F_{as2}):

$$N_\gamma = 1+F_{as1}\left(\frac{H}{B}\right)+F_{as2}\left(\frac{H}{B}\right)^2 \tag{2.39}$$

$$F_{as1} = 2\left[\tan\psi_p+(\tan\phi'_p-\tan\psi_p)C_1\right] \tag{2.40}$$

$$F_{as2} = \frac{4}{3}\left[\tan\psi_p{}^2+(\tan\phi'_p-\tan\psi_p)\tan\psi_p C_1\right] \tag{2.41}$$

$$C_1 = \left\{\frac{(1+K_o)}{2}-\frac{(1-K_o)}{2}cos2\psi_p\right\} \tag{2.42}$$

where; *D* is the anchor diameter, *H* is the embedment depth, F_{as1} and F_{as2} are uplift factors, K_o is the coefficient of lateral earth pressure at-rest condition, γ' is the effective unit weight,

ψ_p is the peak angle of dilation, and ϕ'_p is the peak friction angle. Afterwards**,** Giampa et al., 2017 reassessed the constant C_1 for axisymmetric (as) condition for circular plate anchor by interpreting previous analyses on strip plate anchors (ps) in a non-associated frictional soils *NAF* performed by several authors. Relevant conclusions from previously strip plate anchor analyses included the following:

- Initial at rest earth pressure coefficient (K_o) has a minor effect on uplift resistance (Rowe and Davis 1982).
- When $\psi_p = 0$, $F_{ps} \approx \sin \phi'_p$, *i.e.*, $C_1 = \cos \phi'_p$ (Rowe and Davis 1982; Vermeer and Sutjiadi 1985; Koutsabeloulis and Griffiths 1989).
- When $\psi_p = \phi'_p$, $F_{ps} \approx \tan \phi'_p$, *i.e.*, $C_1 = 1$ (Rowe and Davis 1982; Vermeer and Sutjiadi 1985; Murray and Geddes 1987; Smith 1998; Koutsabeloulis and Griffiths 1989; White et al. 2008; Smith 2012).

Based on the above review of the previous studies, Giampa et al., 2017 assumed that C_1 can be taken as:

$$C_1 = cos(\phi_p - \psi_p) \tag{2.43}$$

Thus, the friction coefficient equals ($\tan \phi'_p - \tan \psi_p$), and the peak-mobilized shear stress (τ_f) can be defined by Eq. 2.44:

$$\tau_f = C_1 \gamma' z(\tan \phi'_p - \tan \psi_p) \tag{2.44}$$

Integrating Eq. 2.44 along the failure surface and combining with Eq. 2.36, the breakout factor for circular plate anchor can be simplified to:

$$N_\gamma = 1 + F_{as1}\left(\frac{H}{B}\right) + F_{as2}\left(\frac{H}{B}\right)^2 \tag{2.45}$$

$$F_{as1} = 2\left[\tan\psi + (\tan\phi'_p - \tan\psi)C_1 \right] = 2F_{ps} \tag{2.46}$$

$$F_{as2} = \frac{4}{3}\left[\tan\psi^2 + (\tan\phi'_p - \tan\psi)\tan\psi C_1 \right] = \frac{4}{3}F_{ps}\tan\psi \tag{2.47}$$

where F_{as1} and F_{as2} are uplift factors for axisymmetric conditions and F_{ps} is the uplift factor for plane strain condition that obtained by White et al. (2008). As with the plane strain solution discussed by White et al. (2008), the combination of Eq. 2.45 with Eqs. 2.46 and 2.47 become the upper bound (*UB*) solution when assuming associated flow material (*AF*). For the *UB* solution F_{ps} = tan ϕ'_p, F_{as1} = 2tan ϕ'_p, and F_{as2} = 4/3tan$^2\phi'_p$, which is in agreement with a reorganization of the *UB* solution of Murray and Geddes (1987). Giampa et al., 2017 performed an experimental study for 22 intermediate-scale, helical anchors installed in dry sand to develop and validate an analytical expression that will accurately predict the uplift capacity of shallow circular anchor. Three test trenches were prepared to different dry unit weights (γ) with peak friction angles range between 40° and 50°, while laboratory triaxial tests indicated that the dilation angle varied between 10° and 25° for these peak friction angles. Anchor depth to diameter ratios (*H/D*) varied from 1.8 to 7.1. Comparison of analytical with experimental results gives confidence in the further application of the non-associated limit equilibrium analytical solution presented in this study. Analyses involving that shear planes on each side of the failure block are inclined at the angle of dilation ψ yield the following simple relation which proposed by Vermeer and Sutjiadi (1985) for the breakout factor of strip plate anchor embedded in sand:

$$N_\gamma = 1 + \frac{H}{B} \tan \phi_{ps} \cos \phi_{cv} \quad (2.48)$$

In which $\phi_{ps,}$ ϕ_{cv} are the peak and critical state friction angle in plane strain.

2.2.2: Plastic Limit Analysis Method

Limit analysis is an alternative method, based on the theory of plasticity, to predict the ultimate uplift resistance of plate anchor. Comparing to limit equilibrium method, a limit analysis method does not give an exact prediction of the net uplift capacity Q_u but provide a bounded solution. This section presents some main limit analysis studies of the pullout capacity of plate anchors in cohesionless soil. Generally speaking, the upper bound theorem is applied more frequently than the lower bound theorem when analyzing soil behavior and the main reason for this is, in many cases, it is difficult to construct a statically admissible stress field that extends to infinity. In contrast, it is usually easier to construct a kinematically admissible upper bound failure mechanism [John W. Bull, 2009]. The upper bound theorem has been utilized by several authors to estimate the pullout capacity of plate anchors embedded in cohesionless soils including Murray and Geddes (1987, and 1989), Regenass and Soubra (1995), and Kumar (1999). The upper bound solution is obtained by equating the work done by external forces, which is determined by multiplying the vertical component of displacement by the soil's self-weight, to the dissipation of energy (which is zero for the cohesionless soil because the displacement vector is perpendicular to the frictional resistance force on any discontinuity), and then using a suitable minimization algorithm to determine the collapse load.

2.2.2.1 Murray and Geddes (1987)

Murray and Geddes (1987) developed a limit analysis approach to estimate the uplift capacity of strip, circular, and rectangular plate anchors embedded in sand.

(a) Strip anchor

The ultimate uplift resistance of a strip anchor based on limit analysis solution performed by Murray and Geddes (1987) was represented by the following dimensionless form. There has been a poor lower bound solution because there is a difficulty in determining an effective means of altering the stress field that should not violate yield condition anywhere and equilibrium should be maintained throughout the soil mass (Figure 2.12a). This gives the breakout resistance as equal to the lower limit of Eq. 2.26. As mentioned earlier, that for frictional materials obeying an associated flow rule ($\phi = \psi$), there is no dissipation during shear or on sliding planes, so for an upper bound solution it is necessary to find the minimum value of loading computed for defined failure mechanism, and then to examine different failure mechanism in similar way to evaluate as close bound as possible to the ultimate uplift resistance in the idealized material. The following upper bound solution (Eq. 2.49) was obtained by equating the work done by external forces to the dissipation of energy for Figure 2.10b.

$$\frac{P}{\gamma BH} = 1 + \frac{H}{B} \times \left\{ \frac{\tan(\phi+\omega)\tan(\beta-\omega) - \tan\omega\tan(\beta-\omega-\phi)}{\tan(\phi+\omega) + \tan(\beta-\omega-\phi)} \right\} \tag{2.49}$$

It is obvious from Figure 2.12b that the larger value of β the greater value of $\frac{P}{\gamma BH}$. The smallest possible value of $\frac{P}{\gamma BH}$ must be found. Since $(\beta - \omega - \phi) \geq 0$, the minimum value is given by $\beta = \omega + \phi$ and Eq. 2.27 will be reduced to the upper limit of Eq. 2.26. Murray

and Geddes, 1987 proposed that the failure boundaries consist of two straight lines inclined at an angle ϕ to the vertical at the plate edges as shown in Figure 2.1b and that will provide a minimum upper bound solution for the problem because it was difficult to imagine any other failure mechanism that leads to a lower ultimate uplift resistance.

(b) Circular anchor

Lower bound solution for circular anchor also brought a poor lower bound value such as for strip anchor. This solution is given by the lower limit of Eq. 2.29. The failure boundaries of the minimum upper bound solution appear to be a straight-line incline at angle φ to the vertical at the plate edge. The upper bound solution is equal to the upper

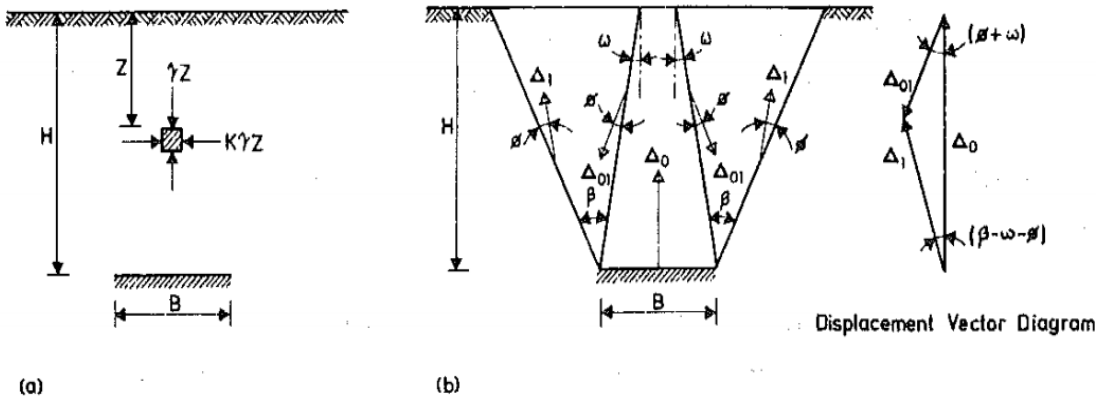

Figure 2.12 Limit analysis solutions: (a) Lower bound solution; (b) Upper bound failure mechanism (after Murray and Geddes, 1989).

(c) Rectangular anchor

Similarly, the upper bound solution of rectangular plate anchor for the uplift resistance is given as follows

$$\frac{P}{\gamma BH} = 1 + \frac{H}{B}\tan\phi\left\{1 + \frac{B}{L} + \frac{\pi H}{3L}\tan\phi\right\} \tag{2.50}$$

2.2.2.2 Murray and Geddes (1989)

Murray and Geddes (1989) used the limit analysis of soil plasticity to estimate the passive resistance of inclined strip anchors in cohesionless soil. The following lower bound solution (Eq. 2.51) is the ultimate passive resistance for a strip plate anchor pulled horizontally. Figure 2.13 indicates a simple admissible stress field that should not violate yield condition anywhere and equilibrium should be maintained throughout the soil mass.

$$\frac{P}{\gamma BH} = K_p \left\{ 1 - 0.5 \frac{B}{H} \right\} \tag{2.51}$$

where P is the ultimate passive resistance per unit length of anchor and K_p is the coefficient of passive resistance. There are difficulties in altering the stress field to formulate a lower bound solution for inclined or horizontal anchors because interface friction, which give rise to energy dissipation, is called into play and this invalidates the analysis.

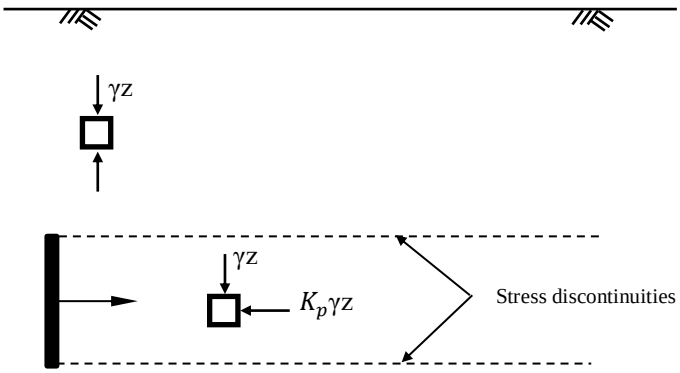

Figure 2.13 Lower bound solution for a strip anchor pulled horizontally (after Murray and Geddes, 1989).

Murray and Geddes (1989) examined two mechanisms in developing an upper bound solution to determine a valid collapse load mechanism such that the displacement field throughout is continuous. The interface friction between anchor plate and soil

(smooth or rough) can be taken into consideration by following the method proposed by Drucker (1954) and allowing dilation on the interface. Therefore, the displacement vector is inclined to this interface at the angle of interface friction δ. The following upper bound solution for mechanism 1 is shown in Figure 2.14.

$$\frac{P}{\gamma BH} = -\frac{W_1 + W_2 + W_3}{\gamma BH\Delta_1}\left\{\frac{\cos\delta}{\cos(\rho+\delta)}\right\} \tag{2.52}$$

where W_1, W_2, *and* W_3 denote the work done by the soil's weight in the regions of the proposed failure mechanism.

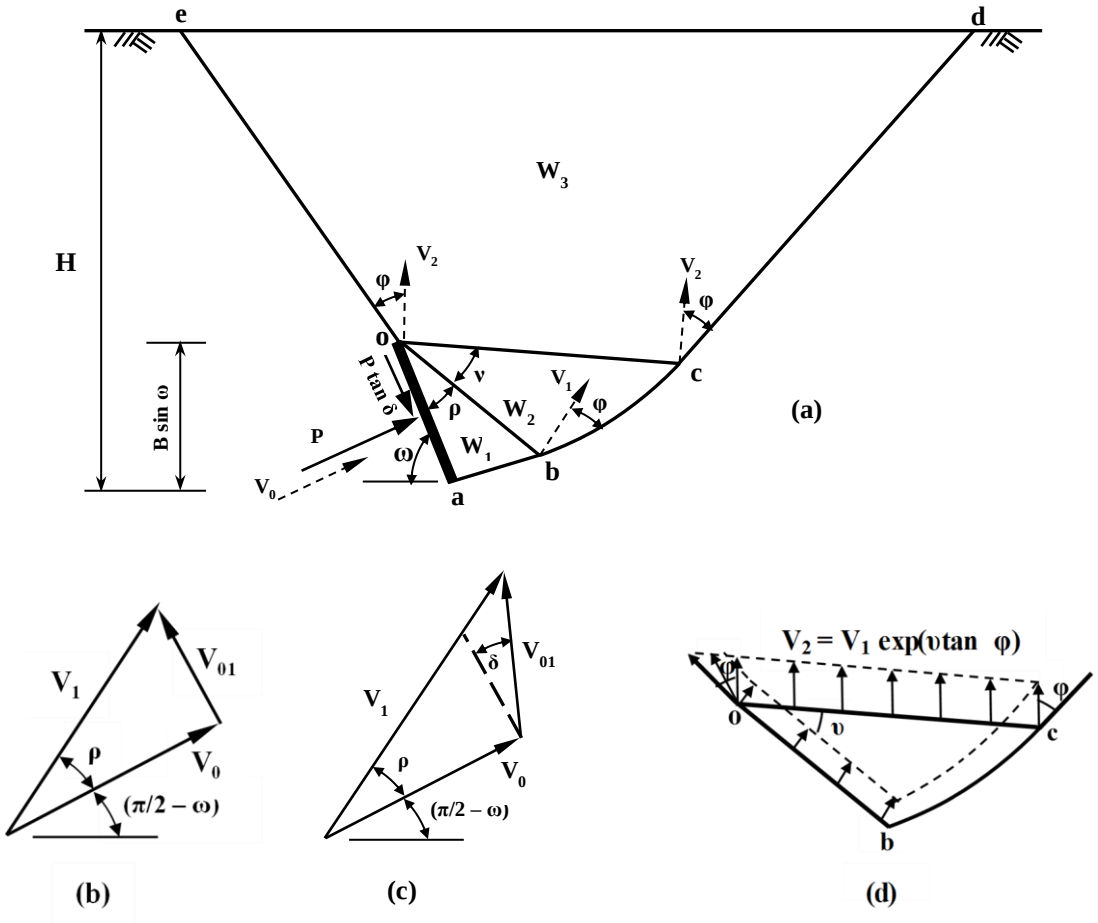

Figure 2.14 Upper bound mechanism 1: (a) overall scheme; (b) vector displacement diagram for $\delta = 0$; (c) vector displacement diagram for $\delta > 0$; (d) log spiral zone abc (after Murray and Geddes, 1989).

For mechanism 2 that shown in Figure 2.15, the upper bound solution for the collapse load as follows:

$$\frac{P}{\gamma BH} = -\frac{W_1 + W_2}{\gamma BH\Delta_1}\left\{\frac{\sin(\lambda+\phi+\omega-\delta)}{\sin^2(\lambda+\phi+\omega)\cos\delta}\right\} \tag{2.53}$$

where W_1 and W_2 denote the work done by the soil's weight in the 2 regions of the proposed failure mechanism 2. For a given mechanism, it is necessary to calculate the minimum solution.

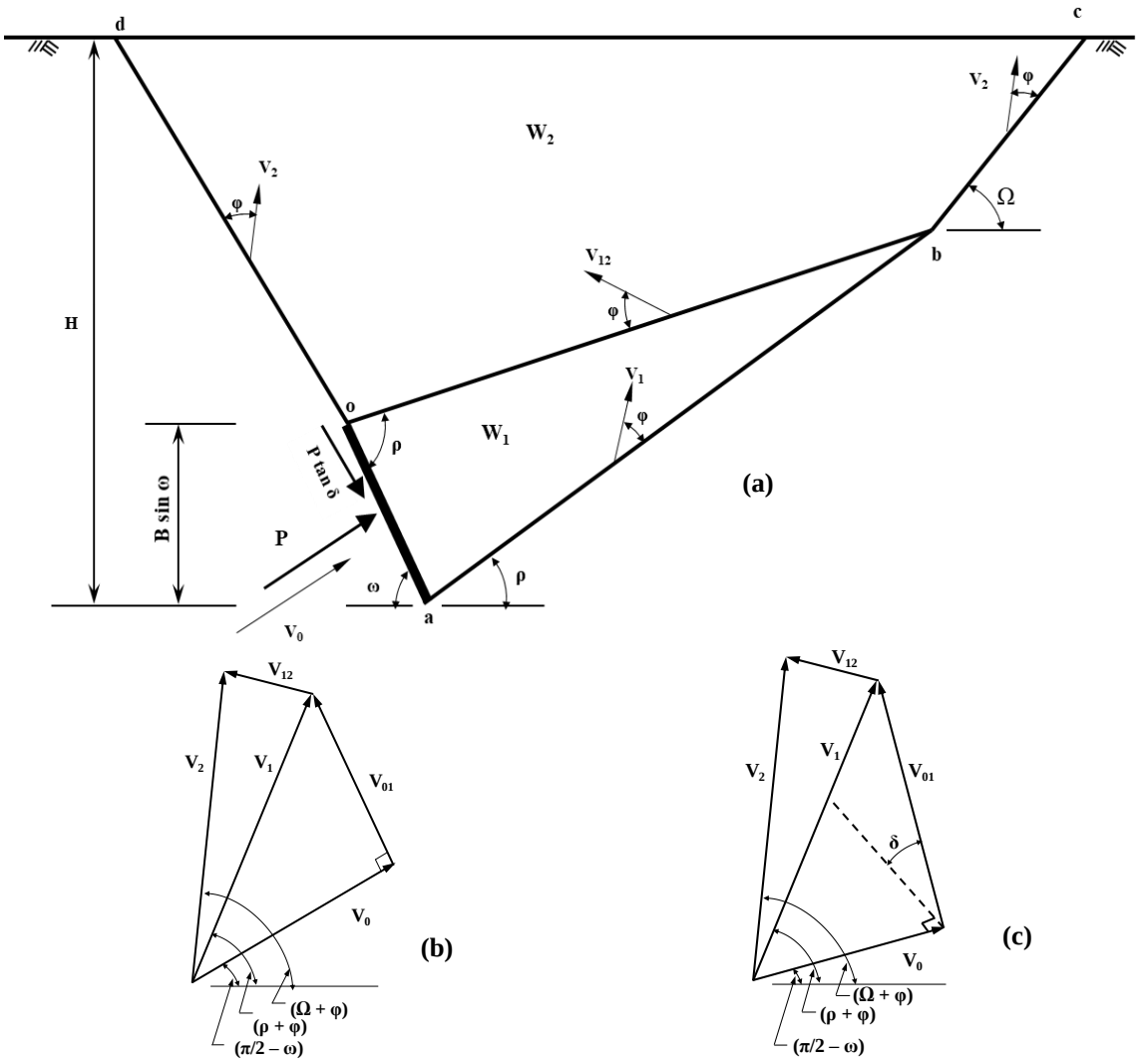

Figure 2.15 Upper bound mechanism 2: (a) overall scheme; (b) vector displacement diagram for $\delta = 0$; (c) vector displacement diagram for $\delta > 0$ (after Murray and Geddes, 1989).

2.2.2.3 Kumar (2003) & Kumar (2014)

Kumar (2003) performed upper bound limit analysis to determine the vertical uplift capacity of shallow strip and circular plate anchors embedded horizontally in a two layered sand. He established uplift factors f_γ and f_q due to the effects of soil unit weight and surcharge load respectively. The collapse mechanism shown in Figure 2.16 was assumed to be a combination of different rigid blocks bounded by linear rupture / velocity discontinuity lines. For the critical collapse mechanism, the entire soil wedge lying above the anchor moves as a single rigid block with the same anchor velocity and the magnitudes of the relative velocities vectors (V_{10}, V_{20}, *and* V_{12}) shown in Figure 2.16 become simultaneously zero and that was similar to what Murray and Geddes (1987) observed for the pullout capacity of anchors embedded in homogenous soil. He noticed that for a given thickness of two layers, the uplift factor f_γ is comparatively greater when the anchor is embedded in dense sand underlying a loose sandy layer. Also, Kumar (2003) found that uplift factors for circular anchors much higher than for strip anchors.

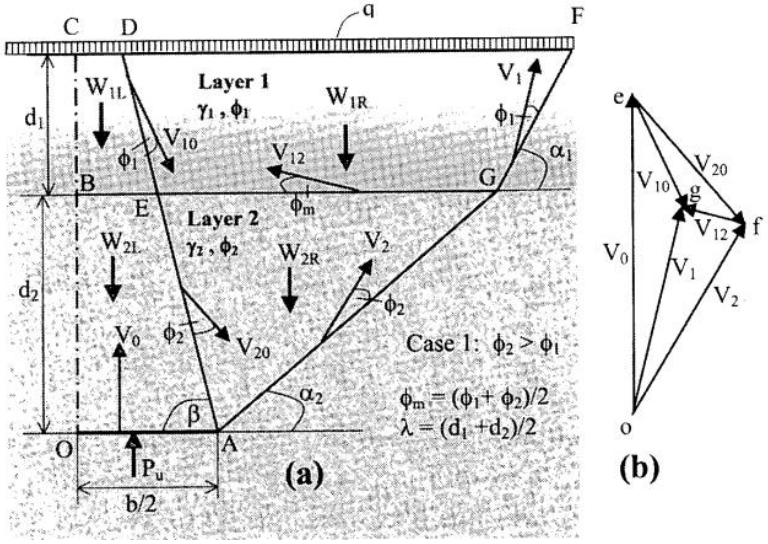

Figure 2.16 Collapse mechanism and velocity hodographs (after Kumar, 2003).

Kumar (2014) using lower bound analysis in combination with finite elements and linear optimization to evaluate the pullout capacity of an inclined strip plate anchor embedded in sand. The pullout resistance results presented in terms of breakout factors by changing the plate inclination angle (θ) from horizontal to vertical. The results showed that the breakout factors, with different combination of embedment depth *H/B*, soil friction angle ϕ, and δ/ϕ, where δ is anchor soil interface friction angle, significantly increase with increasing the horizontal inclination of the plate particularly for $\theta > 30^{o}$. Also, they found that for $\theta < 30^{o}$, the roughness of the plate anchor does not have a significant effect either on the pullout capacity and failure mechanism.

2.2.2.4 Bhattacharya and Kumar (2014)

Bhattacharya and Kumar (2014) performed lower bound analysis in combination with finite elements and linear optimization to determine the pullout capacity of an inclined strip plate anchor embedded in sand. The pullout resistance results presented in terms of breakout factors by changing the plate inclination angle (θ) from horizontal to vertical. The results showed that the breakout factors, with different combination of embedment depth *H/B*, soil friction angle ϕ, and δ/ϕ, where δ is anchor soil interface friction angle, significantly increase nonlinearly with increasing the horizontal inclination of the plate particularly for $\theta > 30^{o}$ as shown in Figure 2.17. Also, they found that for $\theta < 30^{o}$, the roughness of the plate anchor does not have a significant effect either on the pullout capacity and failure mechanism.

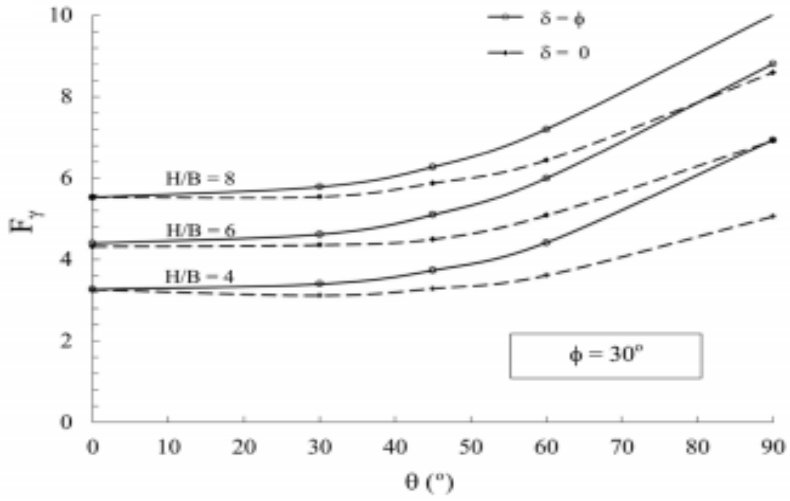

Figure 2.17 Variation of breakout factor F_γ with inclination angle θ for smooth and rough anchor plates of the plate for (H/B = 4, 6, and 8 for ϕ = 30°) (after Bhattacharya and Kumar, 2014).

2.2.2.5 Merifield and Sloan (2006) & Merifield et al., 2003

Merifield and Sloan (2006) performed rigorous lower and upper bound solutions in combination with finite element analyses to estimate the pullout capacity of horizontal and vertical strip plate anchors embedded in sand. Considerations have been highlighted to the effect of soil friction angle, soil dilation, embedment depth, and anchor roughness. The results revealed that the range of N_q values between the lower and upper solution increased as the friction angle increased (Figure 2.18). They also found that the effect of anchor roughness on pullout capacity was a very little for horizontal anchors at all embedment depths while there was a significant effect for vertical anchors especially for shallow embedment depths. The results revealed that the failure mode for vertical anchors indicates active zone of failure behind the anchor especially for $H/B \leq 2$ and for low values of ϕ while for $H/B > 2$, any active zone behind the anchor has little influence on the pullout

capacity while the failure mode of horizontal anchor consists of the upward movement of a rigid column of soil immediately above the anchor which is accompanied by lateral displacement extending out and upwards from the anchor edge and as the anchor pulled vertically upwards, the material above the anchor tends to lock up as it attempts to dilate during deformation (Figure 2.19).

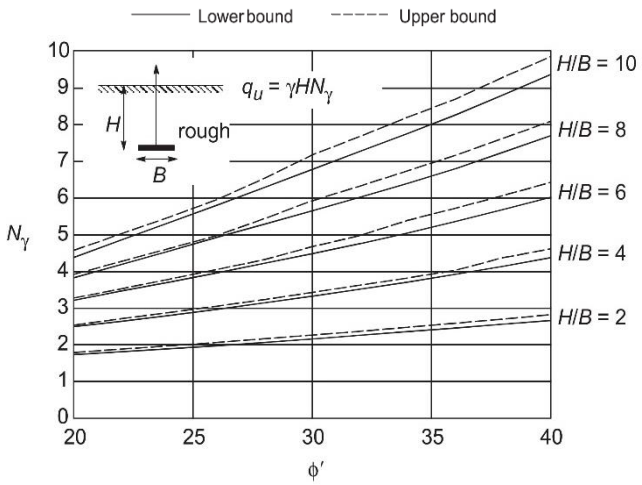

Figure 2.18 Breakout factors for horizontal anchors in sand (after Merifield and Sloan 2006).

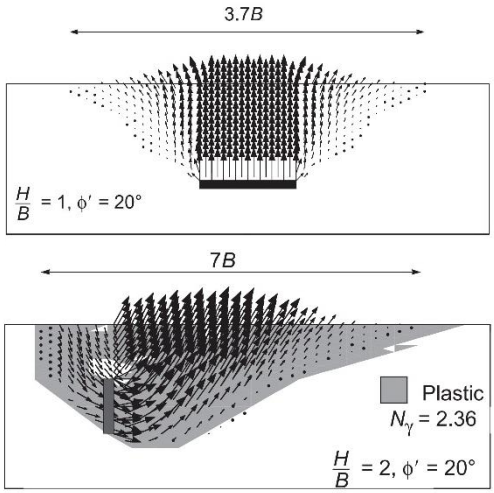

Figure 2.19 Observed velocity plots from UB analyses (after Merifield and Sloan 2006).

Three-dimensional numerical lower bound theorem and axi-symetrical displacement finite element analysis for the ultimate capacity of horizontal square and circular anchors in cohesionless soil have been performed by Merifield et al., 2003. The author's numerical lower bound analysis was based upon associated flow material ($\phi = \psi$). The effect of anchor shape on the pullout capacity has been examined. Merifield et al., 2003 found that the capacity of both square and circular anchors is significantly greater than strip anchors at the same embedment ratio. The results showed that the lower bound

solution compared well with axisymmetric finite element results using the research software *SNAC* but were less favorable with the range of theoretical solutions found in the literature such as Meyerhof & Adams (1968), Murray & Geddes (1987), Saeedy (1987), Sarac (1989), and Ghaly & Hanna (1994).

2.2.3 Finite Element Analysis

The majority of past studies has been theoretically and experimentally based and therefore many design practices are basically depending on empirical solutions. Very few numerical analyses have been performed to determine the pullout capacity of plate anchors in sand. This section presents some rigorous finite element analyses have been performed by several authors.

2.2.3.1 Rowe and Davis (1982)

The most early extensive finite element study has been performed by Rows and Davis, 1982, from which they proposed design charts to estimate the breakout factors of plate anchors. The Rowe and Davis finite element studies considered only strip anchors embedded in sand, but experimentally-based factors were also presented to account for finite length effects. The soil was modeled to satisfy the Mohr-Coulomb failure criterion and either an associated ($\phi = \psi$) or a non-associated flow rule ($\phi \neq \psi$) while the plate anchor was modeled to be perfectly rigid and weightless. The pullout capacity of an anchor plate in a cohesionless soil can be expressed by Eq. 2.54.

$$Q_u = \gamma H F_\gamma' \tag{2.54}$$

Where F'_γ is a breakout factor which is a function of horizontal versus vertical plate orientation, embedment ratio, friction angle, dilation angle, anchor roughness, and initial state of stress. F'_γ may be approximately expressed in terms of a basic breakout factor and number of correction factors:

$$F_\gamma' \cong F_\gamma . R_\psi . R_R . R_k \tag{2.55}$$

where F_γ is break factor of the basic case of a smooth plate anchor in non-dilatant soil ($\psi = 0$) with lateral earth pressure coefficient at rest condition $K_o = 1$. R_ψ, R_R, R_k are correction factors for the influence of soil dilatancy, anchor roughness and initial state of stress, respectively. They found that vertical anchors exhibit higher pullout capacity and greater contained plastic deformations before collapse, than horizontal anchors as shown in Figures (2.20 & 2.21). They also found that the roughness has a negligible influence on the collapse load of horizontal anchors and R_R can be taken as unity but significantly increases for vertical anchors especially for shallowly embedded anchors ($H/B < 3$). Dilation angle was found to have a significant effect on anchor pullout capacity and may appreciably increase the collapse load at $H/B > 3$ in medium to dense sand. However, R_ψ varies linearly with embedment D/B and increases nonlinearly with ψ for associated materials, R_ψ for non associated materials can be determined by linear interpolation. The effect of initial stress state on pullout capacity is significant only for soil exhibiting relatively little dilatancy so that the decreasing K_o slightly decreases the pullout capacity for horizontal anchors and slightly increases the pullout capacity for vertical anchors.

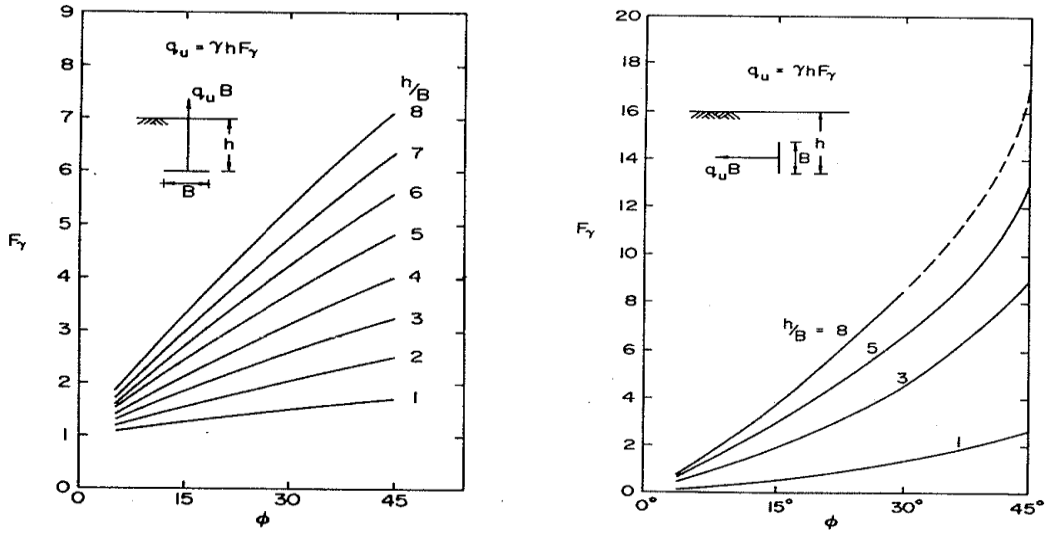

Figure 2.20 Variation of basic horizontal and vertical anchor capacity (after Rowe and Davis 1982).

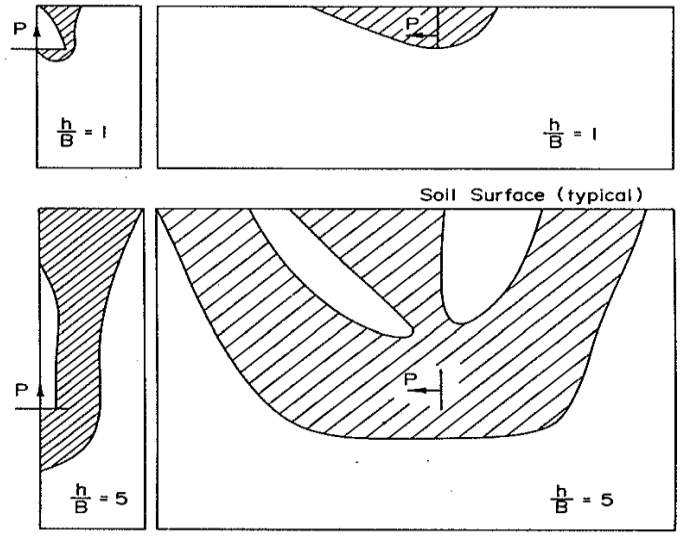

Figure 2. 21 Plastic region at collapse $\phi = 30^o$, $\psi = 0^o$ (after Rowe and Davis 1982).

2.2.3.2 Hao et al., 2014

More recently, parametric finite element study was conducted by (Hao et al., 2014) based on non-associated elastic-perfectly plastic finite element analysis to investigate

uplift behavior of circular plate anchors in sand. The influences of soil elastic stiffness E in terms of rigidity index I_r, soil-plate interface, initial stress state and dilatancy on uplift capacity have been investigated for shallowly embedded anchors. The main findings of that study are:

- Sand dilatancy makes a significant influence on uplift behavior of anchors, where the higher collapse load and displacement will be obtained for greater dilation angle. This influence is more remarkable with increase in friction angle and embedment ratio as shown in Figure 2.22.

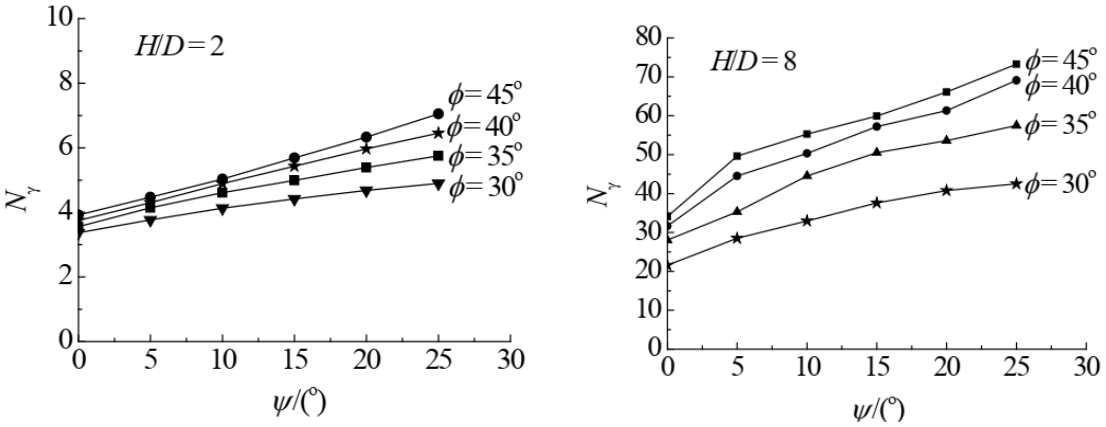

Figure 2.22 Breakout factor for various *H/D* and sand properties (after Hao et al., 2014).

- The sliding planes that develop from the corners of anchor plate to the sand ground surface are approximately inclined at dilation angles with the vertical.
- The numerical analyses overestimated the uplift capacity results of anchors because the elastic-perfectly plastic model that adopted in the study cannot describe the strain softening that occurs in dense sand during plastic shearing.

- The failure displacement corresponding to ultimate load becomes smaller for greater elastic modulus (rigidity index).

2.2.3.3 Kumar (2006)

The load-displacement relationship of shallowly embedded strip plate anchors in sand subjected to centric uplift force has been examined by Kumar (2006) using finite element method. The soil medium was modeled as a linear elastic-perfect plastic Mohr Coulomb failure criterion following an associated flow rule. The results showed that the uplift resistance increases with increase of embedment depth ration *H/D* (linearly) and the friction angle ϕ of the soil. However, the effect of the friction angle ϕ was found to be more appreciable at higher embedment ratios as shown in Figure 2.23. Kumar (2006) also noticed that the collapse of the plate anchors occurs once the development of a thin curved plastic shear zone generates from the bottom of the anchor and then extends up to the free surface

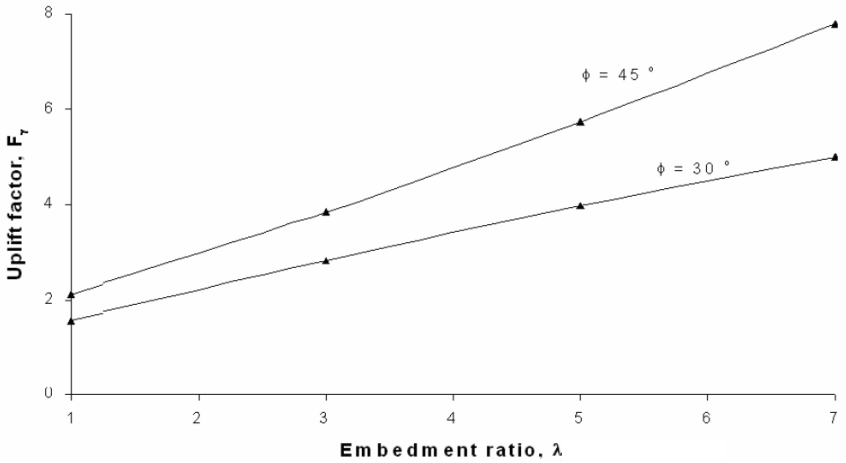

Figure 2.23 Variation of breakout factor N_γ with embedment depth ratio *H/B* and friction angle ϕ (after Kumar, 2006).

2.2.3.4 Khatri and Kumar (2011)

Khatri and Kumar (2011) have been performed lower bound finite element limit analysis to examine the effect of width *B* on the vertical pullout capacity for strip plate anchor embedded horizontally in cohesionless soil. The results showed that for a given embedment depth ratio *H/B*, decreasing in the width of the anchor *B* will cause increasing in the pullout factors continuously and the scale effect becomes more pronounced for deep anchors as shown in Figure 2.24.

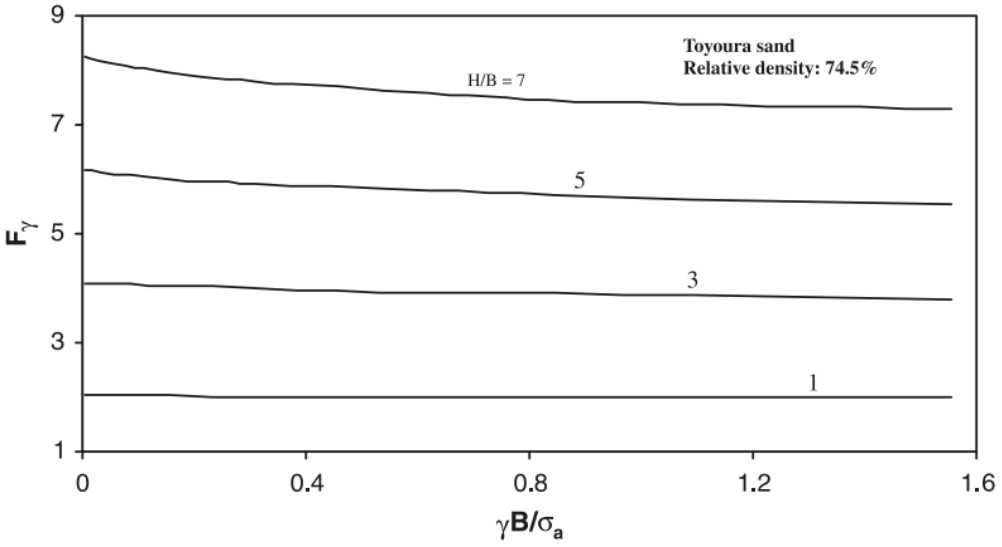

Figure 2.24 Variation of breakout factor F_γ and $\gamma B/\sigma_a$ for different embedment depth ratios (*H/B*) (after Khatri and Kumar, 2011).

2.2.3.5 Dickin and Laman (2007)

Computational and physical investigations have been performed by Dickin and Laman (2007) to model the uplift behavior of 1m strip plate anchors horizontally embedded in sand. They observed a very good agreement between uplift capacities from

centrifuge results and finite element modeling using Hardening Soil Model in Plaxis 2D, based on 0.2m computed maximum displacements, up to *H/B* ratios approximately 6 as shown in Figure 2.25, although the finite element results are slightly higher than observation for loose sand as shown in Figure 2.25a. The results showed that for plate anchor at relatively shallow depths, the soil displacements, and hence increased shear stresses, extend to the soil surface as shown in Figure 2.26a while the mechanism over deeper anchors is more localized in nature, predominating in the region above the anchor as shown in Figure 2.26b.

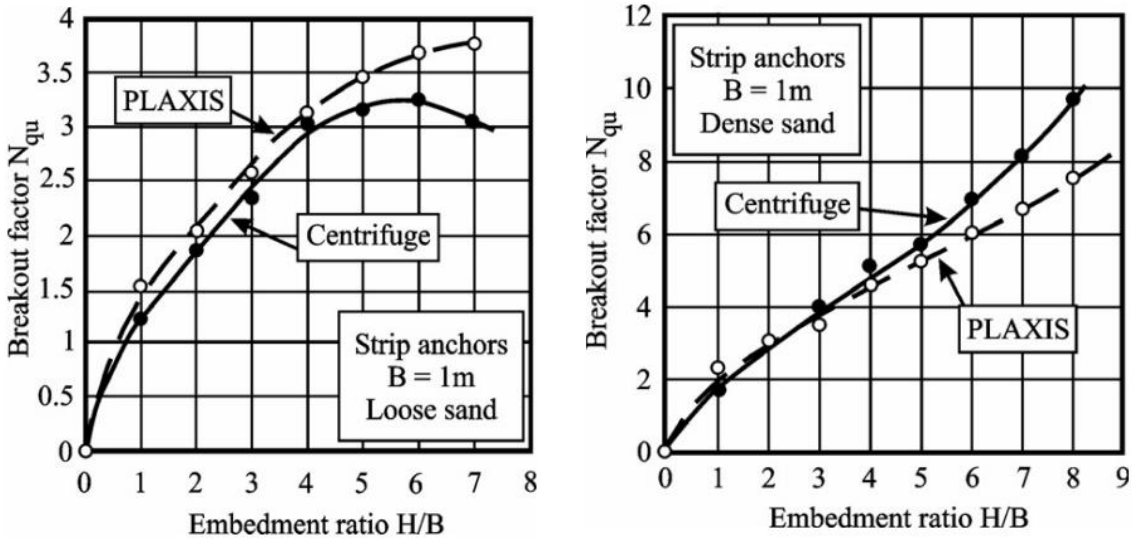

(a) Loose sand

(b) Dense sand

Figure 2.25 Comparison between breakout factors from centrifuge model tests and PLAXIS analyses for loose and dense sand. (after Dickin and Laman, 2007).

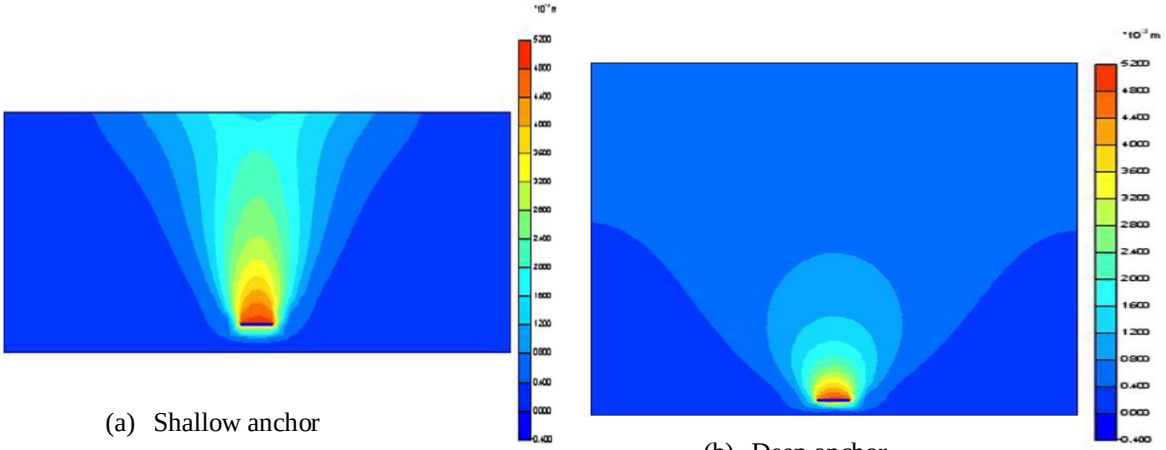

(a) Shallow anchor (b) Deep anchor

Figure 2.26 Displacement contours for shallow and deep strip plate anchor in dense sand (after Dickin and Laman, 2007).

2.2.4 Experimental Studies

2.2.4.1 Dickin (1988)

Dickin (1988) performed a series of centrifugal tests to model the uplift behavior of 1meter wide rectangular horizontal embedded plate anchor in dry uniform loose and dense sand. Four aspect ratios, which is the ratio of length to width of the rectangular horizontal anchor plate *L/B*, (1, 2, 5, and 8) were considered at embedment depth *H/B* up to 8. Several conventional gravity tests were also performed to compare with the centrifugal tests. Dickin (1988) found that the breakout factor N_q for strip anchors increases significantly with anchor embedment depth *H/B* and soil density. It was found that the breakout factor N_q decreases by 75% as the aspect ratio varies from 1 to 8 as shown in Figure 2.27. The predictions showed that as the *L/B* increases the breakout factor N_q decreases independent of the embedment depth ratio *H/B*. It was also noticed that failure displacements increase with the embedment depth ratio *H/B* but reduce with the soil

density and aspect value ratio *L/B*. Comparison with conventional tests on 50 mm models in dense sand demonstrated the overoptimistic prediction of large-scale anchor resistance by direct extrapolation of data from such tests.

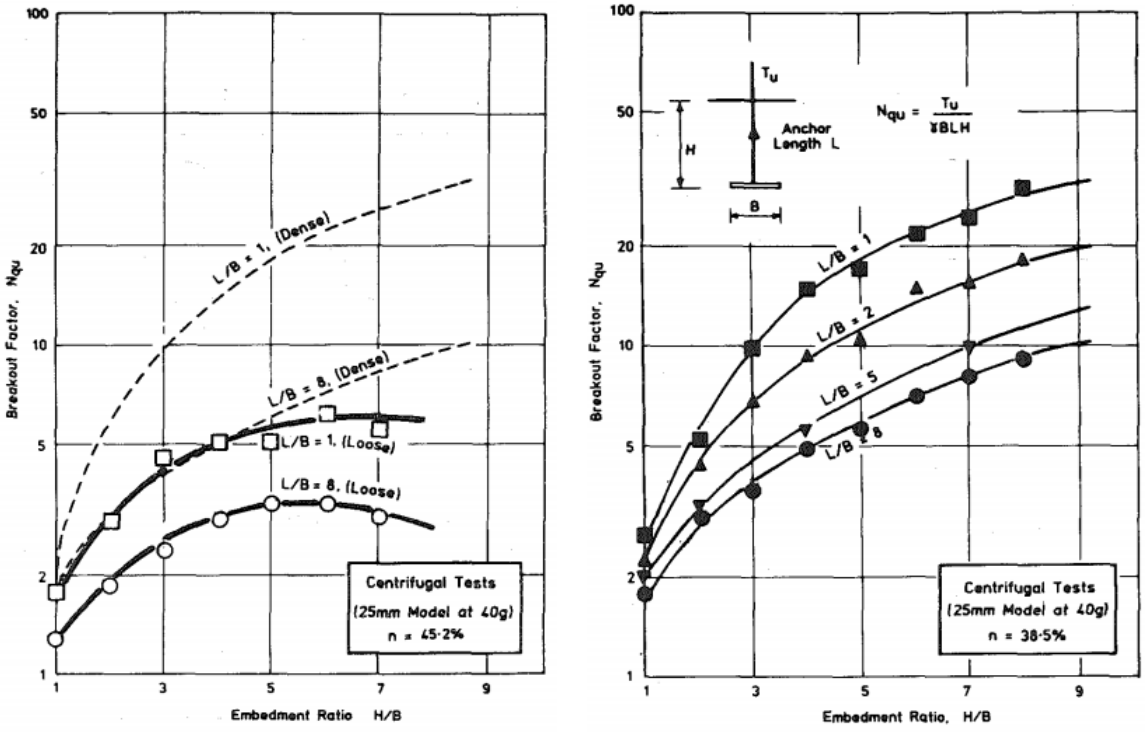

Figure 2.27 Variation of breakout factor N_γ with embedment depth ratio *H/B* for 1 meter horizontal anchors in (a) loose sand; (b) dense sand (after Dickin, 1988).

2.2.4.2 Ilamparuthi et al. (2002)

Ilamparuthi et al. (2002) performed relatively large scale model circular plate anchors 100, 150, 200, 300, and 400 mm in diameter embedded in loose, medium-dense, and dense dry uniform sand. Ilamparuthi et al. (2002) noticed two failure modes can develop with in the soil mass depending on the anchor embedment ratio *H/B*. Irrespective of soil density, shallow anchor failure mode is described by an uplifted frustum of cone of soil extends from the top anchor edge to the free surface, with an inclination angle $\phi/2$ -

2º for loose and $\phi/2 + 2^o$ for dense sand to the vertical as shown in Figure 2.28a. While for deeply embedded anchor and irrespective of soil density of soil, the behavior is characterized by a balloon-shaped rupture zone in the soil mass above the anchor. The plane portion of this rupture surface emerges from the top edge anchor and is inclined at 0.8ϕ to the vertical as shown in Figure 2.28b. It was observed three phase of the load-displacement response for shallow anchors, while two phase of the load-displacement response was observed for deep anchors as shown in Figure 2.29. They also noticed that the critical embedment ratio $(H/D)_{cr}$ increases with an increase in soil density. The critical embedment ratio $(H/D)_{cr}$ was identified by six alternative methods, and values of 4.8, 5.9, and 6.8 were recommended for loose, medium-dense, and dense sand, respectively, for anchors in the 100–150 mm diameter range considered.

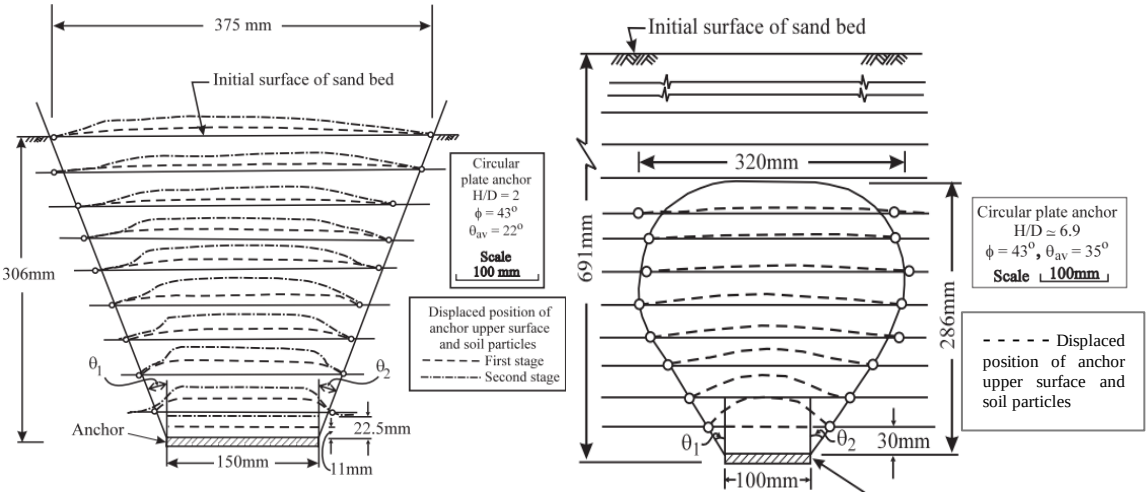

(a) Shallow anchor

(b) Deep anchor

Figure 2.28 Delineation of rupture surface in half-cut model test on shallow and deep circular plate anchor in dense sand (after Ilamparuthi et al., 2002).

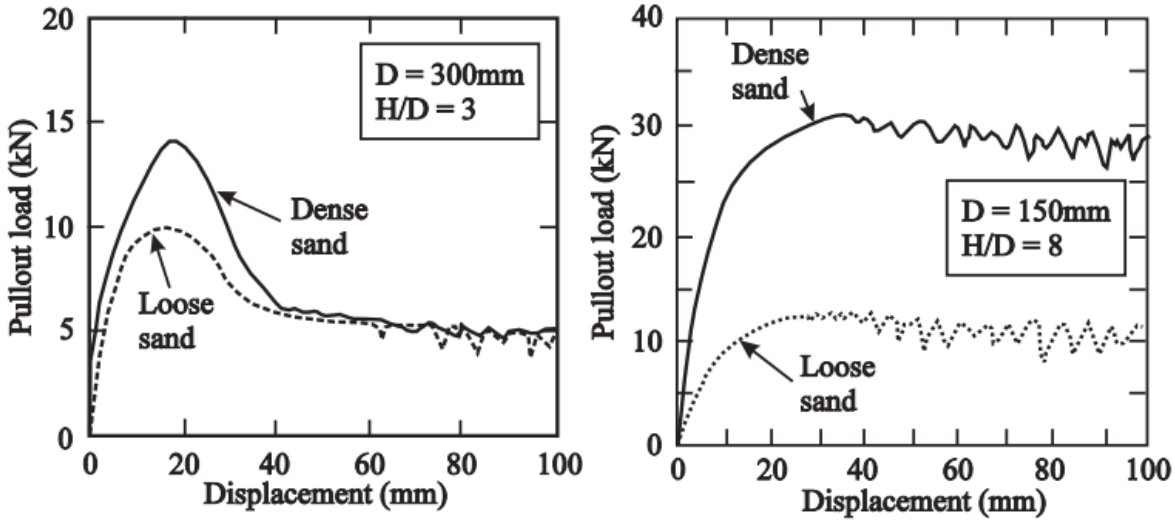

(a) Shallow anchor

(b) Deep anchor

Figure 2.29 Relationship between pullout load and displacement for shallow and deep circular plate anchors in sand (after Ilamparuthi et al., 2002).

2.2.4.3 Murray & Geddes (1989)

Murray & Geddes (1989) presented laboratory experimental results for the ultimate passive resistance and corresponding displacements of rectangular anchor plates pulled at angle of inclination between horizontal and vertical through very dense sand. The experimental results of the ultimate passive resistance were compared with the upper and lower bound limit solutions for anchors pulled horizontally through an assumed elastic –plastic soil. It was observed that the ultimate passive resistance and corresponding displacements at failure increase with depth and angle of loading, the greatest changes occurring within in interval θ =45º to θ = 90º. Also, the experimental results give predictions of failure load, for *H/B* values of about 4 or less, reasonably close to the upper bound solutions (assuming $\phi = \psi$) particularly those involving an interface friction angle

δ between sand and the anchor plates similar to that measured while for higher values of H/B, the results diverge and in general the upper bound solutions tend to underestimate the experimental values since the real soil such as that used in the experiments is probably more accurately described by a non- associated flow rule where $\psi < \phi$. Therefore, the upper bound solution that proposed by Murray & Geddes (1989) may be used to assess the ultimate passive resistance of inclined anchors in dry sand for shallow inclined anchor when *H/B*.

2.2.4.4 Liu et al., 2012

Liu et al., 2012 presented an experimental study using Digital Image Correlation (*DIC*) to investigate soil deformation around uplift circular plate anchors in dry sand. A series of scaled model tests have been performed to study the influence of particle size, soil density, and anchor embedment depth on anchor behavior. The main findings of that study were:

- Anchor pullout capacity and the corresponding displacement are significantly influenced by soil density. Liu et al., 2012 found that in loose sand, the anchor experienced a much larger displacement before reaching its peak pullout resistance compared with a much smaller displacement in dense sand.
- For shallow anchors, a truncated cone is observed in dense sand, which extends from the edges of anchors to the soil surface and forms an angle of 1⁄4 ϕ with the vertical. In contrast, different failure plane is observed in loose sand, in which a cone-shaped failure plane is formed with an angle of $45^{o} + \phi/2$ to the horizontal.
- For deeper anchors, the compressibility of soil in loose sand is the dominating factor on anchor behavior which leads to no obvious failure surface. While for

dense sand, the failure surface changes to a combined shape of a curved cone and a truncated cone. The curved cone starts from the anchor edges and extends to a depth of approximately three times the anchor diameter above the anchor plate as shown in Figure 2.30. The width of the failure surfaces increases with increasing anchor depth for both soil density conditions.

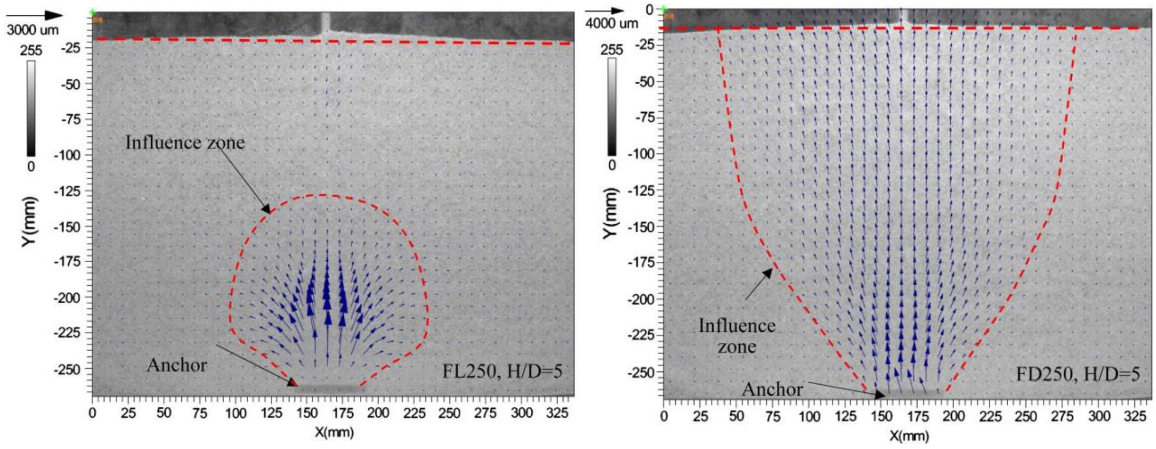

(a) Loose sand

(b) Dense sand

Figure 2.30 The failure surface shape for *H/B* =5: (a) loose sand; (b) dense sand (Liu et al., 2012).

2.2.4.5 Rasulo et al. 2017

A recent series of anchor uplift tests were conducted by Rasulo et al. 2017 to better understand the uplift capacity and the transition from shallow to deep failure mechanism of helical anchors. This study presents results from 74 uplift tests on 50 mm, 152 mm, and 254 mm diameter helical anchors in a saturated sand prepared in two states, one with a moderate and the other with a high friction angle. The results showed that the transition from shallow to deep response in the loose sands appears to begin between 6 to 8 diameters

while with higher friction angle in the medium dense sand appears to push the transition deeper to between 10 to 13 diameters as shown in Figure 2.31. Retest results for anchors that were installed at least one diameter past a previous test seemed to be in general agreement with first time anchor tests. However, in the range of the shallow mechanism, the breakout factor for the medium dense sand was approximately twice the value for a loose sand for a given normalized embedment. In the deep failure mechanism the medium dense sands factor approached approximately 5 to 7 times the loose sands factor at 100 to 135 in the medium dense compared to the value of 20 in the loose sand as shown in Figure 2.31.

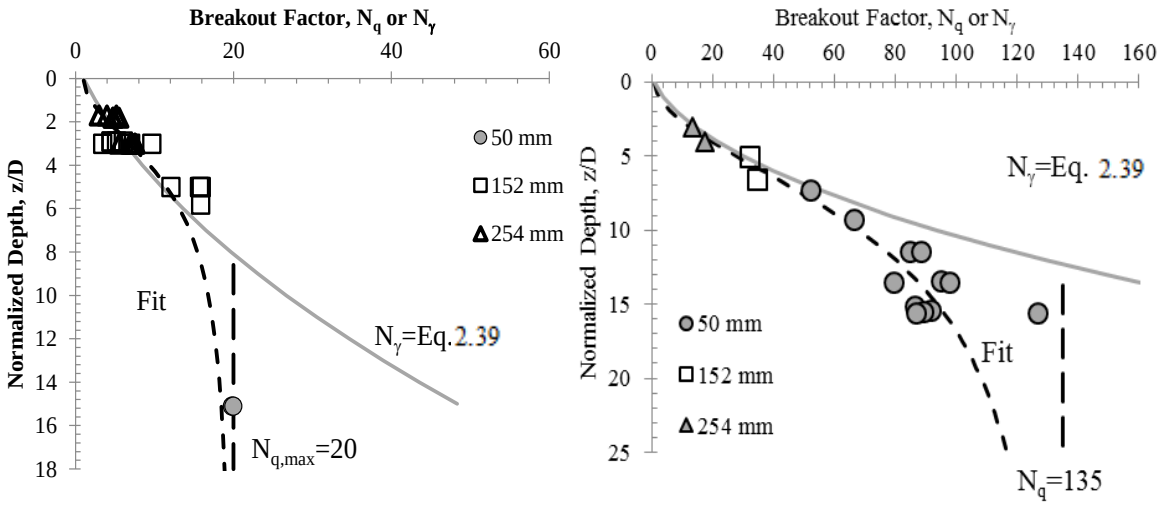

(a) Loose sand

(b) Medium dense sand

Figure 2.31 Breakout factor with depth for uplift tests on circular anchors in (a) loose saturated sand and (b) medium dense saturated sand (after Rasulo et al. 2017).

2.2.5 Other empirical relationships

Various models that use empirical relationships to predict pullout capacity of plate anchors in sand have been published by several authors depending on their experimental and analytical studies. The following empirical formula proposed by Ovesen (1981) based on the series of centrifugal test results that performed on shallow square plate anchor in sand. This formula is limited to shallow square anchor with $1 \leq \frac{H}{B} \leq 3.5$ in sand with $29^o \leq \phi_{tx} \leq 42^o$.

$$N_\gamma = 1 + (4.32 \tan \phi_{tx} - 1.58)\left(\frac{H}{B}\right)^{(3/2)} \tag{2.56}$$

where ϕ_{tx} is the peak friction angle for in triaxial test. Alternatively, an extended version of Eq. 2.56 was given by Vermeer and Sutjiadi (1985) may be used by replacing $\left(\frac{H}{B}\right)$ by $\left(\frac{H}{B} + \frac{H}{L}\right)$. Semi-empirical design approach has been suggested by Meyerhof and Adams (1986) for strip plate anchor and developed by Das and Seeley (1982) may be used in the following form:

$$N_\gamma = \frac{H}{B} K \tan\phi\phi_{ps}\left[\left(2m\frac{H}{B} + 1\right)\frac{B}{L} + 1\right] + 1 \tag{2.57}$$

where *m* is a function of friction angle. A set of empirical formulas (from Eq. 2.58 to 2.63) were formulated by Ilamparuthi et al. (2002) for predicting breakout factors for circular plate anchors with *H/D* ≤12 embedded in loose sand.

$$N_q = e^{(33.5/28)(H/D)} \qquad \text{for } 0.0 \leq (H/D) \leq 1.0 \tag{2.58}$$

$$N_q = (H/D)N_{q1} \qquad \text{for } 0.0 < (H/D) \leq 4.2 \qquad (2.59)$$

$$N_q = (H/2D)(e^{(\tan\phi \ln H/D)})N_{q1} \qquad \text{for } 2.4 < (H/D) \leq 4.2 \qquad (2.60)$$

$$N_q = \left[(H/D) + (H/D)(e^{(\tan\phi \ln D/H)})\right]N_{q1} \qquad \text{for } 4.2 < (H/D) \leq 6.0 \qquad (2.61)$$

$$N_q = \left[(H/D) + (e^{(\tan\phi \ln H/D)})\right]N_{q1} \qquad \text{for } 6.0 \leq (H/D) \leq 10.0 \qquad (2.62)$$

$$N_q = \left[N_{q10} + (e^{(\tan\phi \ln(H/D-10))})\right] \qquad \text{for } 10.0 \leq (H/D) \leq 12.0 \qquad (2.63)$$

where N_q is the breakout factor for any desired *H/D* ratio in loose sand, N_{q1} is the breakout factor for *H/D* = 1.0 (which is equal to 3.3) for ϕ = 33.5º, and N_{q10} is the breakout factor for *H/D* = 10.0. Eq. 2.64 can be used to predict the breakout factor for circular plate anchors at any embedment depth ratio *H/D* in dense sand.

$$N_{qf}{}^{\phi} = N_{qf}{}^{33.5}(e^{(H/3D)(\phi-33.5)/33.5}) \qquad (2.64)$$

where $N_{qf}{}^{\phi}$ is the breakout factor for any ϕ value and *H/D* value, and $N_{qf}{}^{33.5}$ is the breakout factor for ϕ = 33.5º at the same embedment ratio, obtained from Eqs. (2.58 to 2.63). Ilamparuthi et al. (2002) found that a good agreement between breakout values from the proposed empirical equations and those obtained from many experimental studies reported in the literature.

2.3 Keying

An embedded plate anchor has always a vertical orientation after penetration the seabed to the design depth irrespective of plate anchor installation method. Keying process initiates as a sufficient force develops in mooring line connected to the padeye of the anchor (Barron 2014). During keying process, both horizontal and vertical movement of the anchor occurs as the anchor rotates into its target orientation as shown in Figure 2.32. The upward vertical displacement is a particular concern, since a loss of anchor embedment leads to a reduction in pullout capacity. Therefore, quantifying this embedment loss is critical for plate anchor design. The following section presents a brief overview of the main published research into quantifying of loss of embedment during keying process and post uplift capacity of plate anchors embedded in sand and clay. A fairly extensive body of previous research exist for keying of direct embedment in normally consolidated clays, largely in relation to plate anchors installed by suction embedment and dynamic embedment; *e.g*., Lowmass (2006). As noted in chapter one, plate anchors can be directly embedded into the seabed by suction (SEPLA), dynamic installation (DEPLA) and pile driven installation. All methods of installation are effective in normally consolidated clay profiles. By contrast, only limited installation depths are possible through suction or dynamic installation in sands, stiff clays, and stratified soil profiles. Pile driven plate anchors (PDPAs) have no particular limitations on installation depths in either sand, clay or stratified soil profiles.

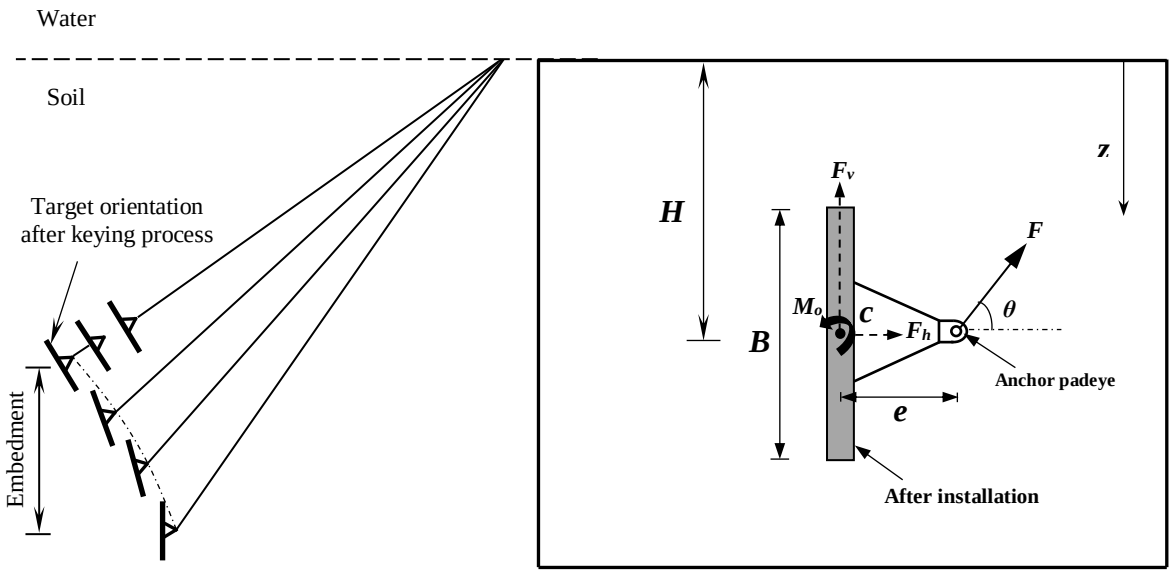

Figure 2.32 Keying process and anchor notation.

2.3.1 O'Loughlin et al. (2006)

O'Loughlin et al. (2006) presented results from a serious of centrifuge of plate anchor embedded in normally consolidated kaolin clay at 100g against a Perspex window (Figure 2.33). The tests performed to quantify the plate anchor embedment loss during keying process by careful examination of the digital images captured during the centrifuge tests. Figure 2.34 shows images at different stages in the keying process with eccentricity ratio *e/B* = 0.17, 0.5 and 1.0, respectively. Evidently, loss in anchor embedment for *e/B* = 0.17 (Figure 2.34a) is much higher than either *e/B* = 0.5 or *e/B* = 1.0 in Figure (2.34b and 2.34c). Figure 2.35 illustrates the influence of the eccentricity ratio *e/B* on the plate anchor loss of embedment. Therefore, O'Loughlin et al. (2006) suggested that in order to keep plate anchor embedment loss at negligible levels, the eccentricity of the anchor padeye or load attachment point *e/B* should be at least 1 plate width *B*.

Figure 2.33 Geometrical notation and testing chamber with installed plate Anchor (after O'Loughlin et al. 2006).

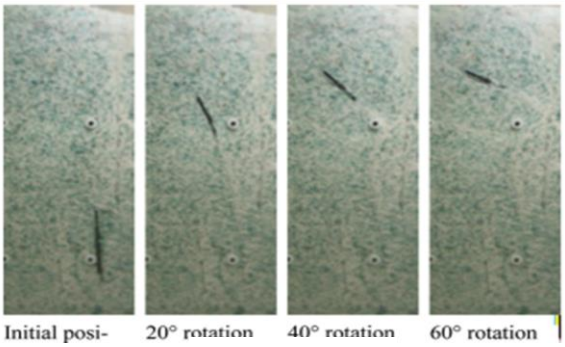

(a) *e/B* = 0.17

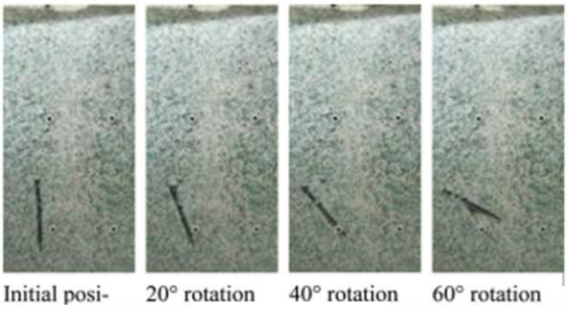

(b) *e/B* = 0.5

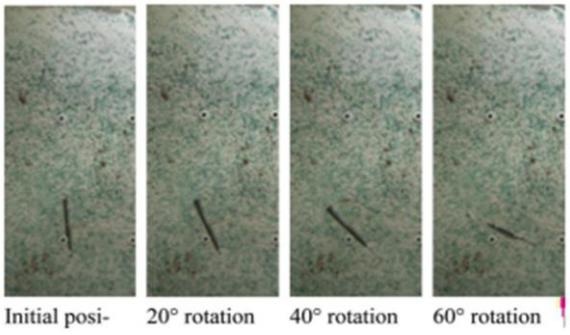

(c) *e/B* = 1.0

Figure 2.34 Plate rotation during keying for (a) *e/B* = 0.17, (b) *e/B* = 0.5, and (c) *e/B* = 1.0 (after O'Loughlin et al. 2006).

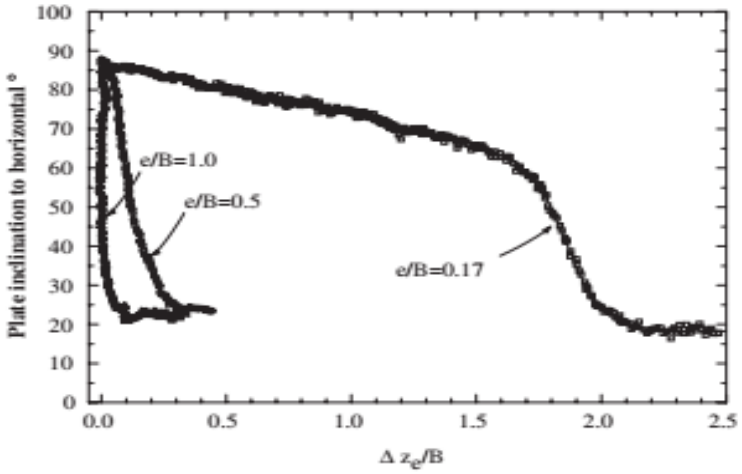

Figure 2.35 Plate anchor rotation (vertical pullout θ *vs.* δ_{ze}/B) (after O'Loughlin et al. 2006).

2.3.2 Song et al. (2006) & Song et al. (2009)

Song et al. (2006) investigated the effect of different loading inclinations on the rotation behavior for vertically installed square plate anchors in uniform Kaolin clay and transparent soil. The tests were conducted at 1g and in centrifuge at 100 g. Figure 2.36 shows that the load-displacement responses are similar for vertical pullout (90^o) and inclined pullout angle (60^o). The only differences are: (1) it takes a little longer for the chain to tighten before the anchor rotate during inclined pullout; (2) it takes a little longer for the anchor to be fully rotated during vertical pullout. Song et al. (2006) observed four phases during the orientation of the plate anchor to the direction of loading (Figure 2.36): (1) chain tightening (from point 1 to point 2); (2) half way anchor rotation (from point 2 to point 3); (3) full rotation and pullout capacity development (from point 3 to point 4); (4) steady pullout, where pullout capacity remains steady (from point 4 to point 5). At the end of each phase, the pullout capacity was shown to be independent of the load inclination. The results showed that for full rotation (90^o) during vertical pullout, the plate

anchor moves a vertical displacement δ_z plate = 0.65B, compared to 0.33B for inclined pullout load with angle of 60º.

Similar studies were performed by Song et al. (2009) evaluated the effects of anchor geometry, anchor submerged unit weight, and pullout angle on the loss in anchor embedment during keying process. Song et al. (2009) reported results from large deformation FE analyses using RITSS method and centrifuge model tests of a vertically installed plate anchor in uniform and NC soils. They developed an expression to predict the plate anchor embedment loss for vertical pullout in terms of a non-dimensional geometric factor $\left(\frac{e}{B}\right)\left(\frac{t}{B}\right)^{0.3}\left(\frac{M_o}{ABS_u}\right)^{0.1}$ as stated in Eq. 2.65.

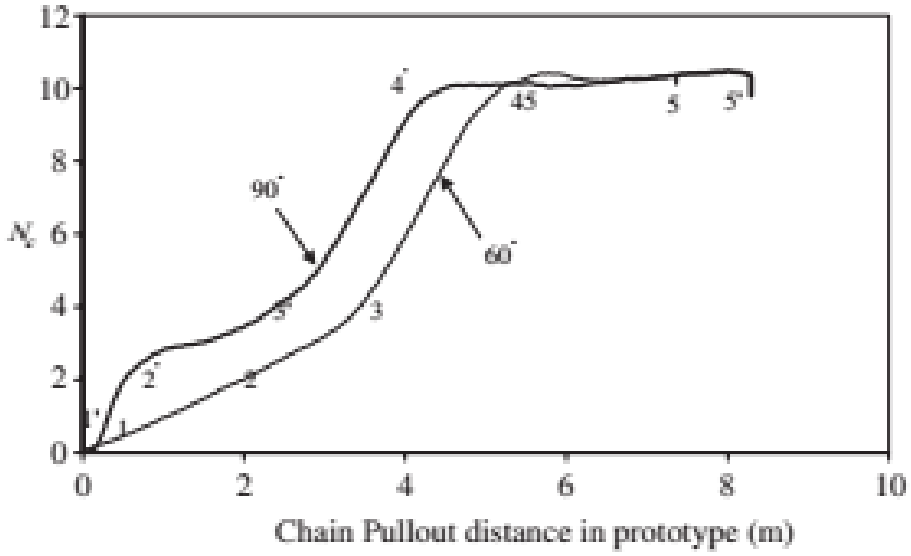

Figure 2.36 Load – displacement Response during Pullout and Keying (after Song et al. 2006).

$$\frac{\delta_z}{B} = \frac{n}{\left(\frac{e}{B}\right)\left(\frac{t}{B}\right)^{0.3}\left(\frac{M_o}{ABS_u}\right)^{0.1}} \tag{2.65}$$

where *t, B,* and *e* are geometric parameters shown in Figure 2.32. *A* is the anchor area, S_u is the undrained shear strength, and M_o is the initial moment around the anchor center as shown in Figure 2.32. They found that the embedment loss during rotation may be expressed in terms of a non-dimensional geometric factor $\left(\frac{e}{B}\right)\left(\frac{t}{B}\right)^{0.3}\left(\frac{M_o}{ABS_u}\right)^{0.1}$, which is a function of the loading eccentricity ratio, pullout angle, and the net moment applied to the anchor at the stage where the applied load balances the anchor weight. Then values range between n=0.15 for the best data fit and n = 0.2 for an upper bound of the fitted line, which provides a conservative design curve. The results showed that loss of embedment decreases linearly with decreasing pullout angle as shown in Figure 2.37, since less rotation is needed to complete the anchor keying when a lower anchor pullout angle is applied. Song et al. (2009) predicted the effect of plate anchor thickness ratio (t/B) on the normalized embedment loss δ_z/B and found that as (t/B) increase, the loss of embedment δ_z/B decreases as shown in Figure 2.38. The causes of this are: firstly, thicker anchor has higher end capacity, thus it is more difficult to move upwards and secondly a thicker anchor is heavier, thus the rotational moment plays a more important role during initial pullout to promote anchor rotation.

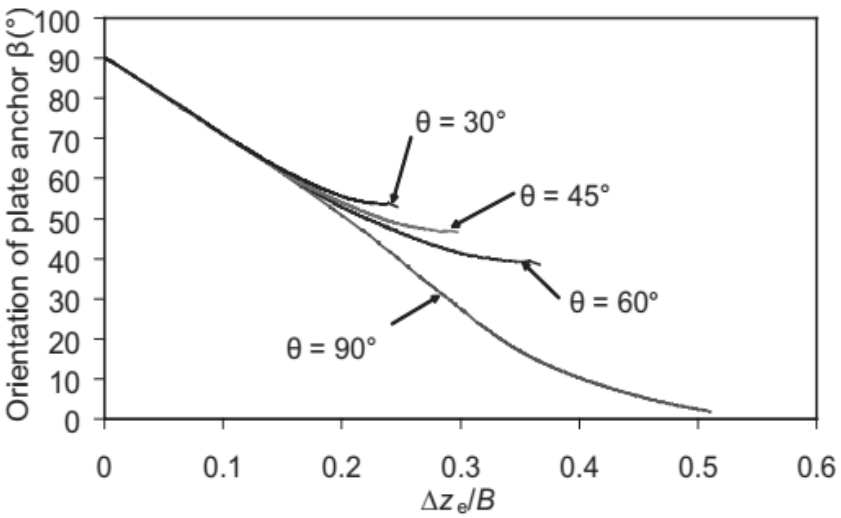

Figure 2.37 Pullout angle θ effect on anchor keying e/B=0.625, t/B =0.05, and γ' =60 kN/m^3 (after Song et al. 2009).

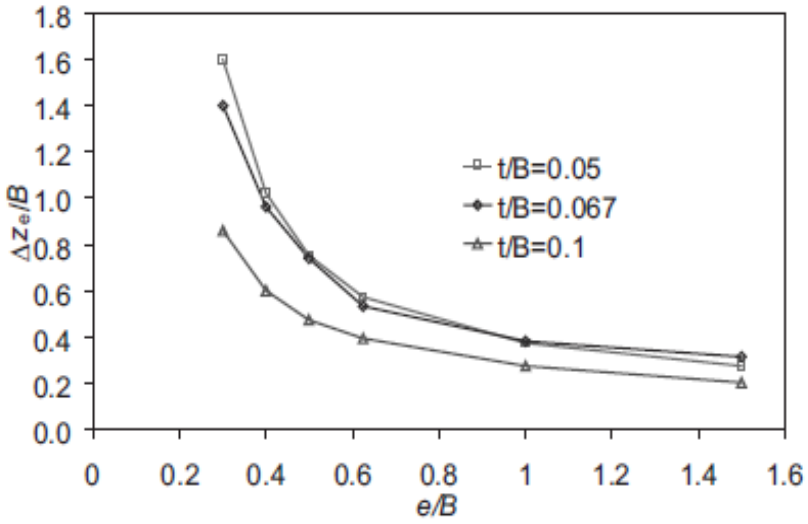

Figure 2.38 Influence of plate thickness on the embedment loss (after Song et al. 2009).

2.3.3 Long et al. (2009)

Long et al. (2009) analyzed square and strip anchors installed vertically and deeply embedded in normally consolidated (NC) clay using the RITSS large deformation finite

element method to simulate the keying process. This study investigated the effects of pullout direction and the loading eccentricity ratio *e/B* on the loss of embedment during keying process. However, the loss in anchor embedment during rotation decreases with increasing eccentricity *e/B* as shown in Figure 2.39, while the trajectory of the anchor padeye during keying is independent of eccentricity.

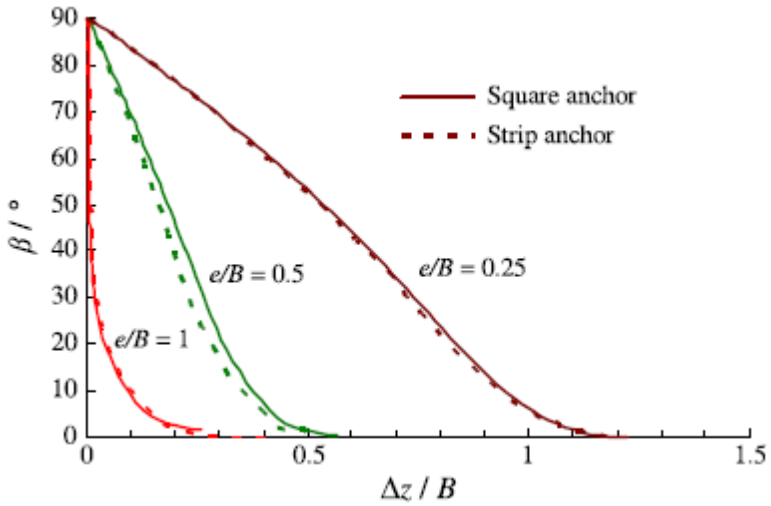

Figure 2.39 Anchor keying response in NC clay (after Long et al. 2009).

The numerical results showed that the effect of *e/B* on the loss in anchor embedment mainly occurs during the initial 60º of anchor rotation. Long et al. (2009) noticed that during the initial 60º of anchor rotation, the anchor's center displacement is reduced to zero with $e/B = 1$ while with $e/B < 1$, the anchor center's displacement increases with decreasing *e/B*. They also found that the shape effect, square versus strip, increases pullout by a factor of 1.1-1.19, while increasing embedment loss by a factor of about 1.05-1.09. They recommended that the pad-eye eccentricity *e/B* exceed 0.5 to contain the loss of embedment to $\delta_z/B < 0.5$ during keying process, where δ_z is the loss in embedment

during keying. The effect of pullout loading angle on anchor keying was also investigated for square and strip plate anchors by considering three pullout angles, θ = 45º, 60º, and 90º, with a loading eccentricity of e/B = 0.66. They found that the loss in anchor embedment increases with increasing pullout angle as shown in Figure 2.40. Their numerical results showed that e/B has a much larger influence on the embedment loss than the pullout angle does.

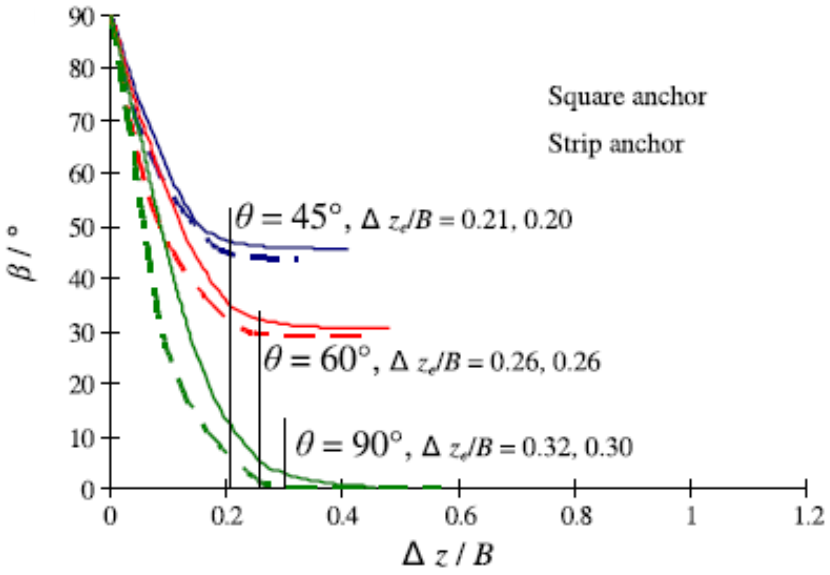

Figure 2.40 Rotation versus the loss in anchor embedment (after Long et al. 2009).

2.3.4 Gaudin et al. (2009)

Gaudin et al. (2009) performed a series of centrifuge tests of strip plate anchors embedded in normally consolidated clay NC along with PIV analysis to investigate the plate anchors keying mechanism of various eccentricities subjected to pullout at various inclinations. Figures (2.41a and2.41b) present digital images which captured against a

Perspex window at different stages of the rotation for the tests were performed with an eccentricity loading ratio of e/B = 0.25. It was clearly apparent that the anchor pullout at 45º experienced a lower loss of embedment that pulled out at 90º. The Particle Image Velocity (PIV) was used to identify the failure mechanisms generated during keying process. Different failure mechanisms were noticed based on the eccentricity e/B ratio, the load inclination and the loading stages. Gaudin et al. (2009) noticed a pure rotational mechanism for high e/B ratio, and plane shearing mechanisms was identified along the anchor for low e/B. Figures (2.42 & 2.43) show that a higher eccentricity is beneficial in reducing the embedment loss during rotation because it mobilizes a larger failure mechanism during the keying stage and consequently requires a higher pullout load.

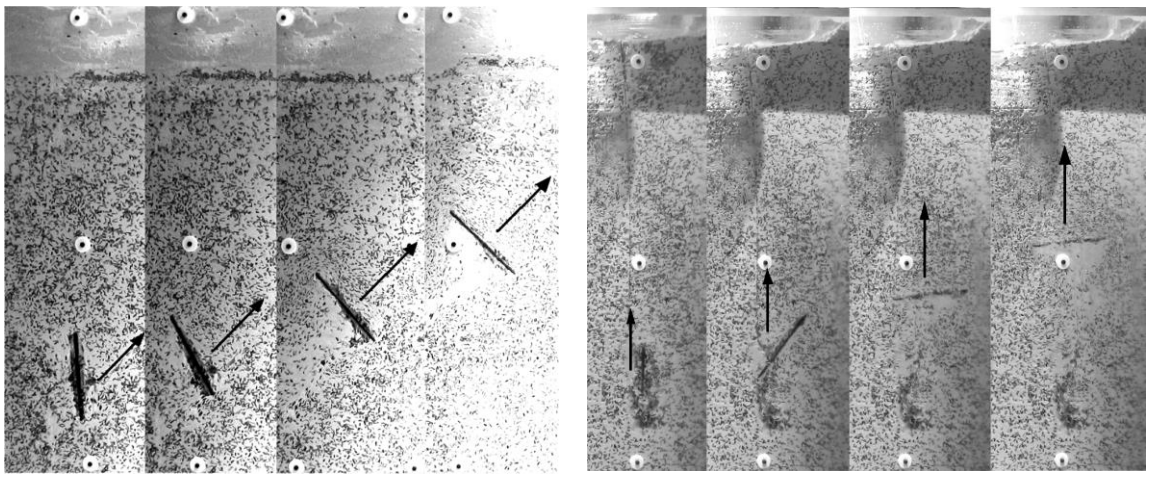

(a) θ = 45º (b) θ = 90º

Figure 2.41 Anchor rotation during pullout at 4 different successive stages for e/B = 0.25 (after Gaudin et al. 2009).

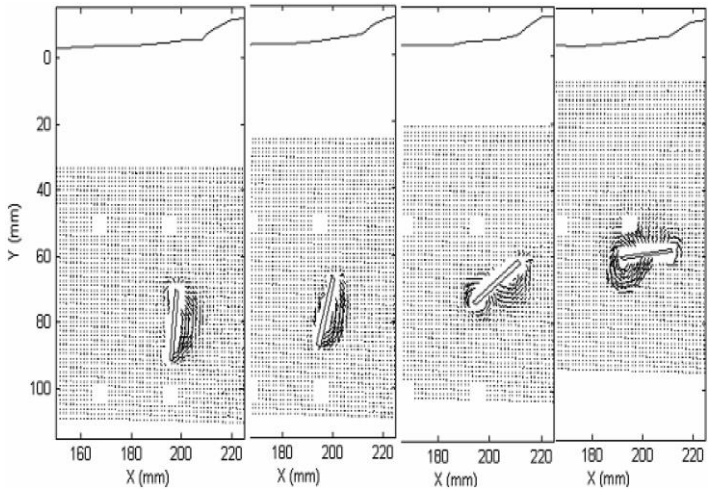

(a) $e/B = 0.25$

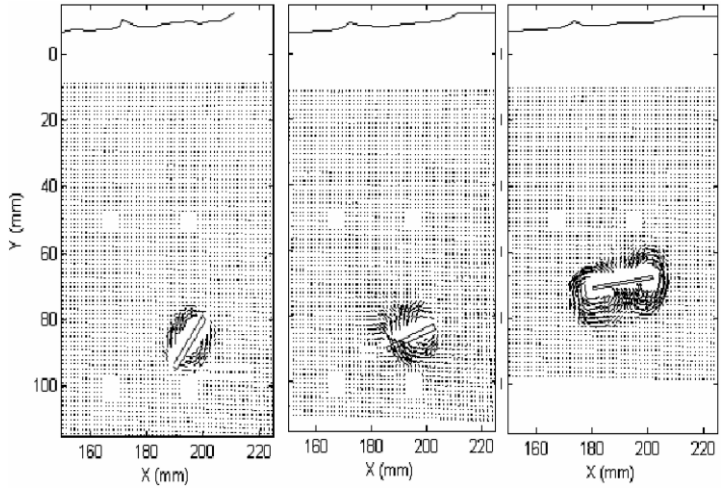

(a) $e/B = 1.0$

Figure 2.42 Failure mechanism (e/B = 0.25, 1.0 for θ = 90º) (after Gaudin et al. 2009).

The total anchor embedment loss has been quantified for each test at the end of the rotation, and is plotted against the load inclination such as in Figure 2.44. It can be noticed that the load inclination has no effect on the loss of embedment for an e/B = 1. However, for e/B = 0.25, two different behaviors can be observed. For load inclinations lower than

45º, the embedment loss remains constant and limited approximately to 0.25*B*, while for pullout load inclinations higher than 45º, the loss of embedment increases linearly up to a value of 1.15*B*, which is slightly lower than the value of 1.25 recorded by O'Loughlin et al. (2006) for an eccentricity ratio of 0.17.

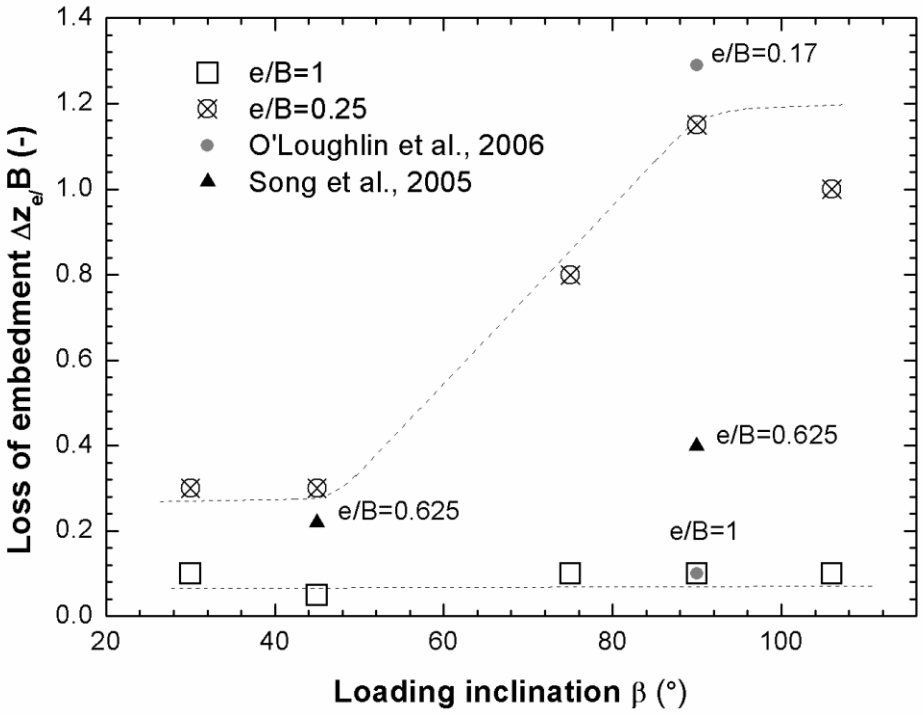

Figure 2.43 Loss of embedment during keying for different load inclination angle θ (after Gaudin et al. 2009a).

2.3.5 Wang et al. (2011)

Wang et al. (2011) simulated the keying process of rectangular and strip plate anchors embedded in normally consolidated clay using 2D and 3D LDFE allowing for evolution of the anchor-chain profile. They conducted a parametric study to quantify the loss in embedment during keying process in terms of the soil properties, anchor geometry,

loading eccentricity, and inclination and may be expressed as a function of key non-dimensional groups according to the following:

$$\frac{\delta_z}{B} = f\left[\left(\frac{e}{B}\right),\left(\frac{B}{L}\right),\left(\frac{t}{B}\right),\left(\frac{S_{uo}}{\gamma' B}\right),\left(\frac{E}{S_u}\right),\left(\frac{kB}{S_{uo}}\right),\left(\frac{e\gamma_a'}{BS_{uo}}\right)\right] \tag{2.66}$$

where $\left(\frac{e}{B}\right)$ is the loading eccentricity ratio, $\left(\frac{B}{L}\right)$is the aspect ratio, $\left(\frac{t}{B}\right)$is the thickness ratio, $\left(\frac{S_{uo}}{\gamma' B}\right)$is the local shear strength ratio, which should only become relevant for anchors near the surface of the seabed where the overburden stress affects the failure mechanism, S_{uo} is the local shear strength at the initial embedment depth of the anchor, $\left(\frac{E}{S_u}\right)$is the soil rigidity index, $\left(\frac{kB}{S_{uo}}\right)$is the soil non-homogeneity index (*k* is the soil strength gradient), and $\left(\frac{e\gamma_a'}{BS_{uo}}\right)$is the normalized moment. They determined that the loss in the anchor embedment decreases dramatically with increasing loading eccentricity ratio (they recommended that the *e/B* of plate anchor should never be less than 0.5*B*) and decreasing chain angle to the horizontal. Also, they found that the embedment loss may be underestimated if the rectangular anchor is simplified to a strip anchor because the loss in the anchor embedment decreases with increasing aspect ratio of rectangular anchors. Also, the keying response is essentially independent of the soil rigidity and the normalized strength gradient, kB/S_{uo} as shown in Figure 2.44. On the basis of the parametric LDFE, Wang et al. (2011) proposed the following expression (Eq. 2.67) for the ultimate embedment loss of square plate anchor subjected to vertical pullout loading.

$$\delta_{z\max} / B \approx a[(e/B)(t/B)^p]^q \tag{2.67}$$

where the three coefficients are fitted as a = 0:144, p = 0:2, and q = -1:15.

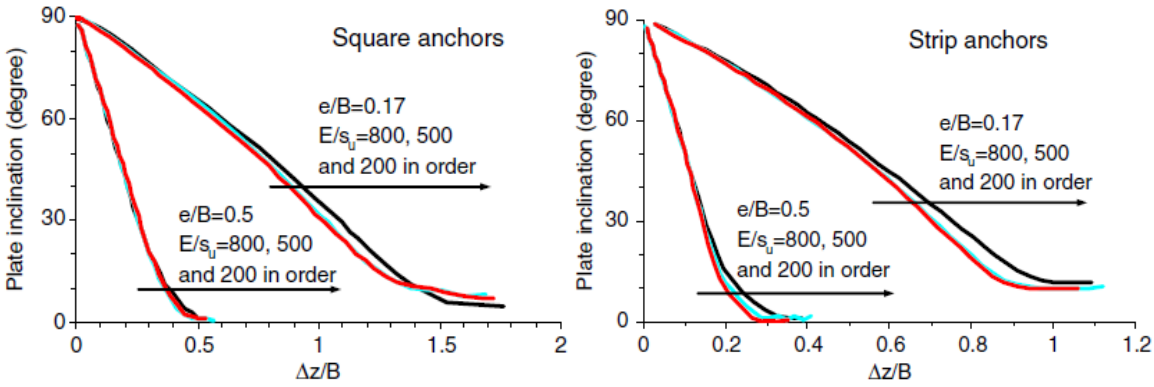

Figure 2.44 Effect of soil rigidity on anchor keying response for strip square and strip anchor. (after Wang et al. (2011).

2.3.6 O'Loughlin and Barron (2012)

O'Loughlin and Barron (2012) examined the capacity and keying behavior of strip plate anchors embedded in dense silica sand by a series of 30 g centrifuge tests. Image analyses showed that the failure mechanism to transition during keying from a deep localized rotational mechanism to a shallow block mechanism extending to the soil surface and the onset of this transition coincides with the peak uplift resistance of the plate which occurs when the plate anchor rotated approximately 65° to the vertical. Also, it was noticed that the pullout resistance of the plate anchor as it becomes horizontal is in good agreement with a limit equilibrium solution proposed by White et al. (2008) in which normality condition is neglected.

2.3.7 Barron (2014)

Barron (2014) focused on the keying behavior and the plate anchor capacity in sand. Barron (2014) identified the strong relationship between plate anchor capacity with sample density, anchor geometry and embedment ratio. 37 model anchor tests were conducted in dense silica sand in a geotechnical centrifuge at 30g using Perspex window to facilitate observation and quantification of the keying response. Six anchor tests with the same geometry with varying eccentricity ratios ($0.25 < e/B < 2$) were used. Barron (2014) found out that the dependence of loss in embedment on the pad-eye eccentricity for sand is very similar to that reported for clay and can be quantified using a modified form of the loss in embedment expression proposed by Wang et al. (2011). He also found out that a minimal loss in embedment during keying can be achieved with an anchor with an $e/B \geq 1$. The experimental study observed that the peak anchor capacity before the end of keying process, at a plate orientation between 50º and 80º to the horizontal, increasing as the eccentricity loading ratio *e/B* increased. Barron (2014) noticed that the peak load (*e.g.* Figure 2.45) does not represent the final stage of the plate orientation because the Particle Image Velocity (PIV) analyses demonstrated that the peak load corresponds to a transition in failure mechanism from a deep localized to a shallow mechanism that extends to the free surface

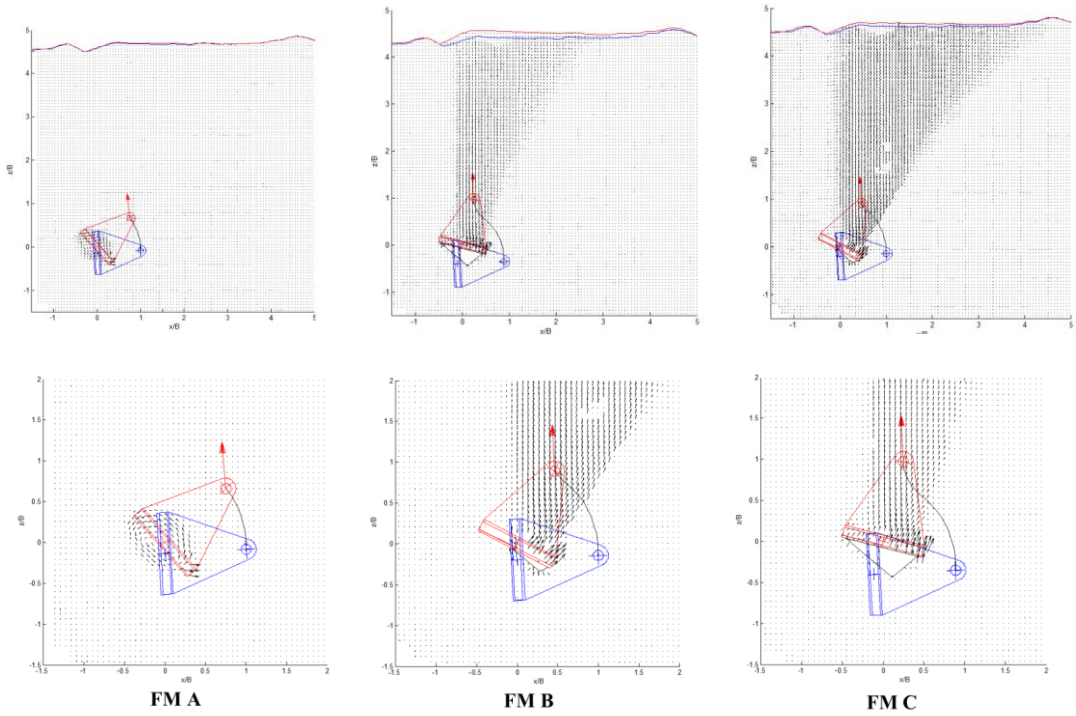

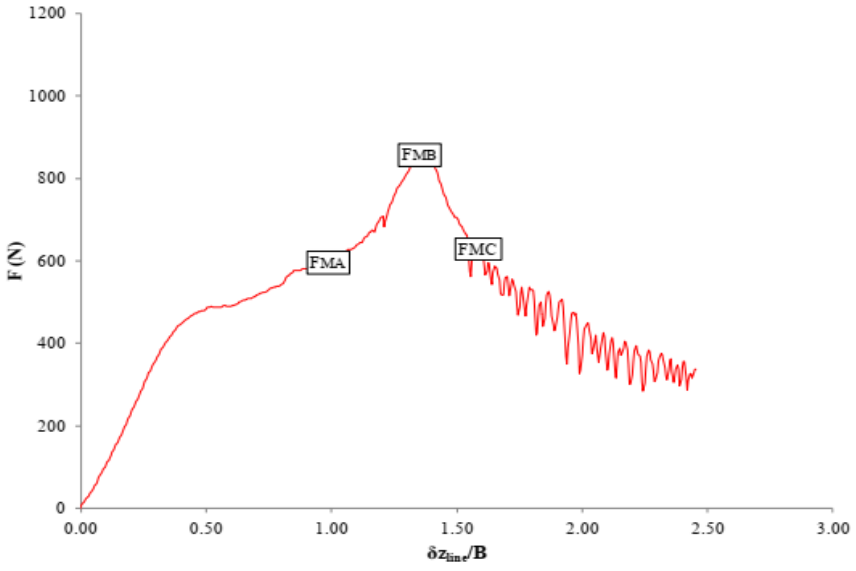

Figure 2.45 Load – displacement Response during Keying and Pullout (vertical anchor line displacement) - PIV Analysis (*e/B* = 1) (after Barron 2014).

2.4 Summary

This chapter summarized the main reported research literature on the uplift capacity of plate anchors in sand and the keying behavior of plate anchors in clay and sand. From the research literature reviewed in this chapter, it was noticed that the most previous analytical, numerical, and experimental researches on plate anchor performance in sand cover a relatively shallow anchor embedment range (8-10 plate widths or diameters), which is not sufficiently deep to characterize the transition to deep embedment. Also, the influence of elastic soil stiffness E (soil rigidity) in evaluating anchor performance in sand especially for deeply embedded anchor has received very little attention in the research literature and need to be systematically investigated. Additionally, most past plate anchor research has focused either on the horizontal or vertical uplift capacity problems while the effect of inclined anchor and load inclination have received a very limited attention. In regard to the keying behavior of plate anchor in sands, it is noted that very few experimental studies have been conducted to understand the behavior of plate anchor in sand during keying process and to the author's knowledge, no finite element studies have been performed in this field. Hence, a full assessment of plate anchor performance in sand must consider the above-mentioned points into account to achieve a reliable prediction of pullout capacity of plate anchors in sand.

CHAPTER III

MATERIAL AND FINITE ELEMENT MODELING

3.1 Introduction

In this research, an extensive numerical displacement finite element study was conducted to acquire a reliable understanding of the performance of plate anchors embedded in cohesionless soils. This research considers the effects of: (1) anchor embedment depth, (2) plate orientation (keying process), and (3) inclined and non-eccentric applied loads. Large deformation finite element analyses employing a Mohr-Coulomb failure criterion and non-associated flow rule were utilized to accomplish this goal.

3.2 Material Modeling

Soil is a complex material that has elastic, plastic, and viscous properties. Therefore, selection of the proper constitutive model to represent a soil's complexity requires taking into account several factors, such as the material's characteristics, availability of experimental data, and type of analysis. This ensures that a balance is struck between accuracy, simplicity, and the problem's requirements. The Mohr Coulomb Model (MCM) is one of the most common constitutive models used in geotechnical engineering applications to model soil behavior, particularly cohesionless soil. The MCM is an elastic, perfectly plastic model that combines Hooke's law and the generalized form of Coulomb's failure criterion (Brinkgreve, 2005). The MCM assumes that the material behaves in a linearly elastic fashion until the stress reaches its yield value; no further change in stress

accumulates after yielding as a plastic strain (see Figure 3.1). Based on this model, if the strain is known, the stress can be specified (but not vice versa).

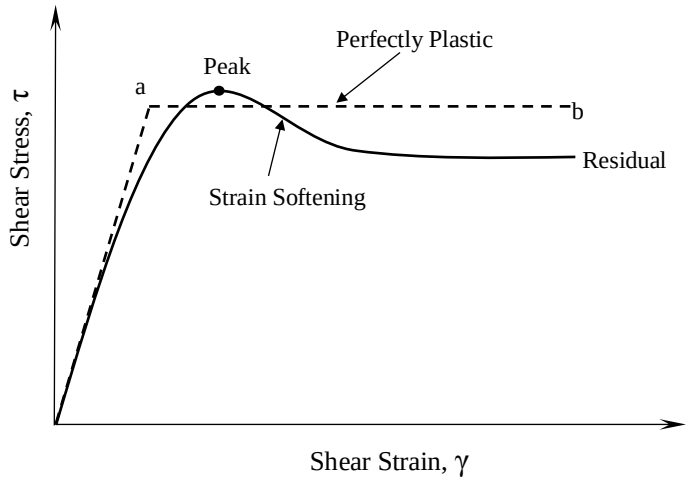

Figure 3.1 Typical original and simplified (elastic-perfectly plastic) bilinear stress-strain relationship of dense soil.

3.2.1 Mohr-Coulomb Yielding Criteria in the Principal Stress Space

Yielding is a condition defining the limit of elasticity and onset of plastic behavior. The combinations of stress states at which yielding occurs is referred to as the yield criterion. Generally, any yield or failure criterion can be visualized by the mathematical function f. The conventional arguments for the yield function f are the individual independent components of stress, as follows:

$$f(\sigma_{xx}, \sigma_{yy}, \sigma_{zz}, \tau_{xy}, \tau_{yz}, \tau_{zx}) = k \tag{3.1}$$

The yielding is signaled once the function f equals the constant k. For greater simplification in an isotropic soil, one can replace the six stress components with three principal stresses (σ_1, σ_2, σ_3) plus information about the principal directions. The developments that follow will benefit from the introduction of an isotropic material's

characteristics, which removes all dependence on the orientation of the principal direction. This means that at any point in the soil body there will always be at least three surfaces on which the shear stresses τ_{xy}, τ_{yz}, and τ_{zx} will vanish (Davis & Selvadurai, 2005). Therefore, for isotropic material, Eq. (3.1) can be rewritten in terms of principles stresses, as in Eq. (3.2).

$$f(\sigma_1, \sigma_2, \sigma_3) = k \tag{3.2}$$

In a coordinate system in which the coordinate directions are parallel to the principal direction, the stress matrix will have this simple form:

$$\sigma = \begin{bmatrix} \sigma_1 & 0 & 0 \\ 0 & \sigma_2 & 0 \\ 0 & 0 & \sigma_3 \end{bmatrix} \tag{3.3}$$

The stress tensor is usually divided into a purely hydrostatic stress (i.e., mean stress) σ_m, as defined in Eq. (3.4), and the deviatoric stress tensor *S* is defined in Eq. (3.5):

$$\sigma_m = p = \frac{1}{3}(\sigma_1 + \sigma_2 + \sigma_3) = k \tag{3.4}$$

$$S = \begin{bmatrix} S_1 & 0 & 0 \\ 0 & S_2 & 0 \\ 0 & 0 & S_3 \end{bmatrix} = \begin{bmatrix} \sigma_1 - \sigma_m & 0 & 0 \\ 0 & \sigma_2 - \sigma_m & 0 \\ 0 & 0 & \sigma_3 - \sigma_m \end{bmatrix} \tag{3.5}$$

where S_1, S_2, and S_3 are the principle values of the stress deviator tensor *S*. The principal invariants of the characteristic equation of the stress tensor σ (see Eq. (3.3)) are defined as:

$$I_1 = \sigma_1 + \sigma_2 + \sigma_3$$

$$I_2 = \sigma_1\sigma_2 + \sigma_2\sigma_3 + \sigma_3\sigma_1 \tag{3.6}$$

$$I_3 = \sigma_1\sigma_2\sigma_3$$

The associated invariants that indicate the second-order identity tensor are defined below as deviatoric stress invariants.

$$J_1 = 0$$

$$J_2 = \frac{1}{6}\left[\left(\sigma_1 - \sigma_2\right)^2 + \left(\sigma_2 - \sigma_3\right)^2 + \left(\sigma_3 - \sigma_1\right)^2\right] \tag{3.7}$$

$$J_3 = \begin{bmatrix} \sigma_1 - \frac{1}{3}I_1 & 0 & 0 \\ 0 & \sigma_2 - \frac{1}{3}I_1 & 0 \\ 0 & 0 & \sigma_3 - \frac{1}{3}I_1 \end{bmatrix}$$

Many yielding criteria have been proposed by various researchers, but Coulomb's failure criteria, developed in 1773, has become the cornerstone of understanding soil behavior. Coulomb (1773) observed that soil strength comes from both cohesion and friction. He suggested that the soil failure associated with a surface rupture and plastic yielding begins as long as the shear stress τ and normal stress σ (i.e., compression positive) reach the critical combination demonstrated in Eq. (3.8) (Davis & Selvadurai, 2005). In other words, the shear stress τ on any point in a material in the failure plane reaches a value that depends linearly on the normal stress σ.

$$\tau = c + \sigma \tan \phi' \tag{3.8}$$

where σ and τ represent the normal and shear stresses on the physical plane, at which soil plastic yielding begins. The constant c is the cohesion with the dimensions of stress (c = 0 for cohesionless material). The magnitude of $\tan\phi'$ is similar to the friction coefficient in the generalized Coulomb's friction law, based on sliding friction where ϕ' is the angle

of internal friction. For soil material, it was not stipulated in Coulomb's (1773) failure criteria whether ϕ' refers to the friction angle ϕ'_{cv} at the critical state, or the peak friction angle ϕ'_p. The Mohr–Coulomb yield criterion for the combination of $\sigma_1 \geq \sigma_2 \geq \sigma_3$ is visualized in the Mohr plane representation shown in Figure (3.2), and can be expressed in terms of principal stresses, with compressive stress taken as positive (as in Eq. (3.9)).

$$f = (\sigma_1 - \sigma_3) - (\sigma_1 + \sigma_3)\sin\phi' - 2c\cos\phi' = 0 \tag{3.9}$$

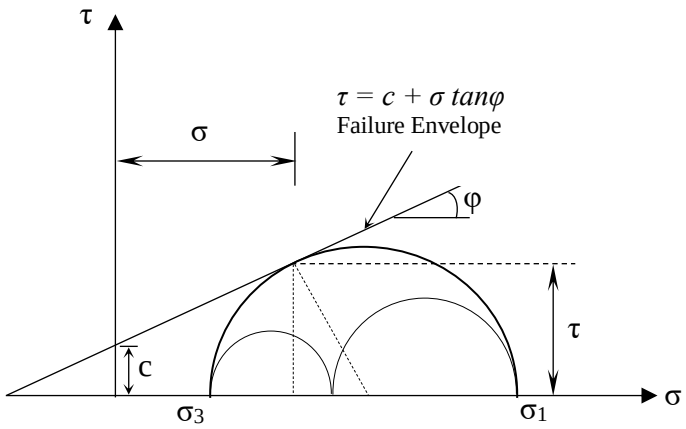

Figure 3.2 The Coulomb failure criterion.

For cohesionless soil ($c = 0$), Eq. (3.9) becomes:

$$f = (\sigma_1 - \sigma_3) - (\sigma_1 + \sigma_3)\sin\phi' = 0 \qquad \text{for} \quad \sigma_1 \geq \sigma_2 \geq \sigma_3 \tag{3.10}$$

For other possible combinations of principal stresses, the yield functions are:

$$\begin{aligned}
f &= (\sigma_2 - \sigma_3) - (\sigma_2 + \sigma_3)\sin\phi' = 2c\cos\phi' && \sigma_2 \geq \sigma_1 \geq \sigma_3 \\
f &= (\sigma_2 - \sigma_1) - (\sigma_2 + \sigma_1)\sin\phi' = 2c\cos\phi' && \sigma_2 \geq \sigma_3 \geq \sigma_1 \\
f &= (\sigma_3 - \sigma_1) - (\sigma_3 + \sigma_1)\sin\phi' = 2c\cos\phi' && \sigma_3 \geq \sigma_2 \geq \sigma_1 \\
f &= (\sigma_3 - \sigma_2) - (\sigma_3 + \sigma_2)\sin\phi' = 2c\cos\phi' && \sigma_3 \geq \sigma_1 \geq \sigma_2 \\
f &= (\sigma_1 - \sigma_2) - (\sigma_1 + \sigma_2)\sin\phi' = 2c\cos\phi' && \sigma_1 \geq \sigma_3 \geq \sigma_2
\end{aligned} \tag{3.11}$$

Each equation defines a plane in the principal stress space. Each plane has one face of the Mohr-Coulomb pyramid aligned with the space diagonal, whose apex is located at zero

for sand and $\sqrt{3}\ c\ cot\ \phi$ for c-ϕ soil, as shown in Figure (3.3). Therefore, for $\sigma_1 \geq \sigma_2 \geq \sigma_3$, the intersection of the Coulomb yield surface with the π plane is a straight line, and for all possible combinations of principal stresses, the shape will be irregular hexagonal shown in Figure (3.4). The size of the surface on the π plane strongly depends on the mean stress p', but the shape of the Coulomb yield surface on the π plane changes only because of a change in the friction angle ϕ'. The uppermost major vertex represents the loading case, where $\sigma_1 > \sigma_2 = \sigma_3$, which corresponds to the conventional compression triaxial test; the lowermost minor vertex, where $\sigma_1 < \sigma_2 = \sigma_3$, corresponds to the triaxial extension test. The vertices of the irregular hexagonal shape represent loading cases in which the two principal stresses are equal (Davis & Selvadurai, 2005). The initial position and size of the yield surface is a direct expression of the material memory of the past loading history. Also, it should be noted that in Eqs. (3.9-3.11), the yield function representation is not influenced by the magnitude of the intermediate principal stress.

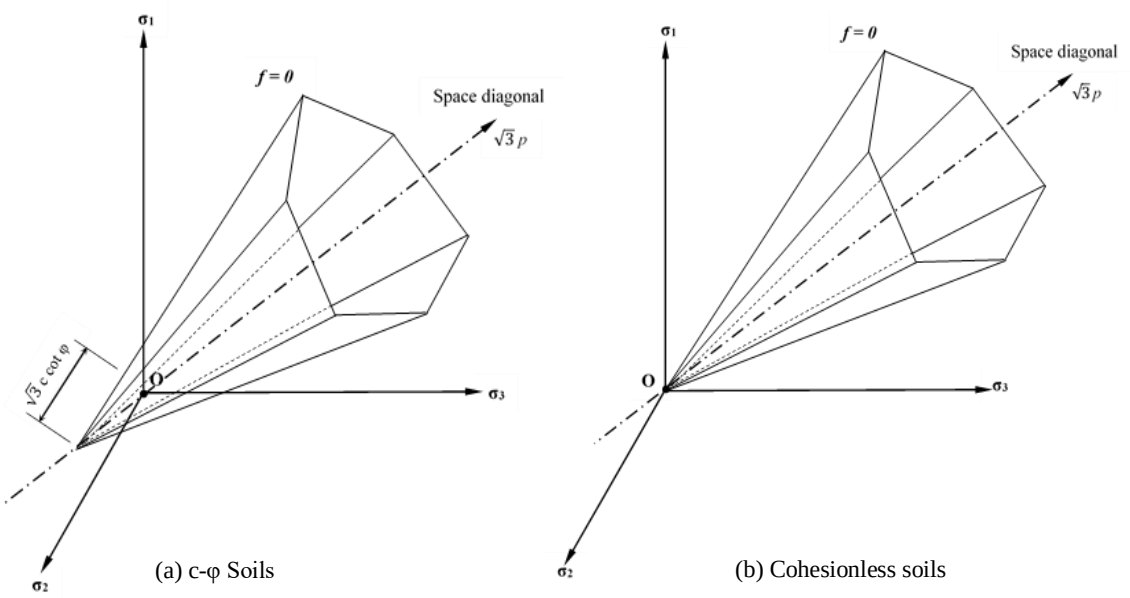

Figure 3.3 Perspective view of the Coulomb yield surface in a principal stress space.

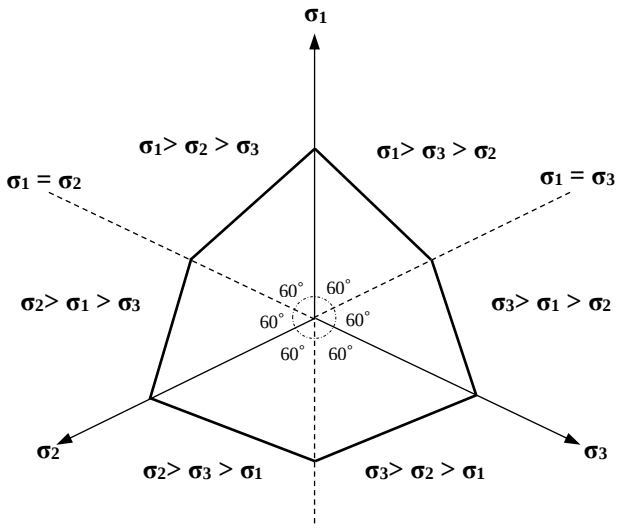

Figure 3.4 Cross section (π plane) of the Coulomb yield surface in a principal stress space.

If one considers the intersection of the Coulomb yield surface in the principal stress space as a plane surface defined by $\sigma_2 = 0$ and each of the six possible combinations of principal stresses mentioned above, the following Eq. (3.12) gives the Coulomb yield surface shape in a two-dimensional space, as shown Figure (3.5). The *m* and *n* variables take values between 1 and 3.

$$f = \sigma_m(1-\sin\phi') - \sigma_n(1+\sin\phi')\sin\phi' = 2c\cos\phi' \tag{3.12}$$

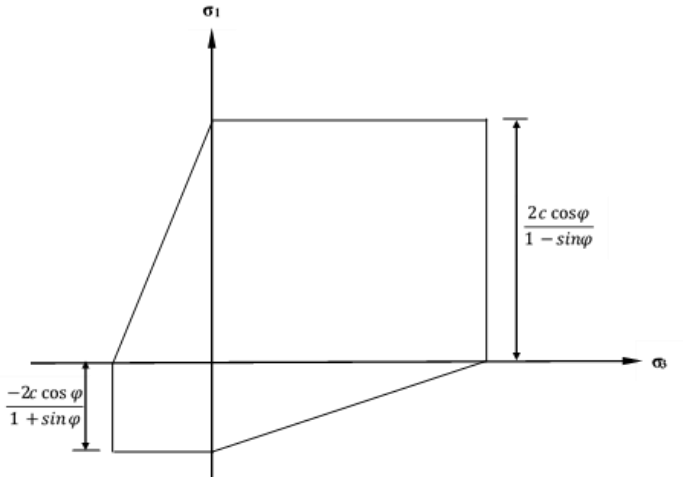

Figure 3.5 Perspective view of the Coulomb yield surface in a two-dimensional space.

Additionally, the three-dimensional representation of the Mohr-Coulomb yield function can be expressed in many other forms in terms of the abovementioned stress invariants (Zienkiewicz & Taylor, 1977), as in Eq. (3.13).

$$f(I_1, J_2, \theta) = \frac{1}{3} I_1 \sin\phi' + \sqrt{J_2}(\cos\theta - \frac{1}{\sqrt{3}} \sin\phi' \sin\theta - c\cos\phi' = 0 \quad (3.13)$$

where I_1 is the first stress invariant, J_2 is the second deviatoric stress invariant (see Eqs. (3.6) and (3.7), respectively), and θ is the Lode angle (i.e., deviatoric polar angle), defined as:

$$\cos\theta = \frac{1}{\sqrt{3}} \frac{S_1}{\sqrt{J_2}} \qquad (-30^o \leq \theta \leq 30^o) \quad (3.14)$$

The invariant θ is controlled by the relationship of the intermediate principal stress to the major and minor principal stresses. For instance, in the combination of $\sigma_1 \geq \sigma_2 \geq \sigma_3$, when the intermediate principal stress σ_2 equals σ_3, the value for θ becomes 60º. When the intermediate principal stress σ_2 equals σ_1, the value for θ becomes 0º. Thus, θ is an indication of the magnitude of the intermediate principal stress in relation to the major and minor principal stresses. It should be noted that the yield behavior may be influenced by the magnitude of the intermediate principal stress. However, the Mohr–Coulomb failure (i.e., yield) surface is expressed in ABAQUS 2014 by rewriting Eq. (3.13) in Haigh-Westergard space in terms of the invariants p, q, and θ, as shown in Figure (3.6):

$$f = R_{mc} q - p\tan\phi' - c = 0 \quad (3.15)$$

where R_{mc} is the measure of the shape of the yield surface in the deviatoric stress plane, defined as:

$$R_{mc}(\theta,\phi') = \frac{1}{\sqrt{3}\cos\phi'}\sin(\theta+\frac{\pi}{3}) + \frac{1}{3}\cos(\theta+\frac{\pi}{3})\tan\phi' \tag{3.16}$$

$$\cos 3\theta = \left(\frac{r}{q}\right)^3 \tag{3.17}$$

where p is the mean stress as stated in Eq. (3.4), r is the third invariant of deviatoric stress (J_3) as defined in Eq. (3.7), and q is the Mises equivalent stress (i.e., the deviatoric stress) as defined in Eq. (3.18).

$$q = \left[\frac{3}{2}\left(\sigma_1-\sigma_2\right)^2 + \left(\sigma_2-\sigma_3\right)^2 + \left(\sigma_3-\sigma_1\right)^2\right]^{1/2} \tag{3.18}$$

where ϕ' is the slope of the Mohr-Coulomb yield surface in the p - R_{mc} q stress plane, as shown in Figure (3.7a). This is commonly referred to as the friction angle of the material, and ranges from $0^o \leq \phi' \leq 90^o$. In the case of $\phi' = 0^o$, the Mohr-Coulomb model reduces to the mean stress-independent Tresca model with a perfectly hexagonal deviatoric section, as shown in Figure (3.7b). In the case of $\phi' = 90^o$, the Mohr-Coulomb model reduces to the "tension cutoff" Rankine model with a triangular deviatoric section and $R_{mc} = \infty$. However, this limiting case is not permitted within the Mohr-Coulomb model described here (ABAQUS, 2014).

The MC yield surface in ABAQUS consists of two different criteria: a shear criterion known as the MC surface, and the optional tension cut-off criterion using the Rankine surface to give a better approximation of the tensile behavior of certain materials such as concrete (ABAQUS, 6.14). Figures 3.7a and 3.7b show the Mohr Coulomb criterion in the principal stress plane (i.e., the Meridional plane) and deviatoric plane (i.e., the π plane), respectively.

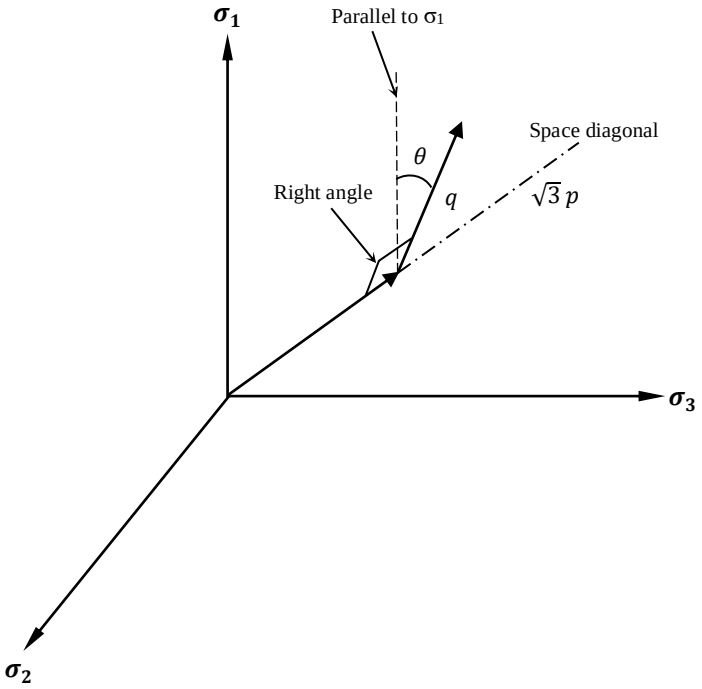

Figure 3.6 Graphical representation of the stress invariants (p,q,θ) (ABAQUS, 2014).

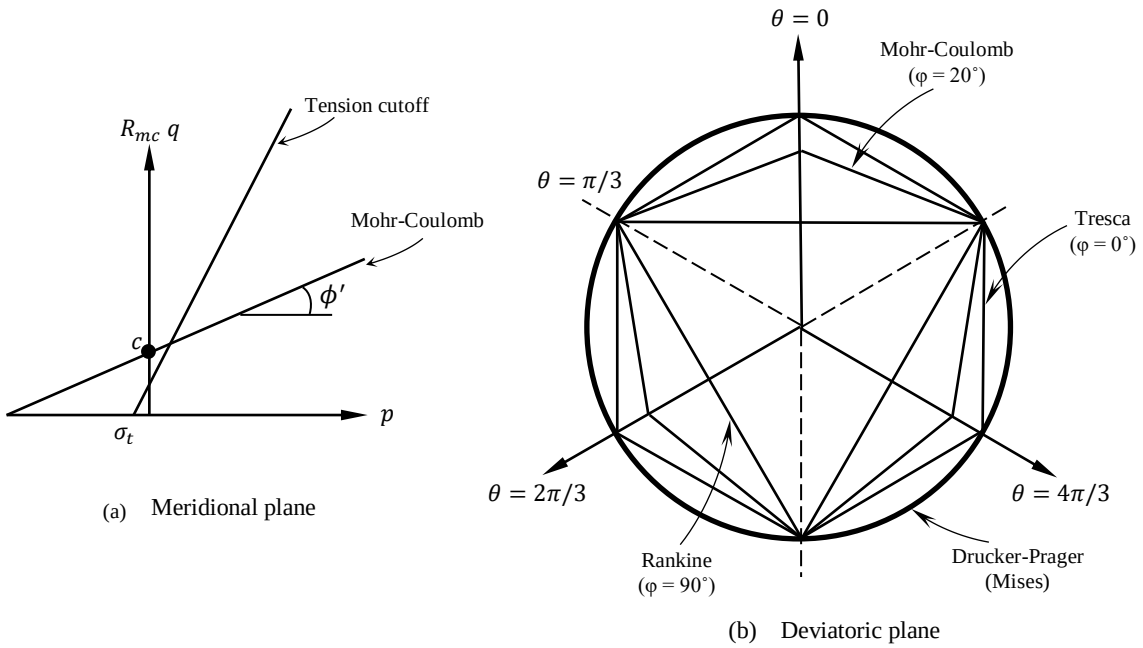

Figure 3.7 Yield surfaces in: (a) the meridional plane, and (b) the deviatoric plane (π plane) (ABAQUS, 6.14).

3.2.2 Flow Rule for Plastic Strain

The flow rule is used to describe the deformations expected to follow yielding. To determine the plastic strain increment $d\varepsilon_i^p$ when the current stress state is on the yield surface, a functional relationship (i.e., plastic potential function *G*) must be formulated linking the components of the plastic strain and current stress state. The plastic potential function *G* in the MCM adopted by ABAQUS was employed by Menétrey and Willam (1995); it presents a hyperbolic function in the meridian plane and a smooth elliptic function combined by three elliptic arcs in the deviatoric plane that together make *G* continuous and smooth in both the meridional and deviatoric planes; thus, the flow direction is defined uniquely in those planes.

The smooth triple-elliptic function *r(θ,e)* is expressed in Eq. (3.19), based on the five-model parameter by Willam and Wranke (1974). This model was originally formulated with three parameters for the failure surface, and then refined by adding two additional parameters to describe the curved meridians.

$$r(\theta,e)=\frac{4(1-e^2)\cos^2\theta+(2e-1)^2}{2(1-e^2)\cos\theta+(2e-1)\sqrt{(4(1-e^2)\cos^2\theta+5e^2-4e)}} \tag{3.19}$$

The deviatoric eccentricity parameter *e* describes the out-of-roundness of the deviatoric trace, in terms of the ratio between the shear stresses along the extension meridian ($\theta = 0$) and compression meridian ($\theta = \pi/3$) (Menetrey & Willam, 1995; ABAQUS, 2014). The deviatoric eccentricity *e* is determined by the following:

$$e=\frac{3-\sin\phi'}{3+\sin\phi'} \tag{3.20}$$

ABAQUS allows for this deviatoric eccentricity to be considered an independent material parameter. The flow potential function *G* used for the Mohr-Coulomb yield surface is described below.

$$G = \sqrt{(\varepsilon c \backslash o \tan\psi)^2 + (R_{mw} q)^2} - p \tan\psi \tag{3.21}$$

where

$$R_{mw} = r(\theta, e) R_{mc}(\frac{\pi}{3}, \phi') \tag{3.22}$$

and

$$R_{mc}(\frac{\pi}{3}, \phi') = \frac{3 - \sin\phi'}{6\cos\phi'} \tag{3.23}$$

where ψ is the dilation angle measured in the p - R_{mw} q stress plane (see Figure 3.8) at a high confining pressure; ε is a parameter referred to as the meridional eccentricity, which defines the rate at which the hyperbolic function approaches the asymptote (the flow potential tends to a straight line in the meridional stress plane as the meridional eccentricity tends to zero) and the default value taken is 1; $c \backslash o$ is the initial cohesion yield stress; and ϕ' is the Mohr-Coulomb friction angle. This calculation matches the flow potential to the yield surface in both triaxial compression and tension in the deviatoric plane. The smoothness of the elliptic function requires that the deviatoric eccentricity parameter is $0.5 < e \leq 1.0$. The upper limit, $\phi' = 0^o$ ($e = 1.0$), leads to $r(\theta, e) = 1$ and R_{mw} (θ, $e = 1.0$) $= R_{mc}(\pi/3, \phi')$, which describes the Mises circle in the deviatoric plane, as shown in Figure (3.9). The lower limit, $\phi' = 90^o$ ($e = 0.5$), leads to $r(\theta, e) = 2\cos\theta$, $R_{mw}(\theta,$

e = 0.5) = $2R_{mc}(\pi/3, \phi')\cos\theta$, which describes the Rankine triangle in the deviatoric plane, as shown in Figure (3.9).

To represent the Mohr-Coulomb model, ϕ' must be defined between $90^o > \phi' \geq 0^o$ ($1.0 \geq e > 0.5$). The plastic flow potential function G is smooth and non-associated with the yield function f, and the angle of internal friction ϕ' is replaced by the dilatancy angle ψ. However, the role of the dilation angle ψ in the plastic potential function is analogous to the role of the angle of shearing resistance ϕ' in the yield function. The dilation angle ψ attains a constant value just slightly before and after peak strength, but is always smaller than the friction angle. Cohesionless geomaterials generally exhibit the non-associated behavior characterized by the dilation angle $0 \leq \psi \leq \phi'$. However, a non-associated flow rule is often assumed with the MCM, in which the plastic potential function takes the yield function but the friction angle is replaced by the dilation angle (Yu, 2007).

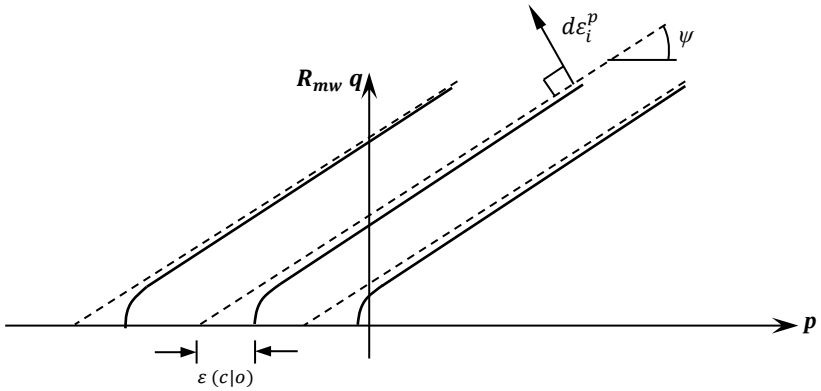

Figure 3.8 Family of hyperbolic flow potentials in the meridional stress plane (ABAQUS, 6.14).

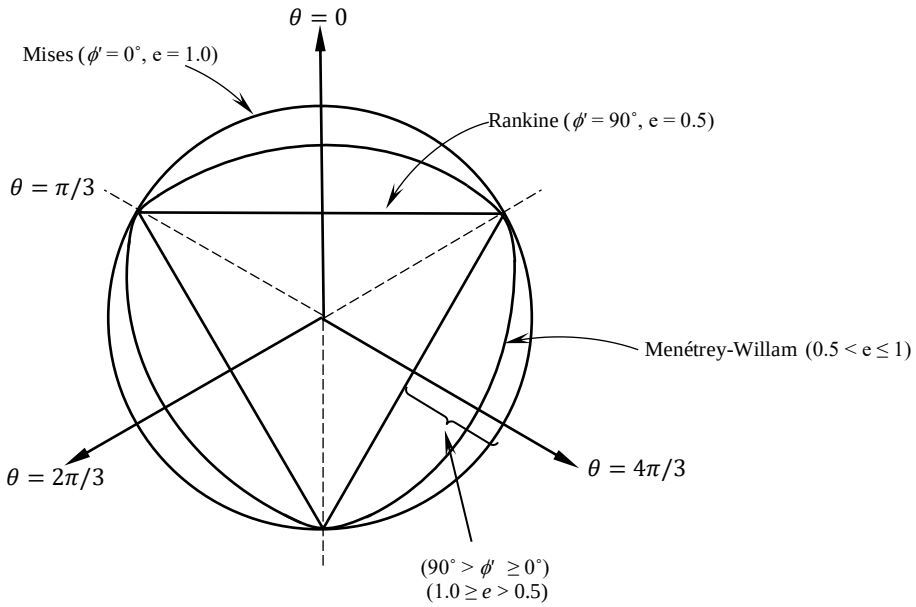

Figure 3.9 Menétrey-Willam flow potential in the deviatoric stress plane (ABAQUS, 2014).

3.2.3 MCM Parameters

As can be seen above, the MCM consists of five main parameters: Young's modulus E and Poisson's v ratio from Hooke's law, which represent the elastic range, cohesion c (c = 0 for cohesionless soils) and angle of internal friction ϕ' from Coulomb's failure criterion, and the dilation angle ψ for characterizing a dilatant material, which describes the irreversible volumetric change developed during plastic shearing. All of these parameters have a clear physical meaning and can be obtained by performing a triaxial test. The MCM (non-hardening) model is very useful in failure problems such as anchor capacity problems, as limit loads can be captured quite accurately, especially for drained conditions. Additionally, true triaxial tests performed when stress combinations cause failure in real soil samples have been shown by researchers to be in close agreement with the irregular hexagonal-shaped MC failure (Goldsheider, 1984).

Next, this research defines the stress-dilatancy equation by determining a suitable relationship between the peak friction angle and dilation angle, linking the plastic potential function to the yield function. Before that, however, the significance of the dilation angle on cohesionless material must be described in details.

3.2.4 The Significance of Dilatancy

An introduction to the concept of dilatancy will serve to underscore its importance. The compacted state of granular material tends to expand in volume (i.e., dilate) during shearing. Taylor (1948) found that the shear strength of cohesionless soil consists of two components: frictional and interlocking particles. Taylor (1948) argued that the interlocking component is responsible for volume change, but did not mention the term "dilatancy." Figure (3.10) shows a pack of incompressible spherical sand particles arranged in loose and dense states respectively. For the initial loose-state condition where there is no significant particle interlocking, changes in the relative positions of the particles when any shear distortion is applied causes a reduction in the total volume of the pack (i.e., contractive), as shown in Figure (3.10a). Conversely, for the initial dense state condition where there is a considerable degree of interlocking between particles, applying any shear distortion will change the relative positions of the particles and cause an increase in the total volume of the pack (i.e., dilatative), as shown in Figure (3.10 b). Therefore, dilatancy is the measure of post-yield volumetric change in granular materials that develops during plastic shearing. The angle of dilation ψ (see Figure 3.10b) is the

parameter used to characterize dilatant material such as dense soil. The dilation angle represents the average value of this angle for the pack as a whole.

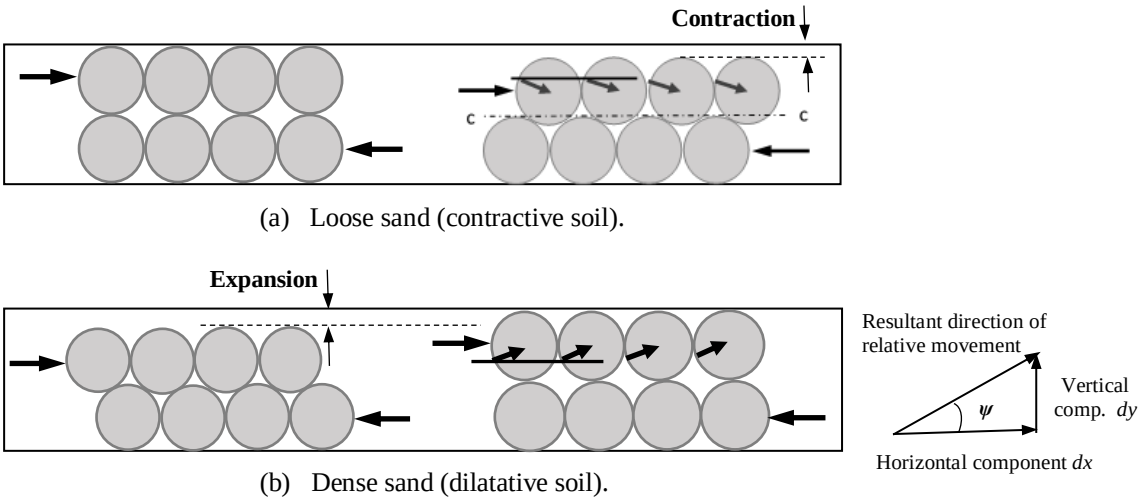

Figure 3.10 Sliding between groups of particles.

As Figure (3.11) shows, in concrete, the dilation phenomenon is caused by frictional sliding along micro-cracks.

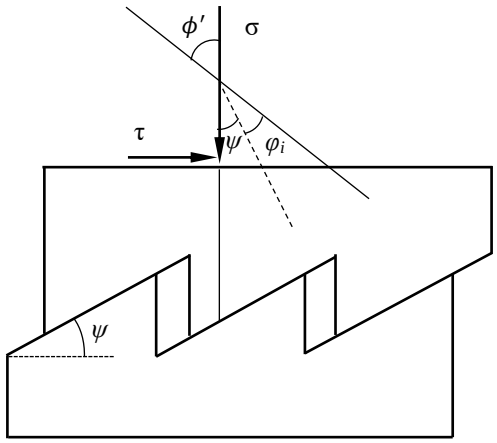

Figure 3.11 Sliding along microcracks leads to dilation

The dilation angle can be determined from the Mohr's circle of strain for plane strain, as shown in Figure (3.12), and also from a conventional triaxial compression or shear box test. For simplicity, one can idealize frictional soil by assuming a bilinear approximation of the triaxial test results, as shown in Figure (3.13). It is clear that the stress-strain relationship in Figure (3.13) involves three deformation parameters (i.e., Young's modulus E, Poisson's ratio υ for elastic range, and angle of dilatancy ψ for the plastic shearing stage) (Vermeer & Borst, 1984).

The angle of dilation ψ can be determined from the plot of volumetric strain versus axial strain for a conventional triaxial compression test on dilatant soil (the broken line) or resulting from the Mohr-Coulomb model (the continuous line), as shown in Figure (3.13). It is important to note that the initial part of this plot represents the elastic regime, while the second part represents the plastic regime.

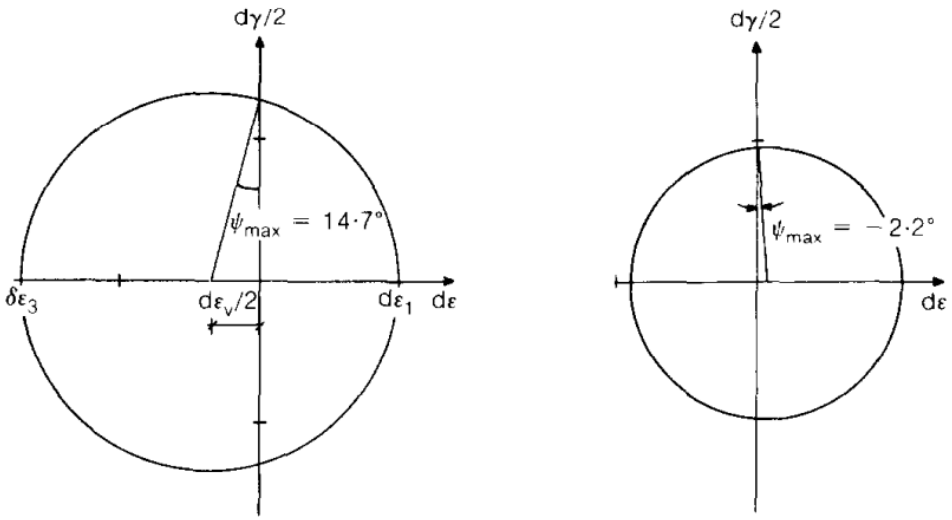

(a) (b)

Figure 3.12 Mohr circles of strain increments for a dense sand sample in a plane strain test: (a) at low stress, and (b) high stress (Bolton, 1986).

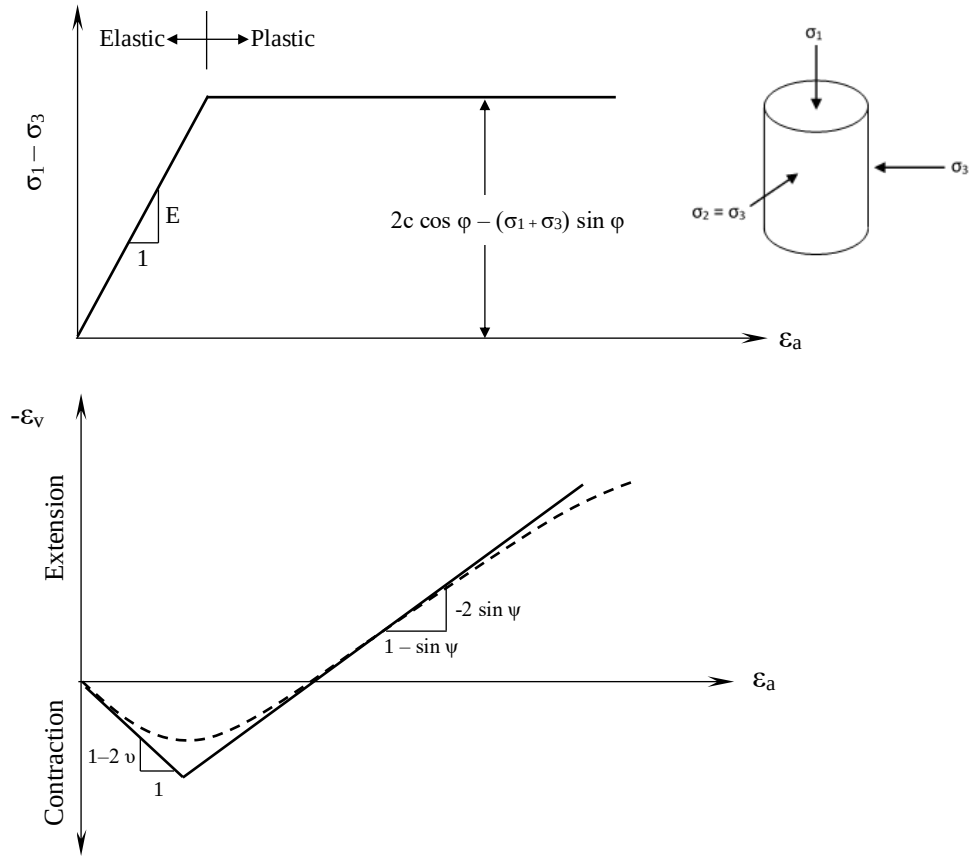

Figure 3.13 Bilinear idealization of the triaxial compression test.

Strictly speaking, a dilatancy angle only has geometrical meaning for plane strain conditions, as shown in Figure (3.12). Therefore, Andersen and Schjetne (2013) characterized the tendency for volume change under triaxial test conditions from the plot of volumetric strain versus axial strain, as shown in Figure (3.13). The angle of dilation ψ from the triaxial test is defined as:

$$\sin\psi = \frac{-d\varepsilon_{vol}}{2d\varepsilon_a - d\varepsilon_{vol}} \tag{3.24}$$

where ε_{vol} and ε_a are the volumetric and axial increment components of strain measured in a drained triaxial test. The angle ψ is still termed a dilatancy angle, recognizing that it cannot be defined in geometric terms on a Mohr diagram, as is possible in the case of

plane strain (see Figure 3.12). The dilation angle ψ performs a similar geometric role with regards to strain rates, as the angle of shearing resistance does with regards to stresses (Row & Davis, 1982). Therefore, the plastic volume strain rate to major principal strain rate are given by the following equations:

$$\frac{d\varepsilon_{vol}}{d\varepsilon_a} = 1 - N_\psi \tag{3.25}$$

$$N_\psi = \frac{1+\sin\psi}{1-\sin\psi} \tag{3.26}$$

The shear box analogy shown in Figure (3.14) is well suited to illustrate the physical meaning of the dilation angle ψ. In the beginning of the shear box test, the horizontal stress σ_{xx} changes to cause some elastic strain, but eventually σ_{xx} will be constant so that both the elastic and plastic contributions vanish (Vemeer & Borst, 1984):

$$\tan\psi = \varepsilon_{yy}^{p} \Big/ \gamma_{xy}^{p} \tag{3.27}$$

$$\varepsilon_{xx}^{p} = 0.0\,;\ \varepsilon_{yy}^{p} = d_y \Big/ y \tag{3.28}$$

where ε_{yy}^{p} represents the volumetric strain component and γ_{xy}^{p} is the shearing strain component. The rate of dilation can be represented by the ratio of plastic volume change over plastic shear strain, $d\varepsilon_{vol} / d\gamma$. The MC model idealizes dilation at a constant rate during plastic shearing. However, this is unrealistic due to the decrease in dilation that occurs as yielding progresses. Also, it has been found to be constant just near and at peak strength. Therefore, the MCM adopting non-associative plasticity causes the dilation rate to be less, but it is still constant during shearing. Figure (3.15) illustrates the effects of dilation on Coulomb's failure envelope.

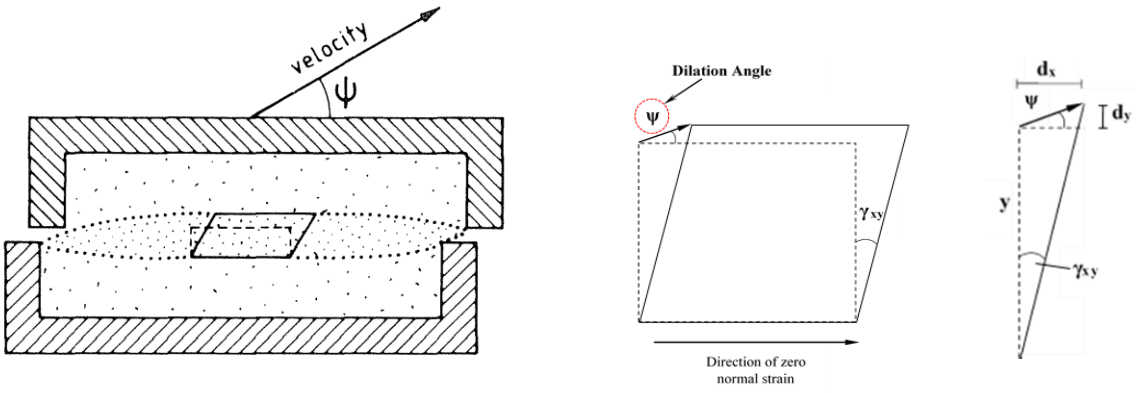

Figure 3.14 The prediction of dilation angle ψ from the shear box test (Vemeer & Borst, 1984).

The linear failure envelope (OA) in Figure (3.15) represents the soil at the critical state condition, while the curved failure envelope (i.e., OBCA) models the actual behavior of the dilatant soil, due to changes in the normal stress. Point C represents the critical state condition in which dilatancy is suppressed. This occurs at the critical normal effective stress $(\sigma_n)_{crit}$. Therefore, the dilation angle ψ is not a fundamental soil parameter, but rather depends on the initial stress state and loading conditions.

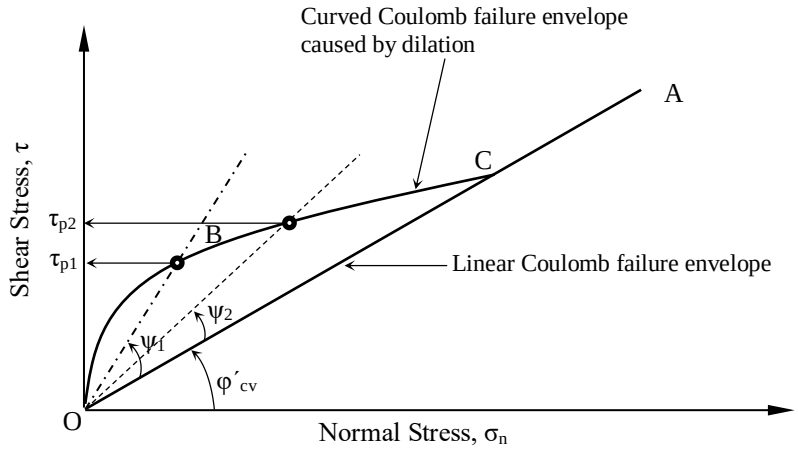

Figure 3.15 Dilatancy effects on Coulomb's failure envelope (Budhu, 2000).

3.2.5 Critical State Friction Angle ϕ'_{cv} and Peak Friction Angle ϕ'_p

The typical shear stress and strain behaviors for initially dense and loose sand in the triaxial test are illustrated in Figure (3.16). This figure shows that the shearing resistance and volume of the soil specimen become constant with continued shearing at a constant shear stress to normal effective stress ratio. This is referred to as the critical state condition. The corresponding angle of shearing resistance of ϕ'_{cv} and angle of shearing resistance of ϕ'_{cv} at the critical state do not change, irrespective of initially loose or dense sand and/or loading conditions. The material behaves at the critical state as a frictional fluid, rather than yielding as a solid. Also, the void ratio in the critical state may sometimes be greater than the accepted maximum void ratio (Schofield & Wroth, 1968). The critical state is identified as the point of constant yield stress that corresponds to the point of zero rate of dilation on the volumetric shear strain curve ($tan\ \psi = \Delta\varepsilon / \Delta\gamma = 0$). Stresses at the critical state define a straight-line failure envelope intersecting the origin, the slope of which is ϕ'_{cv}, as shown in Figure (3.15) (Craig, 2004). It may be difficult to determine the value of the critical state friction angle ϕ'_{cv} because of the relatively high strain (>10%) required to reach the critical state (Craig, 2004). However, the critical state angle of shearing resistance ϕ'_{cv} is a fundamental soil property and principally a function of mineralogy. This can be determined experimentally within a margin of about l°, being roughly 33° for quartz and 40° for feldspar (Bolton, 1986).

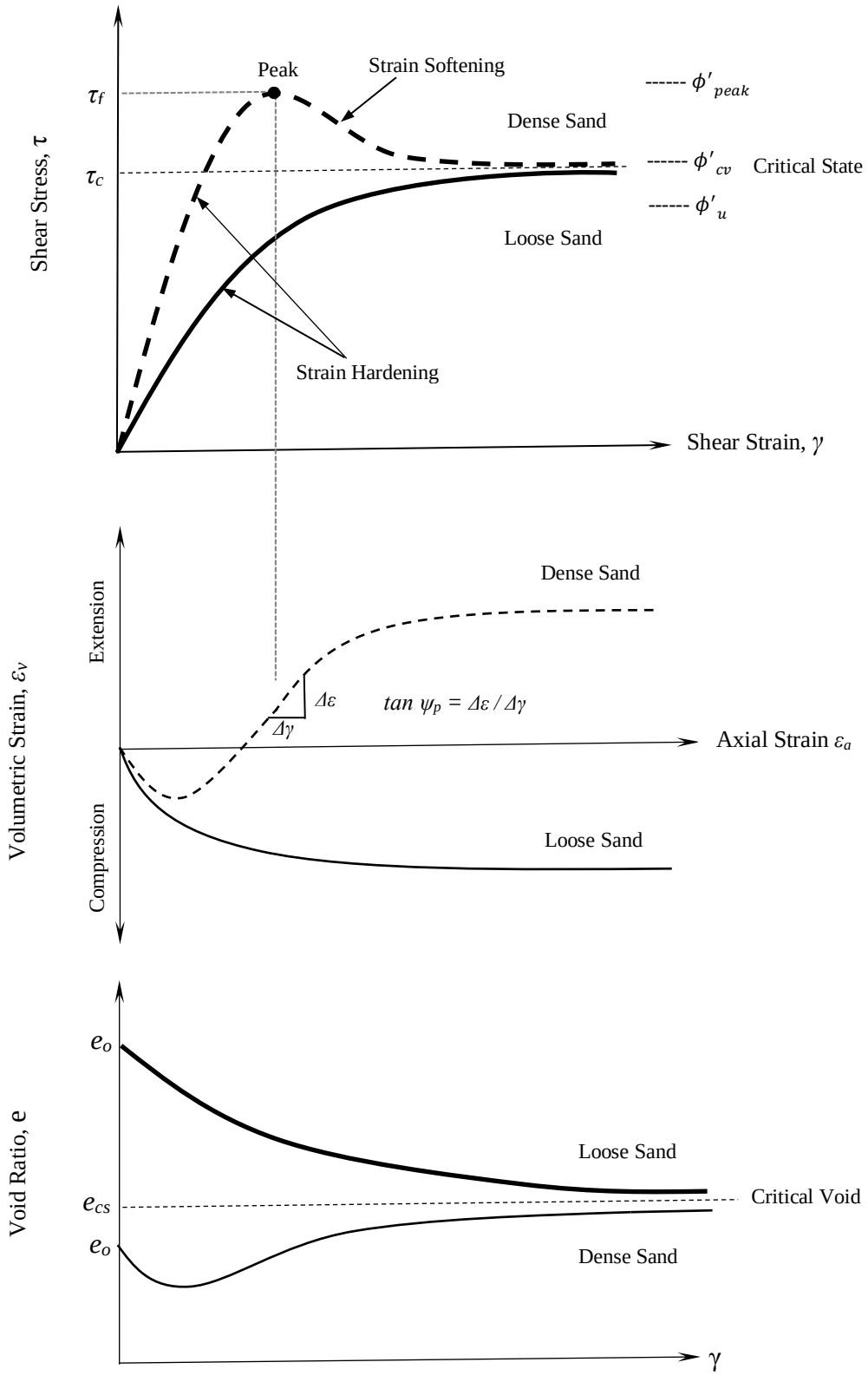

Figure 3.16 Typical shearing responses of cohesionless soils.

In dense sand, the maximum angle of shearing resistance ϕ'_p is determined at the peak stress. This angle is significantly greater than the true angle of friction ϕ'_u between individual particles. The difference represents the work required to overcome interlocking and rearrange the particles. In loose sand, the difference between ϕ'_u and ϕ'_{cv} represents the work required to rearrange the particles. The peak friction angle ϕ'_p generally depends on the initial relative density of the soil sample and stress level at which the test is performed (Andersen & Schjetne, 2013). At a high normal effective stress, ϕ'_p is approximately equal to ϕ'_{cv}, while at a low normal effective stress, ϕ'_p has a very high value. Though the shear strength parameters (ϕ'_p, ϕ'_{cv}) of sand and soil can be determined from either direct shear or drained triaxial tests, in practice, only the drained strength of a sand is normally relevant. The characteristics of dry and saturated sands are the same, provided there is zero excess pore water pressure in the case of saturated sands. In practice, the peak angle of shearing resistance ϕ'_p is used for situations in which it can be assumed that the strain remains significantly less than that corresponding peak stress. If, however, the strain is likely to exceed the corresponding peak stress, the situation may lead to progressive failure. Then, the critical-state friction angle ϕ'_{cv} should be used (Craig, 2004).

3.2.6 Stress - Dilatancy Relationships

Bolton (1986) performed detailed dilatancy and strength analyses of 17 uniform sands in plane strain and axisymmetric loading conditions, and proposed an empirical approach to Rowe's (1962, 1969) and Rowe et al.'s (1964) stress-dilatancy theory. The

strength of cohesionless material is characterized by the angle of internal friction ϕ' and dilation angle ψ. The first limiting value of ϕ' is the critical state friction angle ϕ'_{cv}, which is the fundamental soil property (as discussed above). The second limiting value is the maximum angle of shearing resistance ϕ'_p, which is determined at the peak stress, as shown in Figure (3.16). Bolton (1986) introduced a new relative dilatancy index I_{RD}, in terms of the initial relative density D_r and effective stress level, as follows:

$$I_{RD} = D_r(q - \ln p') - R \tag{3.29}$$

The values $Q = 10$ for quartz and feldspar sands and $R = 1$ were recommended by Bolton (1986) from the test results of the 17 sands. Eq. (3.29) links the dilation angle to the relative density in terms of the dilatancy index I_{RD} and grain-crushing stress, which is sufficient to eliminate dilation and relates to the mean effective stress p' at failure. Andersen and Schjetne (2013) found that for drained compression tests with a friction angle between 35° and 40°, the corresponding average consolidation stress σ_c' is of the order of 60% of the stress at failure p'. Bolton (1986) also proposed that the maximum dilation angle ψ_{max} is related to the peak ϕ'_p and critical state friction angle ϕ'_{cv}. Assuming that the angle of critical state friction angle ϕ'_{cv} does not change irrespective of whether the soil in initially loose or dense sand and/or loading conditions, Bolton (1986) proposed the following empirical stress-dilatancy relationships:

$$\phi_p' - \phi_{cv}' = AI_{RD} \tag{3.30}$$

$$\phi_p' - \phi_{cv}' = k\psi_{\max} \tag{3.31}$$

The preceding correlations proposed by Bolton (1986) were found to be available in the range of $0 < I_{RD} < 4$ for silica sand. According to Bolton (1986), the parameters *k* and *A* were taken as 0.8 and 5, respectively, under plane strain conditions, while *k* and *A* for triaxial strain were taken as 0.5 and 3, respectively. Bolton (1986) also determined the following relationship, which relates the maximum dilation rate in the failure state to the dilatancy index I_{RD}, applicable to both triaxial and plane strain configurations:

$$\left(-\frac{d\varepsilon_{vol}}{d\varepsilon_a}\right)_{\max} = 0.3I_{RD} \tag{3.32}$$

where ε_a and ε_{vol} are the axial and volumetric strains, respectively. Andersen and Schjetne (2013) described the dilation angle ψ defined by Eq. (3.33):

$$\sin\psi = \frac{-d\varepsilon_{vol}}{2d\varepsilon_a - d\varepsilon_{vol}} \tag{3.33}$$

It may be expressed by the following form, in combination with Eq. (3.32):

$$\sin\psi = \frac{0.3I_{RD}}{2 + 0.3I_{RD}} \tag{3.34}$$

Charkraborty and Salgado (2010) proposed the empirical equation for *Q* in Eq. (3.29) as a function of σ_c', instead of the constant value proposed by Bolton (1986). Houlsby (1991) developed a parametric relationship similar to Eq. (3.30) based on the critical state theory. Xiao et al. (2014) developed an empirical equation showing the variations of *A* with the fine contents of sand. These researchers found that in triaxial tests, *A* ranges between 3.0 and 5.53 for Ottawa sand with 0% to 20% fine content. The parameters *Q* and ϕ'_{cv} exhibit minimal variations among cohesionless soils. Therefore, these parameters are not needed as further variables in preparing a parametric study (White et al., 2008).

The drained peak friction angle ϕ'_p from all of the triaxial tests performed by Andersen and Schjetne (2013) shows that ϕ'_p increases as the relative density D_r increases, and decreases with the increasing effective consolidation stress level σ'_c. Also, the dilatancy angle ψ increases with an increasing D_r, and ψ increases with a decreasing σ'_c at a high relative density D_r. Although the value of ϕ'_{cv} might slightly increase with a decreasing p' (Lings & Dietz, 2004), ϕ'_{cv} = 33º is used in the present study, based on the data presented by Randolph et al. (2004). From Eqs. (3.29-3.31), one can predict the peak angle of shearing resistance ϕ'_p and maximum dilatancy angle ψ_{max}, which are required in the finite element calculations, combined with the assumed value of the mean effective stress at failure p'. For dense sand and low stress levels, the peak friction angle from the plane strain test ϕ'^{PS}_p is higher than the peak friction angle from the triaxial test ϕ'^{TX}_p (Schanz & Vermeer, 1996), knowing that the triaxial and direct shear tests are conventionally used to determine the angle of internal friction ϕ'. For plane strain analysis, the value of ϕ'^{PS}_p should be properly adjusted. Lings and Dietz (2004) stated that $\phi'^{PS}_p = \phi'^{DS}_p + 5^o$.

3.3 Large Deformation Modeling

Relative significant displacement of the structural element through the soil medium, which causes significant movement of soil masses, occurs in many geotechnical problems, especially in offshore applications such as pile installation problems (Xu, 2016; Sheng et al., 2009), penetration of spudcan foundations (Craig & Chua, 1990; The et al.,

2008; Hossain & Randolph, 2009), uplift capacity and keying of mooring anchors (Song et al., 2008; Wang et al., 2010; Wang & O'Loughlin, 2014; Tian et al., 2014), lateral buckling of pipelines (Dingle et al., 2008; Yu et al., 2012), etc. Numerical modelling of large deformation problems remains one of the most challenging aspects of geotechnical issues, combining geometric nonlinearity and, often, material constitutive nonlinearity (Tian et al., 2014). The main FE formulations used for large deformation problems in continuum mechanics are presented below.

3.3.1 Lagrangian Approach

In this approach, each individual node of the FE mesh is attached to the material particle in the deformable body during motion. The elements deform as the material deforms, as shown in Figure (3.17a). As the nodes are associated with the material particles, variations in state variables such as stress, strain, velocity, etc., throughout the process can easily be tracked. Also, implementation of the boundary conditions (i.e., free surfaces and interfaces between different materials) is simple. The main drawbacks of the Lagrangian approach are gross distortion of the individual finite elements that accompany large strains within the body, and high computational time (Rout et al., 2017). The Lagrangian approach can be adopted in two ways:

- Total Lagrangian (TL) formulation, and
- Updated Lagrangian (UL) formulation.

The difference between the two formulations concerns the reference state of the body, which is taken at time zero in the TL approach, while the current (i.e., updated) geometry

is used in the UL approach. In the other words, all kinematic or static variables (e.g., stress, strain, velocity, displacement, etc.) in the TL correspond to a time zero configuration, while they correspond to the updated deformed configuration in the UL. In practice, the TL formulation is probably only useful for problems involving large deformations but small strains, or where the complex stress-strain law valid for large strains is to be followed. UL descriptions are commonly used to deal with large displacements, rotations, and strains of solids (Hu & Randolph, 1998). As discussed above, the UL corresponds to the updated deformed configuration, and configuration is updated with each strain increment. With sufficient accumulatively large strains, the FE mesh can suffer from excessive distortion and entanglement, leading the analysis to be terminated or become inaccurate. However, with a proper remeshing criterion or mesh rezoning technique, this approach can also be used for large deformation problems, overcoming the limitations related to element distortion (Cheng & Kikuchi, 1986; Rout et al., 2017). In both approaches, it is necessary to include second derivatives in the description of strains in order to account for finite rotations of the body (Hu & Randolph, 1982).

As mentioned above, both the TL and UL formulations are limited by excessive distortion of the FE mesh as the analysis progresses. However, numerical convergence issues related to this mesh distortion, especially around the structural member where the shear strain localization zones are located, could terminate the analysis, even if serious distortion occurs within a few elements in the entire FE mesh. This termination of the analysis for a distorted element mainly occurs because of a zero or negative value of the Jacobian matrix determinant, understanding that the Jacobian matrix is used in FE analysis

to map the variables from the local coordinate system to a global coordinate system, or vice versa (Sun, 2013).

In regard to the uplift capacity problems in this research, the results of the traditional Lagrangian FE analysis can sometimes be suspect when large deformations are required to mobilize the collapse load. Also, the Lagrangian approach does not take into consideration the geometric changes that might occur as the plate anchor moves upwards towards the ground surface, or into lower strength soil layers. This geometrical nonlinearity is so large that it cannot be ignored during analysis.

3.3.2 Eulerian Approach

In the Eulerian or spatial approach, the nodes of the FE mesh are fixed, while the material flow with respect to the mesh is as shown in Figure (3.17b). As the FE mesh is fixed, the excessive distortion that occurs in large deformation problems can be handled. Eulerian elements may not always be 100% full of material; many may be partially or completely void. The Eulerian material boundary must, therefore, be computed during each time increment, and generally does not correspond to an element boundary. Eulerian analysis is effective for applications involving extreme deformation, which may potentially lead to high nonlinearity, up to and including fluid flow. In these applications, traditional Lagrangian elements become highly distorted and lose accuracy. As material flows through a Eulerian mesh, state variables are transferred between elements via advection. The variables are assumed to be linear or constant in each old element. These values are then integrated over the new elements, after remeshing. The new value of the

variable is found by dividing the value of each integral by the material volume or mass in the new element (ABAQUS, 2014).

The following sections present a review of the most popular numerical approaches proposed over last three decades to handle the issue of excessive distortion of finite element mesh, due to significant soil deformation. The focus is on techniques used in the present study.

3.3.3 ALE Approach

As mentioned above, the mesh velocity in the Updated Lagrangian UL approach equals the material velocity, while the mesh velocity is fixed to zero in the Eulerian approach. In an attempt to combine the best features of both the Lagrangian and the Eulerian approaches, a more flexible approach called the Arbitrary Lagrangian-Eulerian (ALE) was developed by Ghosh and colleagues **(**Ghosh & Kikuchi, 1991; Ghosh, 1990). In the ALE approach, the nodes of the FE mesh may be moved with the material in the normal Lagrangian fashion, or be held fixed in the Eulerian manner. Also, as suggested above, they may be moved in some arbitrarily specified way to give a continuous rezoning capability. Because of this freedom in moving the FE mesh that is offered by the ALE, greater distortions of the continuum can be handled than would be allowed by a purely Lagrangian method, with more resolution than that afforded by a purely Eulerian approach (Donea et al., 2004). In other words, the FE mesh motion based on the ALE technique can move with the material in a normal Lagrangian fashion only where necessary, such as at free boundaries (as shown in Figure (3.17a)). Otherwise, the mesh and material motions are independent, as shown in Figures (3.17c & 3.18).

There are several FE methods that essentially fall within the ALE approach and are used in the analysis of many of geotechnical engineering problems, such as the uplift of plate anchors. Three main techniques will be discussed in the following section, with a focus on those used in the present research. The performance of each method is facilitated by specific time integration schemes for the governing equations, remeshing strategy, and mapping technique (see Table 1), resulting in each approach having certain advantages and disadvantages for particular problems (Wang et al., 2015).

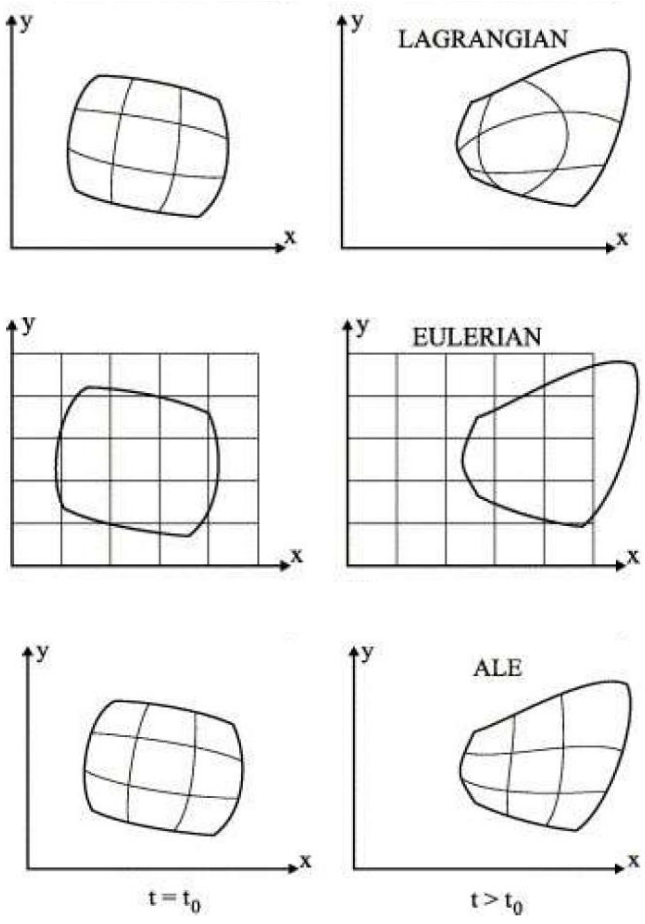

Figure 3.17 An explanatory demonstration of the Eulerian, Lagrangian, and ALE formulations (courtesy of Proudian, 2012).

Table 3.1 Differences Among the Three Techniques (Wang et al., 2015).

	RITSS	**EALE**	**CEL**
Integration scheme	Implicit	Implicit	Explicit
Elements	Quadratic	Quadratic, quartic, quintic	Linear
Implementation	2D, 3D	2D	3D
Meshing	Periodic mesh regeneration in global or local region	Mesh refinement by adjusting the location of nodal points	Mesh fixed in space
Mapping of field variables	Interpolation	ALE convection equation	First- or second-order advection
Cost of Lagrangian phase	Heavy	Heavy	Moderate
Cost of Eulerian phase	Minimal	Minimal	Heavy
Applications	Static, dynamic, consolidation	Static, dynamic, consolidation, dynamic consolidation	Quasi-static, dynamic
User-friendliness	Commercial pre- and post-processors, but requires script programs to control	In-house pre- and post-processors	Commercially available, graphical interface available

3.3.3.1 Efficient ALE Approach

There are two categories of efficient ALE (EALE), including the operator-split (i.e., the decoupled ALE method) and coupled ALE methods. With the decoupled ALE, each time step is decoupled into two phases. First, there is a conventional Lagrangian UL

phase, which is performed on the deformable mesh. Then, the deformed mesh is updated by adjusting the positions of the nodes, but maintaining the topology. Next, the field variables (such as stresses and material properties) are updated and mapped from the old (i.e., distorted) mesh to the new (i.e., refined) mesh, representing the Eulerian flow phase through the mesh. In the decoupled ALE, one first solves the material displacements via the equilibrium equation, and then computes the mesh displacements through a mesh refinement technique. In the UL phase, the incremental displacements are calculated for a given load increment by satisfying the principle of virtual work. It is of note that in a large deformation analysis, the stress–strain relations must be frame-independent to guarantee that possible rigid body motion does not induce extra strain within the material. This requirement is satisfied by introducing an objective stress rate into the constitutive equations. An important feature of an objective stress rate is that it should not change the values of the stress invariants, thus guaranteeing that a previously yielded point remains on the yield surface after being updated, due to rigid body motion (Wang et al., 2014).

After satisfying equilibrium, the UL phase is usually finalized by updating the spatial coordinates of the nodal points according to incremental displacements. Unfortunately, the continuous updating of nodal coordinates alone may cause mesh distortion in regions with relatively high deformation gradients. Hence, the distorted mesh is refined using a suitable mesh refinement technique. Most mesh refinement techniques are based on special mesh generation algorithms, which must consider various factors such as the dimensions of the problem, type of elements to be generated, and regularity of the domain. In fact, it is possible to use any mesh-refining algorithm designed to improve the

shape of the elements once the topology is fixed. Simple iterative averaging procedures can be implemented when possible (Donea et al., 1982; Trepanier et al., 1993; Ghosh & Raju, 1996; Aymone et al., 2001; Wang et al., 2014).

When the ALE description is used as an adaptive technique, the objective is to optimize the computational mesh to achieve improved accuracy, possibly at a low computing cost. (The total number of elements in the mesh and element connectivity remain unchanged throughout the computation.) Mesh refinement is typically carried out by moving the nodes towards the zones with a strong solution gradient, such as localization zones in large deformation problems involving softening materials. Developing such algorithms for any arbitrary domain is usually both difficult and costly. Moreover, these algorithms often do not preserve the number of nodes and elements in the mesh, and may cause significant changes in the topology. To overcome these problems, a general method for determining mesh displacement based on the use of an elastic analysis was presented by Nazem et al., 2006. In this method, the nodes on all of the boundaries of the problem – including the boundaries of each body, material interfaces, and loading boundaries – are first relocated along the boundaries, resulting in prescribed values for the mesh displacements for those nodes. With the known total displacements of these boundary nodes, an elastic analysis can then be performed using the prescribed displacements to obtain the optimal mesh and, hence, the mesh displacements for all of the internal nodes. An important advantage of this mesh optimization method is its independence of element topology and problem dimensions. This method uses the initial mesh during the analysis and does not regenerate a mesh, (i.e., the topology of the problem

does not change, and hence can be implemented easily using existing FE codes). After mesh refinement, all variables at the nodes and integration points are mapped from the old (i.e., distorted) mesh to the new (i.e., refined) mesh (Wang et al., 2014).

Conversely, in the so-called coupled ALE method, this separation usually introduces unknown mesh displacements into the governing global system of equations, doubling the number of unknown variables and leading to significantly more expensive analyses. Several numerical studies have shown that ALE adaptive meshing using the commercial software ABAQUS maintains a high-quality mesh and avoids numerical problems that would develop from a high distortion of the soil surrounding the structural member, especially in different geotechnical applications such as cone penetration (Susila & Hryciw, 2003; Wang et al., 2015; Huang et al., 2004; Walker & Yu, 2006) and uplift capacity problems (Hong et al., 2014 for embedded suction caisson anchors in sand, and Hao et al., 2014 for circular plate anchors in sand). Hao et al. (2014) analyzed uplift capacity problem for plate anchors in sand, using the explicit dynamics procedure and adaptive meshing tool in ABAQUS/Explicit. The different mesh re-discretization strategies used in the analysis did not produce obvious differences in uplift capacity, as determined by comparing the load displacement curve based on different mesh control parameters and smoothing algorithms.

3.3.3.1.1 ALE Method in ABAQUS/Explicit

ABAQUS/Explicit provides a very general and robust adaptive meshing capability for highly nonlinear problems ranging from quasi-static to high-rate dynamic. Adaptive meshing is performed in ABAQUS/Explicit using the arbitrary Lagrangian-Eulerian

(ALE) based on the operator-split technique for implementing mesh distortion issues attributable to large deformations in the surrounding soil. This is especially useful for deeply embedded plate anchors with uplift capacity problems. The ALE adaptive meshing in ABAQUS uses a single mesh definition that is gradually smoothed within the analysis steps. The basic characteristics of the ALE algorithm in ABAQUS/Explicit is that the FE mesh is smoothed at regular incremental steps, keeping the element distortion as minimal as possible within an acceptable element aspect ratio. Also, this technique maintains the same mesh topology, number of elements and nodes, and connectivity, in order to keep a high-quality mesh throughout the analysis (ABAQUS, 2014). Figure (3.18) shows the differences between the Lagrangial and ALE simulations in improving the finite element mesh through a reduction of element distortion.

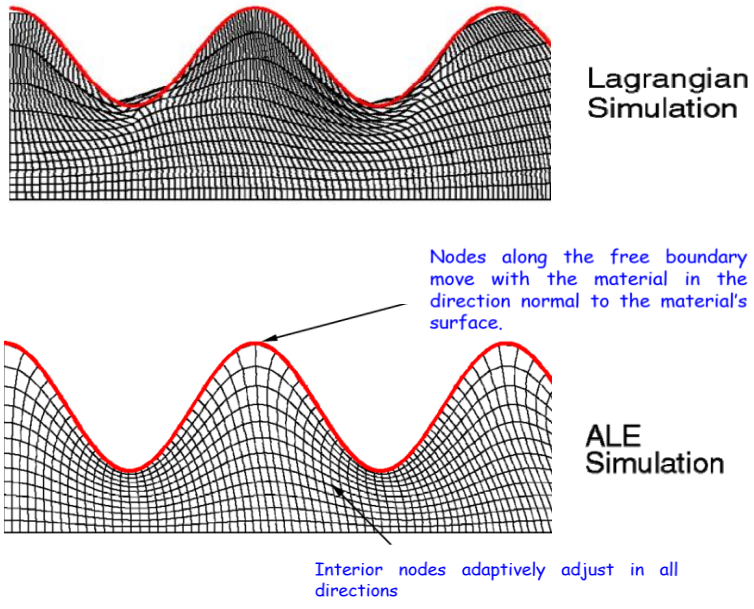

Figure 3.18 Deformed configuration using Lagrangian and ALE simulations, upon completion of the analysis (ABAQUS Handbook, 2014).

In most cases, the frequency of the adaptive meshing is the parameter that most affects the mesh quality and computational efficiency of adaptive meshing. During each adaptive meshing increment, the new mesh is created by performing one or more mesh sweeps, and then advecting the solution variables to the new mesh. ALE adaptive meshing in ABAQUS/Explicit consists of two main tasks:

Mesh sweeps (smoothing the mesh)

In problems where large deformations are anticipated, the improved mesh quality resulting from adaptive meshing can prevent the analysis from terminating as a result of severe mesh distortion. In an adaptive meshing increments, a new, smoother mesh is created by sweeping iteratively over the adaptive mesh domain. These iterations, conducted according to the chosen smoothing algorithm, are called mesh sweeps. During each mesh sweep, the nodes in the domain are relocated based on the current positions of neighboring nodes and elements, in order to reduce element distortion. In a typical sweep, a node is moved a fraction of the characteristic length of any element surrounding the node. Increasing the number of sweeps increases the intensity of the adaptive meshing in each adaptive meshing increment. The default number of mesh sweeps is one. Smoother mesh can be determined in ABAQUS/Explicit based on four aspects, as illustrated below. Each of these aspects can be controlled by defining the adaptive mesh controls. Defaults have been chosen so that the overall algorithm works well for most problems. The resulting meshes will differ depending on the method used.

Volume smoothing

Figure (3.19), the new position of node M is determined by a volume-weighted average of the positions of the element centers C of the four surrounding elements (i.e., two dimensions). This is the default method in ABAQUS/Explicit, and will tend to push the node M away from element center C1 and toward the element center C3, in order to reduce possible element distortion.

Laplacian smoothing

In Figure (3.19), the new position of node M is determined by averaging the positions of the four nodes L connected to M by element edges. The locations of nodes L2 and L3 will pull node M up and to the right in order to reduce element distortion. For domains with boundaries of a complex curvature, volume smoothing generally results in a more balanced mesh.

Equipotential smoothing

Equipotential smoothing is a higher-order method that relocates a node by calculating a higher-order weighted average of the positions of the node's eight nearest neighbor nodes in two dimensions (or its 18 nearest neighbor nodes in three dimensions). In Figure (3.19), the new position of node M is based on the positions of all the surrounding L and E nodes.

Combining smoothing methods

To combine smoothing methods, one must specify the weighting factor for each method. When more than one smoothing method is used, a node is relocated by computing a weighted average of the locations predicted by each chosen method. All weights must

be positive, and their sum should typically be 1.0. If the sum of the chosen weights is less than 1.0, the mesh smoothing algorithm will be less aggressive at each adaptive mesh increment. If the sum of the chosen weights is greater than 1.0, their values are normalized so that their sum is 1.0.

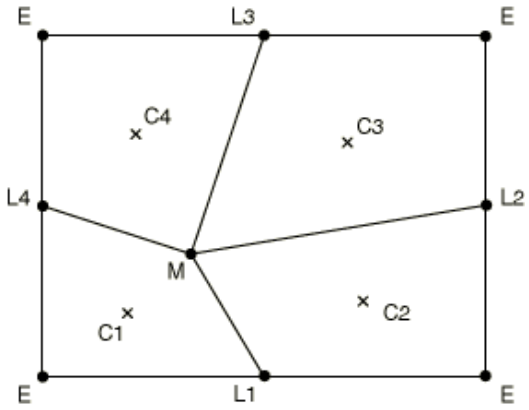

Figure 3.19 Relocation of a node during a mesh sweep
(ABAQUS Handbook, 2014).

Advection sweeps (remapping solution variables)

The process of mapping solution variables from an old to a new mesh is referred to as an advection sweep. At least one advection sweep is performed in every adaptive mesh increment. However, the numerical stability of the advection sweep is maintained only if the difference between the old and new mesh is small. Therefore, if after a mesh sweep the total accumulated movement of any node in the domain is greater than 50% of the characteristic length of any adjacent element, an advection sweep is performed to remap the solution variables from the old to the intermediate mesh. The mesh sweeps will continue until the specified number is reached or the movement of any node again exceeds the 50% threshold. At this time, an advection sweep is again performed to map the

variables from the last intermediate mesh to the new intermediate mesh. The cycle will continue until the number of mesh sweeps reaches the specified number. The number of advection sweeps per adaptive mesh increment required for each adaptive mesh domain is determined automatically by ABAQUS/Explicit. The framework for ALE adaptive meshing in ABAQUS/Explicit introduces advective terms into the momentum balance and mass conservation equations to account for independent mesh and material motion. After the mesh has been smoothed, the element variables, nodal variables, and momentum are remapped by advection. Two advection methods are available in ABAQUS/Explicit:

1. The default second-order advection method improves accuracy during the remapping phase of the adaptive meshing.
2. The first-order method tends to diffuse any sharp gradients of element variables during the remapping phase. This technique should be used only as a computationally efficient alternative for quasi-static simulations that do not require frequent adaptive meshing.

Both advection methods conserve the value of any solution variable integrated over the domain, keeping it unchanged by adaptive meshing. For more information, refer to the ABAQUS Analysis User's Manual.

The Analyses in Chapters 4 and 6 of this research were performed using the decoupled EALE technique. This technique allows the anchor to experience relatively large deformations, avoiding numerical divergence issues due to mesh distortion that occurs around the corners of the anchor plate, where the large shear strain localization zones exist. Basically, the nature of the pullout process of a plate anchor is a quasi-static

process. The large deformation finite element analysis was formulated in the frame of dynamic explicit use of ABAQUS/Explicit software rather than a static implicit procedure to promote numerical stability and avoid the divergence problems from mesh distortion that could occur in a static formulation. To simulate the quasi-static condition as closely as possible, a pullout rate of 0.02 m/sec was applied at the reference point of the anchor.

Explicit finite element programs using a central difference integration scheme are more efficient than implicit programs when solving transient large-deformation problems. The time step size of explicit programs is limited by the Courant stability criterion, which says that the largest stable time step is the minimum time necessary for a sound wave to cross the smallest element in the mesh. As an analysis proceeds, elements stretch in length and shrink in width, and the size of the time step decreases. When the size of the time step becomes too small, continuing the analysis becomes prohibitively expensive (Benson, 1989).

3.3.3.2 RITSS Technique

The Remeshing and Interpolation Technique with Small Strain (RITSS) was developed by Hu and Randolph (1998). It was employed by Randolph (2006) for large deformation problems in geotechnical engineering, such as cone penetration, spudcan penetration, and caisson installation issues. The RITSS technique is a combination of the conventional Lagrangian small strain finite element analysis, automatic periodic remeshing process, and linear field variables by polynomial interpolation from the old mesh to the new. Large deformations occurring during the keying process of the plate anchor may cause numerical instability as a result of severe mesh distortion. The RITSS

approach was adopted successfully in the second part of this research in order to investigate the plate keying process.

The basic characteristic of this approach is that the deformation of the structure object (in this research, a plate anchor) is divided into increments that are adequately small enough to ensure that there is no mesh distortion that could terminate the analysis. After every analysis step for each small deformation increment, the last deformed geometry is extracted for the next new analysis step (see Figure 3.20) and remeshed based on the updated structural object. The main difference between RITSS and EALE is that the topology of the mesh can be updated as needed in RITSS, while the topology of the problem does not change when using EALE. Thereafter, all field variables such as stresses and material properties are mapped from the old mesh to the new. This remeshing-remapping process is repeated in a loop until the accumulated displacement of the structural object reaches the desired value. Figure (3.21) describes the algorithm for the RITSS technique.

3.3.3.2.1 RITSS Implementation

Generally, the RITSS approach includes four steps (Randolph et al., 2008): (1) initial mesh generation, (2) incremental step of the Lagrangian analysis, (3) updating of the boundary conditions and remeshing, and (4) mapping of the field variables and material properties from the old mesh to the new. In any analysis, steps (2) to (4) are repeated until completion of the whole LDFE analysis. Step (2) can be fulfilled by any traditional Lagrangian finite element program, such as AFENA (Carter & Balaam, 1995). More recently, FE commercial packages such as ABAQUS (Wang et al., 2010a; Wang et

al., 2010b), ANSYS (Yu, 2008), and LS-DYNA (Liyanapathirana, 2008) have been used to implement step (2) (Tian et al., 2014). Once the last deformed geometry is extracted, a new mesh (i.e., steps (1 & 3)) that is more suitable to the current state of the problem must be generated via third party software by using the mesh generation capabilities (e.g., ABAQUS, ANSYS) or even the affiliated pre-processor of any Lagrangian finite element program. The accuracy of large deformation analysis using RITSS depends significantly on the interpolation and mapping procedure of step 4 in the analysis. Irrespective of whether the field variables are mapped to the new integration points (e.g., total or effective stresses and material properties) or the new nodes (e.g., velocities, accelerations, and pore pressure), the interpolation is always conducted locally within an old element, old element patch, or triangle connecting old integration points, depending on the mapping technique adopted. Therefore, the mapping process for the field variables is the core of the RITSS approach.

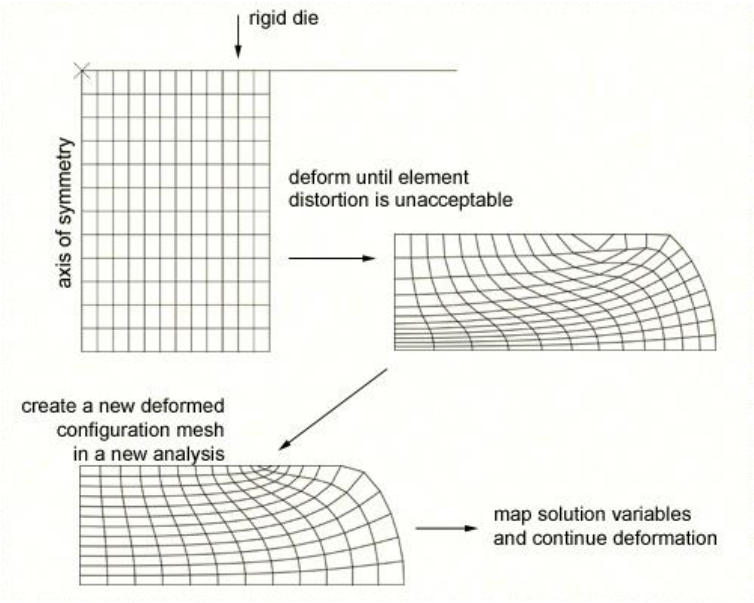

Figure 3.20 Use of mesh-to-mesh solution mapping as a component of a rezoning technique (ABAQUS User's Manual, 2014).

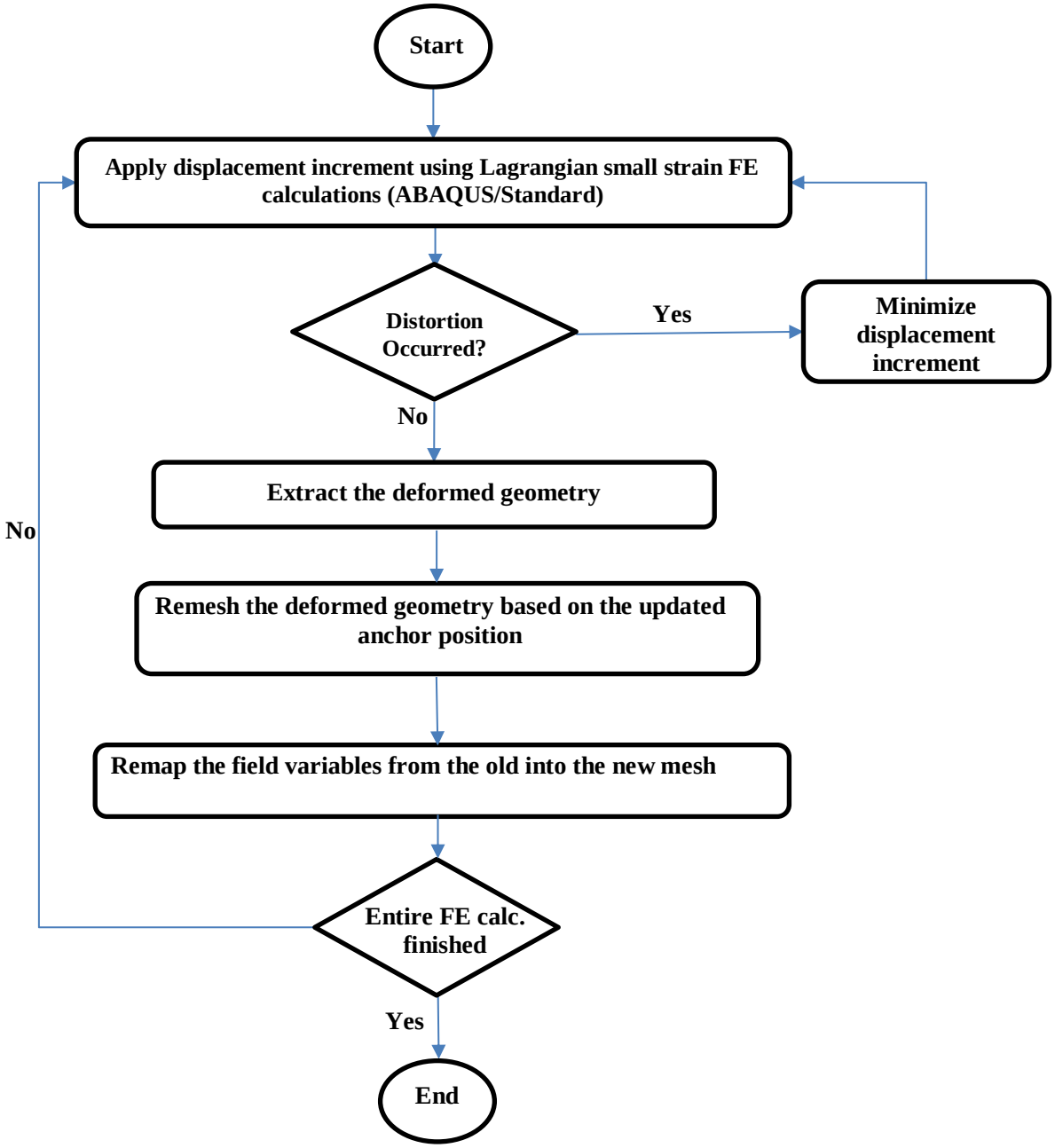

Figure 3.21 RITSS approach flow chart.

Three main mapping techniques for the field variables (i.e., stresses and material properties) moving from the old mesh to the new were explored in previous FE simulations (Wang et al., 2015). Super-convergent Patch Recovery (SPR) was first proposed by

Zienkiewicz and Zhu (1992), and Recovery by Equilibration of Patches (REP) was described by Boroomand and Zienkiewicz (1997). These techniques are employed to recover stresses from old integration points and move them to old element nodes. Subsequently, the old element containing each new integration point is searched for, and the field variables are then interpolated from the old element nodes. In contrast, in the Modified Unique Element Method (MUEM) proposed by Hu and Randolph (1998), the field variables are mapped directly from the old integration points in the old mesh to the integration points in the new mesh. To implement step (4), powerful commercial computation and programming packages such as FORTRAN and MATLAB may be required to write user-subroutine code, adopting one of the abovementioned mapping techniques.

3.3.3.2.2 Mesh-to-Mesh Solution Mapping

This algorithm, similar to MUEM, is used to map field variables between meshes with different topologies. It has been adopted by a number of researchers due to the simplicity and applicability of the RITSS approach to geotechnical applications. These researchers demonstrated the performance of the RITSS approach, applying the algorithm to several geotechnical problems such as deep penetration of a T-bar penetrometer (Tian et al., 2014), penetration of shallow strip footing (Tian et al., 2014), keying of a plate anchor (Tian et al., 2014; Yu et al., 2009), cone penetration tests (Sun, 2013; Wang et al., 2015; Randolph, 2006), and penetration and buckling of shallowly embedded pipelines (Wang et al., 2015). Most recently, the RITSS approach was adopted by Xu (2016), using an SPR or MSM mapping solution technique to model a concrete pile penetration problem.

The numerical analysis was carried out using ABAQUS software, and the RITSS approach was implemented by a script written in Python code.

ABAQUS adopted the MSM solution mapping technique by using a built-in function termed “mesh-to-mesh solution mapping,” The keyword ***MAP SOLUTION*** operates by interpolating results from the nodes in the old mesh to points (either nodes or integration points) in the new mesh. Most recently, Tian et al. (2014) avoided the need for user-defined code to map field variables by utilizing this function to present a simple implementation of RITSS. According to Dassault Systèmes, MSM is performed according to the following steps:

1. Extract the coordinate information from the old mesh.
2. Associate the solution variables with the nodes in the old mesh. For nodal solution variables such as nodal temperature or pore pressure, the association is already made.
3. For integration point variables (e.g., stresses), ABAQUS obtains the solution variables at the nodes of the old mesh by extrapolating values from the integration points to the nodes of each element of the old mesh, and then averaging these values over all similar elements abutting each node.
4. Specify the element of the old mesh in which the new integration point lies. Next, determine the location of each point in the new mesh with respect to the old mesh by inverse transformation of the position information from a global coordinate system to a natural local coordinate system (Xu, 2016).

5. Interpolate the field variables (i.e., stresses and material properties) from the nodes of the old element to the points in the new model. All necessary variables should be automatically interpolated in this way so that the solution can proceed with the new mesh.

3.3.3.2.3 RITSS Implementation for Keying Process by ABAQUS

The whole LDFE of the plate keying process requires a large number of increments to reach its final orientation. Therefore, the RITSS approach can be implemented by submitting a Python script code to the ABAQUS/Standard software to automate the process of keying. The Python script code includes the main steps:

1. The original problem geometry is built with initial geostatic stresses and the first small incremental displacement is applied, producing an ODB (Output File) result file after completion of the analysis. In the keying process problem, the FE analysis is controlled by displacement increments at the anchor pad eye.
2. After every small increment, the updated position of the plate anchor, soil boundaries, and interfaces are extracted from the previous ABAQUS ODB result file. The ABAQUS built-in functions **PartFromOdb** and either **Part2DGeomFrom2DMesh** or **PartFromNodesAndElements** are utilized to store the geometric information of the deformed mesh and generate a new geometry. In the plate anchor keying problem, the extraction scheme is divided into three conditions:

- During the keying process, the soil surface or free boundary is allowed to be changed in the following numerical analysis.
- The soil–anchor interface is limited to the "no breakaway" condition during the keying process. (This eliminates the potential gap between the anchor and soil body.) A pair of nodes is placed at the same initial geometric location. One is attached to the rigid anchor (i.e., the master surface) and the other is affixed to the interface soil body (i.e., the slave surface). To tie these two surfaces, ABAQUS eliminates the degrees of freedom of the slave surface nodes that are constrained and ties the two surfaces together for the duration of the simulation. By default, ABAQUS uses a position tolerance criterion to determine the constrained nodes, based on the distance between the slave nodes and the master surface. Alternatively, one can specify a node set containing the slave nodes to be constrained, regardless of their distance to the master surface.
- Other boundaries are kept unchanged during the keying process

All finite element nodes coordinate and deformation information for the abovementioned boundaries are detected and stored in a scratch file by the ABAQUS. Before a new displacement increment begins, the geometry of a new finite element model is created based on the updated coordinates of the nodes from the scratch file for all soil boundaries and interfaces in the last displacement increment.

3. A new finite element model is set up, based on the deformed geometry and remeshing.
4. Field variables such as stresses and material properties are mapped from the old mesh to the new, using the keywords ***RESTART**, **WRITE**, and ***MAP SOLUTION** in the Python script file. The first keyword is used to extract and store the field variables from the old mesh, and the second keyword is used to map the field variables by extrapolation and interpolation calculations, as discussed above with regards to the MSM algorithm.
5. The Python script input file is run for another incremental step of displacement. Steps (2 - 4) are repeated until completion of the analysis.

With the ***MAP SOLUTION** function built in to this procedure to avoid any need to write user subroutine code, the whole LDFE simulation can be conducted with ABAQUS/CAE. However, by writing one piece of ABAQUS Python script, a large number of increments required in the LDFE can be automated (rather than operated manually in ABAQUS/CAE). This Python script can be submitted to ABAQUS for running without any user intervention (Tian et al., 2014). The structure of the Python code is illustrated below. It is described briefly for implementation into the RITSS approach for use with the keying problem.

START OF THE PYTHON CODE (MASTER PROGRAM)

```
import os, sys, re, osutils
import driverUtils, sys
from Functions_Utility import *
……
```

INITIAL MODEL PHASE (SUBROUTINE)

```
execfile('MESH-0Mod.py')
# CODE TO CREATE INITIAL MODEL WITH THE FIRST DISPLACEMENT INCREMENT OF KEYING

        mymodel=mdb.models[’Model-1’]
        p = mdb.models['MESH-0'].Part(name='Soil', dimensionality=TWO_D_PLANAR,
type=DEFORMABLE_BODY)
        p.BaseShell(sketch=s)
        p = mdb.models['MESH-0'].Part(name='Anchor', dimensionality=TWO_D_PLANAR,
        type=DISCRETE_RIGID_SURFACE)
        p.AnalyticRigidSurf2DPlanar(sketch=s1)
        mdb.models['MESH-0'].Material(name='Soil')
        a = mdb.models['MESH-0'].rootAssembly
        a.Instance(name='Anchor-1', part=p, dependent=ON)
        a.Instance(name='Soil-1', part=p, dependent=ON)
        p.setMeshControls(regions=faces, elemShape=QUAD, technique=FREE, allowMapped=False)
        elemType1 = mesh.ElemType(elemCode=CPE8R, elemLibrary=STANDARD)
        p.seedEdgeBySize(edges=pickedEdges, size=size_around_anchor, deviationFactor=0.1, constraint=FINER)
        mdb.models['MESH-0'].parts['Soil'].generateMesh()
        …...
        mdb.models['MESH-0'].GeostaticStress(name='Predefined Field-1', region=region, stressMag1=-160,
        vCoord1=0.0, stressMag2=0.0, vCoord2=10.0, lateralCoeff1=0.5, lateralCoeff2=None)
        mdb.models['MESH-0'].StaticStep(name='Static', previous='Initial', timePeriod=1.0, maxNumInc=10000,
        initialInc=0.001, minInc=1e-35, maxInc=0.01, nlgeom=ON)
        ……
        MyJob=mdb.jobs['MESH-0']
…..
```

LOOP PHASE

```
# KEEP THE LOOP UNTIL THE FINAL PLATE ANCHOR ORIENTATION IS REACHED
while (MeshNumber <= MAX):
        nowJobName="MESH-" + "%i" % (MeshNumber)
        prevJobName="MESH-" + "%i" % (MeshNumber-1)
        #SUBROUTINE CODE TO EXTRACT GEOMETRY AND BOUNDARY CONDITIONS DATA OF THE
        OLD MESH FROM PREVIOUS ANALYSIS AND CONVERT IT TO A NEW PART AND REMESH IT
```

```
execfile('RemeshingandSettingUpNewModel3.py')
        …..
        deformed=mdb.models[nowJobName].PartFromOdb(fileName=odbName,name='Soil',instance=o
        rphanInstance,  shape=deformedShape,  step=importStep)
        p1=mdb.models[nowJobName].Part2DGeomFrom2DMesh(name='Soil',part=deformed,
        featureAngle=featureAngle)
        …..
        # REMESH AND SET UP NEW MODEL
        ……
        p.seedEdgeBySize(edges=pickedEdges,  size=size_around_anchor_base,  deviationFactor=0.1,
        #Soil Anchor Surface constraint=FINER)
        mdb.models[nowJobName].parts['Soil'].generateMesh()

#MAP FIELD VARIABLES AND MATERIAL PROPERTIES FROM PREVIOUS ANALYSIS USING
MESH - TO - MESH SOLUTION
….
model.keywordBlock.insert(modelBlock, """*MAP SOLUTION""")
….
# CREATE NEW JOB TO CONDUCT SMALL INCREMENT OF KEYING PROCESS AND SUBMIT
THE ANALYSIS
…..
mdb.jobs[nowJobName]. writeInput(consistencyChecking=OFF)
os.system ('abaqus job=MESH-'+str (MeshNumber) +' oldjob=MESH-'+str (MeshNumber-1)+ '
output_precision=full interactive')
….
```

END OF CODE

3.4 Soil Anchor Interface Modeling

Contact interface modeling is an important factor in the numerical modeling of soil structure interaction problems. A soil-anchor interface transmits shear plus normal forces when they are in contact. The relationship between these two force components is the friction between the contact bodies. However, the friction model available in ABAQUS is the basic concept of the Coulomb friction model, which relates the maximum allowable

frictional (shear) stress across an interface to the contact pressure between the contacting bodies.

According to ABAQUS, two contacting surfaces can carry shear stresses across their interface up to a certain magnitude before they start sliding relative to one another; this state is known as sticking. The Coulomb friction model defines this critical shear stress as τ_{critic}, at which the sliding of the surfaces begin as a fraction of the normal effective contact stress at the interface σ' between the surfaces ($\tau_{critic} = \mu\sigma'$). Stick/slip calculations determine when a point transitions from sticking to slipping or from slipping to sticking. The fraction $\mu = \tan\delta$ is known as the coefficient of friction, where δ is the soil anchor interface friction angle. The value for δ depends on the interface characteristics and relative movement between the anchor and soil; however, it generally lies between 50% and 100% of the peak friction angle (Roy et al., 2015). The value δ = 0% of the peak friction angle ϕ'_p is adopted for perfectly smooth anchors (i.e., frictionless), while δ = 100% is used for perfectly rough anchors; finally, δ = 50% is for use in situations of intermediate roughness.

There are two ways to define the basic Coulomb friction model in ABAQUS when simulating a soil-structure contact interface: rigid plastic and bilinear elasto-plastic models. In the rigid plastic model, once the shear stress at the soil anchor interface reaches the critical value $\mu\sigma'$, permanent relative displacement suddenly occurs, as shown in Figure (3.22a). In the default bilinear elasto-plastic model shown in Figure (3.22b), sticking friction corresponds to the elastic regime, and slipping friction corresponds to the plastic regime. The amount of elastic slip is taken as 5% of the element size in the contact

interface. For instance, if the minimum contact interface soil element size is 10 mm, the full interface strength can be mobilized when the relative displacement is around 1/2. Xu (2016) found in a feasibility study using a RITSS approach and conducted for a pile penetration problem that the rigid plastic contact model will cause serious divergence problems in FE analysis. Conversely, an elastic zone in the elasto-plastic contact model will help to increase the stability of an FE analysis.

Frictional constraints are enforced by default with stiffness (i.e., the penalty method) in ABAQUS/Standard, and with the general contact algorithm in ABAQUS/Explicit. The separation or breakaway of the anchor from the soil is allowed to occur where the normal effective stresses σ' behind the anchor plate face are reduced to zero (particularly in the first and third parts of this research). Immediate breakaway occurs when there is no suction between the soil and anchor for cohesionless soil.

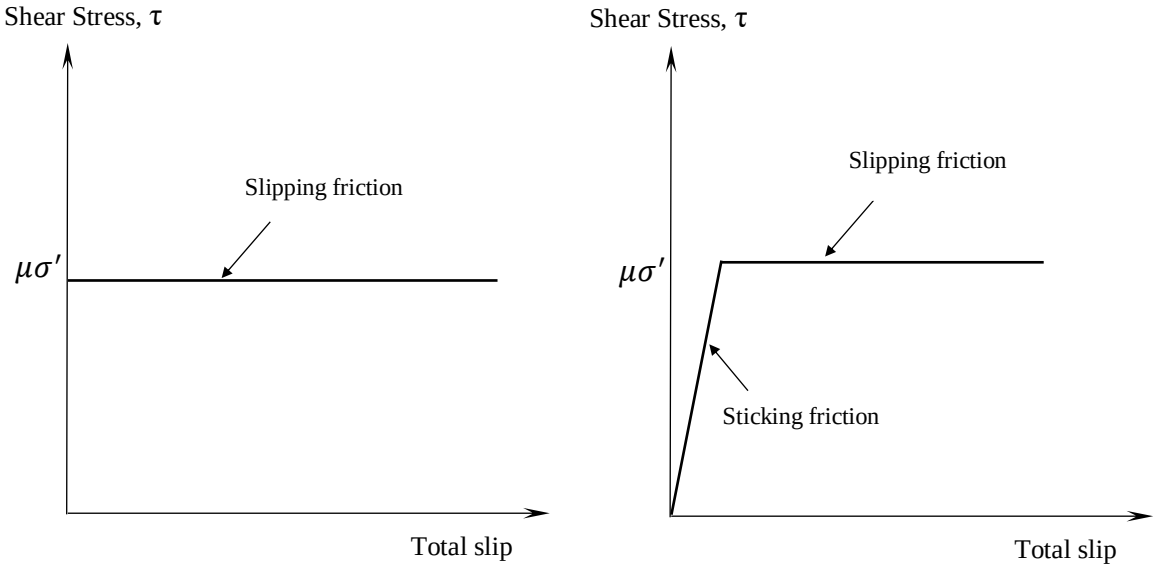

a- Rigid plastic model.

b- Bilinear elasto-plastic

Figure 3.22 Soil anchor contact interface model.

CHAPTER IV

VERTICAL PULLOUT CAPACITY OF CIRCULAR PLATE ANCHORS IN SAND*[1]

4.1 Introduction

As noted in chapter two, attention to plate anchors in sand has been relatively limited in the research literature, particularly for deeply embedded plates. Moreover, most previous studies on embedded plate anchor capacity problems in sand cover a relatively shallow anchor embedment depths (typically ranging between 8-10 plate widths or diameters), which is not sufficiently deep to characterize the transition behavior from shallow to deep embedment. Also, the influence of elastic soil stiffness E in evaluating anchor performance in sand, especially for deeply embedded anchors, has received little attention in the research literature and needs to be systematically investigated. Therefore, this chapter is devoted to improve the understanding of deep plate anchor behavior in sand, with a focus on describing the transition from shallow to deep failure mechanisms. The present finite element study investigates a range of anchor embedment depths from one to more than 20 plate diameters. Additionally, the effect of elastic soil behavior (in terms of Rigidity Index I_r) on anchor performance is investigated, with emphasis on deeply embedded anchors. This study focuses on how dimensionless breakout capacity N_q varies with embedment depth, considering the effects of rigidity index, dilatancy angle and

* Reprinted with permissions from "Numerical Investigation of Uplift Behavior of Circular Plate Anchors in Uniform Sand" by Authors Nabil Al Hakeem and Charles Aubeny, 2019, *Journal of Geotechnical and Geoenvironmental Engineering, ASCE* 145 (9).

friction angle. The validity of the present finite element analyses was evaluated through comparisons to lower bound plastic limit solutions, previous finite element studies, and previously published experimental data.

4.2 Framework of the Parametric Finite Element Study

This chapter presents a parametric finite element study of pullout capacity of circular, horizontally oriented anchors in sand, subjected to centric loading (Figure 4.1a). Additionally, the analyses are directly applicable to helical anchors.

The pullout resistance may be expressed in terms of a dimensionless breakout factor defined as:

$$N_q = Q_{ult}/A\sigma'_z \tag{4.1}$$

where Q_{ult} is ultimate load (force) capacity, A is anchor area and σ'_z is effective vertical overburden stress. Figure 4.1b shows a typical trend in the variation of N_q with anchor embedment depth z as depicted by Rasulo *et al.* (2017) for a circular plate anchor of diameter D embedded at depth z. Shallow embedment failures involve breakout of a soil block to the surface, with the associated N_q-z curve showing a relatively rapid increase in breakout resistance with increasing embedment depth. For deeply embedded anchors a localized flow - around failure mechanism develops, with corresponding constant breakout factor N_{qmax}. Experimental data, supported by numerical simulations presented later in this chapter, show a smooth transition between the shallow and deep mechanisms. Therefore, a full predictive model for plate anchor capacity must (1) describe the shallow failure mechanism, (2) define the maximum breakout factor N_{qmax} for deeply embedded anchors, and (3) define the depth at which N_{qmax} is approached.

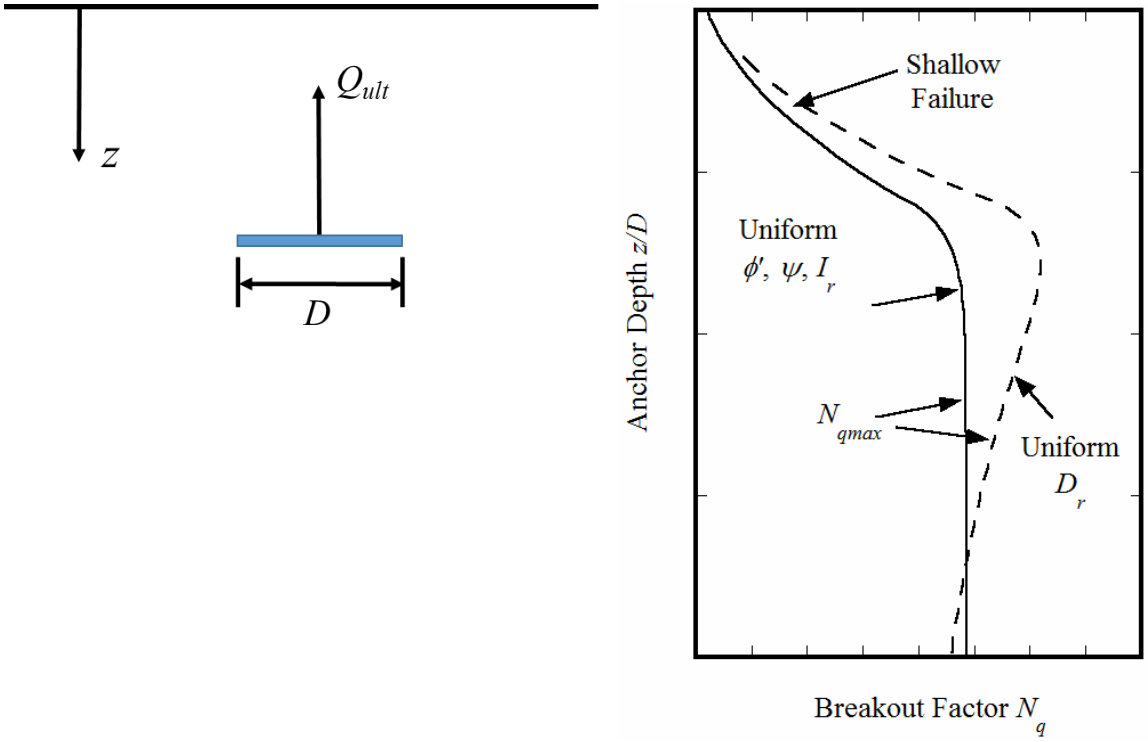

Figure 4.1 Definition sketch and typical anchor behavior. Reprinted with permission from (Al Hakeem and Aubeny, 2019).

This framework applies to a soil profile for which the relevant soil properties (friction, dilation, rigidity index) are constant (Figure 1b). However, it is important to recognize that such conditions virtually never occur, even in hypothetical soil profiles having a uniform relative density D_r. Since the soil parameters controlling breakout resistance are stress-level dependent (e.g. the reduction of friction angle ϕ', dilation angle ψ and rigidity index I_r at high stress levels), it follows that N_{qmax} cannot be considered to be independent of depth, and in fact declines as illustrated by the dashed line in Figure 4.1b. It further follows that a predictive framework for N_{qmax} and the depth at which it mobilizes must account for both soil relative density as well as the stress-level dependency of the various soil parameters affecting load capacity.

In regard to the soil strength-deformation parameters that need to be considered in developing a model of load capacity versus embedment depth (N_q-z/D), the study presented herein considers (1) the strength behavior defined by an angle of internal friction ϕ', (2) post-yield volume change behavior defined by a dilation angle ψ, and (3) elastic behavior defined in terms of the soil rigidity index I_r. Past studies of anchor performance have done much to quantify the influence of the first two parameters (ϕ' and ψ) for relatively shallow levels of embedment, typically z/D less than 8. However, the current investigation revealed that the elastic properties of the soil medium, as characterized by a rigidity index I_r, also exerts a significant influence on the performance of deeply embedded anchors. Accordingly, the predictive model of anchor performance developed in this chapter includes rigidity index along with ϕ' and ψ, which is key to calculating anchor capacity at deep embedment. It is recognized that site investigations for most anchor installations will not typically involve direct evaluation of friction angle ϕ', dilation angle ψ and rigidity index I_r. Rather, a more realistic design approach would generally be based on relative density D_r (typically estimated from Cone Penetration Tests CPT) from which the relevant strength, dilation and elastic parameters would be estimated. At a given relative density, all three parameters vary with confining stress and, therefore, depth. Thus, a framework for predicting plate anchor capacity will ideally express anchor capacity as a function of relative density and embedment depth, implicitly accounting for effects of stress-dependent variations in material parameters on anchor capacity.

In view of the above discussion, the study presented in this chapter proceeds according to the following steps:

- Finite element analyses are employed to investigate the influence of embedment depth z/D and soil parameters ϕ', ψ and I_r on the breakout factor N_q.
- Based on the finite element studies an empirical function is developed for the breakout factor $N_q(\phi', \psi, I_r)$.
- Existing correlations of the relevant soil parameters to confining stress and relative density $\phi'(\sigma'_c, D_r)$, $\psi(\sigma'_c, D_r)$, $I_r(\sigma'_c, D_r)$ – are invoked to develop relationships for breakout factor as a function of relative density, unit weight and depth $N_q(D_r, \gamma', z/D)$.

Most studies to date have considered relatively shallow anchor embedment, although experimental work by Merifield *et al.* (1999) and Rasulo *et al.* (2017) investigated embedment depths z/D greater than 10 to 15. Load capacity measurements in deeply embedded anchors showed a reversal in the curvature of the N_q versus z relationship, suggesting that a transition from a shallow to a deep failure mechanism occurs. The trend of the data in these investigations suggest that the bearing factor trends toward a constant value N_{qmax}, but these experimental and numerical studies were not extended to sufficient anchor embedment depths z/D to fully define the relationship.

As summarized by Rasulo *et al*. (2017), Equation 4.2 characterizes the behavior of shallowly embedded circular plate anchors reasonably well. Equations 4.3 and 4.4 show the bounds of the factors F_{as1} and F_{as2}. The lower bounds shown correspond to conditions of zero dilation.

$$N_q = 1 + F_{as1}\left(\frac{z}{D}\right) + F_{as2}\left(\frac{z}{D}\right)^2 \tag{4.2}$$

$$F_{as1} = 2\sin\phi'_{cs} \text{ to } 2\tan\phi' \quad (4.3)$$

$$F_{as2} = 0 \text{ to } (4/3)\tan^2\phi' \quad (4.4)$$

These equations realistically describe overall measured trends, but uncertainty remains, particularly in regard to the effect of the dilation angle ψ.

In light of the above summary of the state of knowledge on circular plate anchors in sand, finite element studies were undertaken to: (1) fully define the breakout factor N_q versus z/D relationship from shallow embedment through the transition range to a deep embedment characterized by a maximum breakout factor N_{qmax}, and (2) to evaluate the validity of Equations 4.2 - 4.4 and explore the possibility of incorporating these equations as one component of a general model of circular plate anchor behavior.

4.3 Geometry, Material, and Finite Element Model

A wished in place circular plate anchor using the ABAQUS/Explicit finite element analysis was considered in this chapter. As detailed in chapter three, a linearly-elastic, perfectly-plastic Mohr- Coulomb model was adopted in this research to simulate sand soil behavior, while the anchor plate was considered as perfectly weightless rigid because of its very high stiffness. The symmetry in the circular geometry and the applied loads dictated an axisymmetric formulation. Therefore, the soil medium was discretized into a mesh of four node axisymmetric bilinear quadrilateral reduced integration ABAQUS elements CAX4R. A typical structured mesh (Figure 4.2b) is created by zoning the problem geometry. A zone of high element density, with a minimum element size h_{min} $=D/20$, is constructed in the vicinity anchor. Preliminary finite element analyses showed

that the far field boundaries shown in the Figure 4.2a were sufficiently large to diminish any boundary effects on the calculated pullout capacity of plate anchor. Horizontal and vertical displacements were constrained at the bottom of the finite element domain, while only lateral displacements were constrained at the far field vertical boundaries. The displacement-controlled FE procedure was used in the current analysis. Therefore, displacement loading increments were imposed on the reference point of rigid body (plate anchor). However, the stiffness matrix obtained by displacement-based finite element formulations tends to over-estimate the actual stiffness, which the analysis presented herein sought to mitigate by employing a reduced integration formulation. Therefore, using reduced integration point instead full integration element is advisable for many cases in non-linear plasticity problems. Generally speaking, second order elements give better stress distribution with more accuracy and lower number of elements. However, second order elements dramatically increase the simulation time due to having more nodes and therefore far larger stiffness matrix compared to first order elements. Accuracy of the solution for displacement-based finite element formulations, which use first ordered reduced integration point can be improved by increasing the number of elements.

All analyses were performed with an anchor diameter D = 1m and a thickness-diameter ratio t/D = 0.1. Key soil properties considered in the analysis include the friction angle ϕ', dilation angle ψ, and rigidity index of the soil I_r. The present parametric study considered friction angles ranging from ϕ' equal to 30° to 50°, soil dilation angle ψ varying from 0º to 25º, and soil rigidity index I_r varying from 100 to 500. Other soil properties for all cases included a cohesion c = 0.05 *kPa*, Poisson's ratio μ = 0.3, an at-rest lateral earth pressure

coefficient K_o = 0.5, and soil unit weight γ= 18.0 kN/m^3. The soil-anchor frictional interface was simulated using the Abaqus/Explicit contact surface approach which is described in terms of a Coulomb friction coefficient μ= tan φ'_u, where φ'_u is the soil anchor interface friction angle. As detailed in Chapter III, φ'_u values depend on the interface characteristics and relative movement between the anchor and soil. Accordingly, a value of $\varphi'_u = 0.5\ \phi'$ was adopted in this analysis. Separation or breakaway of the anchor from the soil was permitted to occur at locations below the anchor plate where stresses reduce to zero.

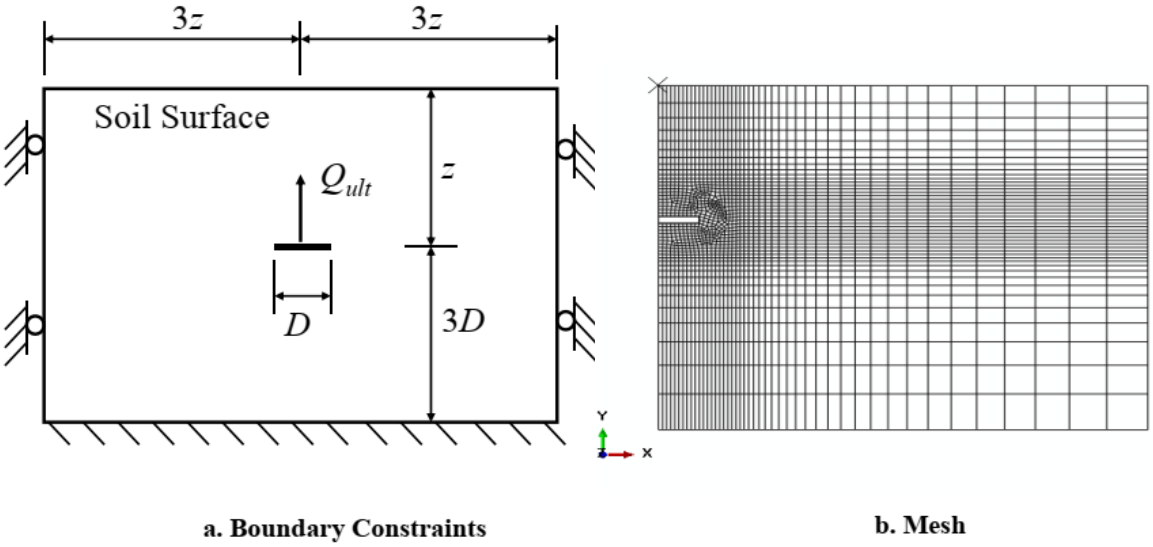

a. Boundary Constraints **b. Mesh**

Figure 4.2 Finite element model.

Although small strain FE analysis, which is mainly adopted by Abaqus/Standard solver, has been noticeably used in the determination of anchor capacities especially for shallow anchors, the accuracy of this approach is suspect where large displacements are required to mobilize the ultimate capacity of relatively deep plate anchors. This is because of the small strain FE analysis cannot take account of geometric changes as the anchor moves upwards toward the free surface, and potentially into soil of lower strength. The

pullout process of a plate anchor is essentially quasi static in nature, while the large deformation finite element analysis was formulated in the frame of dynamic explicit rather than a static implicit procedure. The dynamic formulation using ABAQUS/Explicit solver was selected to promote numerical stability and avoid the divergence problems that could be in the static formulation. Adaptive meshing is performed in ABAQUS/Explicit using the arbitrary Lagrangian-Eulerian (ALE) to implement numerical divergence issues related to the excessive mesh distortion due to the large deformations in the surrounding soil around the corners of the anchor plate where shear strain localization zones exist. ALE adaptive meshing in Abaqus uses a single mesh definition that is gradually smoothed within analysis steps. ALE adaptive mesh domain are set to the four squares around the plate anchor with length of diameter of plate *D*. To seek a balance between minimizing the computational time and at the same time matching quasi-static state as closely as possible, three pullout rates of 0.005 m/sec, 0.01 m/sec and 0.02 m/sec were performed to investigate the influence of the pullout rate. The non-dimensional load-displacement curves are illustrated in Figure 4.3 and for associated material (ϕ' =40º, ψ = 40º) and non-associated material (ϕ' = 40º, ψ =10º) respectively, where z/D = 4, Poisson's ratio μ=0.3, and E = 20000 *kPa*. It can be seen from Figure 4.3 that the uplift non-dimensional curves for three different pullout rates are approximately identical. Therefore, the pulling rate of 0.02 m/s is slow enough to simulate quasi static analysis, which is adopted for all subsequent analyses.

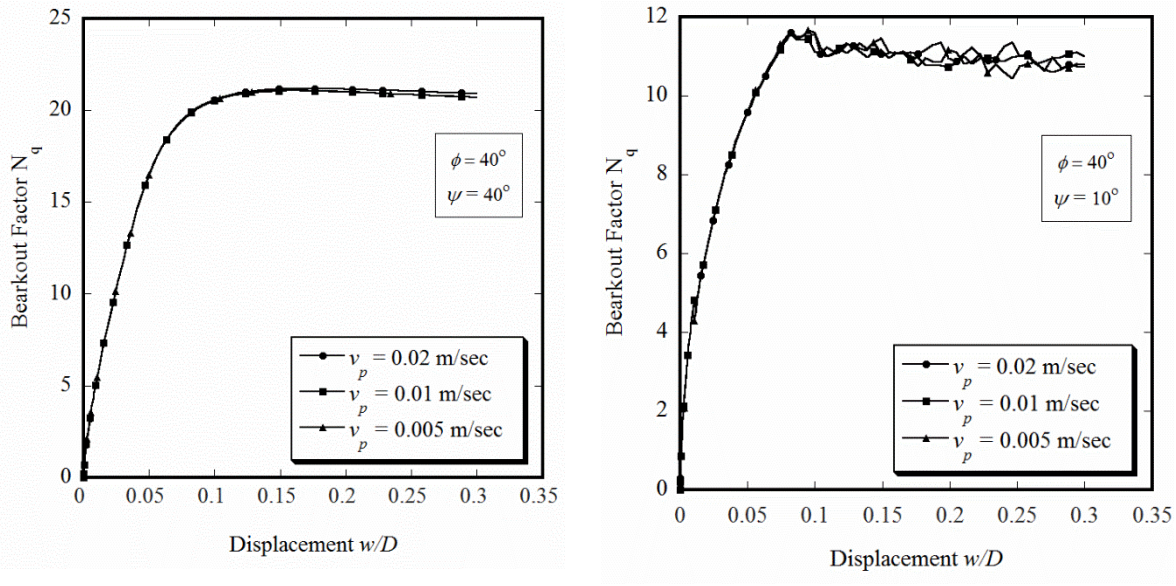

Figure 4.3 Uplift capacity curves at different pullout rates

4.4 Adopted Failure Criterion

In this study the collapse load of the plate anchor was taken as the resistance at which anchor displacement reached 25% of the anchor diameter. This collapse criterion is consistent with that adopted by Song et al., (2008). As shown in Figure (4.4), the collapse load at shallow depths occurs well below this displacement magnitude, so pullout capacity estimates derived from the finite element results are not affected by this failure criterion. However, for deeply embedded anchors, large deformations must occur for resistance to approach its ultimate value, so the displacement limitation described often governs. The 25% of the anchor diameter criterion is somewhat arbitrary, but it represents a balance of maintaining a tolerable level of displacement without discounting too much of the actual capacity of the anchor. In regard to tolerable displacements, it is noted that the high degree of compliance in most mooring systems leads to a lesser importance assigned to anchor

displacements. Nevertheless, the failure criterion adopted in this chapter must be kept in mind, especially in instances where tolerable anchor displacements are an issue. Additionally, the effective stress calculation should account for the embedment loss when deeply embedded anchors are under consideration, as this can influence the breakout factor calculation in Eq. 4.1

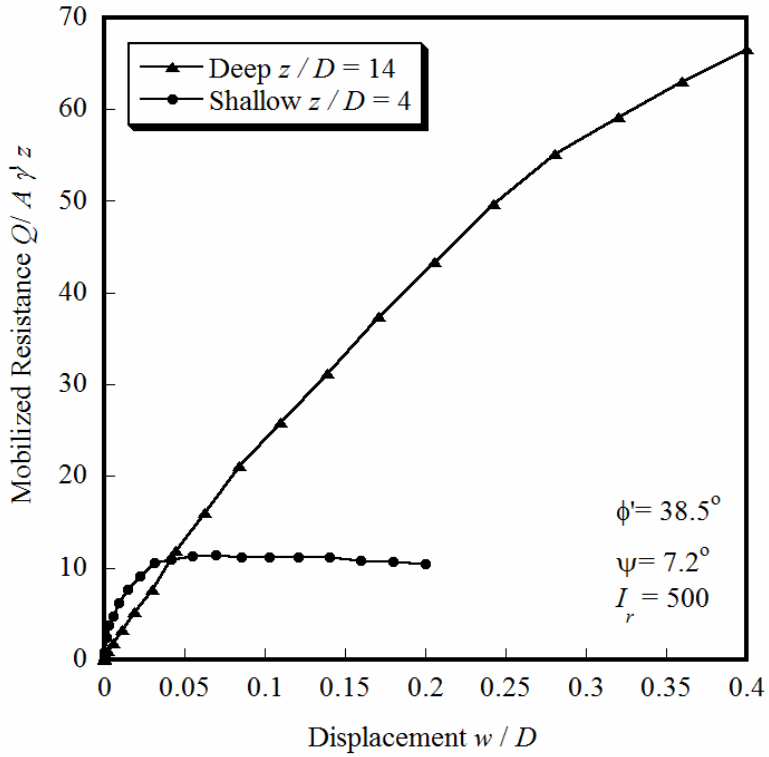

Figure 4.4 Typical load-displacement curves for shallow and deep embedment. Reprinted with permission from (Al Hakeem and Aubeny, 2019).

4.5 Typical Failure Mechanism

To gain insight into the failure mechanisms of plate anchors embedded in sand, Figures 4.5 and 4.6 show contours of total displacement at failure state. The properties of the loose sand used in the simulations to investigate failure mechanisms were taken from a soil

having a relative density of about D_r = 37%, peak friction angle ϕ'_p =35.5º and max dilation angle ψ_{max} = 0º. The properties for the very dense sand, peak friction angle ϕ'_p = 46.7º and max dilation angle ψ_{max} =14.5º were taken as representative of a relative density of about D_r = 95%. A rigidity index I_r = 500 was used in all cases. These properties correspond to data on sands at a confining stress level of 100 *kPa* measured by Schanz and Vermeer (1996). Figures 4 and 5 show the contours of the displacements for the anchors with z/D= 2, 8, and 16 in loose and very dense sands. The mode of failures that one can notice during this study as following:

1. For shallow embedment depths (e.g. *z/D* = 2, Figure 4.5a and Figure 4.6a), irrespective the soil properties (I_r, ϕ', and ψ), the failure slip surface starts from the corner of the plate anchor and extend to the free surface with an angle approximately around the dilation angle ψ from vertical.
2. For intermediate embedment depths (e.g. *z/D* = 8, Figure 4.5b and Figure 4.6b), the development of a shallow versus deep failure mechanism depends on the soil properties (I_r, ϕ', and ψ). It can be noticed that a localized failure mechanism develops in the loose sand. By contrast, in a very dense sand the influence of the free surface on the displacement pattern is still evident.
3. For deep embedment depths (e.g. *z/D* = 16, Figure 4.5c and Figure 4.6c), irrespective the soil properties (I_r, ϕ', and ψ), it can be noticed a localized slip surface around the anchor.

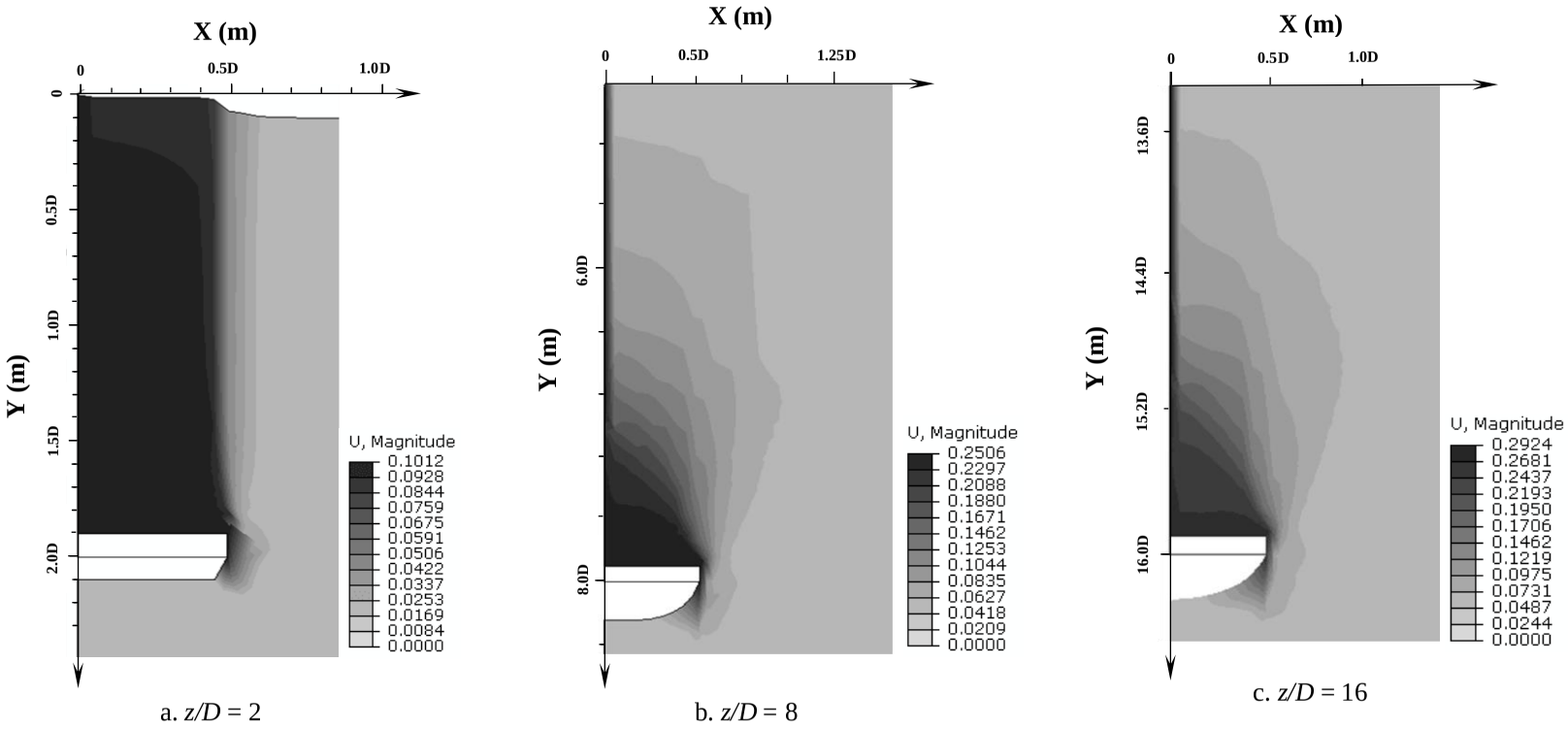

a. $z/D = 2$ b. $z/D = 8$ c. $z/D = 16$

ϕ' =35.5°, ψ = 0°, I_r = 500

Figure 4.5 Contours of resultant displacement in loose Sand. Reprinted with permission from (Al Hakeem and Aubeny, 2019).

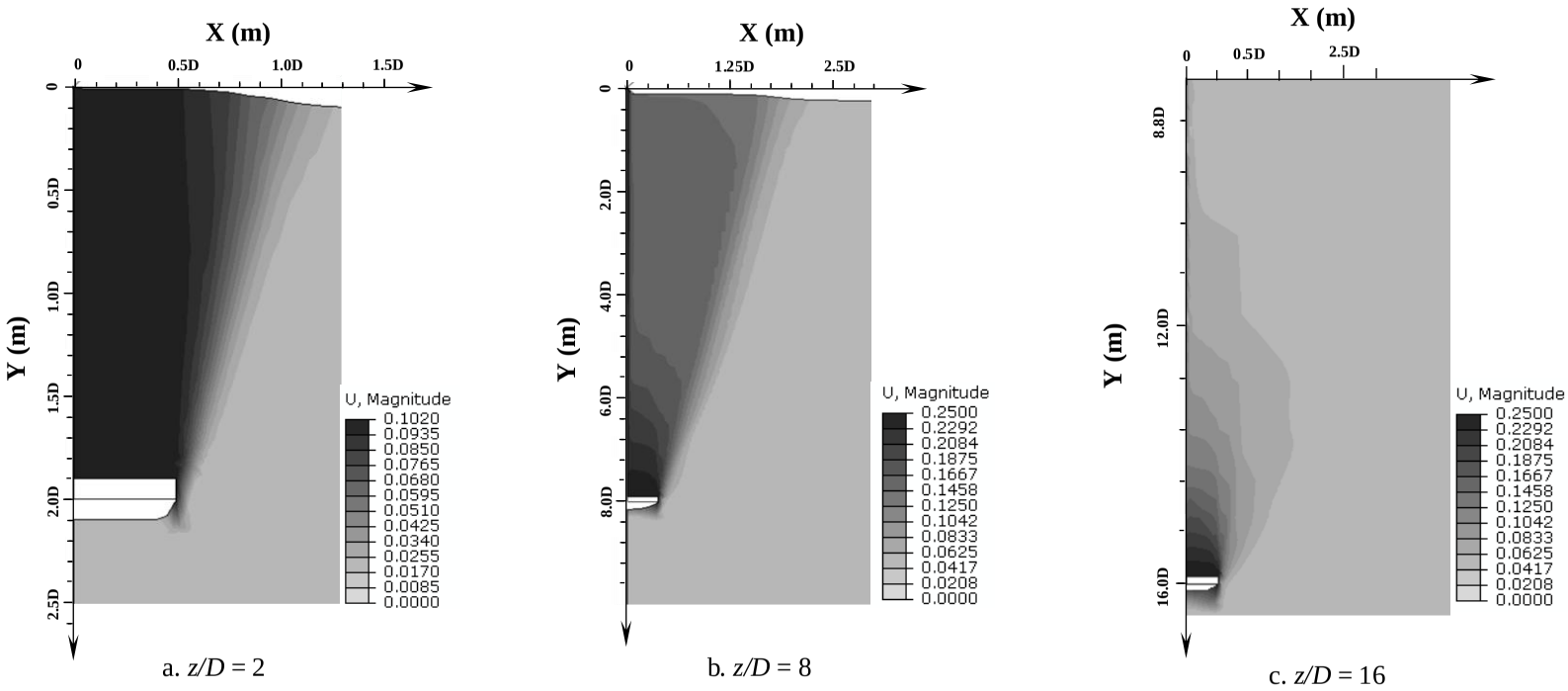

a. $z/D = 2$ b. $z/D = 8$ c. $z/D = 16$

ϕ' =46.7°, ψ = 14.5°, I_r = 500

Figure 4.6 Contours of resultant displacement in very dense Sand. Reprinted with permission from (Al Hakeem and Aubeny, 2019).

4.6 Comparisons with Prior Numerical, Analytical and Experimental Results

The validity of the present numerical study is evaluated through comparisons to previously published numerical, analytical and experimental results. Lower and upper bound solutions provided by plastic limit analyses, which treat the soil as a perfectly plastic material with infinite-elastic modulus before yielding, can provide useful reference solutions for the FE analyses provided that elastic effects are not significant (Wang *et al.*, 2010), which is usually the case at relatively shallow embedment depths. Figure 4.7 compares the current LDFE estimates of circular anchor and lower bound solution of (Merifield *et al.*, 2003). For consistency with the lower bound solution, the FE adopts an associated flow rule, $\psi = \phi'$. As shown in this figure, the breakout factors increase in a nonlinear manner with increasing z/D and the greatest increase occurs with high friction angles ϕ'. It can be seen that the FE results agree very well with the lower bound results by Merifield. This is due to the selection of the rigidity index (taken as $I_r = 500$), since the breakout factors depend on the value of soil rigidity I_r. Therefore, $I_r = 500$ could represent a rigid plastic condition due to the negligible magnitude of elastic strain at the beginning of the yielding stage. Also, it should be noted that the lower bound Merifield solution does not consider rigidity index I_r, but the finite element studies show the results to be essentially independent of I_r at shallow embedment.

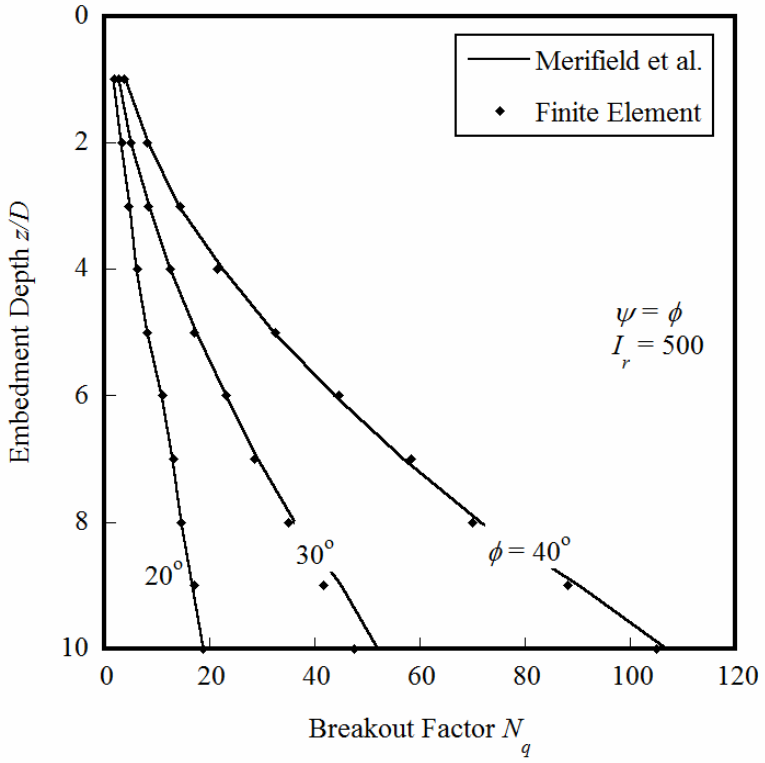

Figure 4.7 Comparison of finite element predictions to Merifield et al. (2003) Lower Bound Solution. Reprinted with permission from (Al Hakeem and Aubeny, 2019).

Laboratory model tests of anchor pullout capacity of anchors in a sand test bed provide a second basis for validation of the LDFE results. While such tests are typically supported by the measured friction angle ϕ' and dilation angle ψ of the test bed, many early model test studies omitted evaluation of the elastic moduli E or G, from which rigidity index I_r is determined. Since the LDFE studies indicate that the effects of I_r can be significant, particularly at high embedment depths z/D, the absence of information on the elastic properties of the soil test bed precludes fully conclusive comparisons of LDFE results to laboratory measurements. A notable exception is the Giampa *et al.* (2017) anchor test study, which did include estimates of the elastic modulus E. Table 4.1 provides a

comparison of LDFE solutions to small-displacement finite element analyses employing a non-associated flow rule by Giampa *et al.* (2017). Differences between the two solutions ranges from 0.1 to 31%. On average, the LDFE values exceed those of Giampa *et al.* (2017) by about 6%; however, no consistent bias is apparent on the high or low side for the two methods. Possible sources of the differences between the two sets of predictions can be the absence of unique solutions for non-associated flow problems, the consequences of small versus large displacement analyses, and the need for judgment in selecting collapse loads, especially for deep anchors; as examples, Giampa *et al.* (2017) reported oscillations on the order of $\pm$10% in their solutions, and this study adopted a 25% maximum displacement criterion for selecting collapse loads from LDFE solutions.

Table 4.2 compare LDFE predictions to experimental data by Giampa *et al.* (2017) for shallow circular anchors in sand. In this case the elastic modulus (E) of the test bed were known, along with the friction and dilation angles. As per the recommendations from Giampa *et al.* (2017), Poisson's ratio $\nu = 0.25$ was used in the calculation of shear modulus and rigidity index and a coefficient of earth pressure at-rest $K_0 = 0.45$ was assumed in the finite element analyses. For each test listed in Table 4.2 a LDFE analyses was performed using the best available inputs for ϕ', ψ and I_r. Table 4.2 shows that the finite element predictions tend to over-estimate the measurements. Various causes may be postulated for this bias, but the author considers that a major contribution to this bias is that the model assumes peak dilation with no softening to occur at all points in the zone of yield, whereas actual dilatational behavior is dependent on strain level as detailed in chapter three. Accordingly, peak dilation does not mobilize at all locations simultaneously and, if

displacements are sufficiently large, a critical state assumption may be more representative of actual conditions.

Table 4.1 Comparison of LDFE Solution to Giampa et al. (2017) Small Displacement FE Solutions.

Case	Unit Weight kN/m^3	E (kPa)	Diameter, D (m)	Depth z (m)	z/D	ϕ' (^{o})	ψ (^{o})	I_r	FE Giampa N_q	LDFE N_q
1	14.75	3000	0.152	0.457	3	40	9.5	335	7.5	9.35
2	14.75	3000	0.152	0.760	5	40	9.5	202	15.4	19.38
3	14.75	3000	0.152	1.06	7	40	9.5	145	29.6	22.8
4	14.75	3000	0.254	0.457	1.8	40	9.5	335	3.5	3.68
5	14.75	3000	0.254	0.760	3	40	9.5	202	6.8	8.334
6	14.75	3000	0.254	1.06	4.2	40	9.5	145	11.6	14.38
7	15.6	12000	0.152	0.457	3	50	25.0	892	12.6	13.13
8	15.6	12000	0.152	0.760	5	50	25.0	536	27.4	30.1
9	15.6	12000	0.152	1.06	7	50	25.0	385	46.1	60
10	15.6	12000	0.254	0.457	1.8	50	25.0	892	5.7	4.54
11	15.6	12000	0.254	0.760	3	50	25.0	536	12.8	12.92
12	15.6	12000	0.254	1.06	4.2	50	25.0	385	19.6	23.57
13	15.35	6000	0.152	0.457	3	45	17.5	540	9.8	10.98
14	15.35	6000	0.152	0.760	5	45	17.5	325	19.5	26.8
15	15.35	6000	0.152	1.06	7	45	17.5	233	38.0	39.95
16	15.35	6000	0.254	0.457	1.8	45	17.5	540	5.0	3.96
17	15.35	6000	0.254	0.760	3	45	17.5	325	9.6	9.87
18	15.35	6000	0.254	1.06	4.2	45	17.5	233	15.9	19.05

Table 4.2 Test Bed Parameters in Giampa et al. (2017) Helical Anchor Tests

Unit Weight kN/m^3	D_r (%)	E (kPa)	ϕ' (^{o})	ψ (^{o})	Depth (m)	Diameter (m)	I_r	Measured N_q	LDFE N_q
14.9	23	3000	42.2	12.9	0.787	0.254	180	6.70	9.36
14.7	16	3000	40.5	10.3	0.787	0.254	190	6.30	8.90
14.8	19	3000	41.3	11.6	0.762	0.254	190	6.40	9.20
15.7	48	12000	48.5	22.8	0.737	0.254	580	11.2	12.10
15.8	51	12000	49.3	24	0.711	0.254	580	11.6	12.50
15.8	51	12000	49.2	23.8	0.787	0.254	530	12.1	13.35
15.6	45	12000	47.7	21.6	0.760	0.152	580	21.7	25.40
15.5	42	12000	47.7	21.6	0.457	0.254	970	4.20	6.23
15.6	45	12000	48.6	22.9	0.441	0.152	970	12.4	13.10
15.2	32	12000	45.3	17.8	0.441	0.152	112	10.7	10.60
15.5	42	6000	46.4	19.6	1.08	0.152	220	23.9	42.35
15.5	42	6000	46.5	19.7	1.03	0.152	220	24.4	41.06
15.4	39	6000	46.2	19.2	0.760	0.152	310	21.1	26.40
15.4	39	6000	46.2	19.2	0.787	0.254	300	9.52	12.05
15.3	36	6000	45.4	18.0	0.762	0.254	320	9.80	11.11
15.3	36	6000	45.4	17.9	0.787	0.254	310	9.60	10.86
15.3	36	6000	46.0	18.9	0.483	0.254	500	5.30	6.40
15.3	36	6000	46.1	19.1	0.431	0.152	540	8.60	11.82

Figures 4.8a & 4.8b show additional comparisons of LDFE predictions to recent measurements of pullout capacity of helical anchors in loose and dense sand, respectively (Rasulo *et al.*, 2017). This data is particularly significant in that it extends to depth *z/D* sufficient for a deep failure mechanism to develop, an associated constant breakout factor

$N_q = N_{qmax}$. In these cases, reliable estimates ϕ' and ψ were available for the testbed soils, which are denoted in the figures. However, elastic properties were not measured, so rigidity index I_r could not be estimated. Therefore, LDFE analyses were performed for the ranges of I_r shown in the figure. In the loose sand at depth z/D = 3, the measured data vary by a factor of about 2, with the upper range of the measurements generally matching the finite element predictions. At shallow depths, z/D < 5, predictions are in reasonable agreement with measurements, irrespective of rigidity index, especially for anchors in very dense sand (Figure 4.8b). However, for deep embedment, measurements can be reconciled to predictions only by assuming rigidity indices in the range I_r = 100-300. Thus, it appears that elastic effects need to be factored into the evaluation of pullout capacity of deeply embedded anchors.

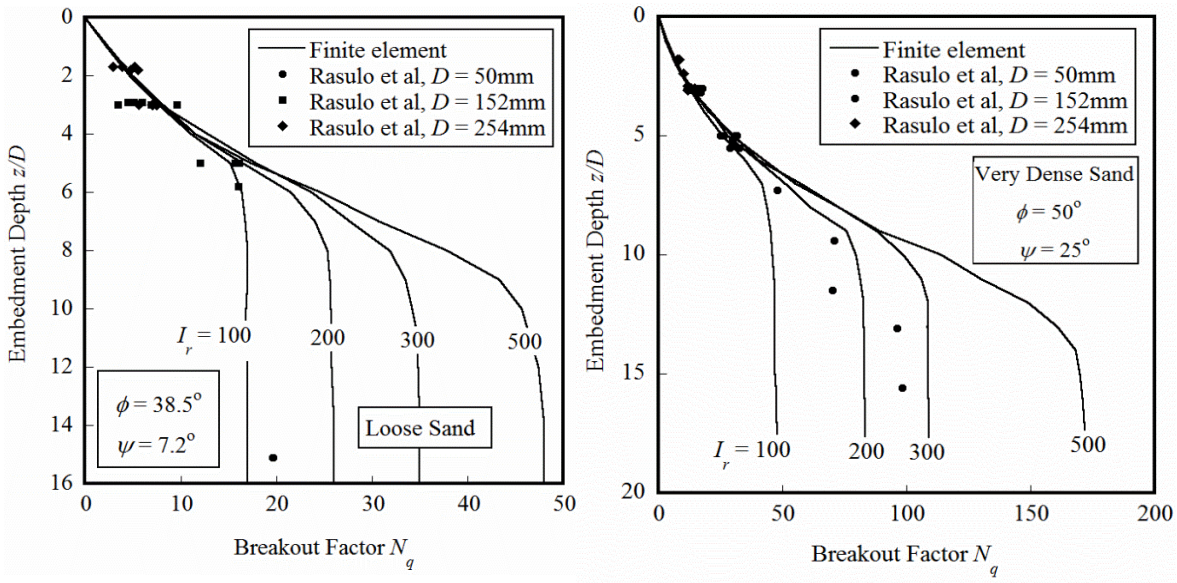

a. Rasulo et al. (2017) Loose Sand

b. Rasulo et al. (2017) Very Dense Sand

Figure 4.8 Comparison of finite element predictions to Rasulo et al. (2017) measurements on helical anchors. Reprinted with permission from (Al Hakeem and Aubeny, 2019).

Figure 4.9 compares LDFE results to data from various experimental investigations in loose and dense sands. All LDFE simulations have a rigidity index I_r = 500, which, as discussed above, correspond to a collapse mechanism in a rigid-plastic collapse medium. In the case of a dense sand (Figure 9b), the LDFE results are in very good agreement with the experimental data measured by Ilamparuthi *et al.* (2002), Pearce (2000), and Murray and Geddes (1987) down to a depth of about $z/D < 8$. At greater depths, the quality of the predictions is mixed, with the LDFE over-estimating the Pearce data by up to 35%. This result is consistent with the notion that in dense soils at relatively shallow depths elastic effects are not significant, and pullout capacity can be estimated based solely on soil strength properties (ϕ' and ψ), independently of any consideration of rigidity index I_r.

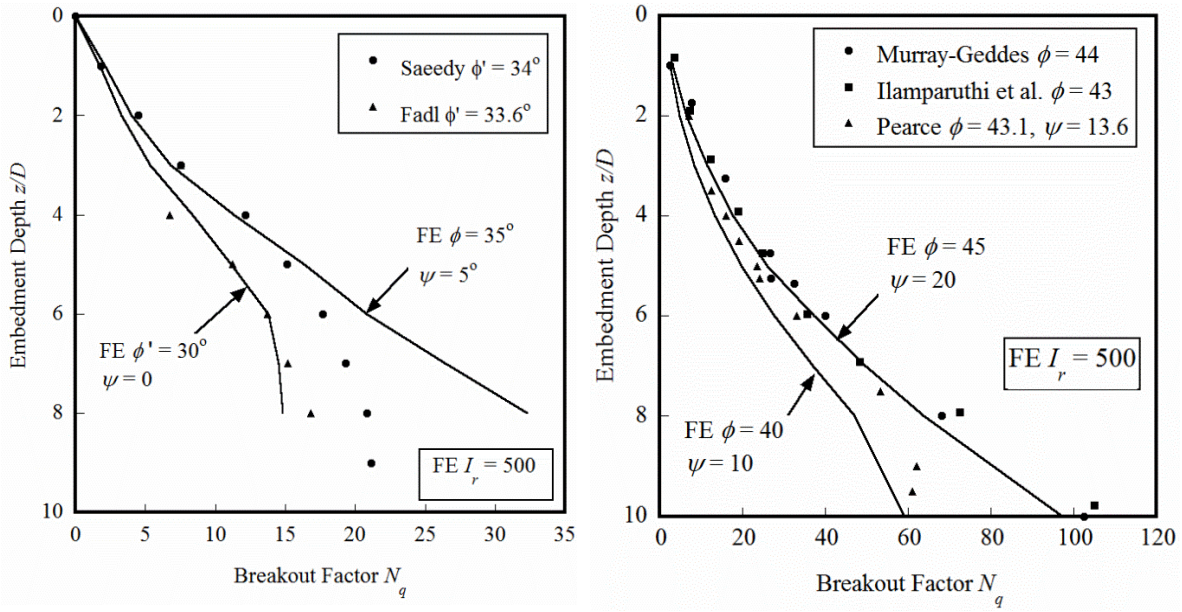

a. Loose Sand

b. Dense Sand

Figure 4.9 Comparison of finite element predictions to previous experimental data. Reprinted with permission from (Al Hakeem and Aubeny, 2019).

When considering the measurements made by Saeedy (1987) and Fadl (1981) for a loose sand (Figure 4.9a), the LDFE results for I_r = 500 are generally in good agreement with data down to an embedment z/D = 5. However, at greater depths the LDFE results seriously over-predict the measured pullout capacity. These comparisons tend to support the notion (discussed further subsequently in this chapter) that (a) elastic effects have minor influence on pullout capacity for shallowly embedded anchors and (b) reduction in pullout capacity due to elastic effects is most serious for deeply embedded anchors in loose soils.

4.7 Finite Element Parametric Study

As a circular plate anchor geometry is easily handled to an axisymmetric two-dimensional analysis, extensive parametric studies can be performed in this chapter with a relatively modest level of computational effort. Moreover, the analyses are applicable to helical anchors, assuming that the pitch does not affect anchor response.

This section investigates the effects of three soil characteristics on anchor performance: elastic effects as represented by a rigidity index I_r, volumetric behavior at yield as characterized by a dilation angle ψ, and the soil angle ϕ'. The parametric study investigated the variation of breakout factor N_q as a function of depth, with ϕ', ψ and I_r held constant along the depth of each soil profile considered. Typically, past studies of plate anchors have performed to investigate the effect of ϕ', and ψ on pullout capacity of shallowly plate anchors which z/D is less than 10. This part of research investigates a range of anchor embedment depths from 1 to more than 20 plate diameters.

4.7.1 Effect of Rigidity Index

The soil rigidity index was introduced by (Vesic, 1965) as a consistent and rational means for analyzing general, local and punching shear of a typical foundation bearing capacity problem. Since it is well accepted that the rigidity index can have significance influence on the foundation bearing capacity in frictional materials, it appears reasonable to extend this understanding to anchor uplift capacity problems (Chen *et al.* 2013). The basic soil rigidity index I_r is defined as the ratio of shear modulus to initial shear strength (Vesic, 1972), which in frictional soils can be defined by the equation:

$$I_r = \frac{G}{S} = \frac{G}{c + q'_n \tan\phi'} \tag{4.5}$$

where G is shear modulus and q'_n is initial mean effective stress $(1 + 2K_0)\sigma'_{v0}/3$. Considering the case of a purely cohesionless soil and expressing in terms of Young's modulus E and Poisson's ratio ν, rigidity index I_r can be expressed in the following alternative form:

$$I_r = \frac{E}{2(1+\mu)q'_n \tan\phi'} \tag{4.6}$$

Vesic (1972) provided a general range of soil rigidity index of 100-500 for loose to dense sand. In the present parametric study, the elastic effect as represented by a rigidity index I_r on breakout factor was systematically investigated (I_r from 100 to 500) for selected ranges of anchor embedment (z/D), friction angle (ϕ'), and dilatancy angle (ψ). Figure 4.10 shows the predicted effect of rigidity index I_r on the pullout capacity of circular plate anchors at depth ratios z/D =8 for friction angle ϕ' = 40º. Associated ($\psi = 40º$) and non-associated ($\psi = 10º$) flow rule conditions are considered. The influence of soil rigidity I_r

on the breakout factor N_q is obvious in Figure (4.10) which shows the uplift dimensionless curve for different I_r values. The predictions show a strong trend of reduced rigidity I_r leading to increased levels of displacement at which the ultimate load is approached. In the non-associated flow rule ($\psi = 10^o$), it can be noticed some numerical instabilities occurred in the form of oscillations in the solution for high rigidity index values (I_r = 500 in this case) at large displacements $w/D > 0.25$. Since interpreted breakout factors consider displacements only up to w/D = 0.25, these oscillations do not affect the interpretations presented later analysis.

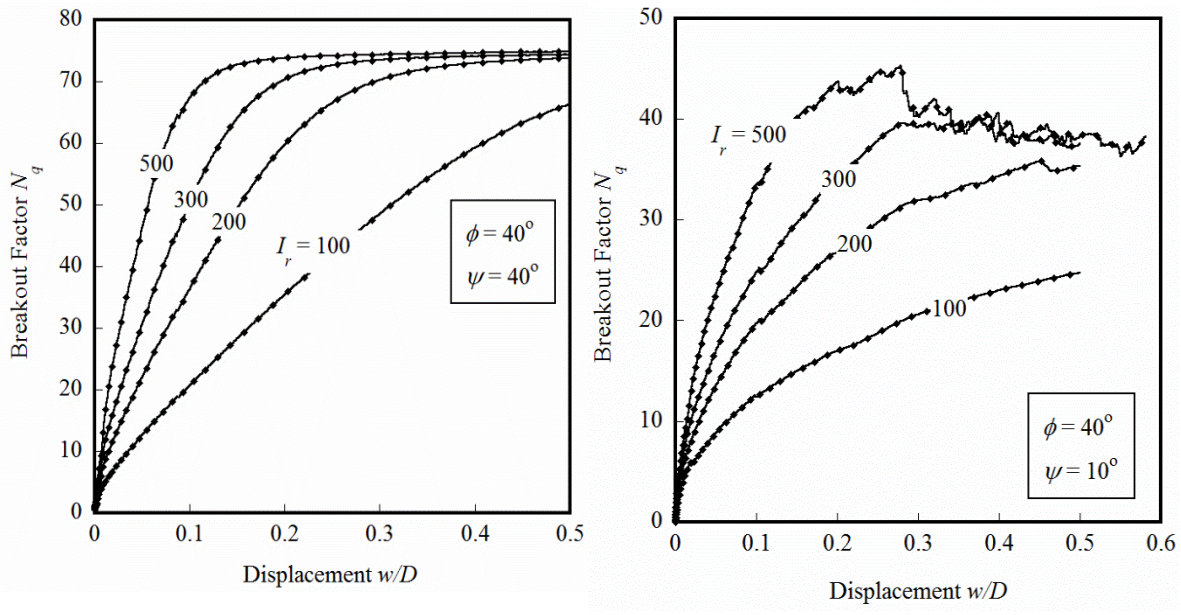

a. Associated

b. Non-associated

Figure 4.10 Normalized uplift capacity curves for different rigidity indices. Reprinted with permission from (Al Hakeem and Aubeny, 2019).

In this parametric study, anchor depths were extended to sufficiently great z/D (ranged from z/D = 12-28) to ensure full definition of the transition from shallow to deep pullout

behavior. In general, this transition depth increases with increasing ϕ', ψ and I_r. The study considered a range of soil internal friction $\phi' = 30^o - 50^o$ and dilation angles $\psi = 0^o - 25^o$. The variation of breakout factor N_q with embedment depth ratio (z/D) for loose ($\phi' = 30^o$, $\psi = 0^o$), medium ($\phi' = 38.5^o$, $\psi = 7.2^o$), and very dense ($\phi' = 50^o$, $\psi = 25^o$) are presented in the Figure (4.11). This Figure shows a general trend of upward curvature at shallow embedment depths for the N_q versus z/D curves. With increasing depth, the curvature eventually reverses and, at sufficiently great depth N_q becomes independent of depth. This depth-independent zone is interpreted as corresponding to a full flow-around failure mechanism that does not reach the free surface. The depth at which the reversal in curvature occurs as well as the depth below which the breakout factor approaches a constant value N_{qmax} is influenced by the soil friction angle ϕ', soil volumetric behavior at yield as represented by dilation angle ψ, and elastic soil stiffness as represented by a rigidity index I_r. It can also be noticed from Figure (4.11) that for shallow depths, $z/D \leq$ 3-6, the breakout factor values are minimally affected by rigidity index I_r, which suggests that simple rigid block limit equilibrium or plastic limit analyses can be used to describe anchor performance in this depth interval.

As mentioned above that the breakout factor N_q in general, and N_{qmax} in particular, shows a high degree of sensitivity soil properties. For example, Figure 4.11a for a loose sand shows N_{qmax} to double as I_r increases from 100 to 500. The sensitivity of N_{qmax} to I_r is even greater in denser soils, with Figure 4.11c showing N_{qmax} increasing by a factor exceeding 3 over a range of I_r from 100 to 500. For a loose sand with low stiffness ($\phi' = 30^o$, $\psi = 0^o$, I_r = 100) N_{qmax} slightly exceeds 6, in contrast to a very dense sand with high stiffness (ϕ'

=50º, ψ =25º, I_r = 500) where N_{qmax} exceeds 170. The sensitivity of the breakout factor N_{qmax} to rigidity index is an important component of the empirical model developed later in this chapter and, therefore, a focus of attention in this parametric study. Also, Figure (4.11) shows that N_{qmax} increasing approximately by a factor of 2-4 with increasing I_r over the range of rigidity indices considered (I_r = 100-500).

For given values of ϕ' and ψ, value of N_{qmax} increases almost linearly with I_r as shown in Figure 4.12. Also, Figure 4.12 shows N_{qmax} to increase substantially with increasing dilation angle for all friction angles especially with high values of I_r.

4.7.2 Effect of Dilatancy and Friction Angle on Pullout Capacity

Soil strength-deformation parameters need to be considered in developing a model of load capacity versus embedment depth (N_q-z/D), the study presented herein considers the strength behavior defined by an angle of internal friction ϕ', and post-yield volume change behavior defined by a dilation angle ψ. Following up on the observations above regarding the effects of dilatancy, frictional soils generally exhibit non-associated behavior ($0 \leq \psi \leq \phi'$). Dilatancy during plastic deformation causes the soil ahead of the anchor to lock, requiring an extensive plastic region to develop before there is sufficient freedom for collapse to occur (Rowe and Davis, 1982). Enlargement of the zone of plastic flow substantially increases the pullout capacity (N_q); therefore, careful attention to soil dilatancy and its effect on pullout resistance is required when evaluating the capacity of anchors in sand. In fact, dilation angle ψ is a function of soil density and confining stress, both of which vary in the stress field surrounding a loaded plate anchor.

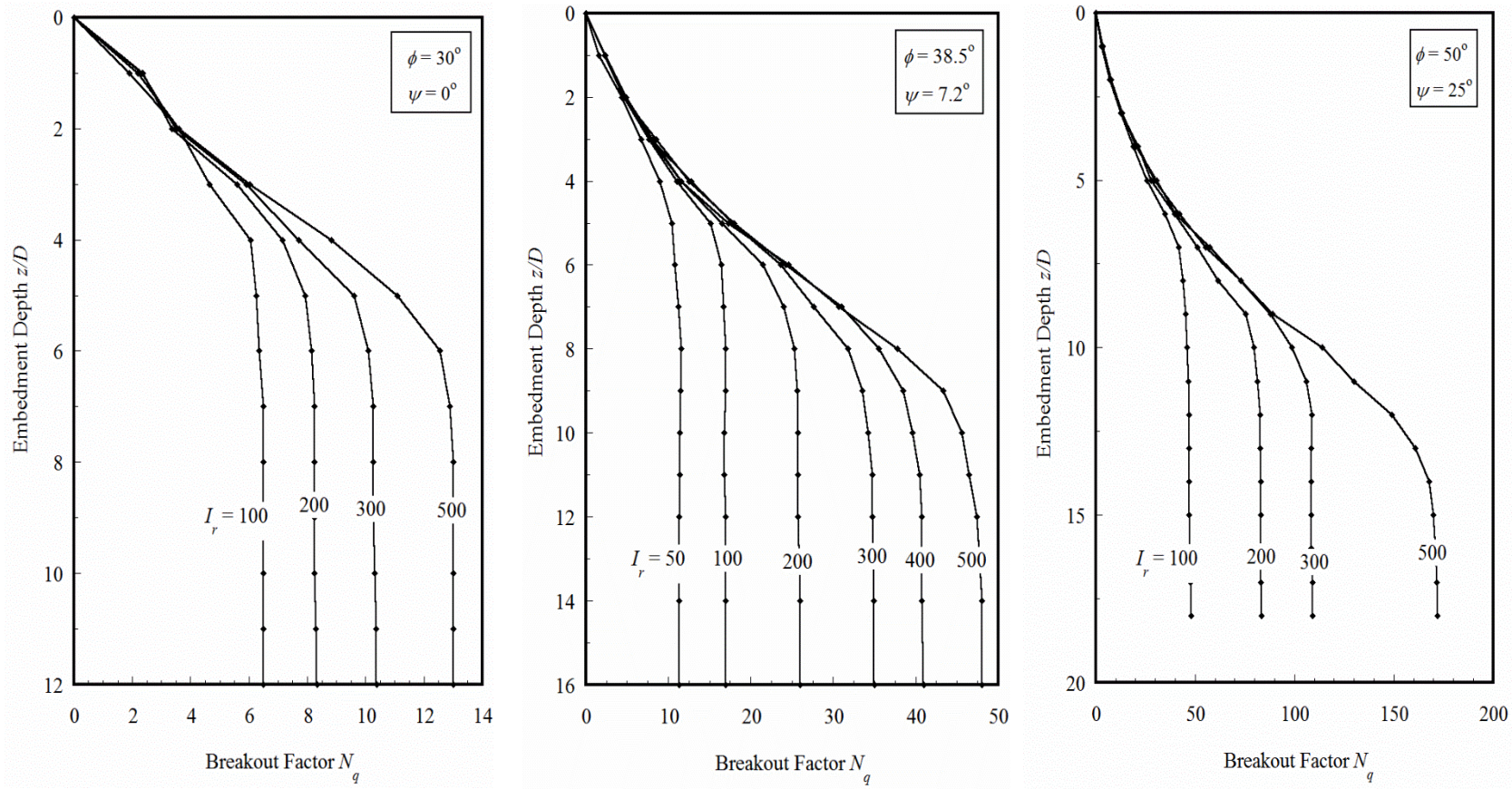

Figure 4.11 Effect of rigidity index on breakout factor. Modified with permission from (Al Hakeem and Aubeny, 2019).

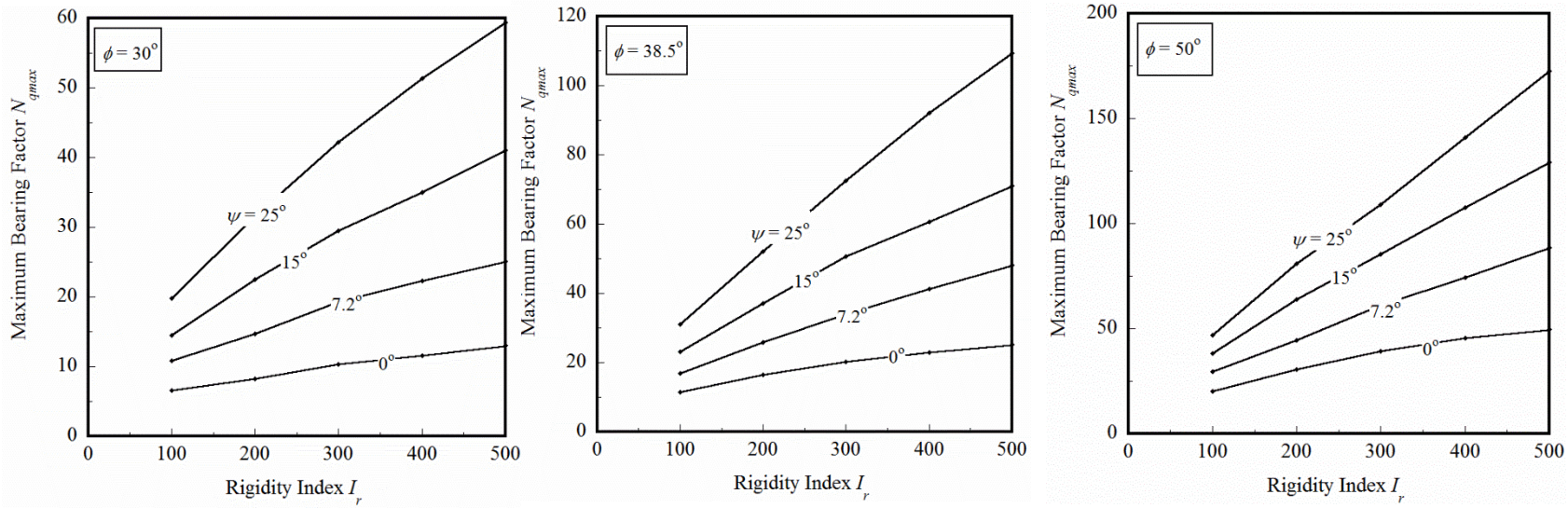

Figure 4.12 Variation of Nq_{max} with rigidity index for various ψ and ϕ. Modified with permission from (Al Hakeem and Aubeny, 2019).

Additionally, dilatancy is strain level dependent, with a peak tangent dilatancy angle occurring at relatively low strains in dense sands, followed by gradual decline to zero dilatancy as the critical state condition is approached. Thus, a single dilatancy angle ψ is a substantial simplification of actual sand behavior, and assuming that a peak dilatancy mobilizes at all points simultaneously in the yielded soil mass surrounding an anchor is unconservative. Nevertheless, a parametric study varying the dilatancy parameter ψ can provide useful insights into the effects of plastic volume change behavior on anchor performance, provided that one recognizes that some equivalent or average ψ angle needs to be applied to practical situations in recognition of the facts that the peak value does not mobilize simultaneously at all points in the yielded soil mass surrounding the anchor and that high stress gradients in the region surrounding the anchor lead spatial non-uniformity in ψ. Figure 4.13a shows the variation of breakout factor N_q with normalized depth (z/D) for ϕ' =38.5 °, I_r =500 and ψ varied from 0 to 25°. The predictions show ψ to have a more than five-fold effect on the maximum breakout factor N_{qmax}. This influence of dilatancy parameter ψ *is* also demonstrated in Figure 4.14 that the maximum breakout factor N_{qmax} increases substantially with increasing ψ particularly for high values of I_r.

Figure 4.13.b shows the effect of friction angle on breakout factor N_q over a range of ϕ' from 30º - 50º for I_r =500 and ψ = 25º. The predictions indicate that N_{qmax} can vary by a factor of up to three over the generally expected range of friction angles for sand. Figure 4.15 shows how the maximum breakout factor N_{qmax} increases with increasing friction angle for various rigidity indices I_r and dilatancy angle ψ.

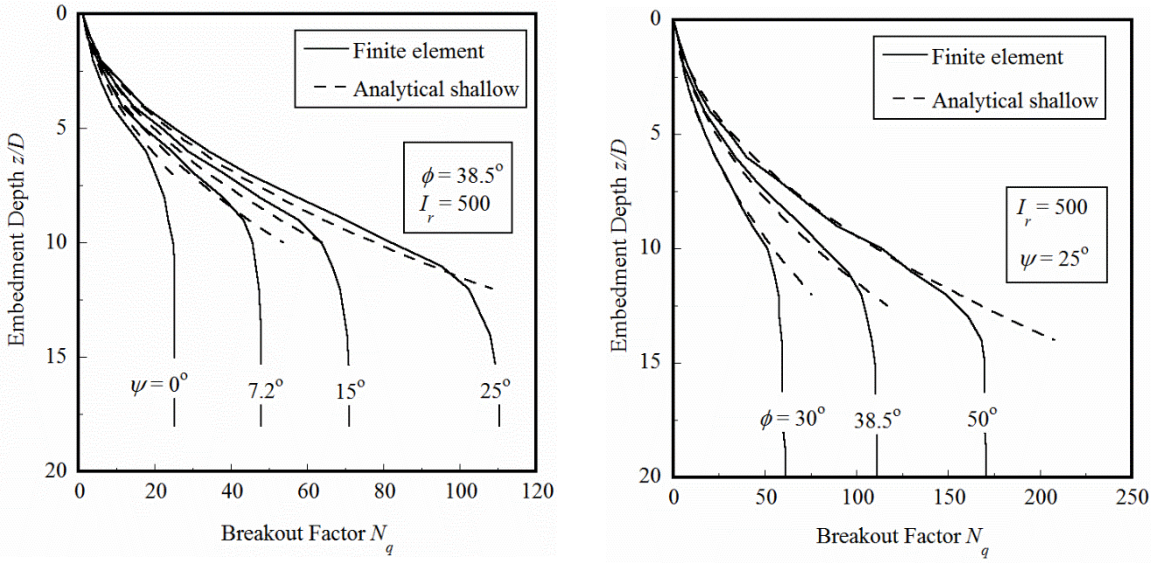

a. Dilation

b. Friction

Figure 4.13 Effect of dilatancy and friction angles on breakout factor. Reprinted with permission from (Al Hakeem and Aubeny, 2019).

4.8 Empirical Model

This section investigates the effects of three soil characteristics on anchor performance: elastic effects as represented by a rigidity index I_r, volumetric behavior at yield as characterized by a dilation angle ψ, and the soil friction angle ϕ'. The parametric study investigated the variation in the breakout factor N_q as a function of depth, with ϕ', ψ and I_r held constant along the depth of each soil profile considered. To produce a predictive model for anchor capacity that is amenable to routine design calculations, this section presents empirical curve fits to the finite element results presented above. The empirical model comprises three components for describing anchor performance for (1) shallow embedment depths, (2) deeply embedded anchors where maximum capacity N_{qmax} mobilizes, and (3) the transition between shallow and deep behavior.

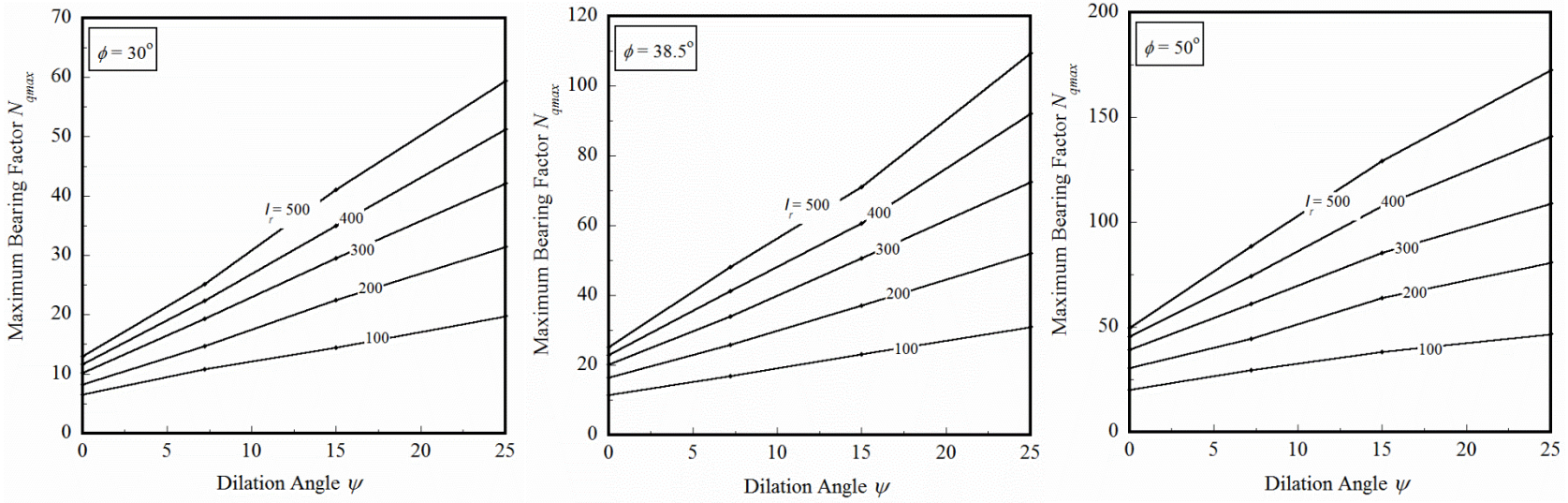

Figure 4.14 Variation of N_{qmax} with dilatancy angle ψ. Modified with permission from (Al Hakeem and Aubeny, 2019).

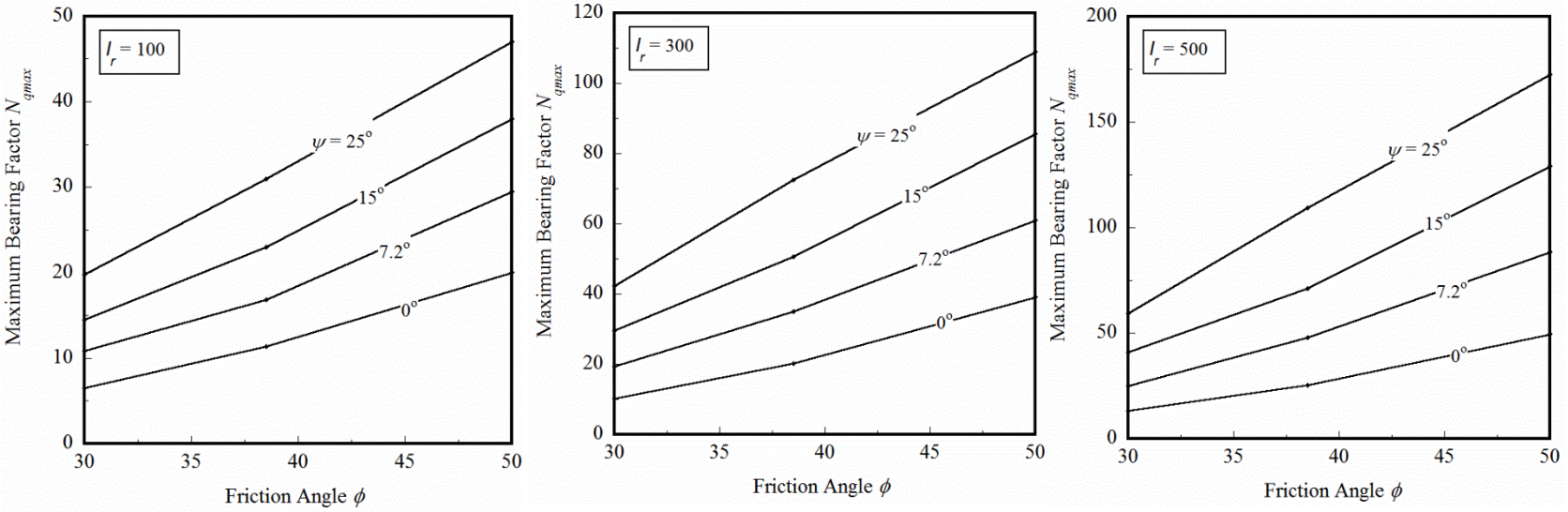

Figure 4.15 Variation of N_{qmax} with friction angle ϕ. Modified with permission from (Al Hakeem and Aubeny, 2019).

4.8.1 Shallow Embedment

The model for shallow embedment depth adopts the basic quadratic form shown in Equation 4.2. The coefficent for linear term F_{as1} (Equation 4.7) interpolates between the lower and upper estimates defined by Equation 4.3, with F_{as1} being a minimum when $\psi = 0$, and maximum for associated flow material $\psi = \phi'$.

$$F_{as1} = 2\left[\sin\phi'_{cs} + \left(\tan\phi'_{p} - \sin\phi'_{cs}\right)\tan\psi / \tan\phi'\right] \tag{4.7}$$

A similar approach is adopted for F_{as2}, except that a minimum value is set at 1/3 for the case of zero dilation $\psi = 0$ (Equation 4.8).

$$F_{as2} = 1/3\left[1 + \left(4\tan^2\phi'_{p} - 1\right)\tan\psi / \tan\phi'\right] \tag{4.8}$$

The load capacity for shallow embedment depths is assumed to be independent of rigidity index I_r, an assumption supported by the finite element results presented in Figure 4.11. Superposition of Equations 4.2, with the modified expressions for F_{as1} and F_{as2} in Equations 4.7 and 4.8, on to the finite element predictions in Figure 4.13 shows satisfactory agreement.

4.8.2 Maximum Resistance N_{qmax}

In contrast to shallow anchor behavior, the finite element parametric studies showed that maximum load capacity N_{qmax} of deeply embedded anchors is highly sensitive to rigidity index I_r, in addition to the dilation and friction angles. The dependency of N_{qmax} on all three variables is described empirically by the equation shown below:

$$N_{q\max} = F + D + R + M \tag{4.9}$$

The terms *F*, *D* and *R* respectively are cubic functions describing the contributions of friction angle, dilatancy angle and rigidity index to N_{qmax} according to the following equations:

$$F = f_1\phi^3 + f_2\phi^2 + f_3\phi \tag{4.10}$$

$$D = d_1\psi^3 + d_2\psi^2 + d_3\psi \tag{4.11}$$

$$R = r_1 I_r^3 + r_2 I_r^2 + r_3 I_r \tag{4.12}$$

The fourth term *M* describing the cross-dependency of friction angle, dilation angle and rigidity index on N_{qmax} is the following third-order function:

$$\begin{aligned} M = {} & m_1\phi^2\psi + m_2\phi^2 I_r + m_3\psi^2\phi + m_4\psi^2 I_r + m_5 I_r^2\phi + \\ & m_6 I_r^2\psi + m_7\phi\psi + m_8\psi I_r + m_9\phi I_r + m_{10}\phi\psi I_r \end{aligned} \tag{4.13}$$

Table 4.3 describes the curve fitting procedure and presents the curve fit constants. The model presented for estimating N_{qmax} requires three parameters: ϕ', ψ and I_r, all of which can be obtained by conventional triaxial shear tests. Additionally, since all three parameters correlate strongly to relative density D_r, directly estimating N_{qmax} from relative density is not unreasonable. This approach is further considered in a later section.

Table 4.3 Curve Fit Parameters for Estimating $N_{qmax.}$ Reprinted with permission from (Al Hakeem and Aubeny, 2019).

Description	Equation	Variable Name	Value
Sensitivity to friction angle ϕ'	4.10	f_1	0.00036
		f_2	-0.024
		f_3	0.477
Sensitivity to dilation angle ψ	4.11	d_1	-0.00046
		d_2	0.06
		d_3	-2.6
Sensitivity to rigidity index I_r	4.12	r_1	6.8×10^{-8}
		r_2	-7.9×10^{-5}
		r_3	0.0185
Cross-dependence of ϕ, ψ and I_r	4.13	m_1	-0.00117
		m_2	4.9×10^{-5}
		m_3	-0.0012
		m_4	5.3×10^{-6}
		m_5	-8.5×10^{-7}
		m_6	1.9×10^{-7}
		m_7	0.1177
		m_8	-0.0058
		m_9	-0.00027
		m_{10}	0.000304

4.8.3 Transitional Behavior

The finite element predictions show that, below a certain transition depth z_T, the breakout factor curve departs from the shallow breakout capacity curve and trends asymptotically towards a maximum value N_{qmax}. This behavior is well described by the following equation:

$$\begin{aligned} N_q &= 1 + F_{as1}\left(z/D\right) + F_{as2}\left(z/D\right)^2 && z \le z_T \\ N_q &= rN_{q\max} && z > z_T \end{aligned} \tag{4.14}$$

The transition function r is defined as:

$$
\begin{aligned}
r &= 1-(1-r_T)\exp\left[-\lambda\left(z-z_T\right)/D\right] \\
\lambda &= r_T'/(1-r_T) \\
r_T &= \left[1+F_{as1}\left(z_T/D\right)+F_{as2}\left(z_T/D\right)^2\right]/N_{q\max} \\
r_T' &= \left[F_{as1}+2F_{as2}\left(z_T/D\right)\right]/N_{q\max}
\end{aligned}
\tag{4.15}
$$

Equation 4.15 was formulated such that N_q transitions from a shallow surface failure mechanism to N_{qmax} in such a manner that the function $N_q(z/D)$ and its first derivative are continuous at all depths. The parameter z_T is conveniently expressed as a fraction of z_{100}, which is defined as the depth at which the shallow breakout factor computed by Equation 4.2 reaches its maximum value, $N_q = N_{qmax}$ (computed by Eq. 4.9). Figure 4.16 shows $z_T = 0.85z_{100}$ achieving a good match to finite element solutions.

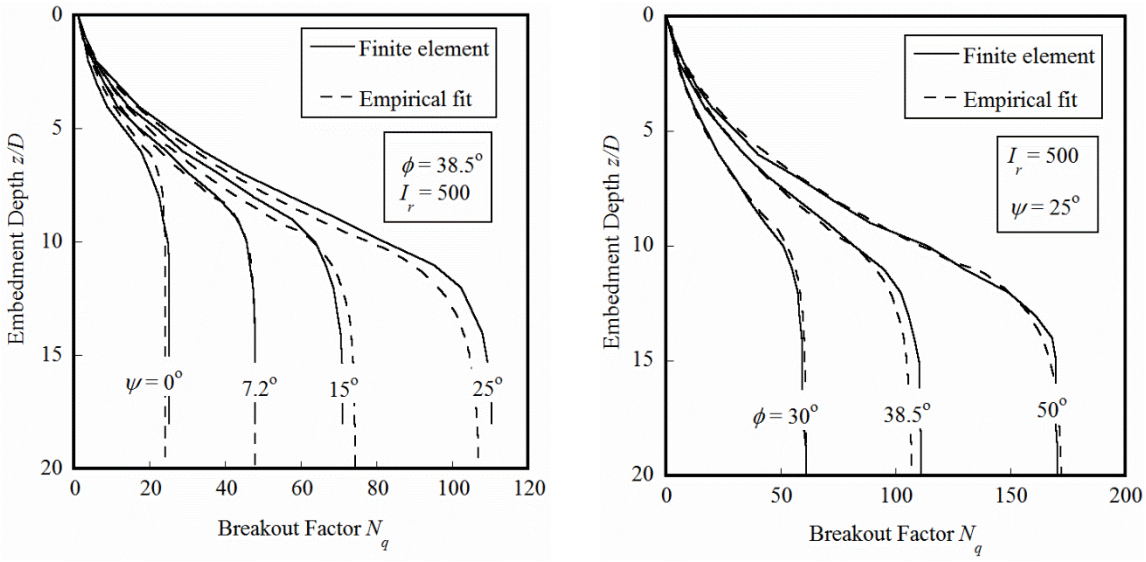

a. Medium Dense Sand

b. Very Dense Sand

Figure 4.16 Transition from shallow to deep failure mode. Reprinted with permission from (Al Hakeem and Aubeny, 2019).

4.9 Estimating Load Capacity from Relative Density

The finite elements studies presented earlier elucidated the influence of friction, dilatancy and rigidity index on load capacity of circular plate anchors as a function of embedment depth. However, all three parameters actually vary with confining stress; specifically, as embedment depth increases all three parameters will continuously decrease as effective confining stress increases. Thus, the load capacity curves shown to this point do not provide an entirely clear picture of the variation of N_q with depth, even in a uniform soil profile. Fortunately, all three relevant soil parameters can be expressed as functions of relative density and effective confining stress. Thus, it is possible to express the previously presented relationship N_q (ϕ', ψ, I_r, z/D) to a more useful format N_q (D_r, γ', z/D). Total unit weight γ can be replaced by buoyant unit weight γ' if an unsubmerged soil profile is under consideration.

4.9.1 Correlations to Relative Density

As mentioned in Chapter III, Bolton (1986) defined a relative dilatancy index in his framework for relating relative density to peak friction angle and dilatancy as in Eq. 3.29:

$$I_{RD} = D_r (Q - \ln p') - R \tag{4.16}$$

The term p' denotes mean effective stress (kPa) at failure, which includes the initial stress state along with alterations in the stress state imposed by the foundation. For preliminary estimates Kulhawy and Mayne (1990) recommend estimating p' as twice the overburden stress σ'_o. This recommendation is sensible for conventional compression foundations,

which invariably increase the stress state in the soil. However, an embedded plate involves a more complex stress field involving both compression and extension, with minimal change in average mean stress. For this reason, the approach adopted in this study simply sets p' equal to σ'_o.

Bolton then relates the relative dilatancy index I_{RD} to the difference between peak and critical state friction angles. For triaxial stress states he gives ϕ'_p - ϕ'_{cv} =3I_{RD}. A triaxial stress state actually occurs only along the centerline of an axially loaded circular plate. Nevertheless, this condition is taken as the closest approximation to actual conditions in the parametric study that follows. The computations for ϕ'_p use ϕ'_{cv} = 33º degrees, based on data presented by Bolton (1986).

Strictly speaking, a dilatancy angle only has meaning for plane strain conditions. Andersen and Schjetne (2013) therefore characterize the tendency for volume change under triaxial test conditions as follows:

$$\sin\psi = \frac{-d\varepsilon_{vol}}{d\varepsilon_a - d\varepsilon_{vol}} = \frac{0.3I_{RD}}{2+0.3I_{RD}} \tag{4.17}$$

where ε_{vol} and ε_a are volumetric and axial components of strain measured in a triaxial test. The angle ψ is still termed a dilatancy angle, recognizing that it cannot be defined in geometric terms on a Mohr diagram, as is possible for the case of plane strain.

The final parameter affecting load capacity is the rigidity index I_r, which also declines with increasing confining stress. Based on data tabulated by Kulhawy and Mayne (1990) and Vesic (1977) for Chattahoochee sand, the dependence of rigidity index I_r on relative density D_r and confining stress σ'_c shown in Figure 4.17a was adopted for this study.

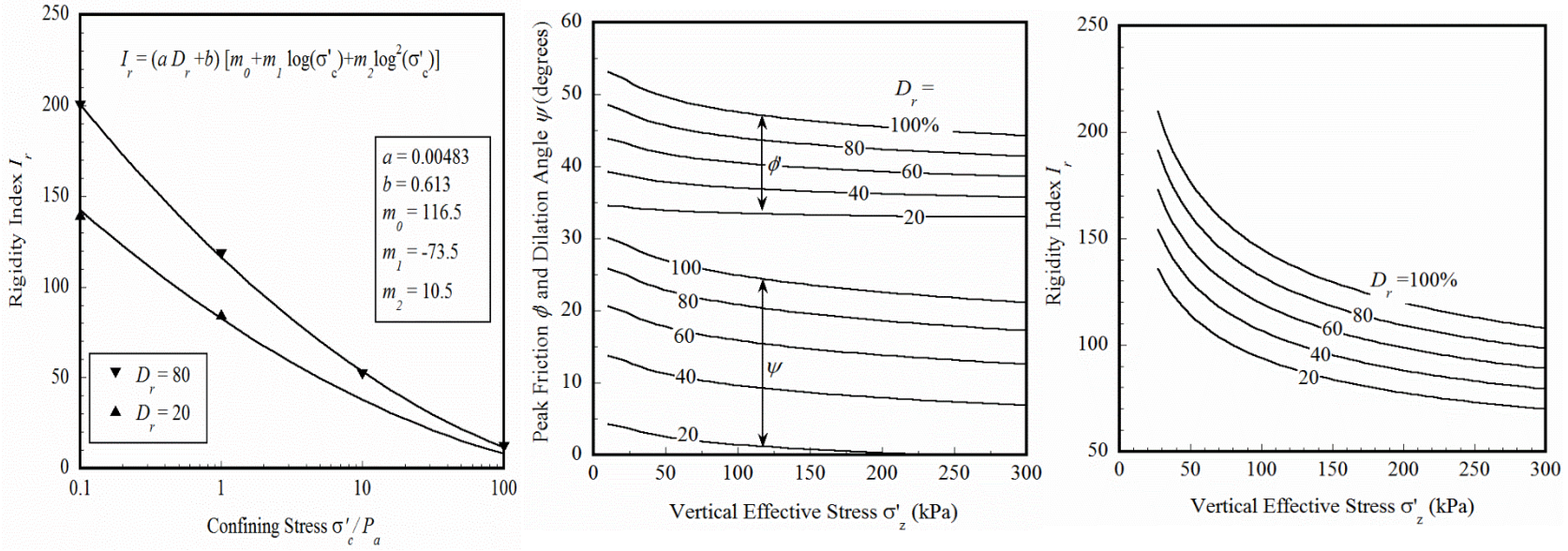

a. I_r Fit to Data

b. Friction and Dilatancy

c. Rigidity Index

Figure 4.17 Variation in soil parameters with confining stress. Reprinted with permission from (Al Hakeem and Aubeny, 2019).

4.9.2 Influence of relative density

Having established a framework for predicting load capacity of anchors in sands in terms of relative density and effective stress level, it is now possible to develop charts for predicting anchor performance that implicitly account for the variation in soil properties with depth. The parametric studies presented below consider a sand profile having a submerged unit weight $\gamma' = 9$ kN/m^3. Figures 4.17b and 4.17c show the assumed variation in soil parameters with confining stress utilized in this parametric study, which are based respectively on Bolton's dilatancy framework (Eqs. 4.16 and 4.17) and the curve fit developed in this study relating rigidity index to confining stress shown in Figure 4.17a. Figure 4.18a shows predictions of the breakout factor N_q as a function of depth for a 1.2-m diameter anchor, with relative density varying over a range D_r = 20 -100%. Model predictions are shown for two cases: "peak" predictions assume fully mobilized peak friction and maximum dilation angles (solid lines), and critical state (CS) predictions assume a critical state friction angle ϕ'_{cv} and zero dilation angle ($\psi = 0$, dashed lines). The reason for considering the latter case is that at large anchor displacements critical state conditions may prove to be a more appropriate assumption. At embedment depths exceeding the shallow zone, the overall range of peak breakout factors is N_q = 8 to 60. The model predictions show a significant decline in breakout factor with increasing depth, especially for the high density soils. This trend is supported by measurements by Dickin (1988), although the tests were not extended to sufficient depths to fully validate the predictions in Figure 4.18a. The reduction in the breakout factor N_q with increasing depth is anticipated, since rigidity index, peak friction angle and dilation angle all decrease with

increasing confining stress. For the 1.2-m diameter plate, the depth at which the transition from a shallow to a deep failure mode occurs varies from about z/D = 3 to 7, with the greater transition depths occurring in denser soils. In the critical state case the effect of relative density is greatly diminished; however, the breakout factor for deeply embedded anchors is still affected by D_r by virtue of its influence on the rigidity index (Figure 4.17c). The dashed lines representing predictions for CS conditions in Figure 4.18a indicate dramatic reductions in the breakout factor when the effects of dilation are omitted from the analysis.

The decline in the breakout factor N_q with increasing embedment depth may lead one to question the practical effectiveness of increasing the embedment of the anchor. However, the accompanying plot of q_{ult} versus depth in Figure 4.18b shows that the rate of increase in effective stress more than offsets the rate of decline in N_q, such that a net benefit is realized through increased anchor embedment. Also shown in Figure 4.18a are full-scale anchor test measurements for pile driven plate anchors in loose, medium and dense sands presented by Forrest *et al.* (1995). The tests were performed on a rectangular plate anchor having a 2:1 length-width ratio and area 1.16 m^2. To permit comparison to circular anchors, the anchor embedment depths were normalized by an equivalent diameter D_{eq} = 1.2 m. While geometry and aspect ratio are known to affect the N_q factor, comparing the predictions to data measurements can provide some sense as to the reliability of the model predictions.

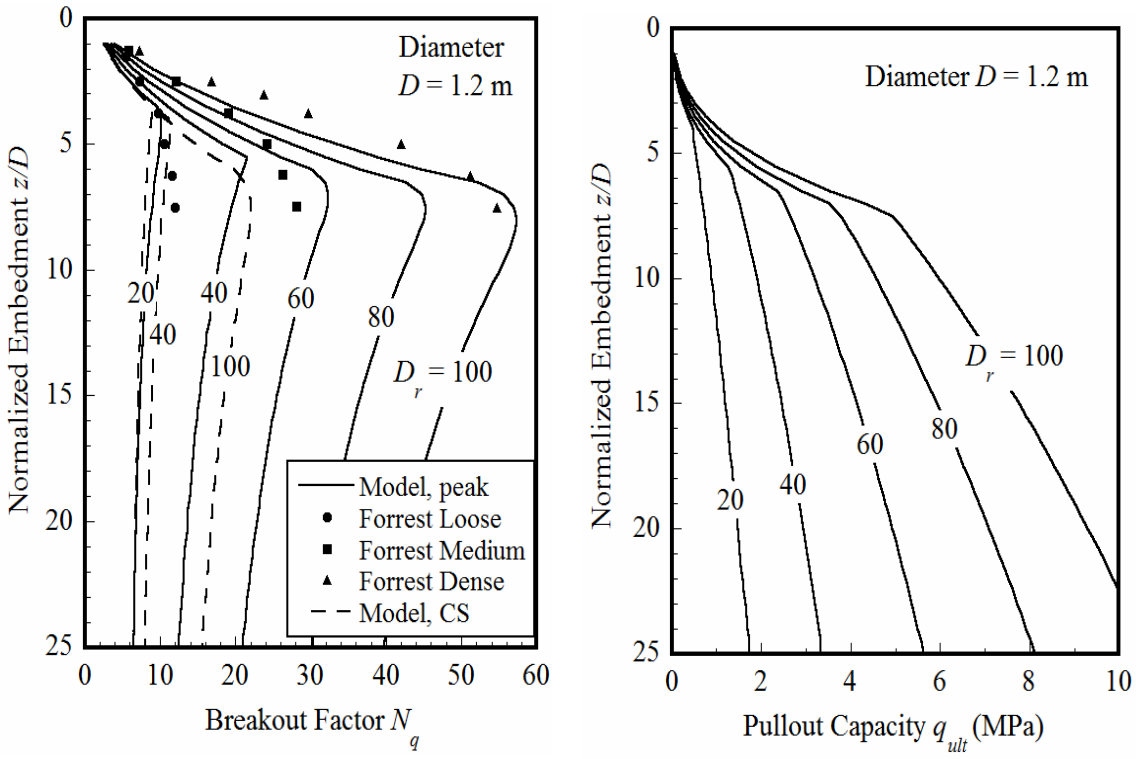

a. Breakout Factor

b. Pullout Capacity

Figure 4.18 Capacity versus depth for 1.2-m diameter plate anchor. Reprinted with permission from (Al Hakeem and Aubeny, 2019).

The comparisons in Figure 4.18a indicate that the model predictions assuming peak resistance are generally consistent with field measurements for medium dense sand (D_r = 40-60%) and somewhat conservative for dense (D_r = 60-80%) sand. For the loose sand the field measurements lie at the low end of the range peak parameter model predictions for D_r = 20 - 40%, while closely matching the CS model predictions. Although some ambiguity exists in this particular case, this suggests that CS conditions may be a more appropriate basis for predicting breakout capacity in loose soils. Comparison of model predictions to measurements by Dickin (1988) discussed in the next paragraph make a much more convincing case for using CS parameters in loose soils.

Figure 4.19 compares empirical model predictions to centrifuge test data presented by Dickin (1988). In this case the tests were conducted in dry sand at two density states: γ'= 14.24 kN/m^3 and D_r = 33% (Test A), and γ' = 16 kN/m^3, D_r = 76% (Tests B and C). At prototype scale, Tests A and B used square plates of width 1m. Merifield *et al.* (2003) show that the shape factor for circular versus square plates varies from $N_{q\text{-}circle}$ / $N_{q\text{-}square}$ = 1.1 to 1.27 over an embedment range from z/D =1 to 10. Although some controversy exists in regard to the need for this adjustment, for the purposes of comparison in this study the Dickin data were adjusted using the Merifield *et al.* (2003) shape factors. As before, model predictions for all test cases are shown for conditions of peak resistance (solid lines) and critical state conditions (dashed lines). For dense sand (D_r = 76%) the model predictions incorporating dilatational effects agree reasonably well with the measurements, with the maximum discrepancy between model and measurement being about 20%. By contrast, the agreement between model predictions and measurements in the D_r = 33% sand is clearly superior when critical state conditions are assumed. These comparisons strongly suggest that plate anchor capacity estimates in loose sands should proceed on the basis of critical state conditions, while estimates in dense sand can assume fully mobilized peak friction and maximum dilation angles. Referring back to the Giampa *et al.* (2017) data in Table 2, considerable discrepancies between measurements and peak resistance LDFE simulations begin to occur at relative densities less than 45%. For this reason, it can be concluded that load capacity estimates should be based on critical state conditions for D_r < 50%.

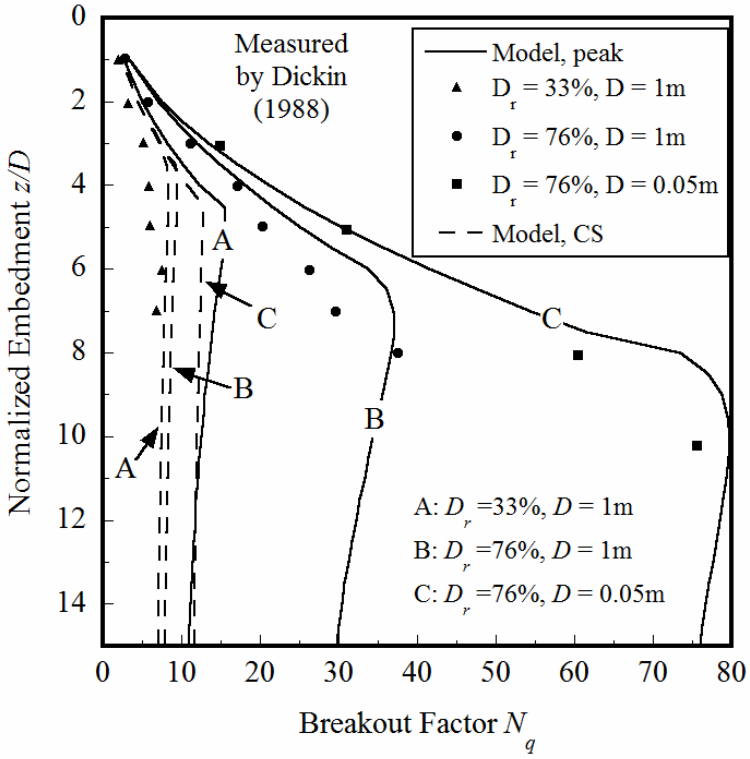

Figure 4.19 Comparison of predictions to data by Dickin (1988). Reprinted with permission from (Al Hakeem and Aubeny, 2019).

4.10 Summary

Attention to plate anchors in sand has been relatively limited in the research literature, particularly for deeply embedded plates. Past studies of anchor performance have done much to quantify the influence of the parameters (ϕ' and ψ) for relatively shallow levels of embedment, typically z/D less than 10. This part of research presents a parametric finite element study of pullout capacity of circular, horizontally oriented anchors in sand, subjected to vertical centric loading. Additionally, the analyses are directly applicable to helical anchors. This study investigates a range of anchor embedment depths from one to more than 20 plate diameters, which is sufficient to characterize the transition of the anchor behavior from a shallow to a deep failure

mechanism. However, this study focuses on how dimensionless breakout capacity N_q varies with a selected range of anchor embedment depths z/D, considering the effects of key soil properties include rigidity index I_r, dilatancy angle ψ and friction angle ϕ'. The predictions showed that pullout capacity of shallowly embedded anchors is controlled by friction ϕ' (Figure 14.3 b) and dilatancy ψ (Figure 4.13 a), and essentially independent of rigidity index I_r (Figure 4.11). Beyond the shallow zone, breakout capacity of deeply embedded anchors is highly sensitive to rigidity index I_r, in addition to the dilation and friction angles. The normalized transition depth from a shallow to a deep collapse mode is expected to range from about $z/D = 3$ in loose soils to more than 10 in very dense soils, depending on rigidity index (e.g. Figure 4.11). Since the three primary soil parameters (ϕ', ψ, and I_r) influencing soil resistance all correlate well to relative density and confining stress, expressing the breakout factor as a function of relative density, unit weight and depth, N_q (D_r, γ', z/D) is an appealing approach for practical applications. Therefore, for design purposes, this part of research developed an empirical model for predicting anchor pullout capacity as function N_q (D_r, γ', z/D). Pullout capacity of shallowly embedded circular plates is well described by Equation 4.14 (Figure 4.13), while Equation 4.15 is an exponential function describing the transition in the breakout factor N_q from the shallow mode (Equation 4.14) to its maximum value (Equation 4.9). Additionally, the parameters ϕ', ψ and I_r all decrease with increasing overburden stress (Figure 4.17), implying that N_{qmax} decreases with anchor embedment, even in a soil profile having a uniform relative density. Figures 4.18 and 4.19 provide predictions on how N_{qmax} is expected to decrease with increasing plate embedment depth. Also, for relative densities $D_r < 50\%$, using

critical state soil parameters ($\phi' = \phi'_{crit}$ and $\psi = 0$) in the empirical model for breakout capacity greatly improves the agreement between predictions and measurements (Figure 4.19).

CHAPTER V

NUMERICAL MODELING OF KEYING PROCESS OF VERTICALLY INSTALLED PLATE ANCHOR IN SAND

5.1 Introduction

Most plate anchor keying studies have been performed for soft clay, since this is the most common type of soil in deep-water environments in which plate anchors are currently used. However, installation of floating wind turbines and wave energy converters at water depths of less than 100m will typically require anchoring systems suitable for sand deposits (O'Loughlin & Barron, 2012). As discussed in previous chapters, plate anchors have been used as a practical and efficient option for mooring floating facilities, due to their high efficiency, suitability for a wide range of soil conditions, and variety of available installation techniques. Irrespective of the installation method, a directly embedded plate anchor has a vertical orientation after penetration to the designated depth. Since such anchors are oriented vertically after installation and seldom subjected to purely horizontal loading, a "keying" step (see Figure 5.1) is required to orient the anchor into the direction of the mooring line load. Simulation of the keying process has not been extensively investigated in previous research, especially with regards to cohesionless soil; however, much work has been done in the last few years on plate anchor performance in clay soil during the keying process.

As noted in Chapter II, limited experimental data are available for plate anchor keying in sands. To the author's knowledge, no finite element studies have been conducted. The present chapter focuses on a significant gap in the knowledge regarding

the performance of vertically installed plate anchors subjected to different angles of mooring line load: in other words, keying behavior in sand. Experimental validation is definitely desirable, but beyond the scope of this study. As shown in Figure 5.1, during the keying process, both horizontal and vertical displacement of the anchor occurs as the anchor rotates into its target orientation, which is approximately perpendicular to the direction of loading. The upward vertical displacement is a particular concern, since a loss of anchor embedment δ_z leads to a reduction in pullout capacity (Al Hakeem and Aubeny, 2018). During the keying process, the soil in the vicinity of the plate anchor is remolded. This remolding causes a reduction in soil strength that may be recovered over the course of soil reconsolidation (Long et al., 2009).

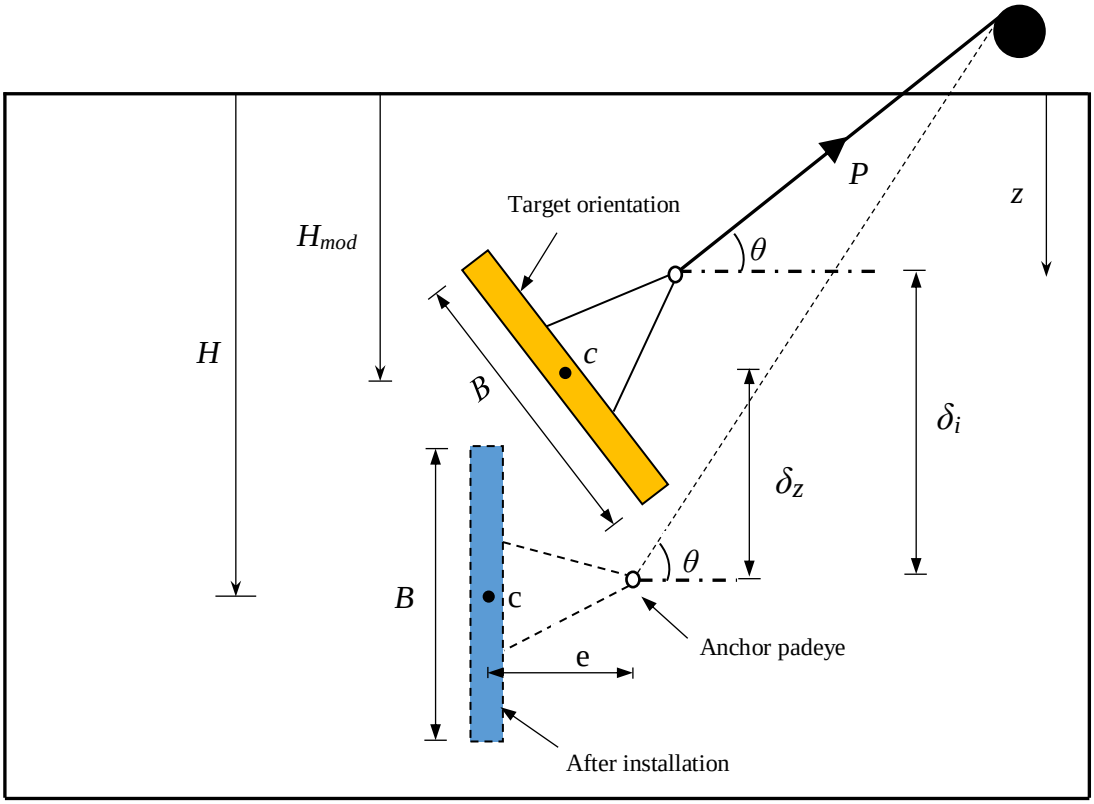

Figure 5.1 Anchor keying process.

5.2 Finite Element Model

The study presented herein considers the performance of a vertically installed strip plate anchor with a length significantly greater than the width, embedded in uniform cohesionless soil and modeled as a two-dimensional plane strain problem. The keying process of the plate anchor is a large deformation problem because large vertical and horizontal displacements occur during orientation (see Figure 5.1); accordingly, a large deformation finite element (LDFE) analysis was employed using the finite element code ABAQUS/Standard (Simulia, 2014). The anchor geometry (both with and without shank) and typical finite element mesh are shown in Figures 5.2 and 5.3, respectively. The soil medium was modeled as an elastic-perfectly plastic material with Mohr-Coulomb yield criterion. The soil domain defined in Figure 5.3 is large enough to eliminate the boundary effects. Both horizontal and vertical movement were constrained at the bottom boundary, while only horizontal movement was constrained at the far field boundary. Different mesh re-discretization strategies using a smoothing algorithm were conducted to check for mesh sensitivity. Therefore, the soil domain with a minimum element size $h_{min} = B/20$, which was constructed in the vicinity of the anchor, produced accurate results in terms of the breakout factor -displacement. The soil domain was discretized into the mesh of an eight-node quadrilateral reduced integration ABAQUS element in CPE8R, while the anchor plate was considered to be perfectly rigid due to its high stiffness, with a unit weight equal to that of the surrounding soil.

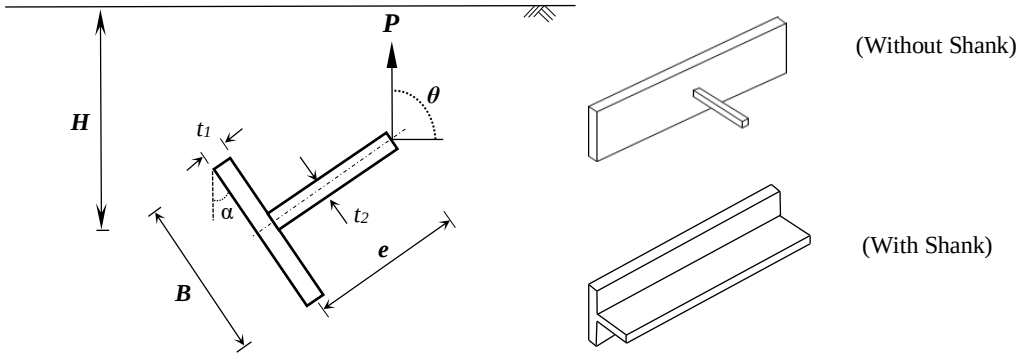

Figure 5.2 Model of a strip plate anchor during keying.

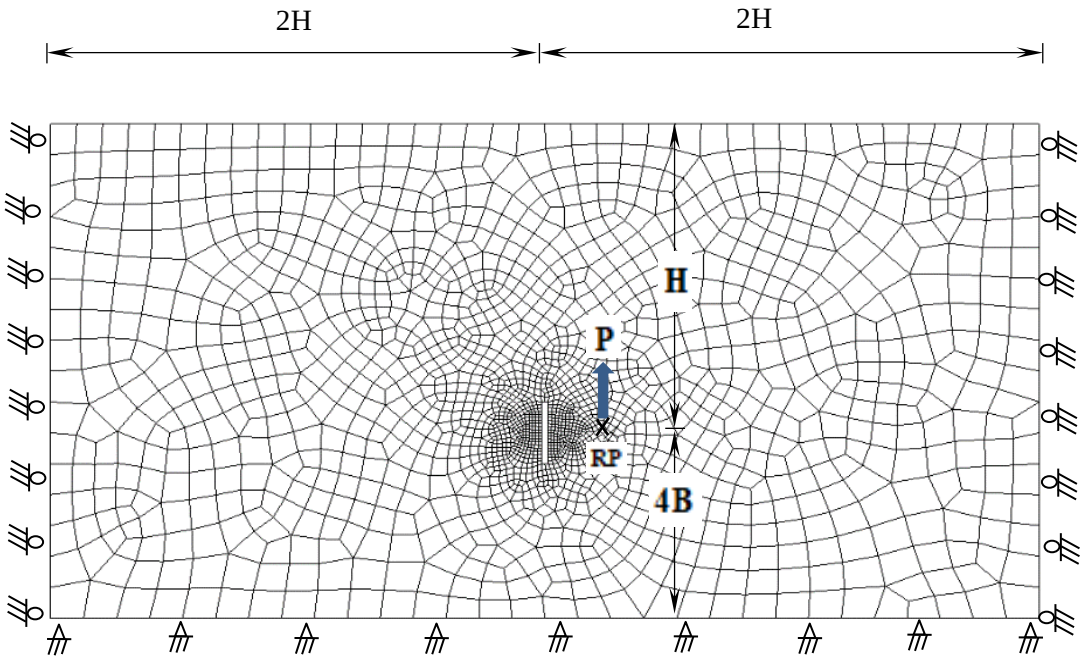

Figure 5.3 Typical mesh and boundary conditions.

A displacement-controlled FE procedure was utilized in the current analysis. Imposed displacement on the reference point of the rigid body (i.e., the plate anchor) at the padeye was used to simulate the keying process of the plate anchor. The selected

displacement increments of $\delta_t = 0.001B$ between the remeshing steps was small enough to ensure that the Lagrangian calculation remains accurate and avoid any mesh distortion. The cases analyzed considered anchor widths of B = 0.5 and 1.0 m, t/B = 0.05 and t/B = 0.1, and embedment depths of H/B = 5 and 10. The soil properties used in the analysis were cohesion c = 0.05 *kPa*, friction angle ϕ' = 30º and 33º, Poisson's ratio ν = 0.3, and at rest condition lateral earth pressure coefficient K_o = 0.5. A non-associated flow rule was assumed, with the soil dilation angles being ψ = 4º and 5º. The ϕ' and ψ properties corresponded to data on sands at a confining stress level in the range of 30 *kPa* to 100 *kPa*, as measured by Rowe and Davis (1982).

As mentioned in Chapter III, the soil anchor interface was modeled using the ABAQUS/Standard contact surface approach. The tangential (*i.e.*, frictional) interface between the outer surface of the anchor and soil was simulated using the Coulomb friction coefficient $\mu = tan\ \phi'_u$, where ϕ'_u is the soil anchor interface friction angle. The ϕ'_u values depended on the interface characteristics and relative movement between the anchor and soil (Roy et al., 2015). The value of μ = 0.5 was used in the present study. The present analysis assumed that the overburden pressure of 5B to 10B was sufficient to overcome any tendency for the base of the plate to separate from the soil during keying. Therefore, all simulations in the present study considered a no breakaway (*i.e.*, fully bonded) condition between the anchor and adjacent soil during the keying process, using an ABAQUS constraint tie. This constraint made the tied pair of surfaces (*i.e.*, the anchor-soil contact surfaces) have the same translational and rotational movement. Since the soil was essentially cohesionless, the suction force under the base of the anchor was taken as

zero. A “wished-in-place” strip plate anchor installed vertically in sand was taken as the initial condition (see Figure 5.1). In other words, installation disturbance effects were not considered in this study. Finite element simulations of keying plate anchors in clay have typically neglected installation disturbance effects, with satisfactory results with regards to comparisons to experimental data (Song et al., 2009; Wang et al., 2010).

To simulate the continuous rotation and pullout of the plate anchor, large Deformation Finite Element Analysis (LDFE) was conducted in this study by using a Remeshing and Interpolation Technique using Small Strains (RITSS) approach. In this approach, deformation of the soil domain is divided into several small increments to avoid any excessive mesh distortion. As mentioned in Chapter III, this approach is based on a standard Lagrangian finite element analysis, using finite element code ABAQUS/Standard for each increment. After the analysis of each small increment, the convection of field variables (*i.e.*, the stresses and material properties) was performed by polynomial interpolation from the old mesh to the new one. The remeshing and convection steps were repeated until the accumulated deformations reached the desired value. In the present study, the complete RITSS analysis approach was implemented by Python script files using ABAQUS built-in functions such as *RESTART and *MAP SOLUTION, as explained in Chapter III to automate the process of keying. Practically speaking, the anchor chain slides and cuts through the soil during uplift in an inverted catenary shape, and this generates an additional frictional capacity along the length of the chain (Long et al., 2009). However, for simplification of the problem and reduction in computational time, the chain was not considered in the following analyses.

5.3 Results and Discussion

5.3.1 Shank versus No Shank

In the present study, the performances of vertically installed strip plate anchors with and without shanks embedded in uniform cohesionless soil were investigated as two-dimensional plane strain problems, as shown in Figure 5.2. The first model implicitly considered soil resistance from the shank to provide a preliminary indication of the effects of including a shank as a solid object on the keying behavior. The effects of soil shank resistance were also investigated for the special case of the shank having the same length as the fluke plate (*i.e.*, $e/B = 1$), as shown in Figure 5.2. However, a full study of the effects of shank resistance would require 3D modeling, which is beyond the scope of the present research. To investigate the effects of shank resistance on keying behavior, LDFE analyses were conducted with the following soil properties: soil unit weight $\gamma = 18\ kN/m^3$, friction angle $\phi' = 30^o$, soil dilation angle $\psi = 5^o$, and $E = 3000\ kPa$. This case considered an anchor width of $B = 0.5m$, $t/B = 0.05$, and embedment depth of $H/B = 5$.

The simulations considering the shank showed higher estimates of pullout capacity and lower estimates of embedment loss than did the case of no shank anchor, as illustrated in Figures 5.4, 5.5, and 5.6. These findings are similar to those reported by Wei et al. (2014), who showed that including shank soil resistance increases pre- and post-pullout capacity and decreases the maximum loss of embedment during the keying process. It should be noted from the LDFE results included in Figure 5.6 that without considering the shank, the maximum loss of anchor embedment would have been overestimated by approximately 17%.

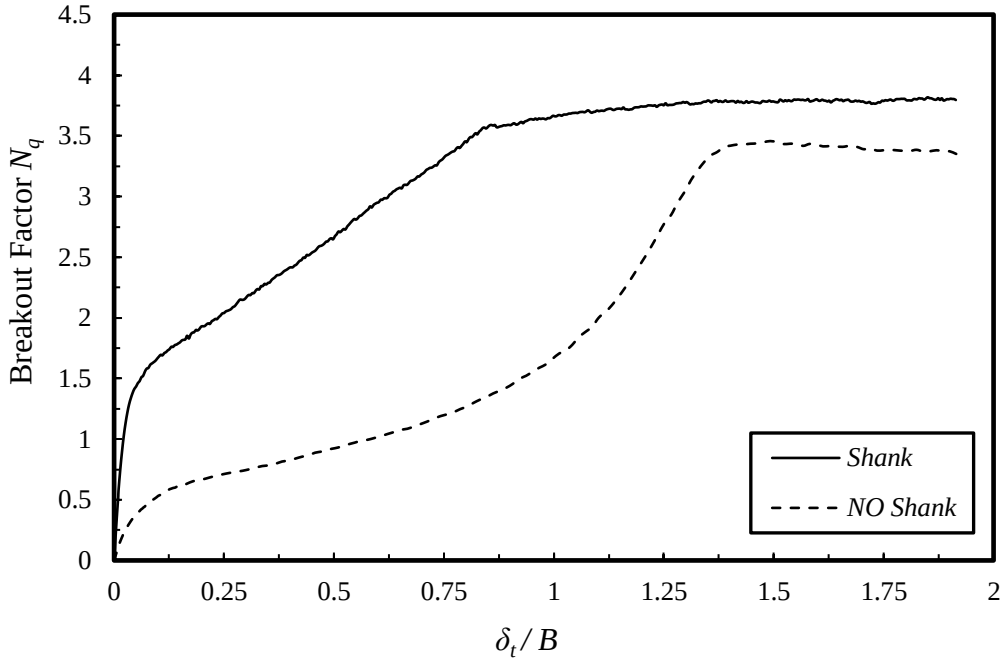

Figure 5.4 Breakout displacement curve with and without shanks when e/B = 1, B = 0.5m, t = 0.1B, and θ = 90º.

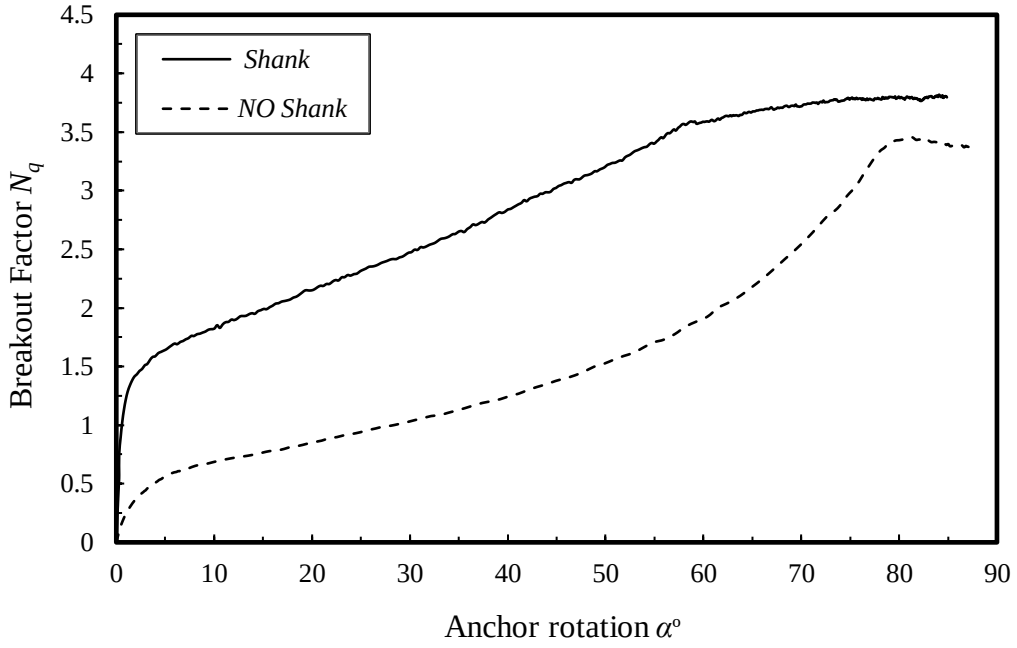

Figure 5.5 Breakout anchor rotation curve with and without shanks when e/B = 1, B = 0.5m, t = 0.1B, and θ = 90º.

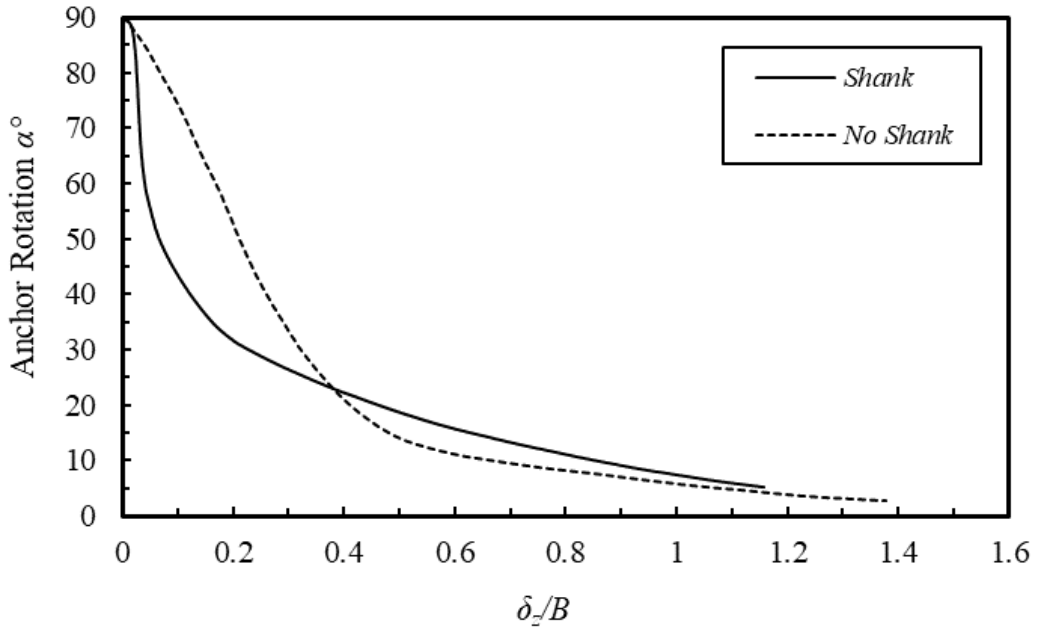

Figure 5.6 Relationship between anchor rotation α^o and δ_z/B when e/B = 1, B = 0.5m, t = 0.1B, and θ = 90º.

The predictions of the plate anchor with a shank showed a slower rotational rate, especially for the first 60° of anchor rotation, than did the plate anchor without a shank. However, the analysis overestimated the loss of anchor embedment and correspondingly underestimated pullout capacity. Therefore, to minimize computational effort and simplify the analysis in this section of the research, the anchor shank was not considered, which is conservative for design purposes.

5.3.2 Typical Breakout, Displacement and Breakout, and Rotation Curve

In the following LDFE analyses, the performances of vertically installed plate anchors without shanks, with t/B = 0.05 and 0.1, and with initial embedment depths of H/B = 5 and 10 are considered, as shown in Figure 5.2. The keying process was simulated

using a submerged unit weight of $\gamma' = 8\ kN/m^3$, friction angle of $\phi' = 33^o$, and soil dilation angle of $\psi = 4^o$. The pullout resistance at any embedment depth can be expressed in terms of the dimensionless breakout factor N_q, defined as:

$$N_q = P_u / \gamma' B H_{mod} \tag{5.1}$$

where P_u is the ultimate load (force), γ' is the unit weight of the soil, B is the anchor width, and H_{mod} is the depth from the soil surface to the anchor center, which changed due to loss in the anchor embedment δ_z. Figure 5.7 shows a typically shaped breakout N_q and normalized vertical displacement δ_t/B curve for a vertical pullout angle of $\theta = 90^o$. The predictions showed four major phases during the keying process (i.e., $\theta = 90^o$), as illustrated in Figure 5.7.

The first phase (*i.e.*, from Point 1 to Point 2) represents the padeye tightening and slight initial rotation, while the second phase (*i.e.*, from Point 2 to Point 3) indicates a half anchor rotation at which can be noticed a small increase in pullout capacity. Next, the third phase (*i.e.*, from Point 3 to Point 4) demonstrates the pullout capacity and full rotation development that occurs before the end of the keying process, while the fourth phase (*i.e.*, from Point 4 to Point 5) represents when the pullout capacity remains steady and the translational movement of the anchor is dominant, where the anchor becomes approximately horizontal. Since the anchor embedment depth H/B varies during anchor rotation from one phase to another, the breakout values were calculated using the updated values of embedment depth H_{mod}/B to keep the results more comparable between phases.

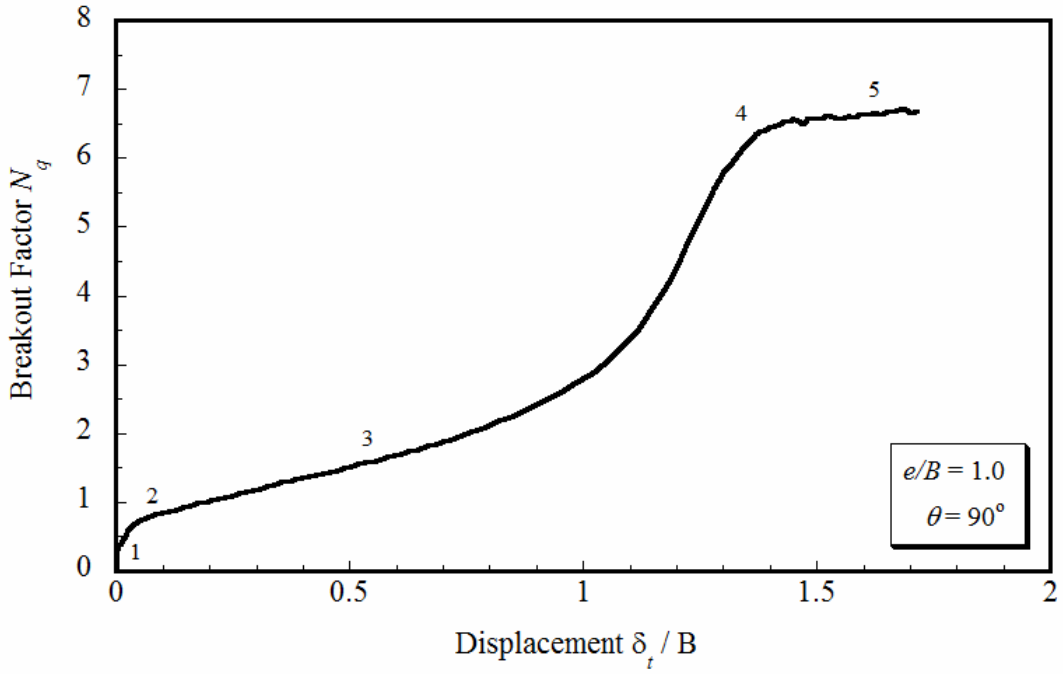

Figure 5.7 Normalized breakout-displacement curve when e/B = 1.0, θ = 90º, and t/B = 0.1.

Figure 5.8 shows the breakout N_q and rotation α curve of vertical keying (i.e., θ = 90º) for various e/B ratios. It should be noted that the angle of orientation α at which the maximum pullout capacity occurs increases with the increasing e/B ratio. For instance, the maximum pullout capacity occurs before the end of the keying process at an orientation approximately where α = 70º when e/B = 0.25, while α was approximately 85º when e/B = 1.5.

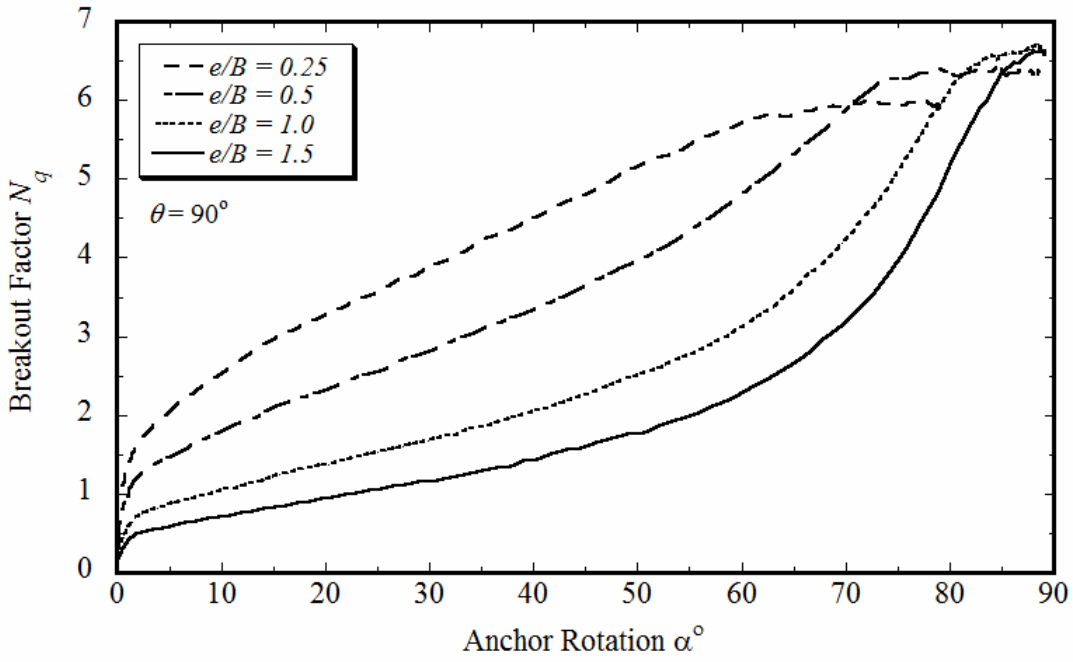

Figure 5.8 Normalized breakout rotation curve (vertical pullout θ = 90º) when *e/B* = 0.5, 1.0, and 1.5.

5.3.3 Factors Affecting the Keying Process

The most critical effect from the rotation of the plate anchor is the loss in embedment depth (presented as δ_z/B), which leads to a reduction in the potential anchor capacity. The main factors investigated in the following analyses include the anchor padeye eccentricity ratio *e/B*, loading inclination angle θ, effect of anchor thickness in terms of *t/B*, and effect of the elastic soil stiffness *E* and initial embedment depth *H/B*.

5.3.3.1 Effects of Loading Eccentricity *e/B* on Anchor Rotation Behavior

The influence of the eccentricity loading ratio *e/B* during vertical pullout was studied using LDFE analysis, considering four eccentricity ratios *e/B*: 0.25, 0.5, 1.0, and 1.5. Figure 5.9 shows the relationship between the anchor orientation α^o and the

normalized loss in anchor embedment δ_z/B, as measured at the anchor center for a strip plate with a width B = 1.0m, H/B = 10, and t/B = *0.1*. The LDFE results show that when e/B = 1.0 and 1.5, the loss in anchor embedment mainly occurred during the last 20° of anchor rotation. When e/B = 0.5 and 0.25, the prediction of loss in anchor embedment δ_z/B was greater and a longer distance was required to approach the same anchor rotation α^o, which meant that as the e/B increased, the anchor rotated at a faster rate. However, the dependence of loss in the embedment on padeye eccentricity in sand is similar to that which was reported by O'Loughlin et al. (2006) and Song et al. (2006) for clay, and this can be quantified. Also, one can see in Figure 5.10 that the vertical anchor padeye movement δ_v/B increased almost in a linear manner with an increase in anchor rotation. This was true until Phase 4, when the increase become nonlinear after the translational movement became dominant.

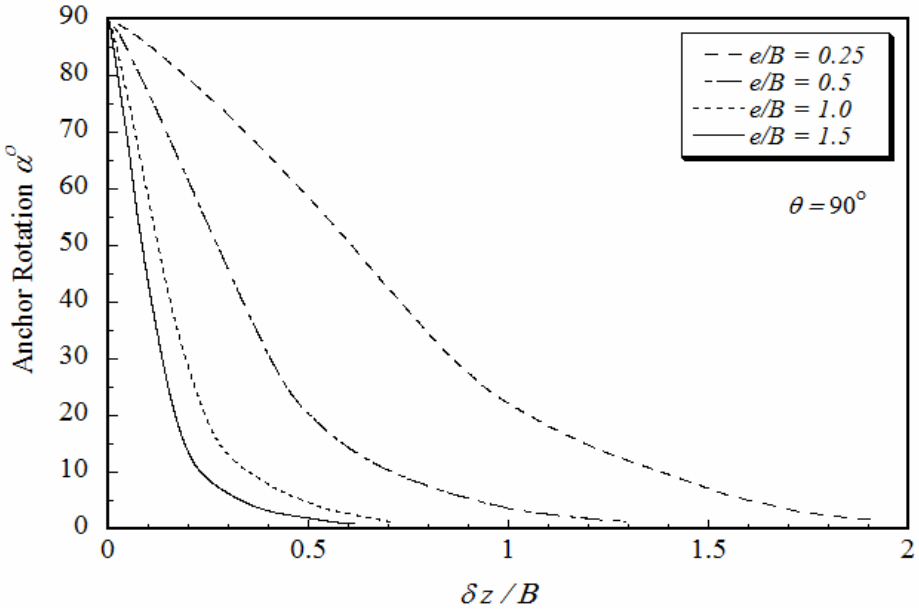

Figure 5.9 Relationship between the anchor rotation α^o and δ_z/B for e/B = 0. 25, 0.5, 1.0, and 1.5).

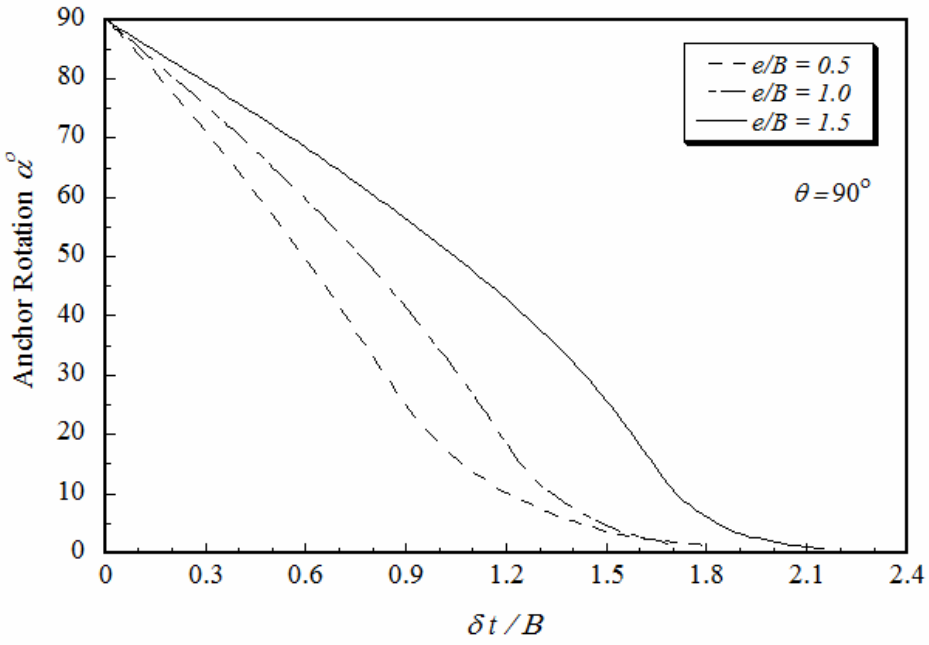

Figure 5.10 Relationship between anchor rotation α° and δ_t /*B* for *e/B* = 0.5, 1.0, and 1.5.

Figure 5.11 shows that a lower eccentricity ratio *e/B* leads to a larger movement required for the anchor to reach its pullout capacity. This larger embedment loss reduced the pullout capacity, as shown in this figure. Also, it can be noted from Figure 5.11 that a minimal loss in anchor embedment (*i.e.*, the highest potential pullout capacity) can be achieved with an anchor with an *e/B* equal at least to the anchor breadth *B*, regardless of the plate thickness. In other words, once the eccentricity $e \geq B$, a minimal loss in anchor embedment can be achieved regardless of the plate thickness. This is consistent with what was reported by Barron (2014). Decreasing *e/B* from 1.5 to 0.25 caused a decrease in pullout capacity of approximately 20%, as shown in Figure 5.11.

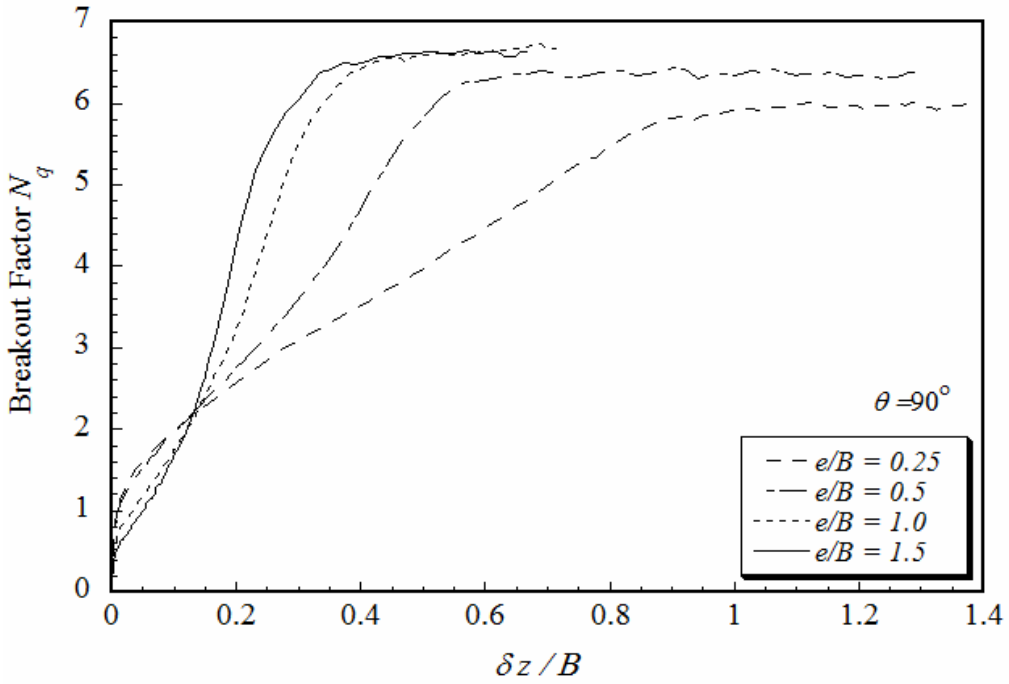

Figure 5.11 Normalized breakout displacement curve with t/B = 0.1 when e/B = 0.25, 0.5, 1.0, and 1.5.

The relationship between the normalized loss in anchor embedment δ_z/B, measured at the anchor center, and the normalized total vertical displacement of the anchor padeye δ_t/B are shown in Figure 5.12. It should be noted that when e/B = 1.5, there was minimal loss in anchor embedment δ_z at the initial value of δ_t. This stiffer response for e/B = 1.5 was changed to a softer response once the eccentricity e/B was reduced to 1.0, 0.5, and 0.25, as illustrated in the figure. It is worth noting that for all e/B ratios, the slopes become approximately 1:1 when the anchor reaches the maximum pullout capacity. In other words, as e/B reduced to 0.25, δ_z/B increases linearly with δ_t/B starting from the beginning of keying process. These findings are similar to those reported by Long et al. (2009) for clay.

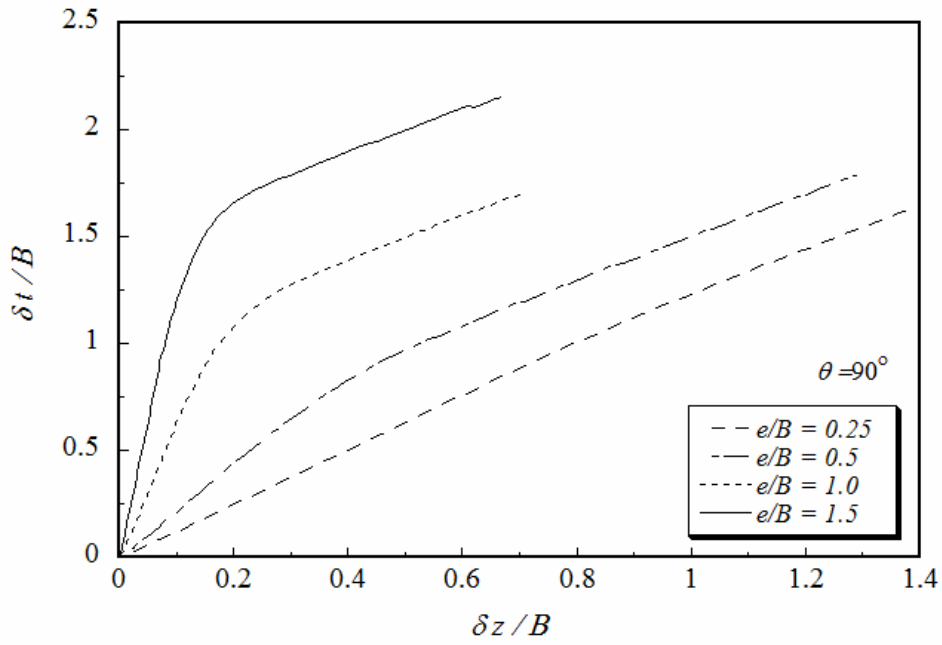

Figure 5.12 Relationship between δ_t/B and δ_z/B for e/B = 0.25, 0.5, 1.0, and 1.5.

The predictions in Figure 5.13 show that the movement of the anchor padeye for vertical pullout followed a similar pattern for different e/B ratios. The results show that as the e/B increased, the total vertical displacement δ_t required to reach pullout capacity, also increased. Once the translational movement became dominant, the pullout anchor capacity developed rapidly.

The results in Figure 5.14 show that the trajectory of the anchor padeye movement, which corresponds to phases 2 to 3 and 3 to 4 in the breakout displacement curve illustrated in Figure 5.7, was accompanied by a backwards horizontal movement. As the anchor approached its full rotation in Phase 4, the vertical displacement became dominant, as shown in Figure 5.14. It should also be noted that as e/B increased, the total accumulated value of the backwards horizontal movement at its full rotation in Phase 4

became larger. The trajectory of the anchor center with t/B = 0.05 (see Figure 5.15) showed vertical and horizontal backwards movements during rotation. As the anchor rotation progressed, it was noted that the backwards movement could change to forwards horizontal movement, followed by a dominant vertical movement. It can also be seen from Figure 5.15 for the trajectory of the anchor center that as e/B increases, the backwards horizontal movement also decreases.

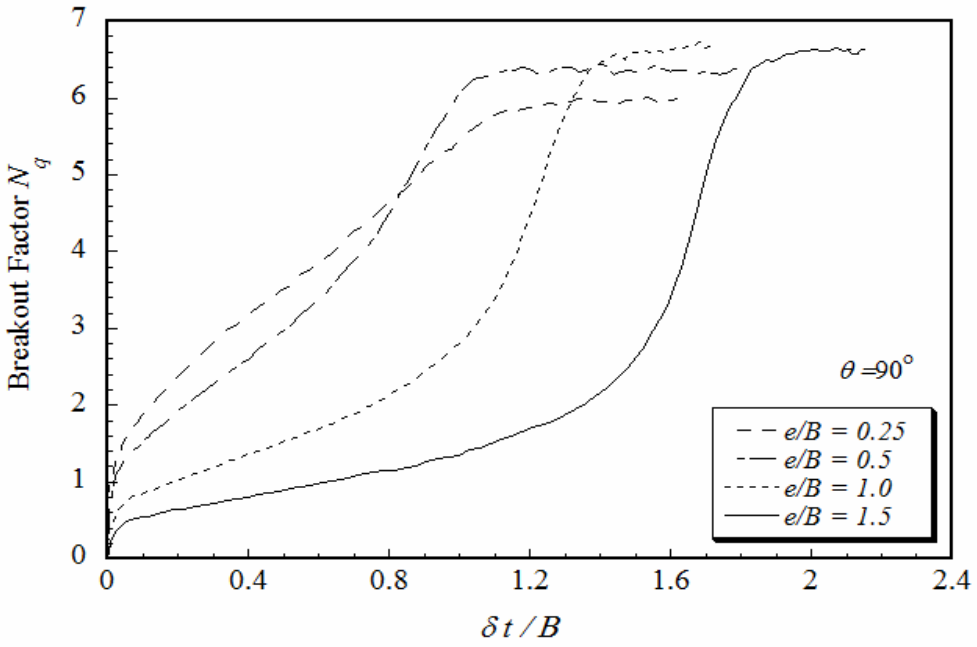

Figure 5.13 Normalized breakout displacement during keying under vertical pullout for e/B = 0.25, 0.5, 1.0, and 1.5.

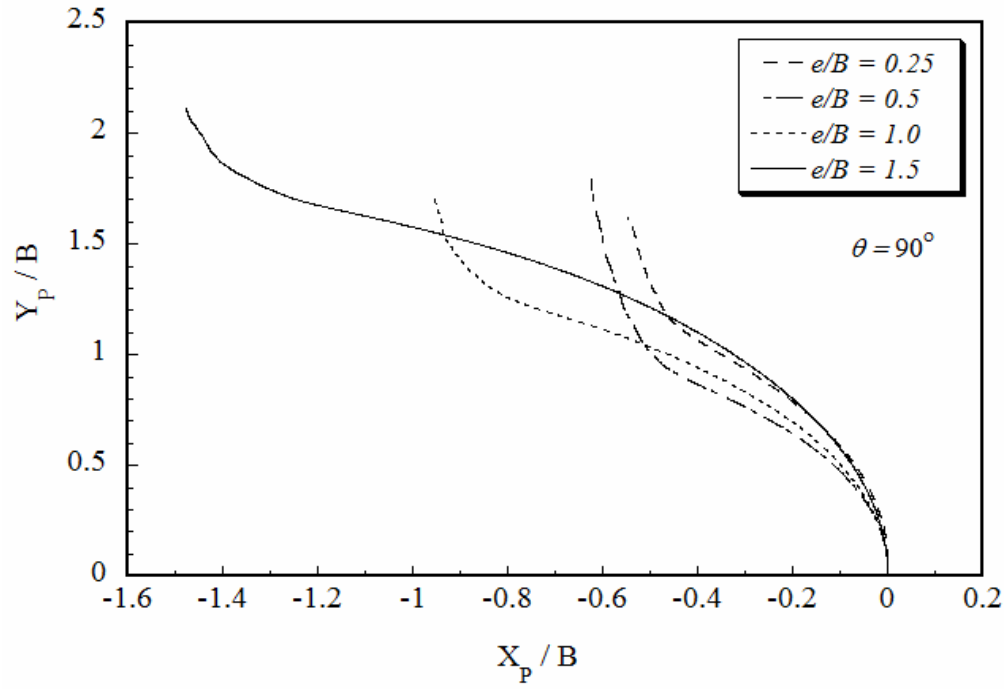

Figure 5.14 Trajectories of the anchor padeye during rotation when *e/B* = 0.25, 0.5, 1.0, and 1.5.

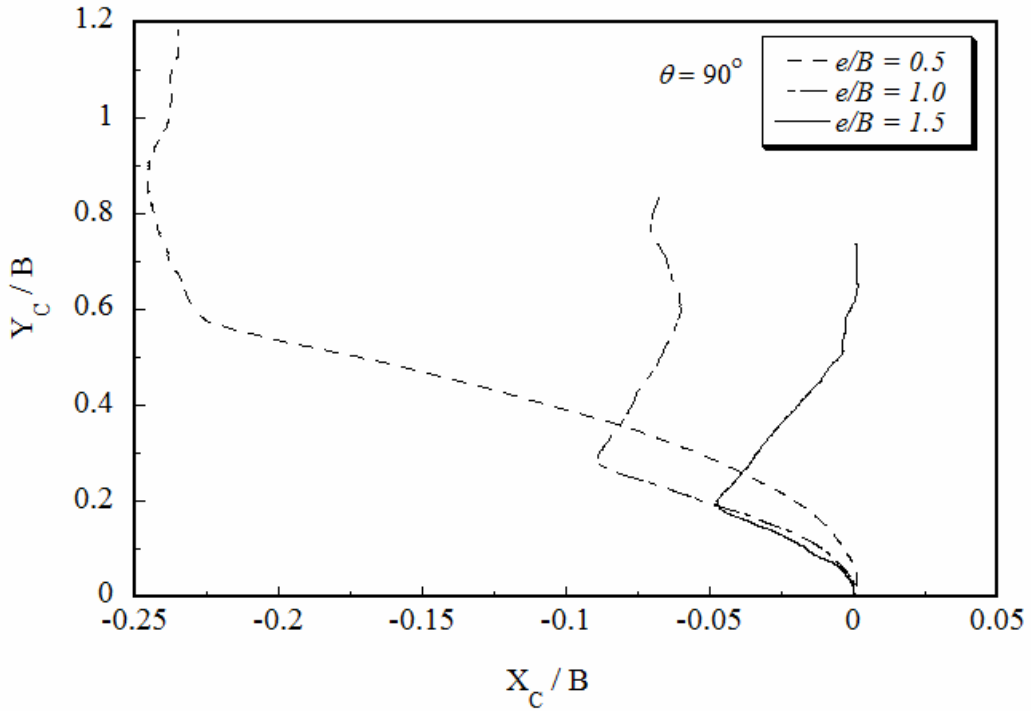

Figure 5.15 Trajectories of anchor center during rotation with *t/B* = 0.05 when *e/B* = 0. 5, 1.0, and 1.5.

5.3.3.2 Effects of Pullout Angle θ on Anchor Rotation Behavior

In the following LDFE analyses, vertically installed strip plate anchors at a padeye eccentricity ratio of e/B = 1.0 and with pullout angles to the horizontal of θ = 30º, 45º, and 90º were considered in an effort to determine the effects of anchor pullout inclination on the loss of embedment δ_z/B. The results for each pullout angle θ in Figure 5.16 for t/B = 0.05 showed that the loss in anchor embedment increased with increases in anchor rotation α to its final orientation. However, the maximum loss in anchor embedment increased with increasing pullout angle θ, since more rotation was required to complete the anchor rotation when the higher pullout angle was applied. It should also be noted from Figure 5.16 that the anchor did not rotate to a full 30º or 45º position, but instead stabilized at a plate inclination of α = 26º and 43º, respectively. Therefore, the maximum loss in embedment δ_z/B was determined at the point where the anchor approached its stable orientation. For instance, it can be seen in Figure 5.16 that when the plate anchor was stabilized at a plate inclination of α = 26º, the plate anchor experienced a maximum loss of embedment δ_z/B, approximately 0.325.

A linear relationship was also observed between the maximum loss in anchor embedment and anchor pullout angle θ at any e/B ratio, as shown in Figure 5.17. However, the dependence on loss of embedment of pullout angle θ for sand is similar to that reported for clay by Song et al. (2009) and Long et al. (2009), as illustrated in Figures 2.37

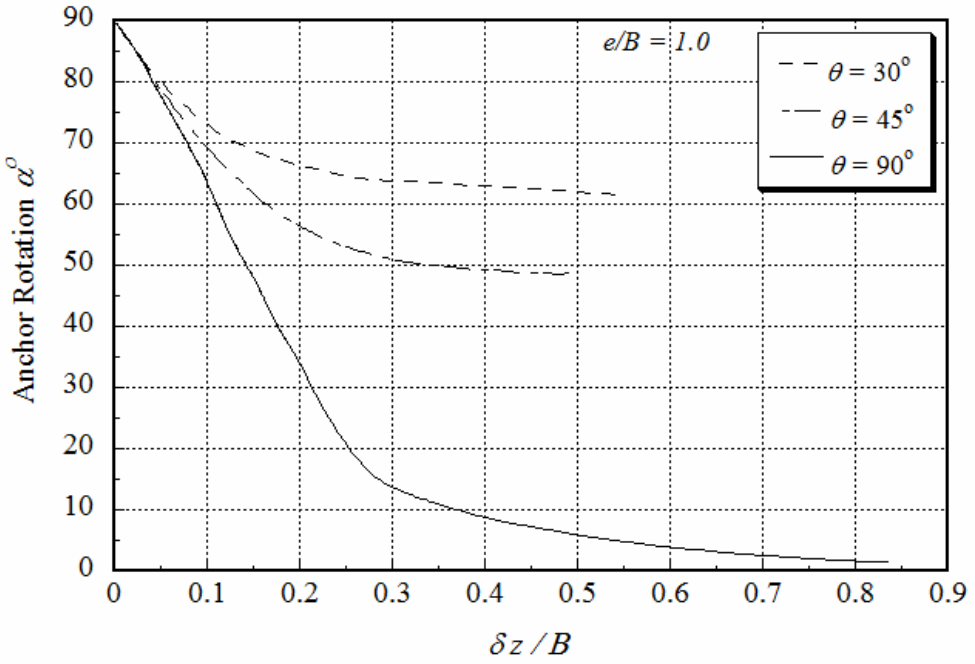

Figure 5.16 Relationship between anchor rotation αo and δ_z/B for e/B = 1.0 when θ = 30º, 45º, and 90º.

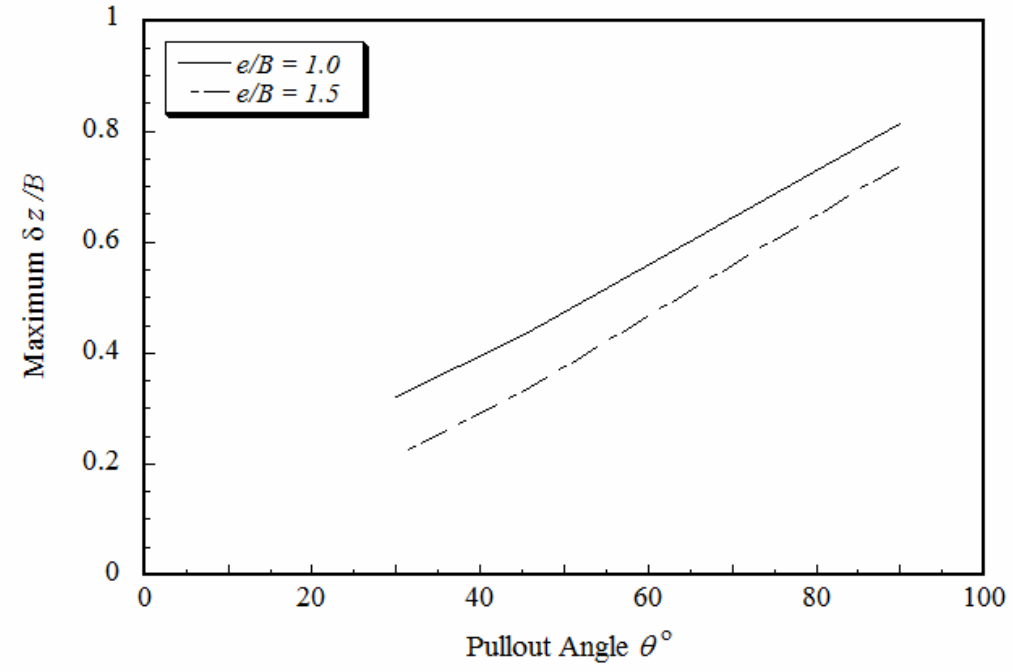

Figure 5.17 Relationship between pullout angle θ and maximum δ_z/B for e/B = 1.0 and 1.5.

The predictions in Figure 5.18 show the trajectory of the anchor padeye's movement for *e/B* = 1.0 at different pullout angles. The results illustrate that the amount of backward movement primarily depended on the pullout loading angle θ and then vanished, and could change to forward movement when the loading angle θ was small.

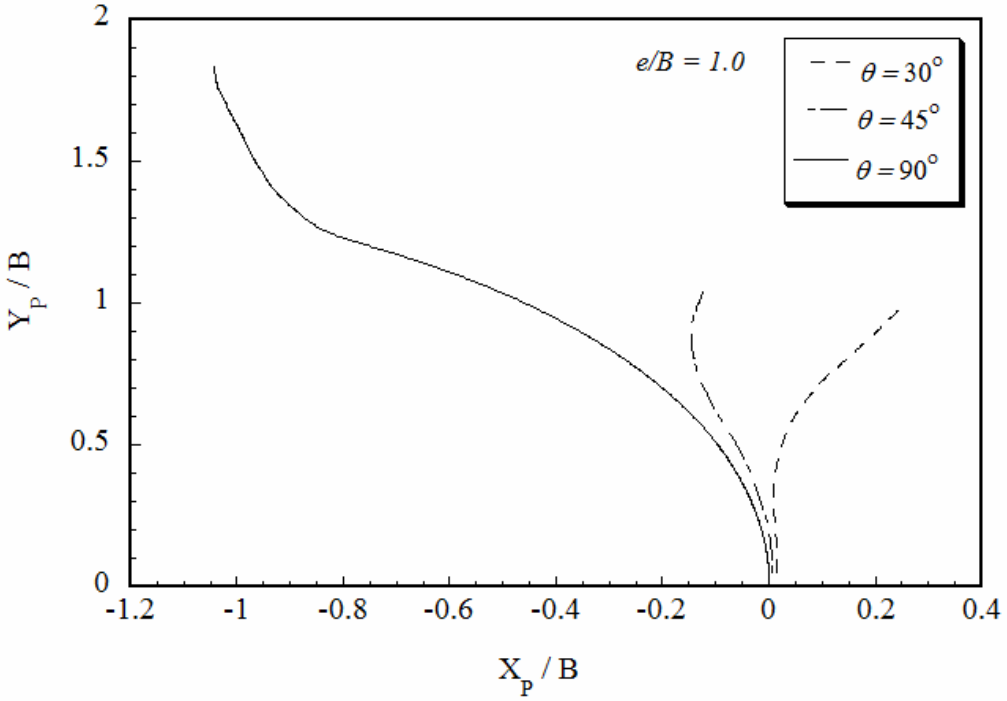

Figure 5.18 Anchor padeye trajectories during rotation for *e/B* = 1.0 when pullout angle θ = 30º, 45º, and 90º.

5.3.3.3 Influence of Anchor Thickness *t/B*

To investigate the effects of the anchor thickness ratio *t/B* on keying behavior, LDFE analyses were performed using *t/B* ratios of 0.05 and 0.1, with different loading eccentricity *e/B* ratios (*i.e.*, 0.25, 0.5, 1.0, and 1.5) for the vertical pullout loading (*i.e.*, θ = 90º). The initial anchor embedment was maintained at *H/B* = 10. Figure 5.19 shows that when *t/B* = 0.05, the prediction of loss in anchor embedment δ_z/B was greater and a longer

distance was required to approach the final orientation, meaning that as *t/B* increased, the anchor rotated faster and lost less embedment during keying. This effect became minimal as *e/B* = 1.5, as shown in Figure 5.19c. It is apparent from Figure 5.20 that the lower the anchor thickness ratio *t/B*, the higher the loss in anchor embedment δ_z/B, especially for small *e/B* ratios. In other words, the effect of *t/B* on the loss of anchor embedment δ_z/B became more pronounced when *e/B* < 0.5. For instance, at *e/B* = 0.25, the increase in maximum loss in anchor embedment δ_z/B was ~ 80% greater than the maximum δ_z/B when *e/B* = 0.5.

Figure 5.20 shows that at certain *e/B* values, as the thickness ratio *t/B* decreases, the maximum loss of embedment δ_z/B increases and, therefore, the corresponding pullout capacity decreases. This effect becomes minimal as *e/B* increases. Increasing the *t/B* ratio may increase resistance to the translational and rotational movement, due to increases in friction and bearing contact area for the anchor thickness. Additionally, the LDFE results showed that the trajectory of the anchor padeye was dependent on *t/B* before the end of the keying process, especially for small ratios of *e/B* (see Figure 5.21), while the padeye trajectory became independent in all keying process phases when *e/B* = 1.5. Therefore, thinner anchors may suffer greater embedment loss during the keying process but practically are beneficial for minimizing the penetration resistance, which is important when installing suction embedded plate anchors (Wang et al., 2009).

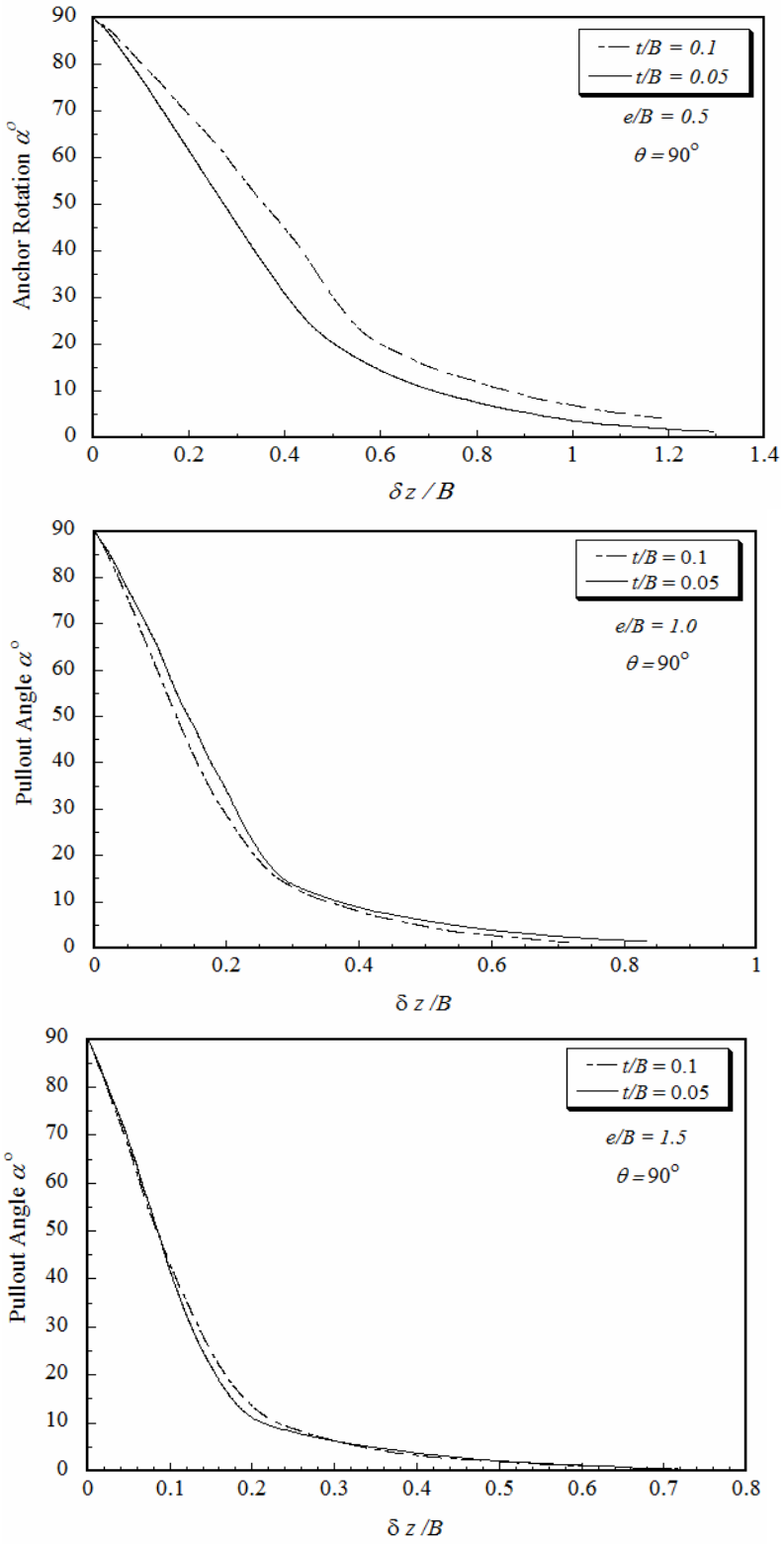

Figure 5.19 Effects of anchor thickness *t/B* on the relationship between anchor rotation α^o and δ_z/B for *e/B* = 0.5, 1.0, and 1.5.

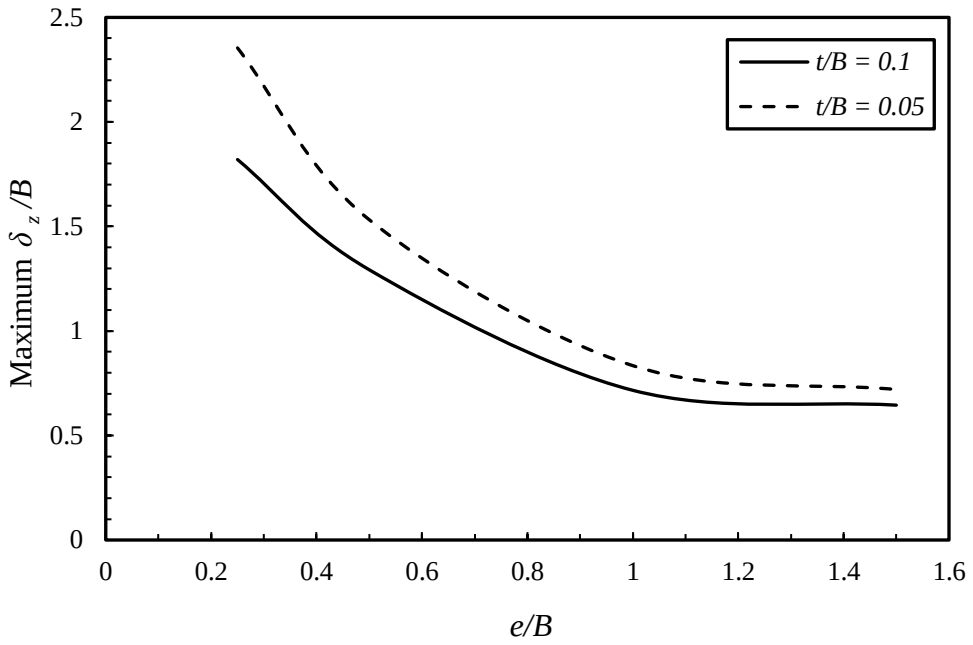

Figure 5.20 Effects of anchor thickness *t/B* on the maximum loss of embedment δ_z/B for $\theta = 90^o$.

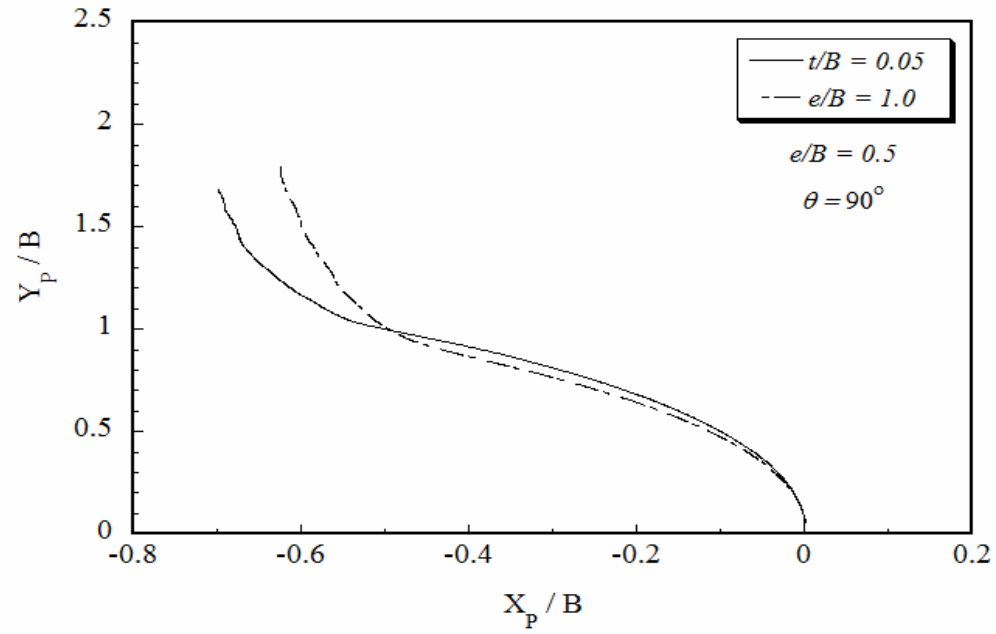

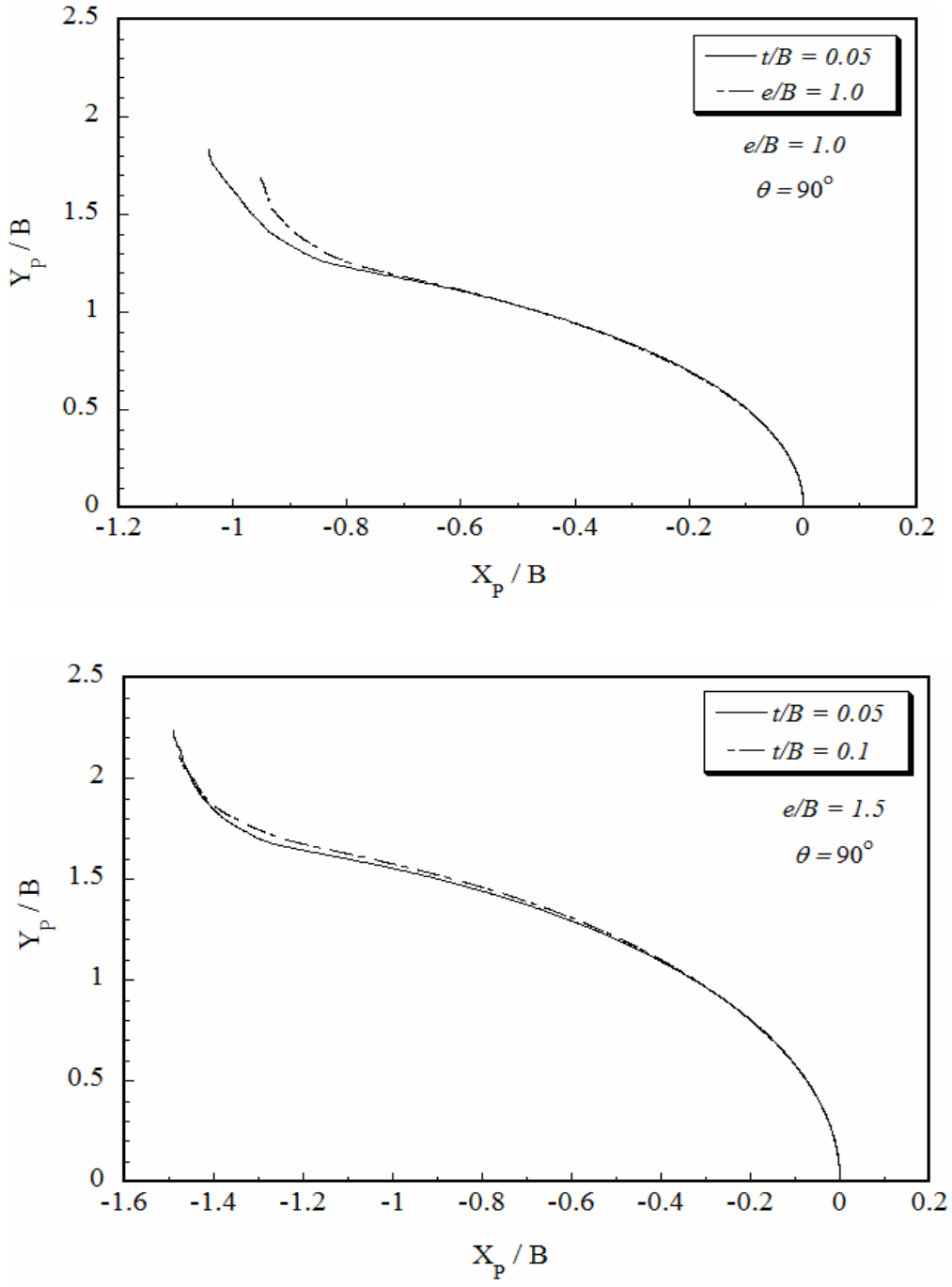

Figure 5.21 Effects of anchor thickness *t/B* on trajectories of the anchor padeye during rotation for the vertical pullout angle $\theta = 90^{o}$.

5.3.3.4 Effects of Soil Stiffness *E* and Embedment Depth *H/B* on Rotation Behavior

The effects of elastic soil stiffness *E* on the responses of a plate anchor during the keying process were also investigated for different elastic soil stiffness *E* (*i.e.*, 3,000, 6,000, and 10,000 *kPa*). The simulation was conducted for *H/B* = 3 and 10, *e/B* = 1.0, *t/B* = 0.05, and vertical pullout θ = 90º. The predictions showed in Figures 5.22, 5.23, and 5.25 demonstrate that the keying behavior of shallow anchors (*e.g.*, *H/B* = 3) is essentially independent of soil elastic stiffness *E*. Beyond the shallow zone, the keying behavior and pullout capacity of deeply embedded anchors (*e.g.*, *H/B* = 10) are sensitive to *E*, as shown in these figures. The influence of elastic soil stiffness *E* on the breakout N_q factor for relatively deeply embedded anchors (*e.g.*, *H/B* = 10) is obvious in Figure 5.22b, which shows the uplift dimensionless curves for different *E* values. The results show a trend in reduced elastic soil stiffness *E*, leading to increased levels of displacement at which the ultimate load is approached. However, it should be noted that there was around a 10% difference in pullout capacity at the end of the keying, as *E* increased from 3,000 to 10,000 *kPa*.

As shown in Figure 5.23a, the results of the plate inclination α embedment loss δ_z/B curve for *E* = 3,000, 6,000, and 10,000 *kPa* are identical for shallow anchors, while the effects of *E* on the embedment loss δ_z/B is evident for deeply embedded anchors (*e.g.*, *H/B* = 10), as shown in Figure 5.23b. Also, the predictions for *H/B* = 10 show that the maximum embedment loss decreases in a nonlinear manner (see Figure 5.24) as the elastic soil stiffness *E* increases. For instance, the maximum embedment loss for *e/B* =1.0 when *E* = 10,000 *kPa* became about 30% smaller than the result of *E* = 3,000 *kPa*. Therefore,

the keying response of a strip plate anchor can be interpreted as essentially independent of elastic soil stiffness E for shallowly embedded anchors, while the responses for deeply embedded anchors during the keying process are influenced by the soil stiffness E.

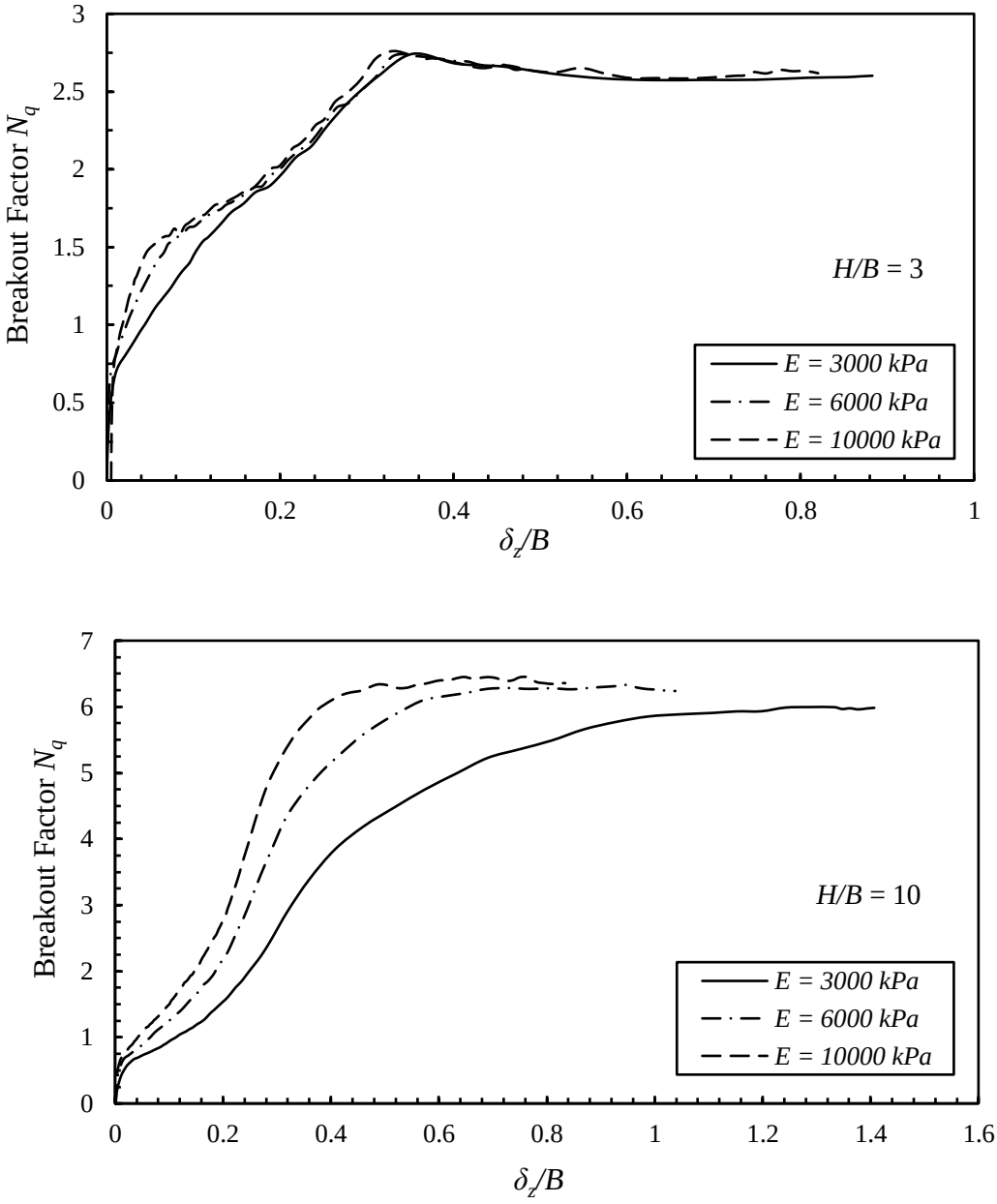

Figure 5.22 Effects of elastic soil stiffness E on the breakout N_q for shallowly and deeply embedded anchors.

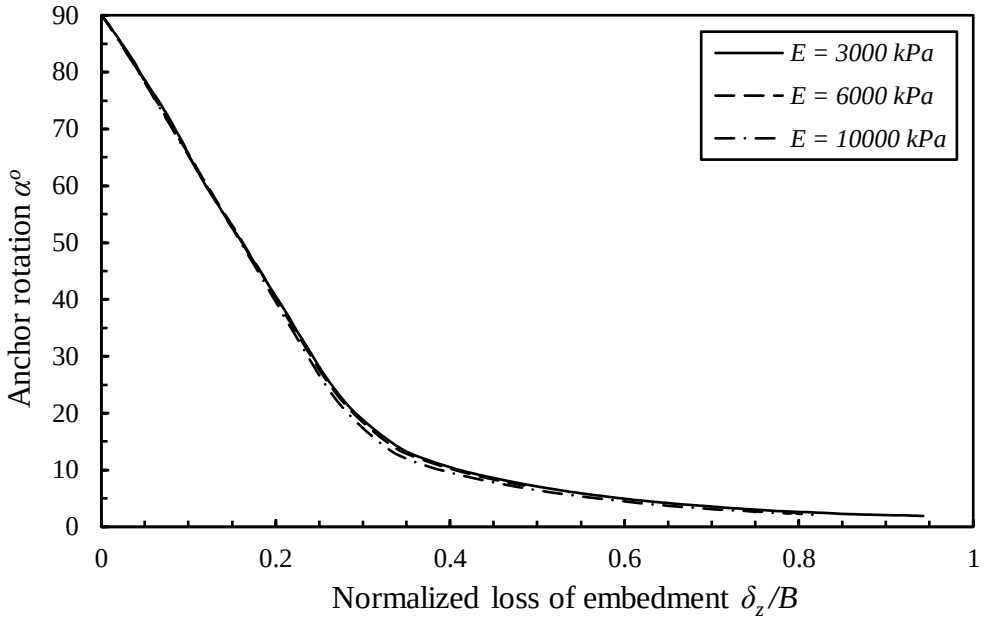

(a) $H/B = 3$

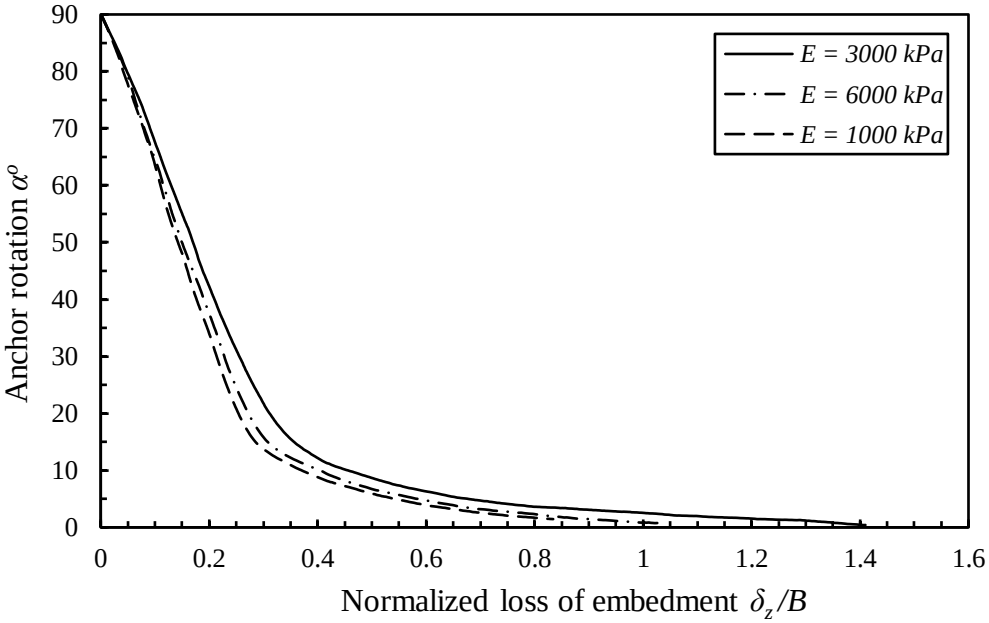

(b) $H/B = 10$

Figure 5.23 Effects of elastic soil stiffness E on the relationship between anchor rotation α^o and δ_z/B for shallowly ($H/B = 3$) and deeply ($H/B = 10$) embedded anchors.

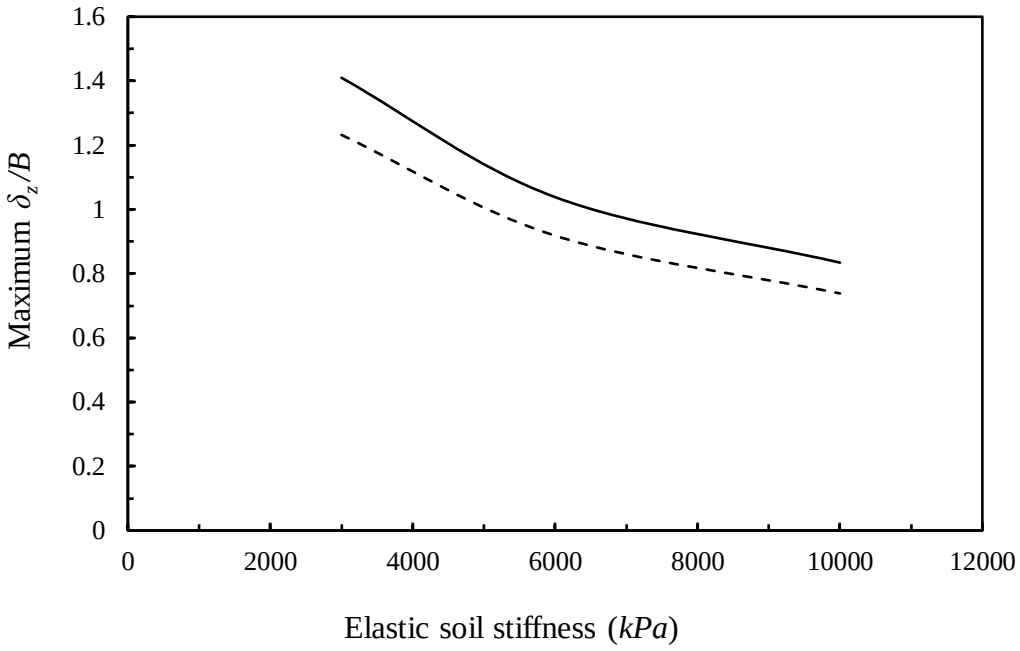

Figure 5.24 Relationship between elastic soil stiffness E and maximum δ_z/B for e/B = 1.0 and 1.5.

The influence of E on the anchor trajectories during the keying process was also investigated for H/B = 3 and 10. The LDFE results showed that the anchor padeye trajectory for H/B = 10 was dependent upon E before the end of the keying process, as shown in Figure 5.25b, while the anchor padeye trajectory for H/B = 3 was independent of E in all anchor keying phases, as illustrated in Figure 5.25a. However, for both trajectories the rotational movement was accompanied by vertical and backwards horizontal movement. The influence of initial embedment depth H/B on anchor response during the keying process is illustrated in Figures 5.26 and 5.27 for H/B = 3, 5, and 10. Figure 5.26 shows that the anchor rotation with the loss in anchor embedment was approximately independent of the embedment depth.

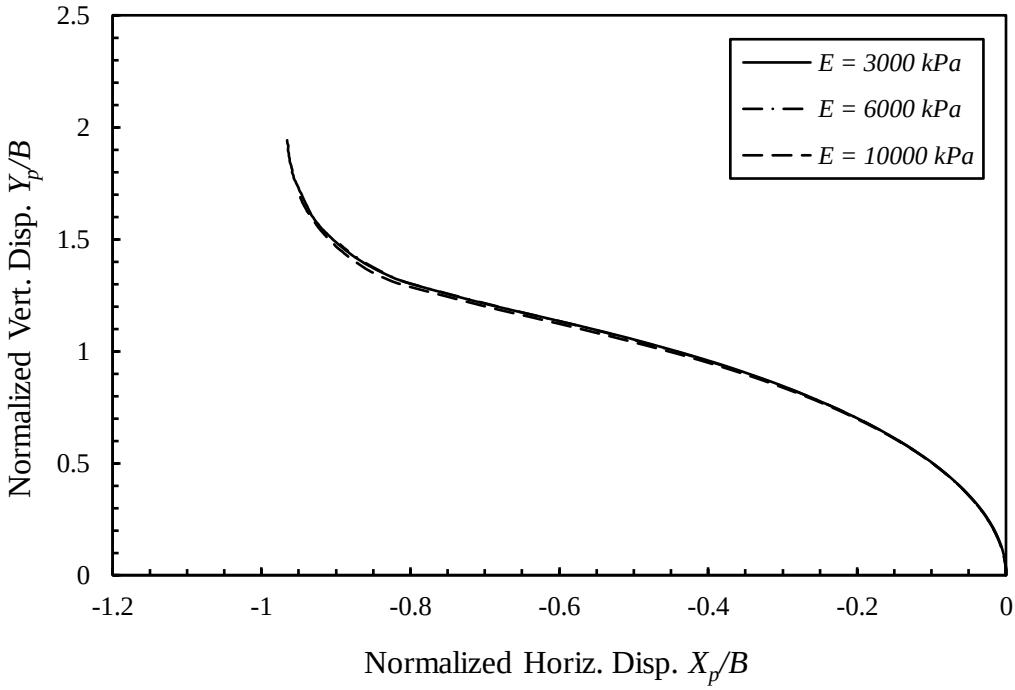

(a) $H/B = 3$

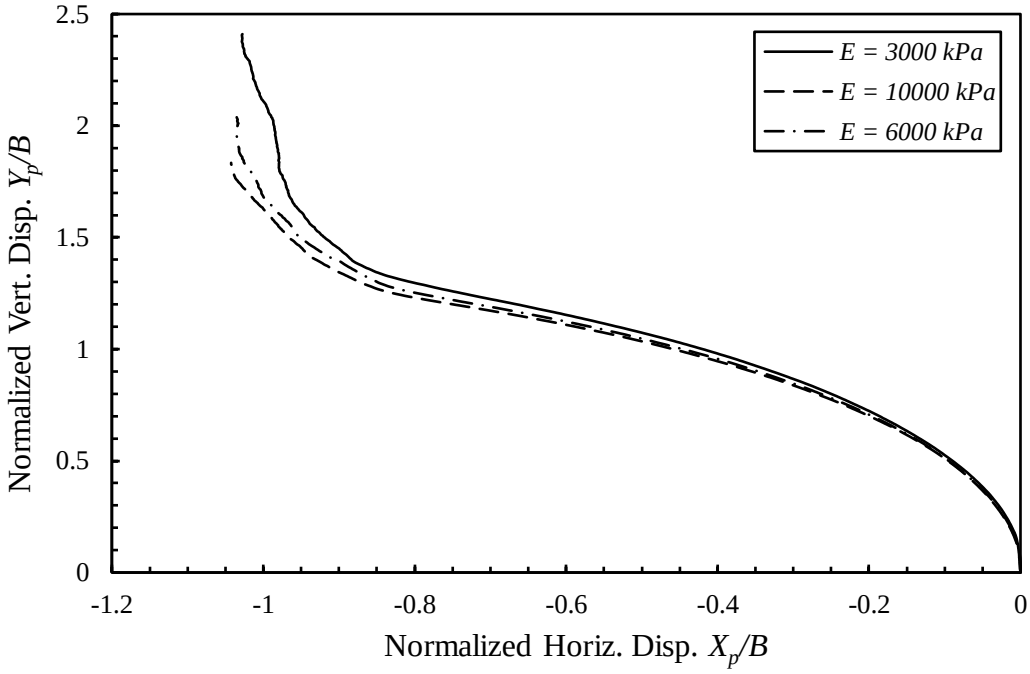

(b) $H/B = 10$

Figure 5.25 Effects of elastic soil stiffness E on padeye anchor trajectories during rotation for shallowly and deeply embedded anchors.

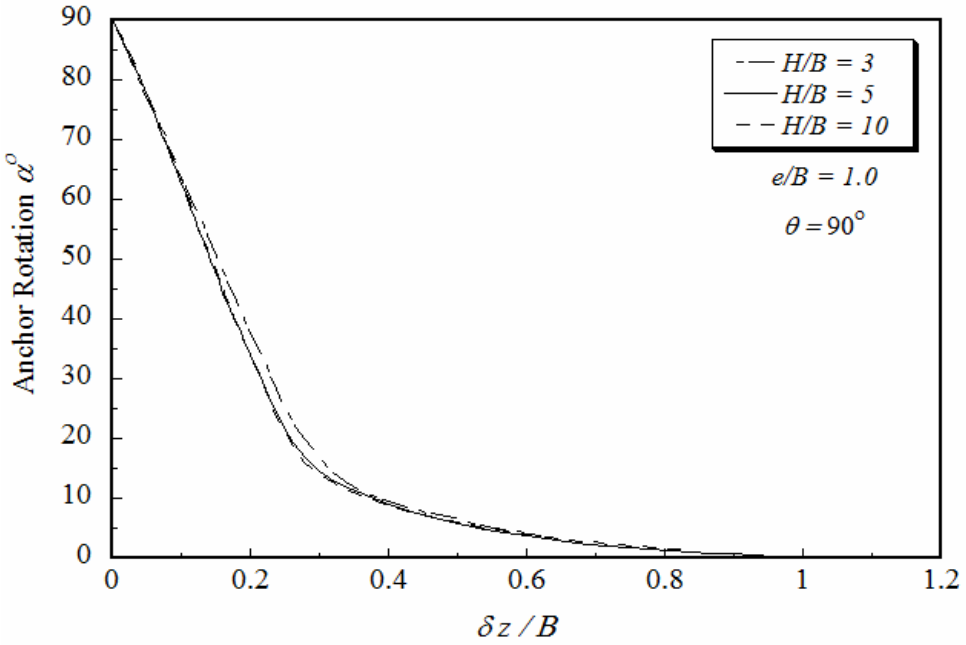

Figure 5.26 Relationship between anchor rotation α^o and δ_z/B for different H/B ratios.

Figure 5.27 shows that the pre- and post-pullout capacities mainly depended on H/B. However, as H/B increased, the loss of embedment depth where the pullout capacity reached the ultimate anchor capacity increased slightly, as shown in Figure 5.27.

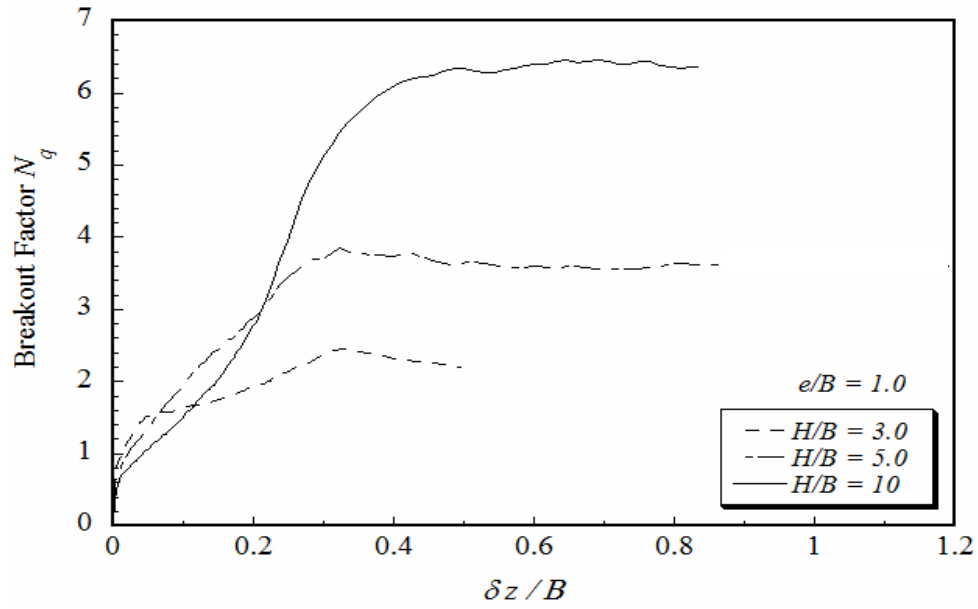

Figure 5.27 Normalized breakout displacement curve for various H/B ratios.

5.4 Soil Flow mechanisms

To investigate the soil flow mechanisms surrounding the anchor plate during the keying process, a typical contour of total displacement for vertical pullout $\theta = 90^o$, e/B = 1.0, t/B = 0.05, and H/B = 10.0 is shown in Figures 5.28, 5.29, and 5.30. These figures present the soil flow mechanism as the anchor position evolved at various phases during the anchor keying process. It was observed that a fully localized soil flow mechanism occurred around the anchor when α increased from 0º to approximately 60º, as shown in Figure 5.28.

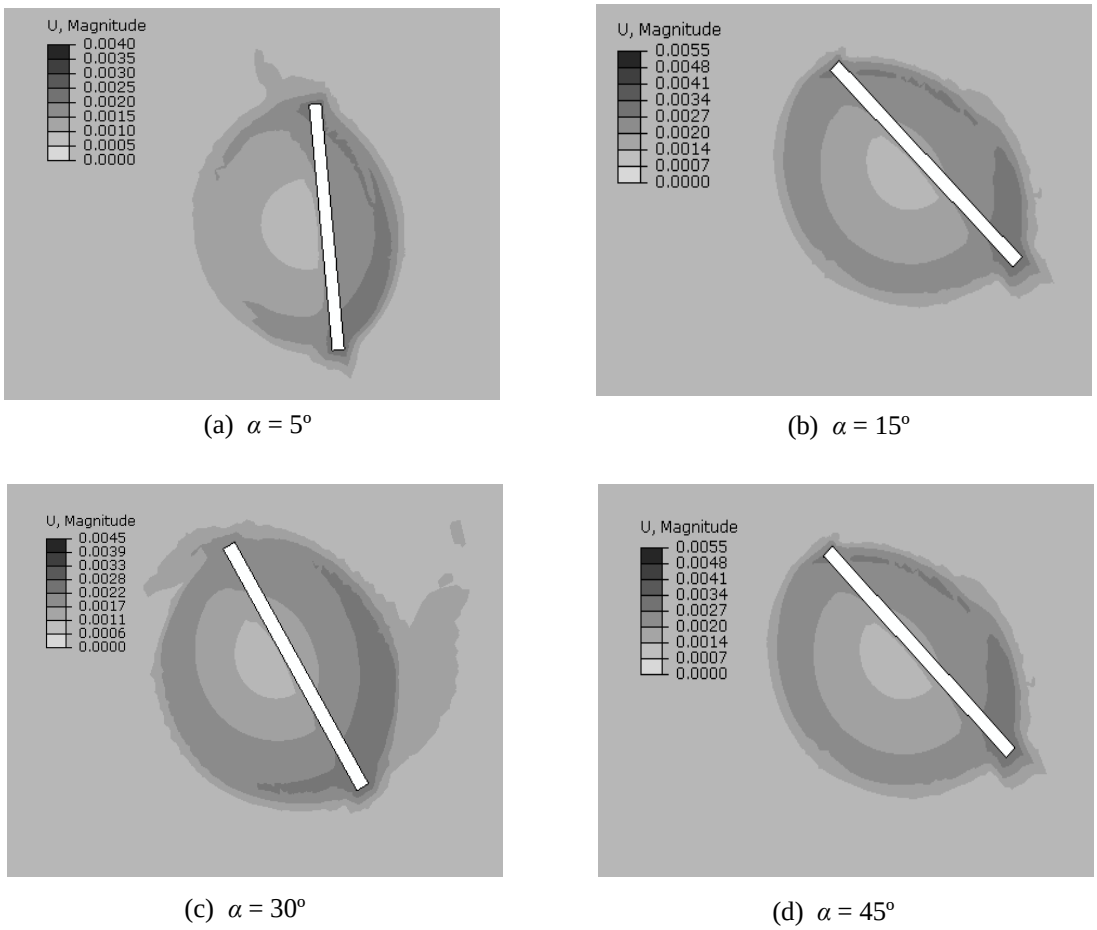

(a) $\alpha = 5^o$ (b) $\alpha = 15^o$

(c) $\alpha = 30^o$ (d) $\alpha = 45^o$

Figure 5.28 Soil flow mechanisms during anchor keying: (a) $\alpha = 5^o$; (b) $\alpha = 15^o$; (c) $\alpha = 30^o$; and (d) $\alpha = 45^o$.

This was due to the rotational movement of the plate anchor during this phase being dominant, and the bearing resistance of the plate anchor remaining steady or increasing slightly during rotation. As the keying progressed and a combination of rotational and translational movements of the anchor occurred (*i.e.*, when α exceeded approximately 60º), it could be seen that localized soil flow was accompanied by some plastic soil flow, which extended to the upper zones ahead of the anchor as shown in Figure 5.29. Consequently, the breakout factor increased rapidly as the translational movement started to be dominant.

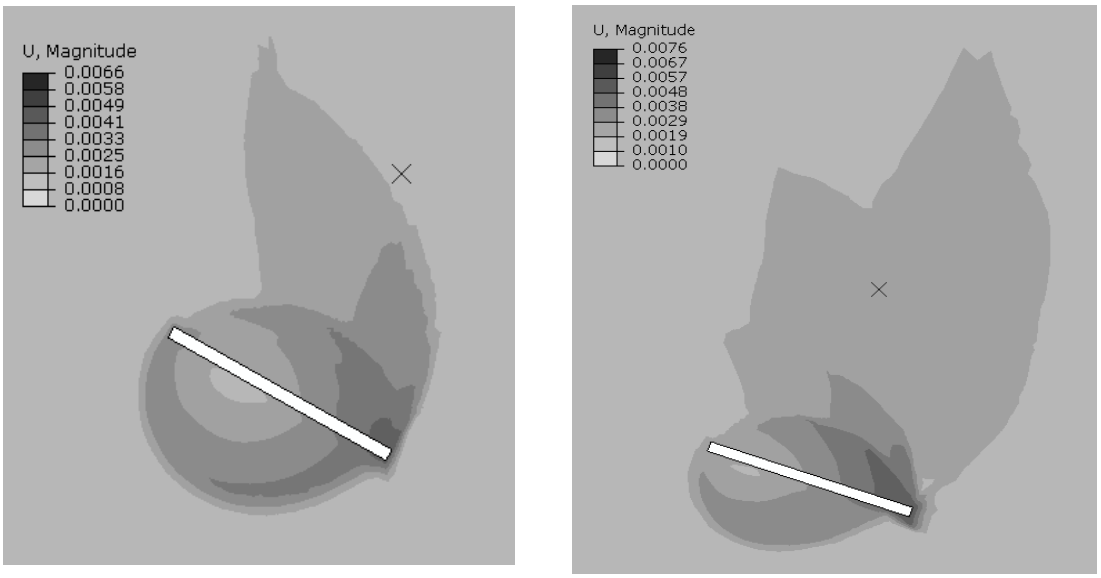

(a) α = 60º (b) α = 70º

Figure 5.29 Soil flow mechanisms during anchor keying: (a) α = 60º; and (b) α = 70º.

As the plate anchor approached the final stages of the keying process (*i.e.*, the highest potential pullout capacity) where the translational movement of the plate anchor became dominant, a transition from deep localized rotational mechanism to shallow soil

flow mechanism, consisting failure bands which begin from the corner of the plate anchor and extend to the free surface as shown in Figure 5.30. For the anchor embedment *H/B* = 10, it was obvious that the soil flow mechanism remained as is, and not fully in deep failure mode. Once the plate anchor was embedded deeper (*e.g.*, *H/B* = 18), the soil flow around the anchor was fully localized (see Figure 5.31) due to the diminishing effect of the free surface.

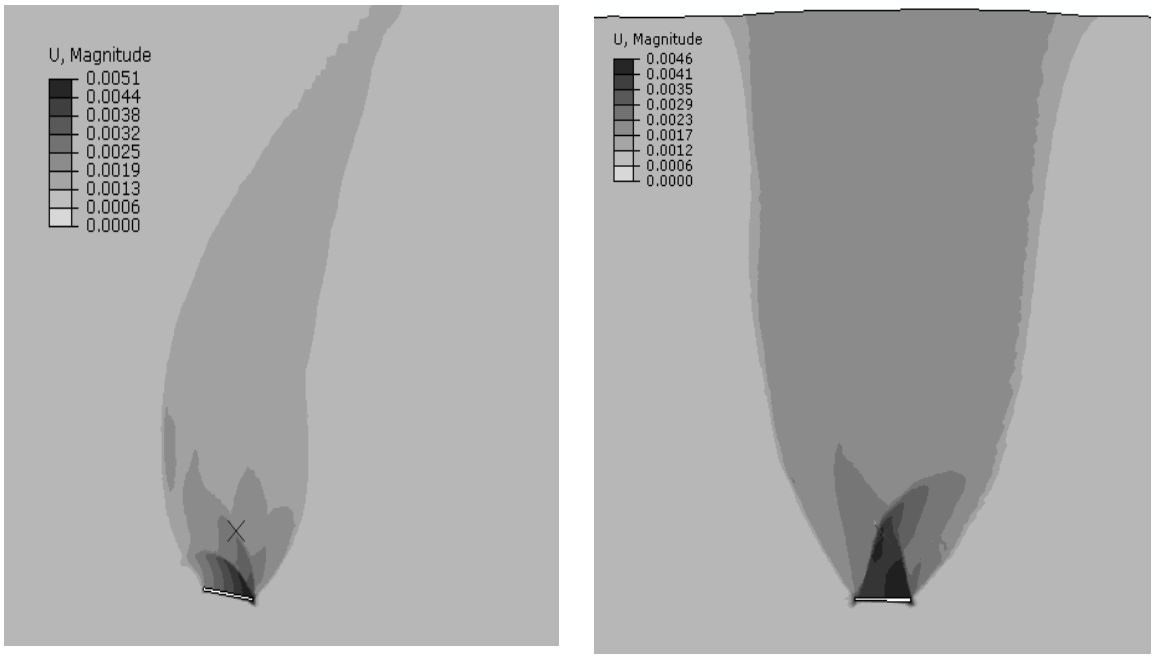

(a) α = 80º (b) α = 89.5º

Figure 5.30 Soil flow mechanisms during anchor keying (*e/B* = 1.0, θ = 90º): (a) α = 80º; and (b) α = 89.5º.

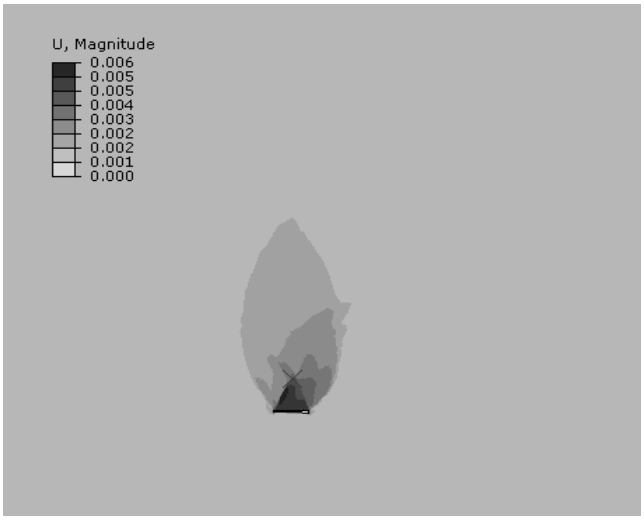

Figure 5.31 Soil flow mechanisms during anchor keying (e/B = 1.0, θ = 90º) when α = 89º for H/B = 18.

5.5 Summary

The keying process behavior and pullout capacity of a vertically installed strip plate anchor embedded in uniform cohesionless soil was simulated using large deformation finite element (LDFE) analysis (*i.e.*, a RITSS technique). Simulation of the keying process has not been extensively investigated in previous research, especially for cohesionless soil. Irrecoverable loss of embedment predictions accompanied the keying rotation, which led to a considerable reduction in the uplift capacity; these were investigated with various loading eccentricity ratios (e/B), pullout angle θ, and thickness ratio t/B. The anchor shank was not considered in this analysis because it was noticed that the including shank soil resistance increases post pullout capacity by approximately 15% when a shank was not considered.

As demonstrated in this study, the peak pullout capacity did not occur at the end of the anchor keying process. The angle of orientation α at which the maximum pullout capacity occurred increased with an increasing *e/B* ratio, ranging between 70º and 85º (see Figure 5.8). The LDFE results showed that as the loading eccentricity ratio *e/B* increases, the loss in anchor embedment δ_z/B during rotation decreases (see Figure 5.10). Also, once the eccentricity $e \geq B$, a minimal loss in anchor embedment (*i.e.*, the highest pullout capacity) can be achieved regardless of the plate thickness. Decreasing *e/B* from 1.5 to 0.25 caused a decrease in pullout capacity of approximately 20% (see Figure 5.11).

It was also found from Figure 5.20 that the lower the anchor thickness ratio *t/B*, the higher the loss in anchor embedment δ_z/B, especially for small *e/B* ratios. Also, the trajectory of the anchor padeye predictions showed that the amount of backward movement primarily depended upon the pullout loading angle θ and then vanished, and could change to forward movement when the loading angle θ was small (see Figure 5.18). The numerical results from the figures (*i.e.*, *e/B* and pullout angle θ) show that the loading eccentricity *e/B* had a much larger effect on the embedment loss than did the pullout angle.

It was found that the effect of *t/B* on the loss of anchor embedment δ_z/B became more pronounced for smaller values of *e/B* (see Figure 5.20). The keying behavior of the plate anchor was determined to be essentially independent of the soil elastic stiffness *E* for shallowly embedded anchors, while it was influenced by *E* for deeply embedded anchors.

CHAPTER VI

INCLINED PULLOUT OF STRIP PLATE ANCHORS IN SAND

6.1 Introduction

Mooring systems for offshore floating structures often involve inclined load orientations where the plate anchors are not horizontally orientated. To meet the design requirements of many of offshore applications, plate anchors are frequently placed at orientations somewhere between vertical and horizontal. The majority of the previously published experimental, analytical, and numerical studies have been concerned with evaluating the pullout resistance of either horizontal or vertical plate anchors. Very few finite element studies have been performed that estimate the pullout capacities of inclined plate anchors in cohesionless soil. This phase of the research directs attention to the effects of anchor inclination. The influence of parameters such as anchor inclination, dimensions, embedment depth, soil relative density, and anchor roughness on overall plate anchor performance were investigated. Finite element analyses were conducted to introduce simple design charts relating the breakout factor to the embedment depth and relative density for different inclination angles and anchor widths. The finite element predictions were then compared to experimental, analytical, and finite element analyses reported in the literature.

6.2 Problem geometry, boundary conditions, and finite element modeling

The problem geometry considered in the present study is shown in Figure 6.1. Anchor inclination is defined in terms of an angle θ, as shown in Figure 6.1a. Horizontal

and vertical anchors have inclination angles of $\theta = 0^o$ and $\theta = 90^o$, as shown in Figures 6.1b and 6.1c, respectively. The depth of the anchor plate is measured in terms of embedment depth ratios (i.e., H_c/B, H/B), where the normalized depth to the center of the plate H_c/B applies to inclined and vertical plates, and the depth to the base of the plate H/B applies to horizontal plates.

In the present study, the stability and performance of wished-in-place strip plate anchors inclined at $\theta = 0^o$, 22.5^o, 45^o, 67.5^o, and 90^o were investigated. While the assumption of the plate anchor behavior being a strip (i.e., in a plane strain condition) may be unrealistic for many applications, in this case it is essential as a reference in much the same way as strip footing serves as a reference when assessing the bearing capacity of shallow foundations (Yu et al., 2014). All analyses in this chapter were performed with a thickness width ratio of $t/B = 0.1$. The soil material must obey the non-associated flow yielding rule, which very often is observed during the failure of cohesionless soil. The soil domain was discretized into the mesh of a four-node bilinear quadrilateral reduced integration element CPE4R, while the anchor plate was modeled as perfectly rough or smoothly rigid. A typical structured mesh (see Figure 6.2) was created by zoning the problem geometry. However, a denser zone with a minimum element size $h_{min}/B = 1/20$ was between the plate and adjoining sand mass.

Far field boundaries, as shown in Figure 6.2 were chosen to be sufficiently far for the plate to diminish any boundary effects on the ultimate capacity of the plate anchor. The analyses were performed using the Arbitrary Lagrangian-Eulerian (ALE) technique adopted by the Abaqus/Explicit software package. As mentioned in Chapter III, using this

technique in Abaqus/Explicit allows the anchor to experience relatively large displacements while avoiding any numerical divergence issues related to mesh distortion, especially around the corners of the anchor plate where the shear strain localization zones are located. Therefore, for cases where large strains occur, the ALE technique was used to solve any resulting element distortions.

The present study utilizes displacement-based finite element analyses with an applied constant pullout velocity, where the pullout load is centrically applied in a direction perpendicular to the anchor plate face. For all subsequent analyses, the pullout rate of 0.02 m/sec was applied at the reference point of the plate anchor. This rate was slow enough to simulate the pullout process, essentially a quasi-static process in nature, as closely as possible. The collapse load of the plate anchor was taken to be the same criterion as in Chapter IV (*i.e.*, the collapse load at which the anchor displacement reached 25% of the anchor width). As mentioned in Chapter IV, the collapse load at shallow depths occurs well before this displacement magnitude, so pullout capacity estimates derived from the finite element results were not affected by this failure criterion. However, for deeply embedded anchors, large deformations are required to mobilize the ultimate capacity and large deformation finite element analysis (LDFE) must be conducted; thus, the displacement limitation described above governs. Immediate breakaway occurs when there is no suction between the soil and anchor for cohesionless soil. Separation or breakaway of the anchor from the soil occurs when the vertical stresses behind the anchor plate face are reduced to zero.

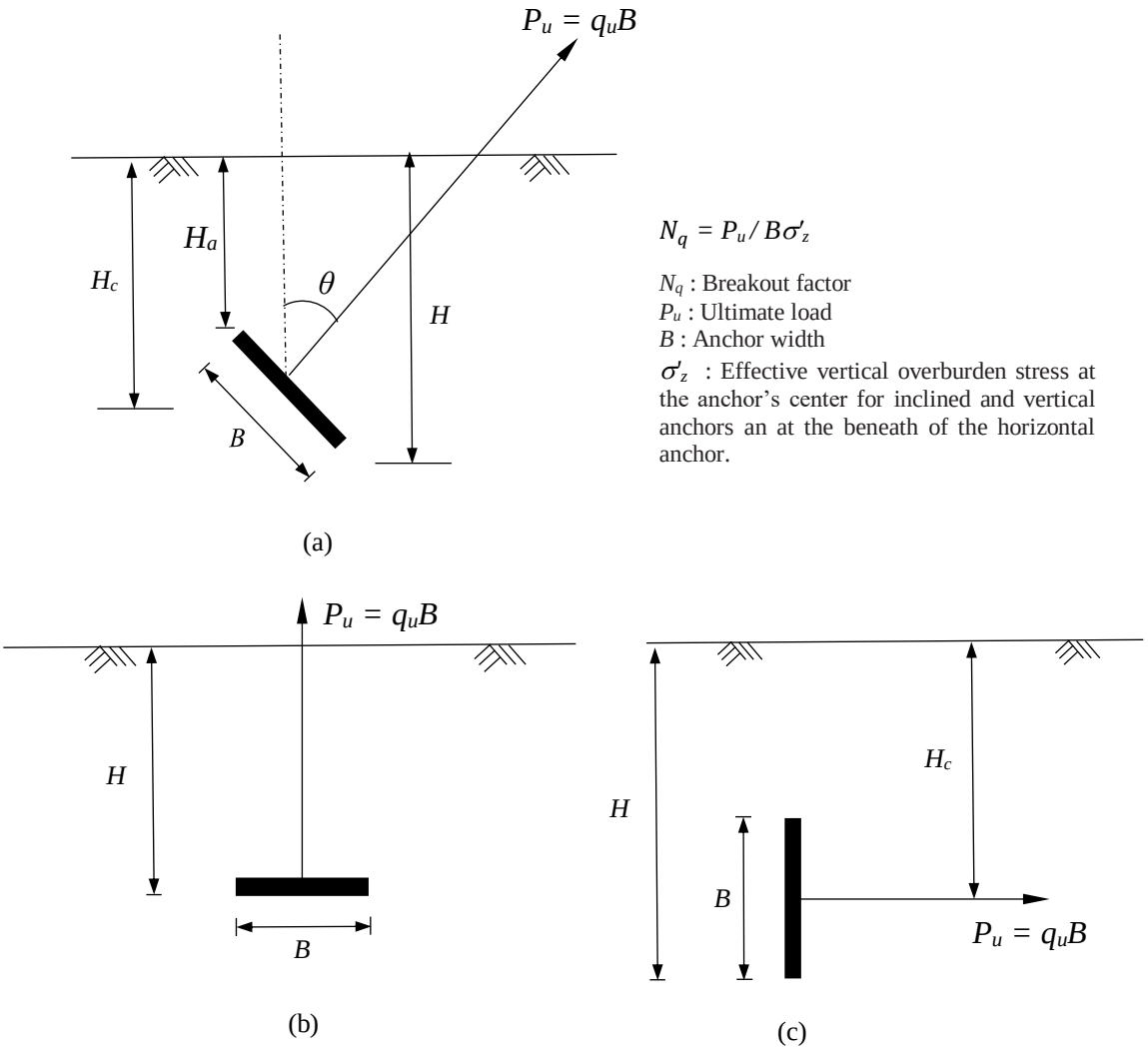

Figure 6.1 Problem analysis for an inclined strip plate anchor.

6.3 Parametric Study

In the present study, LDFE analyses were undertaken to investigate the performance of strip plate anchors embedded in cohesionless soil with various inclination angles ranging from 0º to 90º. The effects of the anchor inclination (in terms of inclination factor F_i), scale effect (*i.e.*, the *B* effect), embedment depth (*i.e.*, *H/B*), relative density of the soil D_r, and anchor roughness were all examined. Theses analyses were performed for

different values of the embedment depth ratio *H/B*, ranging from 1 to in some cases more than 30 anchor widths. The failure mechanism for certain typical cases was also investigated.

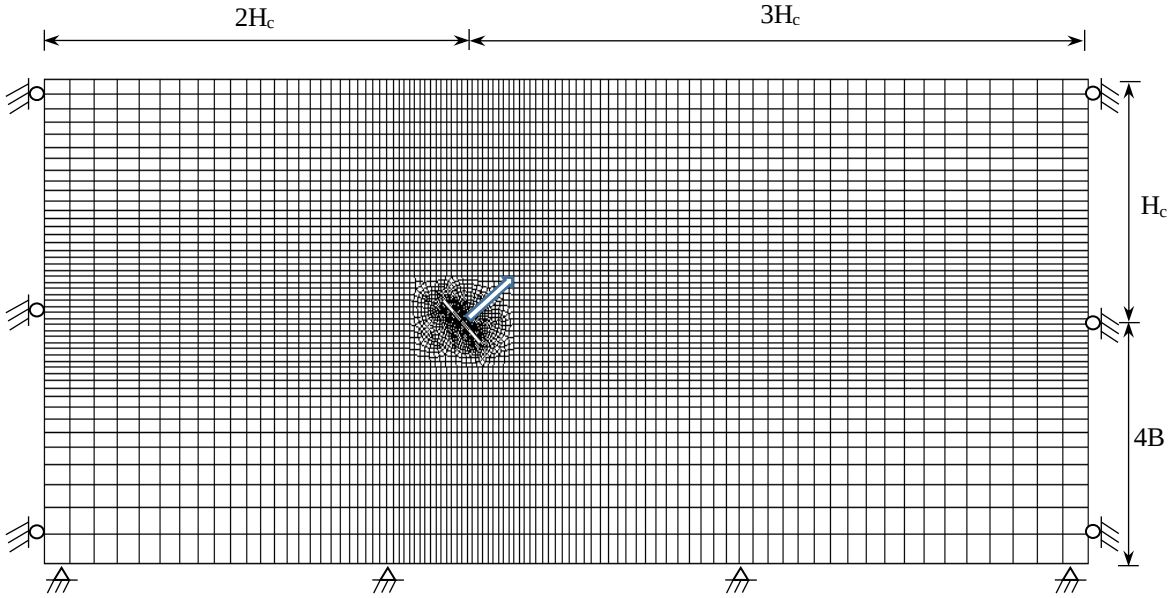

(a) Inclined and vertical anchors

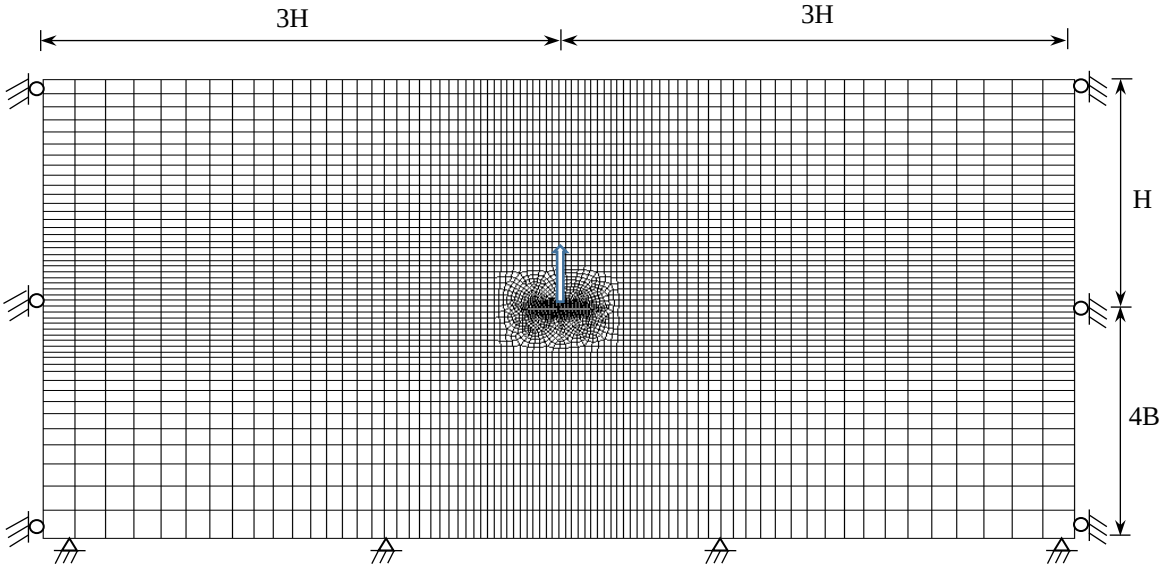

(b) Horizontal anchor

Figure 6.2 Typical finite element mesh and boundary conditions.

6.3.1 Anchor width *B* (scale effect)

This part of the research examined the influence of anchor width *B* on the ultimate capacity of a strip plate anchor, incorporating variations in embedment depth and relative density. To determine the influence of scale effect, analyses were performed for various anchor widths *B* ranging from 0.25 to 3 m and embedment depth ratios varying from 1 to 10. The predictions for a horizontal anchor (*i.e.*, $\theta = 0^o$) embedded in loose sand (i.e., D_r = 30%) showed that an increase in anchor width *B* led to a slight decrease in breakout factor N_q, especially for shallow anchors (as shown in Figure 6.3a). As the *H/B* value increases, the effect of *B* becomes more appreciable for deep anchors. For instance, for *H/B* = 2, an increase *B* from 0.25 to 3 causes a decrease in N_q from 2.17 to 1.95, while for *H/B* = 10, a similar increase in *B* causes a decrease in N_q from 7.19 to 5.1.

However, for horizontal anchors (*i.e.*, $\theta = 0^o$) in dense sand (i.e., D_r = 80%), it is evident from Figure 6.4a that the effect of *B* becomes minimal for all *H/B* ratios considered. For *H/B* = 2, an increase in *B* from 0.25 to 3 causes a decrease in N_q from 2.61 to 2.37, while for *H/B* = 10, a similar increase in *B* causes a decrease in N_q from 8.92 to 8.21. The results also show that the N_q for vertical anchors (*i.e.*, $\theta = 90^o$) in dense sand (see Figure 6.4c) decreases with an increase in *B* at a rate higher than what was observed for loose sand (see Figure 6.3c). However, for vertical anchors, the analyses revealed that the effects of *B* on the N_q values were appreciable for loose and dense sand. For instance, for a vertical anchor with *H/B* = 2 embedded in loose sand, an increase in *B* from 0.25 to 3 causes a decrease in N_q from 7.4 to 6.13, while for *H/B* = 10, a similar increase in *B* causes a decrease in N_q from 11.2.0 to 6.55.

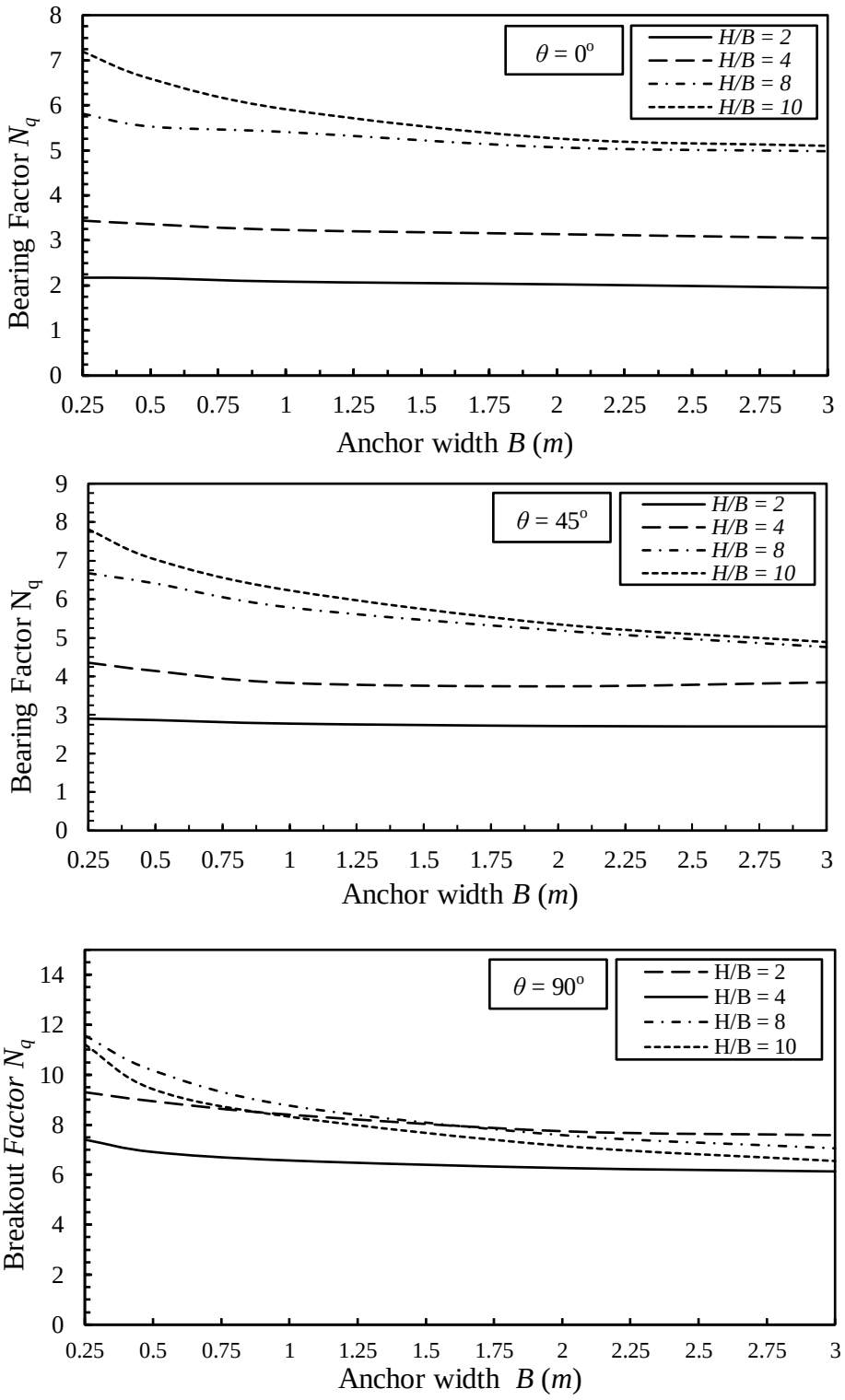

Figure 6.3 Variations of N_q with anchor widths B in loose sand (D_r = 30%) and with different embedment depth ratios H/B for θ = 0º, θ = 45º, and θ = 90º.

Conversely, for a vertical anchor with H/B = 2 in dense sand (D_r = 80%), an increase in B from 0.25 to 3 leads to a decrease in N_q from 19.75 to 13.0, while for H/B = 10, a similar increase in B causes a decrease for N_q from 31.0 to 15.77, which was about a 50% reduction in the N_q value. For an inclined anchor (θ = 45º), as shown in Figures 6.3b and 6.4b, the predictions demonstrated the same trend as for the horizontal and vertical anchors. However, the rate of decrease for N_q with the increase in B for loose sand was higher than what was predicted for inclined anchors (θ = 45º) embedded in dense sand, especially deep anchors. It is also worth noting in Figures 6.5, 6.6, and 6.7 that the effects of anchor width B become more pronounced for anchors embedded in loose and dense sand, especially when the angle of inclination θ is close to the vertical. Also, the effect of scale is more significant for anchors deeply embedded for all inclination angles θ. It can be also observed from these figures as the angle of inclination close the vertical (*i.e.*, θ = 90º), the effect of scale B becomes significant for shallow and deep anchors especially for dense sand as shown in Figure 6.6. For instance, for vertical anchors embedded in loose sand (Figure 6.6a) with H/B = 2, an increase B from 0.25 to 3 causes an approximately 20% reduction in N_q, a similar increase in B at H/B = 10 causes a decrease in N_q about 45%. In view of the above observations, one may conclude that it is definitely important to take the contribution of the scale effect into consideration when designing plate anchors.

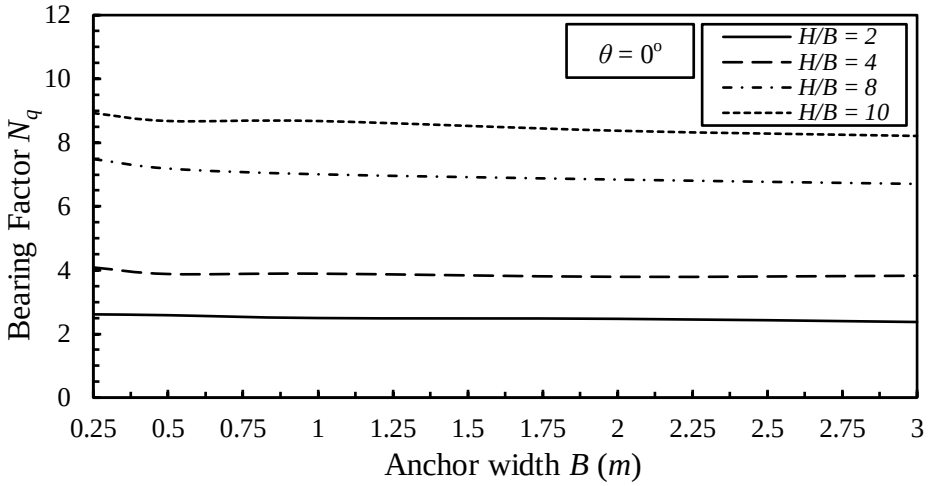

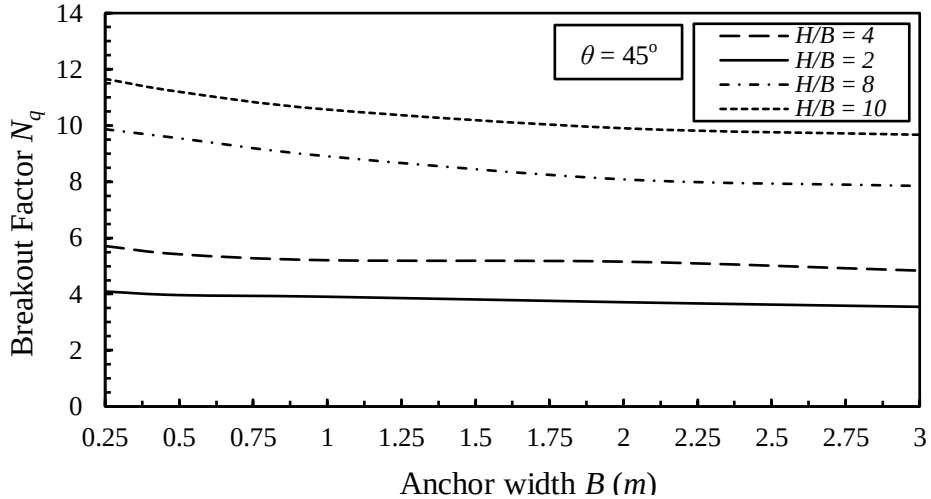

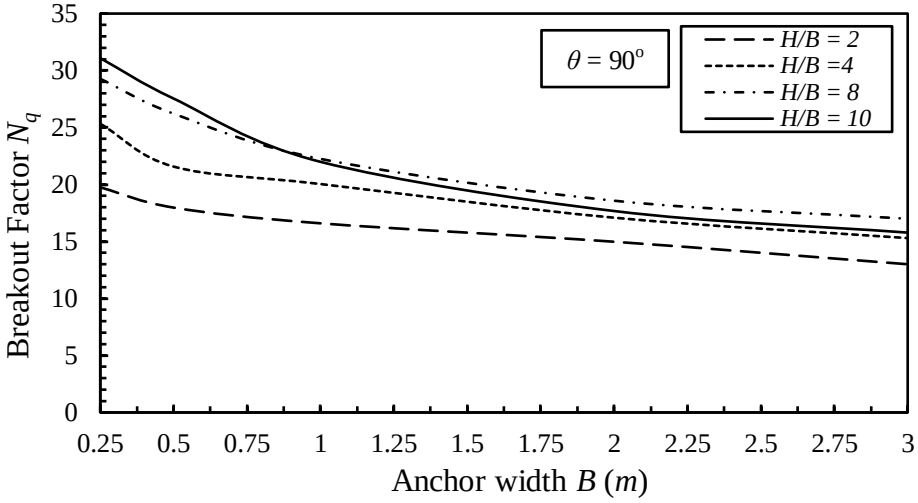

Figure 6.4 Variations in N_q with anchor width B in dense sand (D_r = 80%) for different embedment depth ratios H/B for $\theta = 0^o$, $\theta = 45^o$, and $\theta = 90^o$).

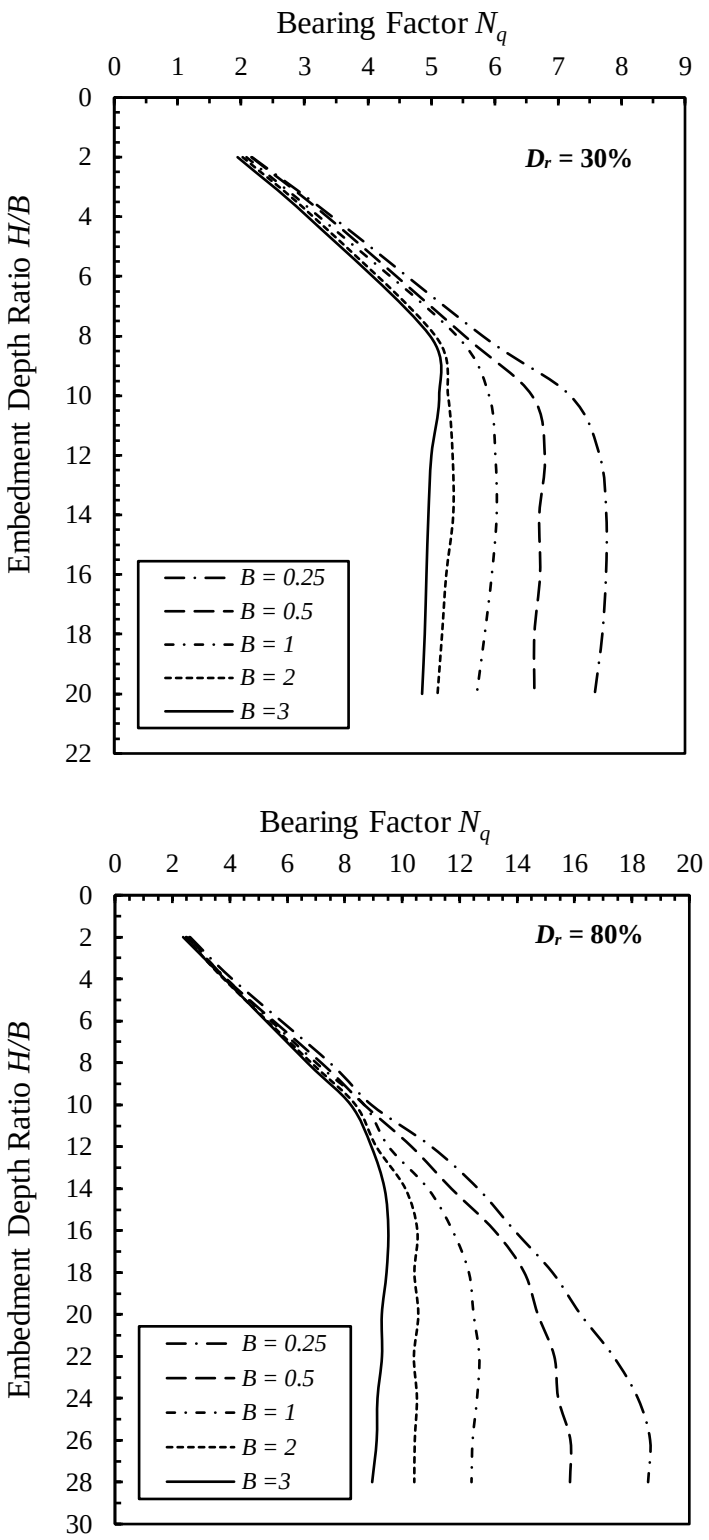

Figure 6.5 Variations of N_q with embedment depth ratios H/B for horizontal anchors ($\theta = 0^o$) with different anchor widths B in loose and dense sand.

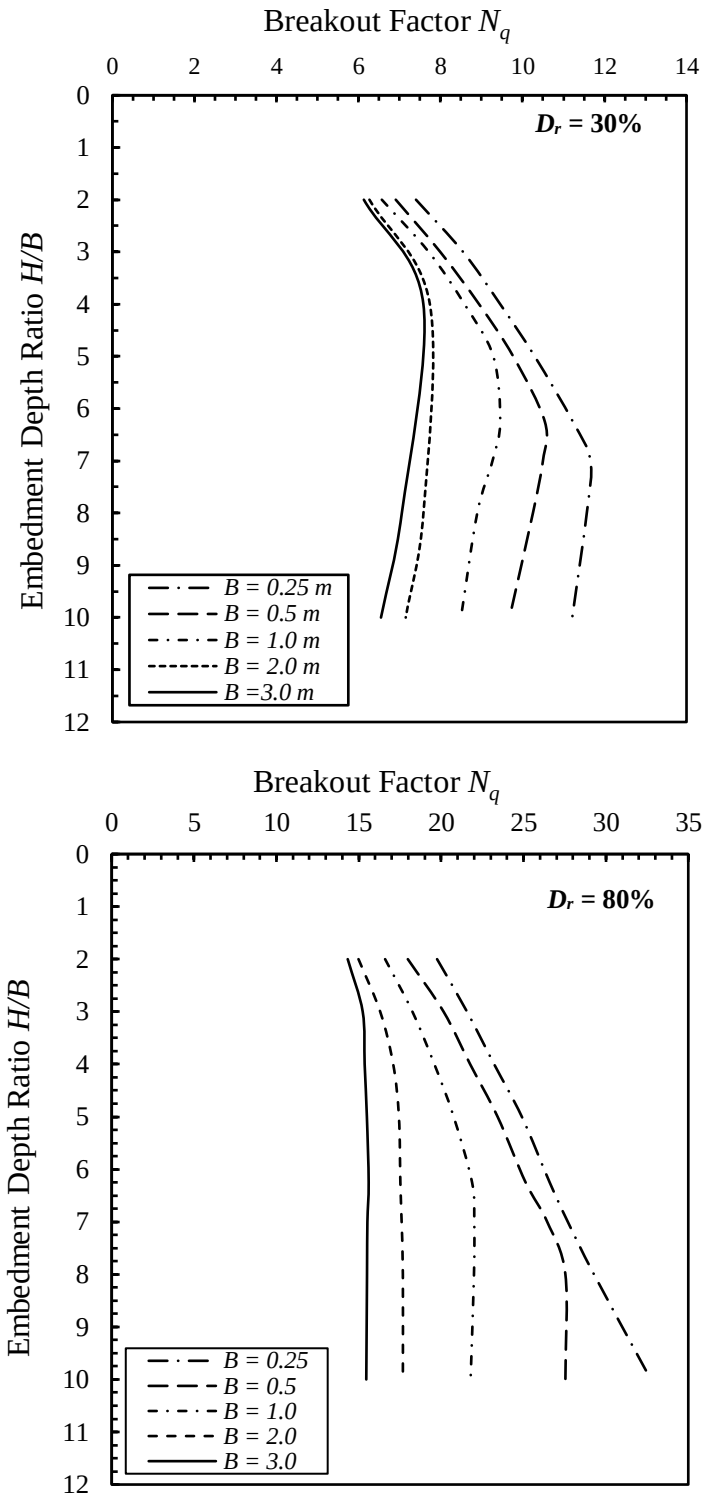

Figure 6.6 Variations of N_q with embedment depth ratios *H/B* for vertical anchors (θ = 90º) with different anchor widths *B* in loose and dense sand.

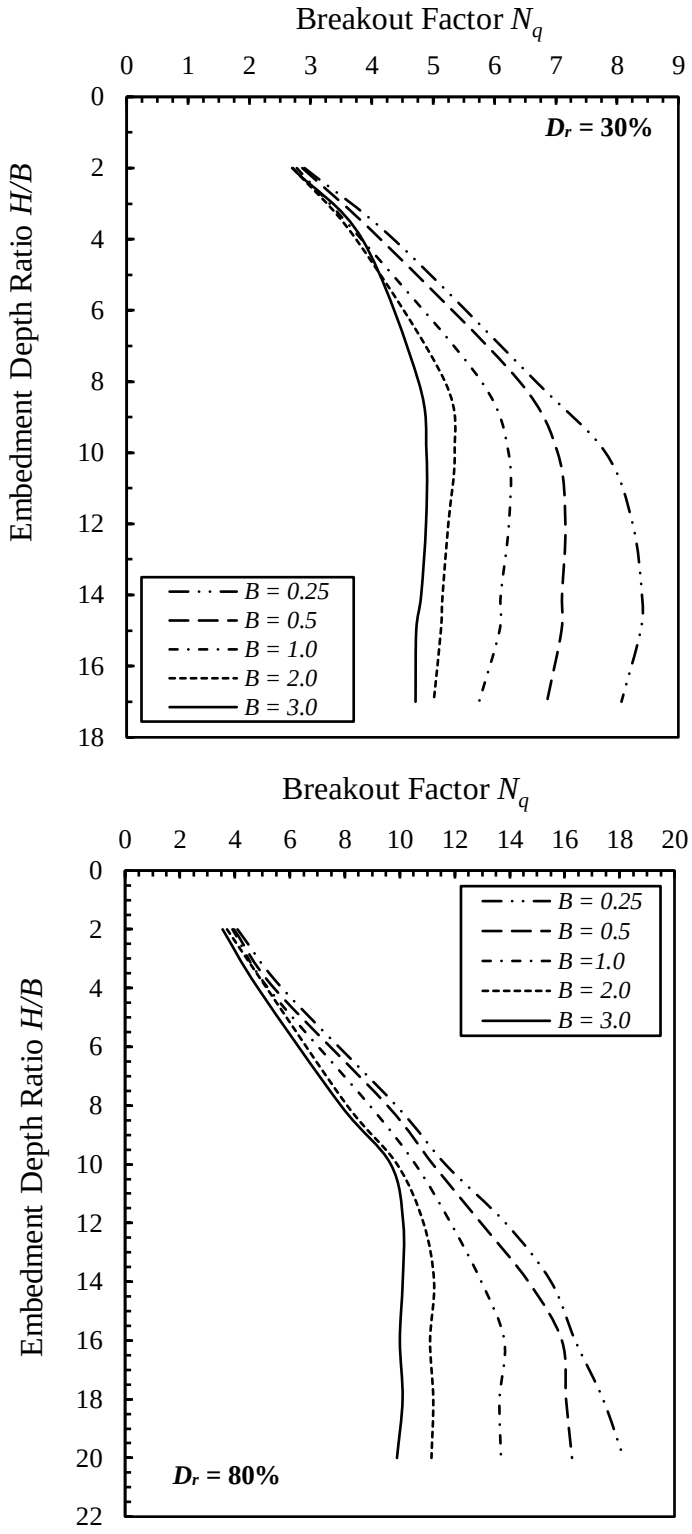

Figure 6.7 Variations of N_q with embedment depth ratios H/B for inclined anchors (θ = 45º) with different anchor widths B in loose and dense sand.

6.3.2 Inclination factor F_i

Among the previous investigations pertaining to strip plate anchors in cohesionless soil, relatively few have examined the effects of anchor inclination. As mentioned above, most reported studies evaluated the breakout capacity of either horizontal or vertical plate anchors. However, these studies revealed that for a given embedment depth, the pullout capacity of a plate anchor changes from the minimum for horizontal to the maximum for vertical plate anchors. The pullout capacity for an inclined plate anchor for any inclination angle θ can be expressed in terms of the dimensionless breakout factor, defined as:

$$N_{q\theta} = P_u / B\sigma'_z \tag{6.1}$$

where P_u is the ultimate load (i.e., force) capacity, B is the anchor width, and σ'_z is the effective vertical overburden stress at the anchor's center. To investigate the effects of inclination, a correction inclination factor was introduced in this study, as:

$$F_i = \frac{N_{q\theta}}{Nq_{90}} \tag{6.2}$$

where F_i = the inclination factor, $N_{q\theta}$ is the breakout factor for an inclined anchor at a given embedment depth ratio, and N_{q90} is the breakout factor for a vertical anchor at the same embedment depth ratio.

The effects of the plate anchor inclination angle on the anchor breakout factor are presented in Figures 6.8, 6.9, 6.10, and 6.11 for loose and dense sand (i.e., relative densities D_r = 30% and 80%) for different anchor widths B. It is evident from these figures that the minimum value of N_q corresponds to the horizontal plate anchor (i.e., $\theta = 0^o$), while the maximum N_q occurs when the plate is vertical ($\theta = 90^o$); the N_q value for any

inclined anchor is intermediate between the maximum and minimum values of N_q. The predictions shown in these figures indicate that the inclination factor F_i increased in a nonlinear manner with an increasing inclination angle θ from 0 to 90º for loose and dense sand. It should be noted from Figures 6.8 and 6.9 that the effects of B on N_q become more pronounced in loose and dense sand with greater values of θ, particularly when the plate anchor becomes vertical. For relatively deep anchors (i.e., H/B = 10) embedded in loose sand, the effects of B on N_q were evident for all values of θ, as shown in Figure 6.9a.

Figures 6.10 and 6.11 indicate that there was a very slight difference between the breakout factor for horizontal (θ = 0º) and inclined anchors when $\theta \leq 30º$. A greater rate of increase in the inclination factor appeared when $30º \leq \theta \leq 60º$. The greatest rate of increase in anchor capacity began approximately at $\theta > 45º$ for loose sand (*i.e.*, D_r = 30%) and at $\theta > 60º$ for dense sand (*i.e.*, D_r = 80%). For a given embedment depth (H_c/B) and relative density D_r, and with an adequate level of accuracy for design purposes, a simple relationship is proposed in this research to estimate the breakout factor of an inclined anchor at any inclination angle θ between 0º and 90º.

$$N_{q\theta} = Nq_0 + [Nq_{90} - Nq_0]\left[\frac{\theta}{90}\right]^3 \qquad (6.3)$$

where N_{q0} and N_{q90} are the breakout factors for the horizontal and vertical anchors, respectively. The general form of Equation 6.3 is approximately similar to the empirical equation proposed by Das and Puri (1989), based on their laboratory investigations estimating the pullout capacity of inclined square anchors in clay. Superposition of

Equations 6.3 on to the finite element predictions in Figure 6.9b shows very good agreement

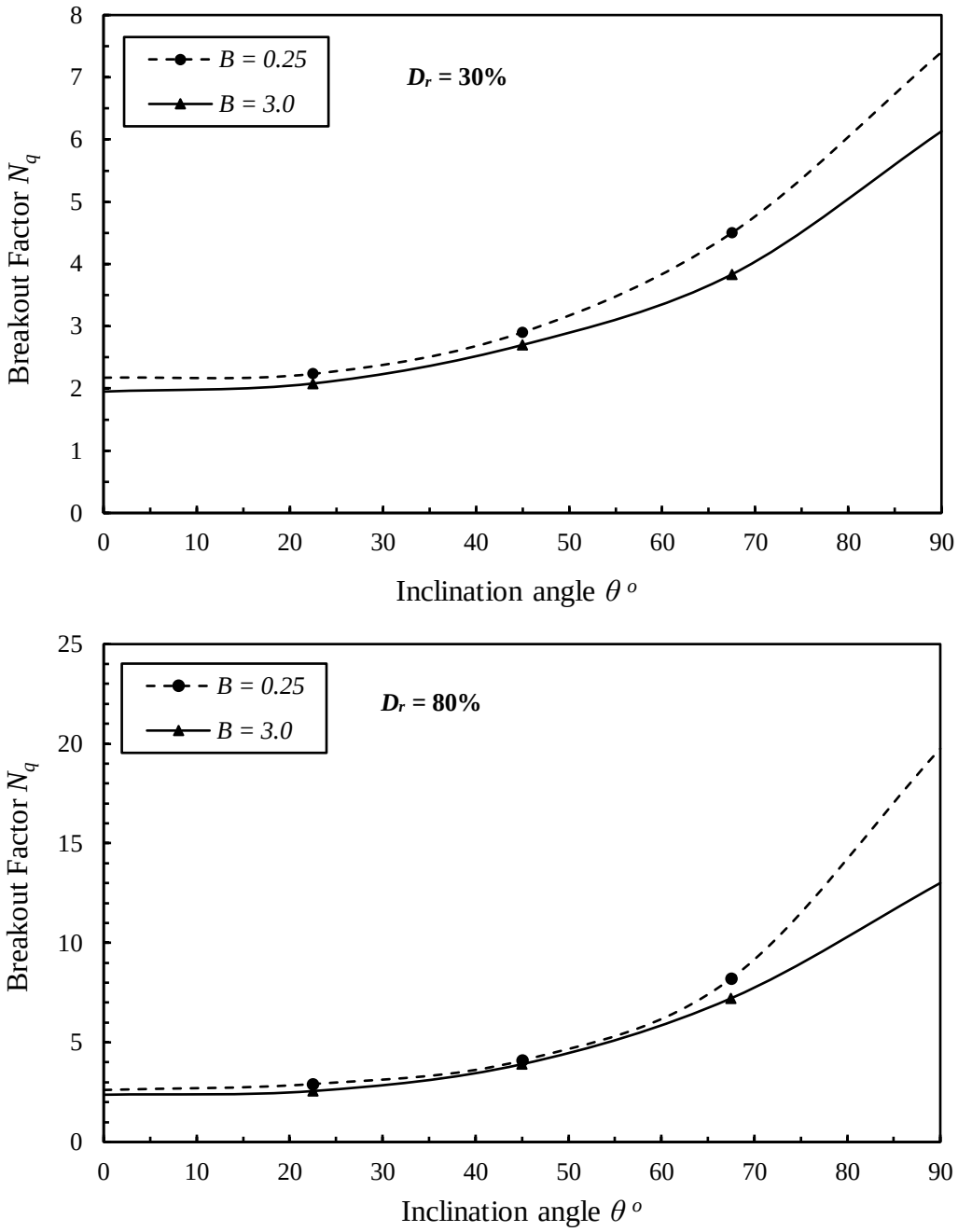

Figure 6.8 Variations of N_q with inclination angle θ for shallow anchors (H/B = 2) in loose and dense sand where B = 0.25 and 3.0.

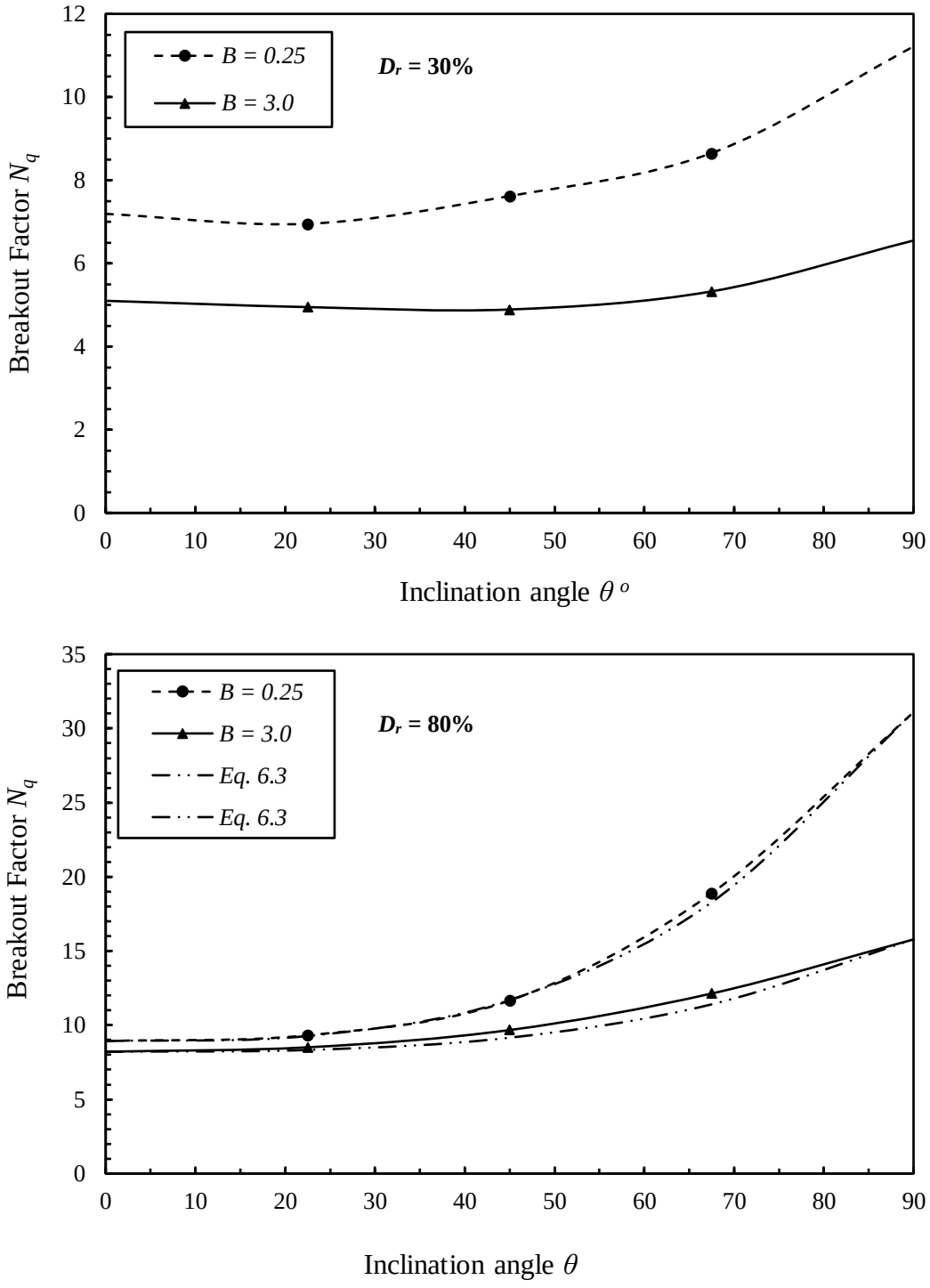

Figure 6.9 Variations of N_q with inclination angle θ for deep anchors (H/B = 10) in loose and dense sand where B = 0.25 and 3.0.

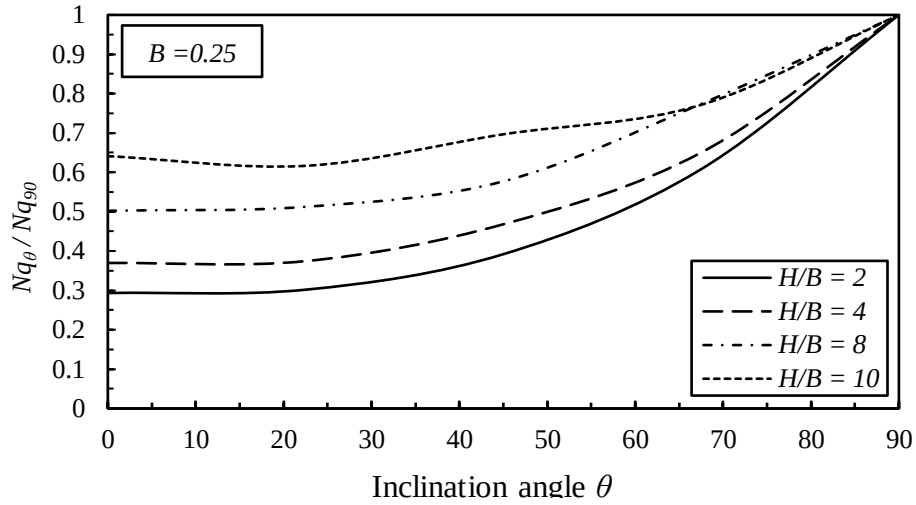

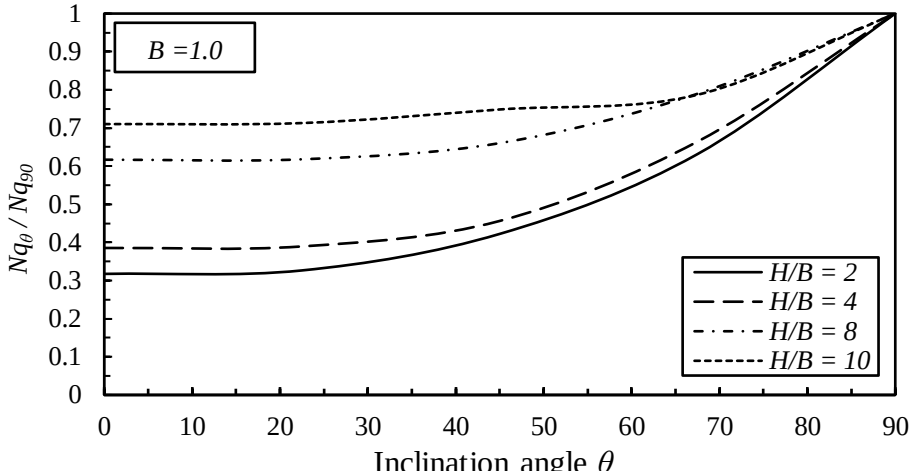

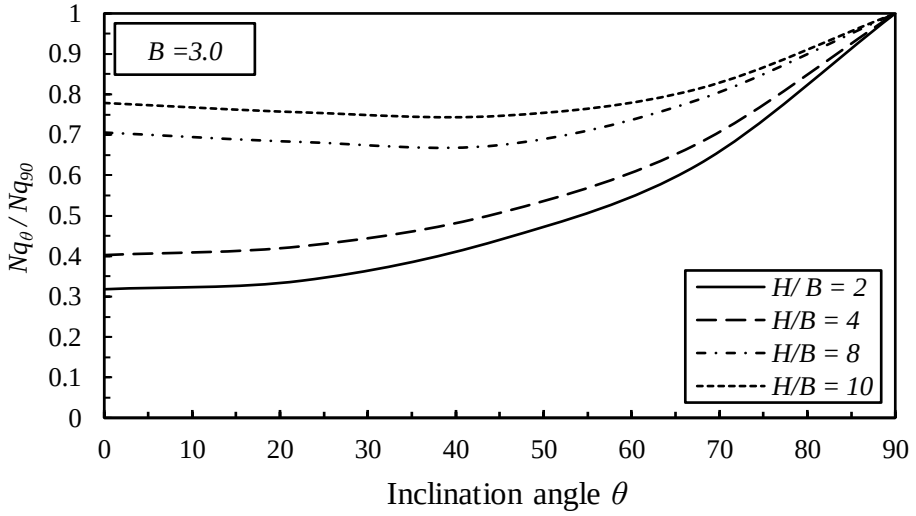

Figure 6.10 Inclination factors for plate anchors embedded in loose sand (*Dr* = 30%) for different embedment depth ratios *H/B* and different *B* values.

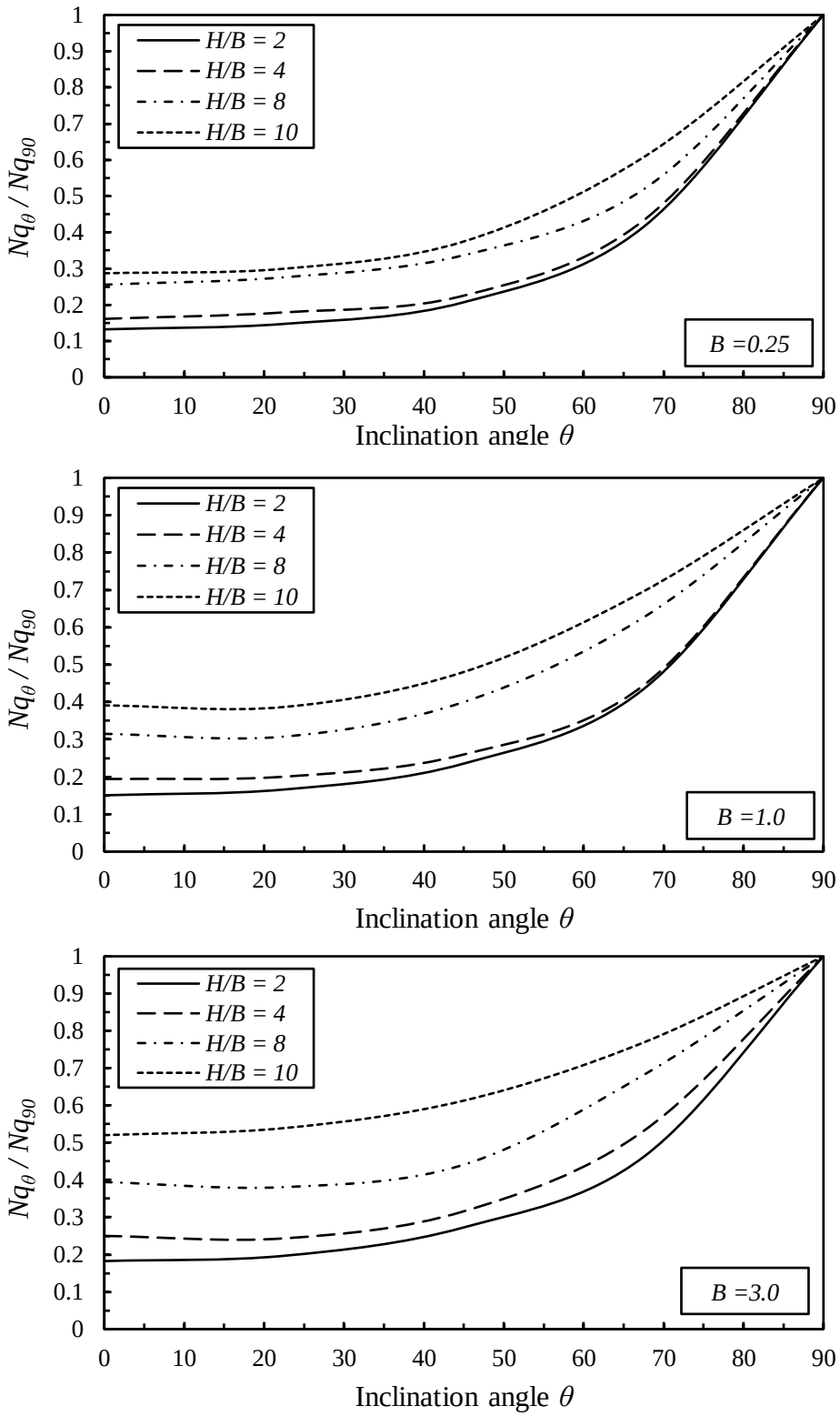

Figure 6.11 Inclination factors for plate anchors embedded in dense sand (D_r = 80%) for different embedment depth ratios *H/B* and different *B* values.

6.3.3 Roughness

The soil anchor interface was modeled using the Abaqus/Explicit contact surface approach. The tangential (*i.e.*, frictional) interface between the outer surface of the anchor and the soil was simulated using the Coulomb friction coefficient $\mu = tan\ \delta$ where δ is the soil anchor interface friction angle. As mentioned in Chapter III, δ values depend on the interface characteristics and relative movement between the anchor and soil; however, they generally lie between 50% and 100% of the peak friction angle ϕ'_p (Roy et al., 2015). The value δ = 0% of the peak friction angle ϕ'_p was adopted in the present study for perfectly smooth anchors, while δ = 100% was applied to perfectly rough anchors. To investigate the influence of roughness on an anchor's ultimate capacity, cases of perfectly smooth and perfectly rough anchors with various θ values were examined.

The finite element analyses confirmed the significance of the roughness of the soil anchor interface when estimating the pullout resistance of vertical anchors (i.e., $\theta = 90^o$), especially for shallow embedment depths ranging from 1 to 4 as shown in Figure (6.12). For instance, changing from perfectly smooth to perfectly rough anchors and $H_c/B = 2$ can cause the anchor pullout resistance to increase by as much as 40%, as compared to an increase of about 5% for $H_c/B = 8$. The increase in ultimate capacity due to the interface roughness is attributable to soil movement when the anchor's passive side is upwards at an angle to soil anchor interface friction angle δ (Merifield and Sloan, 2006). This upward movement develops significant shear stresses at the soil anchor interface, which increases the anchor's ultimate capacity. Figure 6.12 shows the variations in breakout factor N_q for smooth and rough anchors, which demonstrated less sensitivity to soil roughness for

inclined anchors with $\theta \leq 45^{o}$. For example, a roughness interface for $H_c/B = 2$ for $\theta = 45^{o}$ can cause an increase in the anchor's pullout resistance of as much as 18%. However, the ultimate capacity of a horizontal anchor is approximately independent of the roughness interface for all embedment depths, as shown in Figure 6.12a.

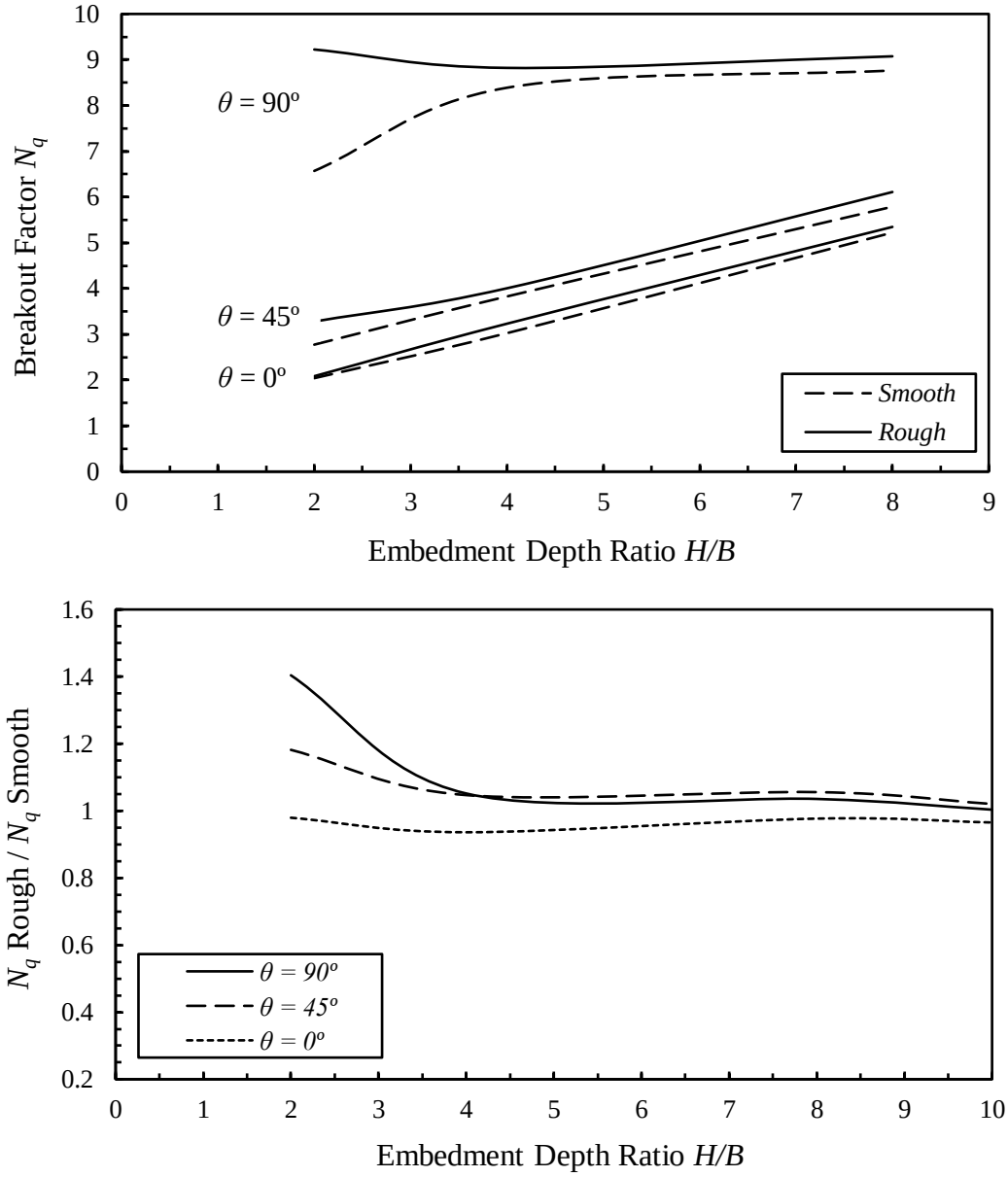

Figure 6.12 Effects of the anchor roughness interface for different inclination angles.

6.3.4 Correlation to relative density

Since estimation of relative density D_r and effective stress level is practiced by a conventional site investigation, it is more practical to utilize a framework for predicting pullout anchor resistance in sand in terms of the relative density D_r and effective stress level. Bolton (1986) introduced a relative dilatancy index I_{RD} in terms of relative density D_r and effective stress level, as follows:

$$I_{RD} = D_r\left(Q - \ln p'\right) - R = I_{RD}\ln\left(\frac{\sigma_c'}{p'}\right) - 1 \tag{6.4}$$

The values $Q = 10$ and $R = 1$ were recommended by Bolton (1986) from test results for 17 sands. As mentioned in Chapter IV, the following plane strain correlation proposed by Bolton (1986) was found to be applicable to the range $0 < I_{RD} < 4$. Eq. 6.5 links the dilation angle to the relative density D_r and confining stress σ_c', which is sufficient to eliminate dilation relating to the mean effective stress p' at failure.

$$\phi_p' - \phi_{cv}' = k\psi_{\max} = AI_{RD} \tag{6.5}$$

According to Bolton (1986), the parameters k and A are 0.8 and 5, respectively, under plane strain conditions, which is appropriate for problems related to strip plate anchor pullout capacity. A single representative dilation angle ψ and mean effective stress at failure p' was assumed in the present research. Assuming a single dilatancy angle mobilized at all points in the yielded soil surrounding the anchor was not conservative. The selection of p' as the effective overburden pressure was taken at the bottom face of the horizontal plate anchor and center of the plate anchor for the inclined and vertical anchors. This selection of p' instead of the mid-depth between the ground soil surface and

the anchor allowed for an increase in mean stress within the shearing zone during uplift, which lead to less dilatancy than would be implied by using the initial stress condition (White et al., 2008). Bolton (1986) proposed a constant value for *A* and *Q*. Xiao et al. (2014) formulated an empirical equation to show that *Q* is a function of confining pressure. Also, Xiao et al. (2014) proposed an empirical equation that shows the variations in *A* with the fine contents of sand. These researchers found that in triaxial tests, *A* ranged between 3.0 and 5.53 for Ottawa sand with 0% to 20% fine content. The parameters *Q* and ϕ'_{cv} exhibited minimal variations among cohesionless soils; therefore, these parameters were not needed as further variables when preparing the design charts (White et al., 2008).

In the present study, constant values of $Q = 10$ and $A = 5$ for plane strain condition were used. Although the value of ϕ'_{cv} might slightly increase with a decreasing p' (Lings and Dietz, 2004), $\phi'_{cv} = 33$ was employed here, based on data presented by Randolph et al. (2004). From Eqs. 6.4 and 6.5, one can calculate the peak angle of shearing resistance ϕ'_p and peak dilatancy angle ψ_{max}, which are required in the finite element calculations, combined with the assumed value of the mean effective stress at failure p'. It was reasonable to develop the design charts for predicting the anchor capacity for different values of relative density. According to Janbu (1963**)** and Harden and Black 1966), elastic stiffness soil *E* varies with p', based on the following power function:

$$E = mp_a \left(\frac{p'}{p_a} \right)^n \tag{6.6}$$

where p_a is the atmospheric pressure (i.e., 101 *kPa*), and *m* and *n* were developed in this study as a function of the relative density, as in Eqs. 6.7 and 6.8, respectively.

$$m = 223.6D_r^2 + 136.7D_r + 106.1 \quad (6.7)$$

$$n = 0.74 - 0.2D_r \quad (6.8)$$

The range of submerged unit weights in seabed sands is relatively modest; therefore, density has not been considered a contributing factor in predicting anchor capacity, except when considering dry versus submerged soil profiles. The present study considers a sand profile with a submerged unit weight of γ' = 8 kN/m^3. Other soil properties for all cases included cohesion c = 0.05 *kPa*, Poisson's ratio μ = 0.3, and an at-rest lateral earth pressure coefficient of K_o = 0.5.

Figures 6.13., 6.14, and 6.15 show the effects of relative density D_r on the ultimate capacity of horizontal and vertical strip plate anchors for different anchor widths *B* (i.e., 0.5, 1.0, and 3.0). The results showed that the effects of relative density were more significant for vertical anchor orientation, especially with deeply embedded anchors. For instance, for the vertical anchor with B = 0.5, N_q increased by a factor of around 4 over a range of D_r from 20% to 80% for shallowly embedded anchors with H/D = 2, while N_q increased by a factor of about 6 for the same range of relative densities for deeply embedded anchors (i.e., H/B = 10). However, for B = 3m, N_q increased by the same factor, about 2.5 for H/B = 2 and H/B = 10. Conversely, for horizontal anchors, N_q increased by a factor ranging between 0.15 and 0.2 for different *B* values over a range of D_r from 20% to 80% for H/B = 2, while for H/B = 10, N_q increased by a factor ranging between 1.4 to 1.7 for different *B* values over a range of D_r from 20% to 80%. Also, Figures 6.5, 6.6, 6.7,

and 6.16 show that the transition depth for vertical anchors occurred in shallower depths than those of horizontal anchors, for all D_r and B values. The results in these figures show a noticeable decline in breakout factors after transition depths for different D_r values. This behavior was anticipated because the increase in mean confining stress p' within the failure zone during uplift as H/B increases led to a decrease in the values of friction angle ϕ' and dilatancy angle ψ.

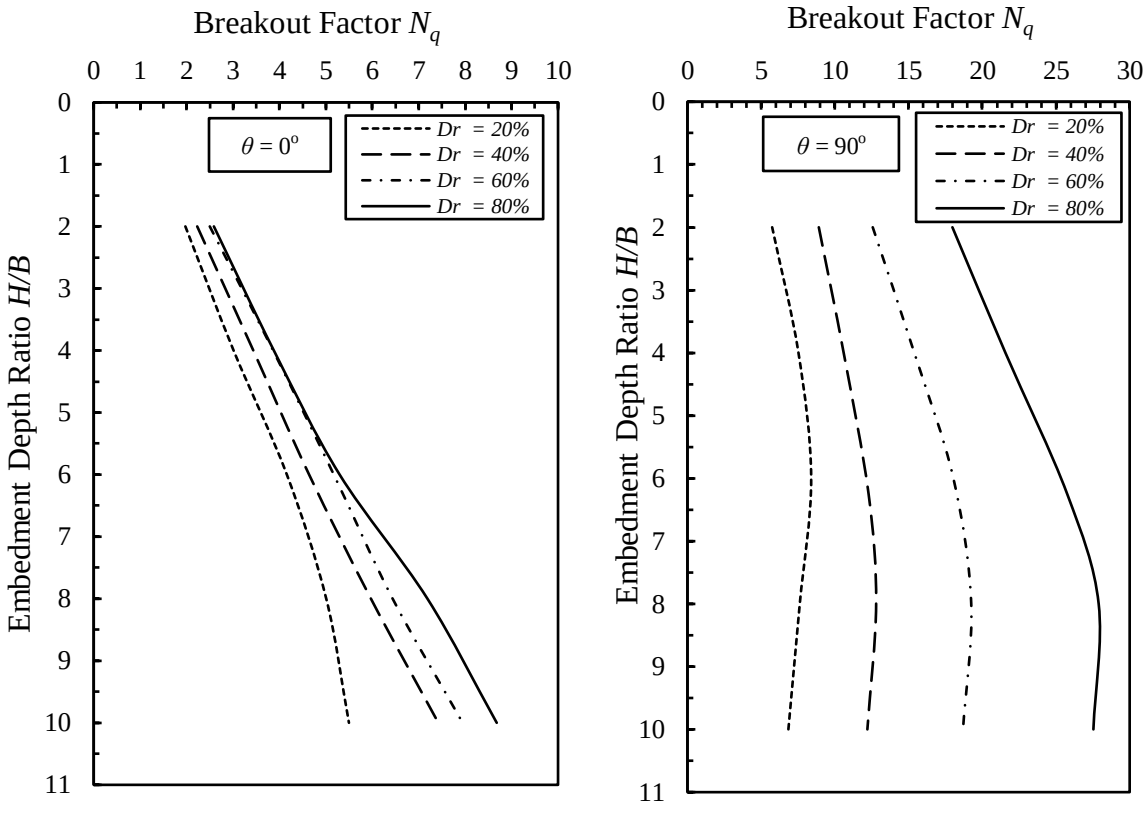

Figure 6.13 Effects of relative density D_r on the pullout capacities of horizontal and vertical strip plate anchors ($\theta = 0^o$ and $\theta = 90^o$) when $B = 0.5$.

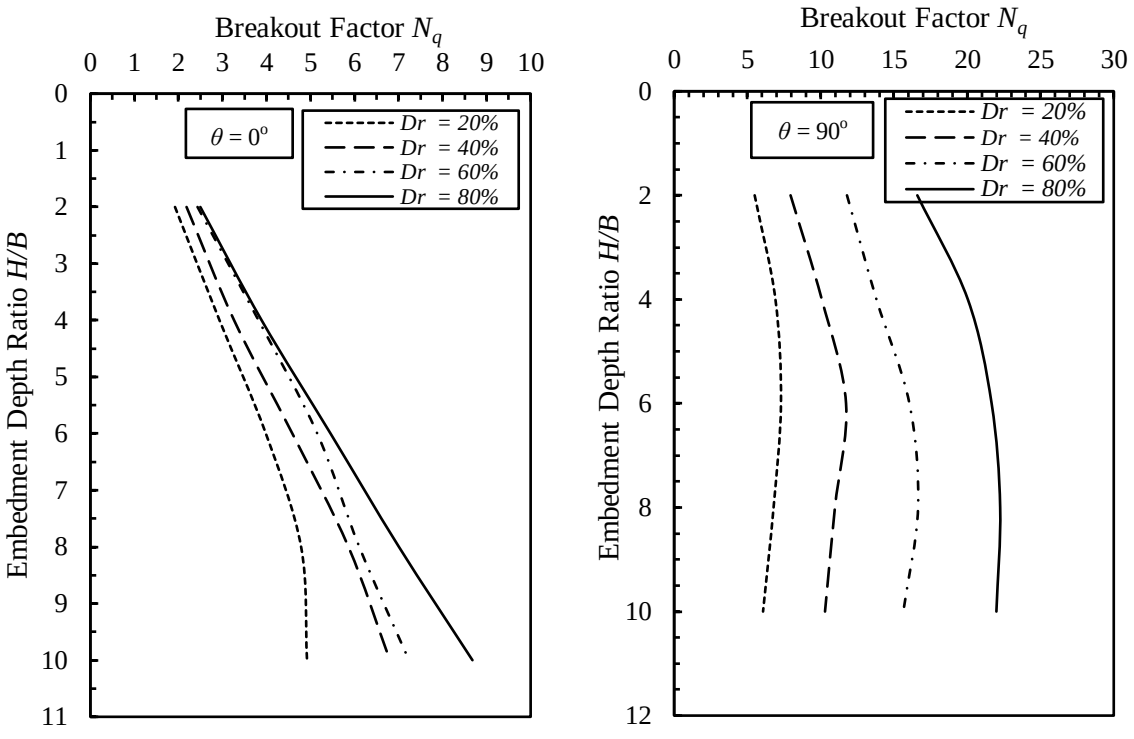

Figure 6.14 Effects of relative density D_r on the pullout capacities of horizontal and vertical strip plate anchors ($\theta = 0^o$ and $\theta = 90^o$) when $B = 1.0$.

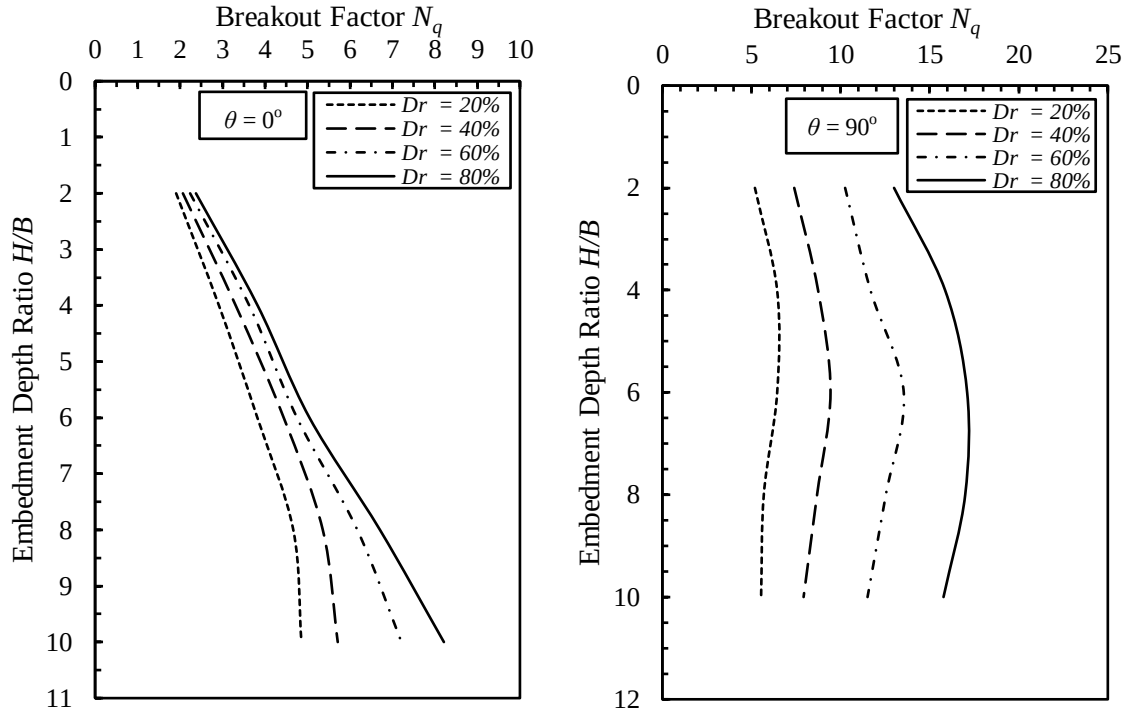

Figure 6.15 Effects of relative density D_r on the pullout capacities of horizontal and vertical strip plate anchors ($\theta = 0^o$ and $\theta = 90^o$) when $B = 3.0$.

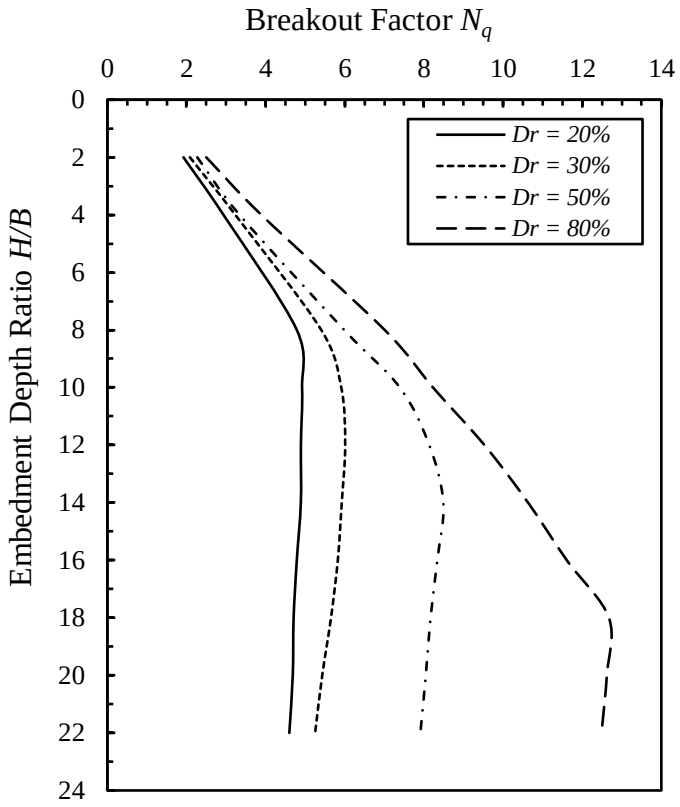

Figure 6.16 Anchor capacity versus depth for a 1 m strip plate width.

6.4 Failure Mechanism

The failure mechanism is explained in this section by the formation of a slip surface showing contours of total displacement as a failure state is approached. Since the first part of this research (see Chapter IV) covered in detail the mode of failure for the horizontal orientation of circular plate anchors, this section presents only the failure mechanism of inclined and vertical plate anchors for shallow and deep embedment depths. Depending on the embedment depth and relative density, the following failure mechanisms can be noticed.

6.4.1 Shallow anchors

The failure mechanism for shallow strip plate anchors where free surface effects are dominant, with different inclination angles θ and relative densities D_r, are illustrated in Figures 6.17 and Figure 6.18. It can be noticed from Figure 6.17 that for a given relative density, inclination angle, and *H/B* (*e.g.*, D_r = 40%, θ = 90º, *B* = 1.0 m, and *H/B* = 2), the failure slip surface for the shallow anchor extends to the ground surface, presenting general shear failure. This failure consists of a rigid movement of soil immediately over the anchor, accompanied by lateral movement extending out of the anchor's edge in the pullout direction. The lateral extent of the passive failure zone (*i.e.*, the right side) increases with the increasing inclination angle, as shown in Figure 6.17. However, soil surface settlement occurs behind the anchor (*i.e.*, the active side), while heave occurs in the front (*i.e.*, the passive side). As the angle of inclination exceeds 45^o towards the vertical (*i.e.*, θ = 90º), the failure zone for the shallow anchor was characterized by the active failure zone immediately behind the anchor for both loose and dense sand.

The slip surface (*i.e.*, the shear band) for the passive failure side extends to the right side as the relative density increases from 20% to 80%, as shown in Figure 6.18, for θ = 90º. This means that the size of zone of the passive failure in front of the anchor increases with an increase in the relative density. It can also be noted from Figure 6.18 that the active failure zone behind the anchor was significant for low relative densities (*i.e.*, loose sand), and the zone decreases as the relative density increases. This is consistent with what Merifield and Sloan, 2006 found; active failure behind the anchor was

significant only when both the embedment ratio and friction angle were low (roughly when $H/B \leq 2$ and $\phi \leq 20$).

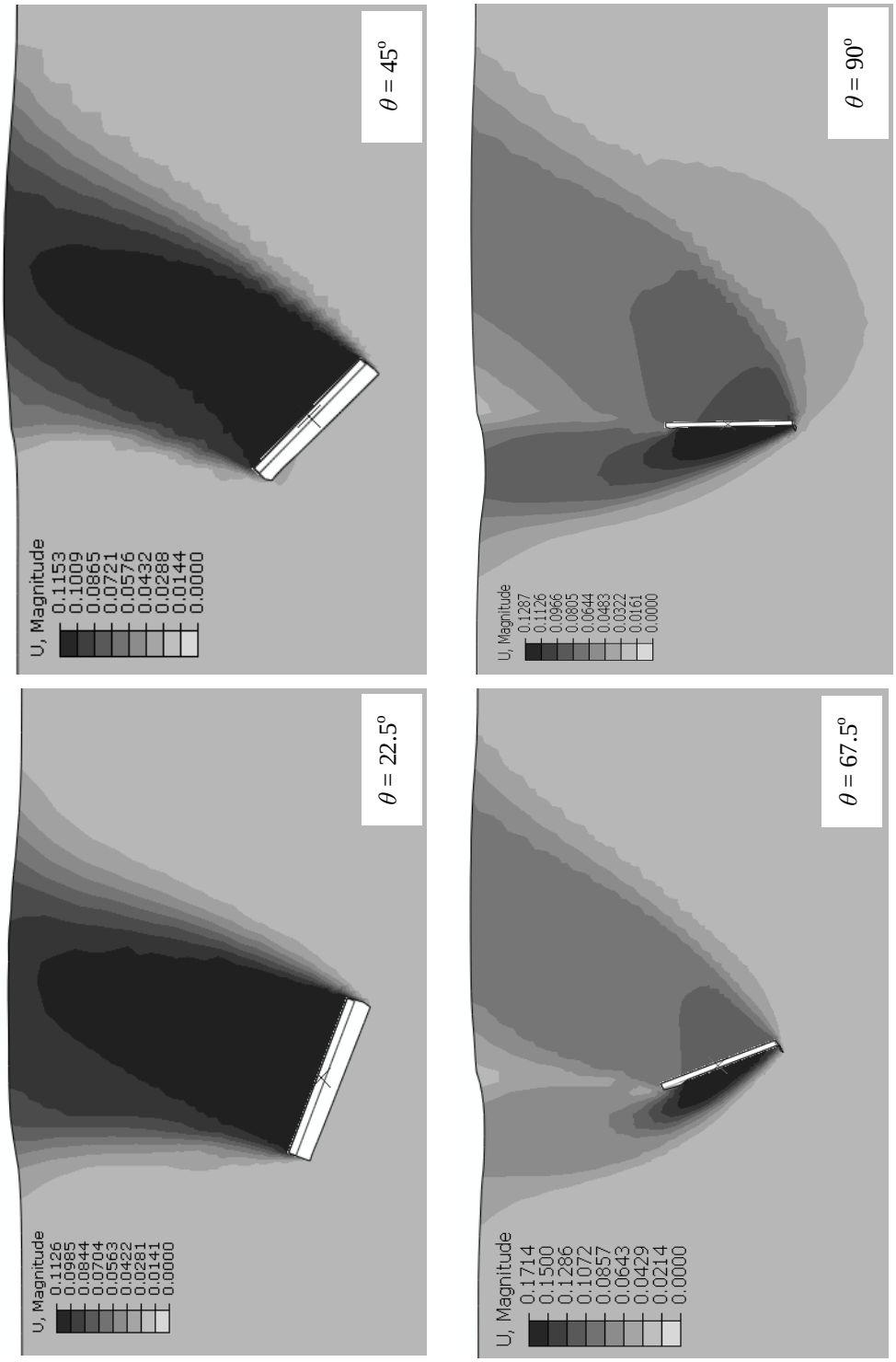

Figure 6.17 Typical failure mode of a shallowly embedded inclined anchor (H/B = 2, D_r = 40%) for different inclination angles.

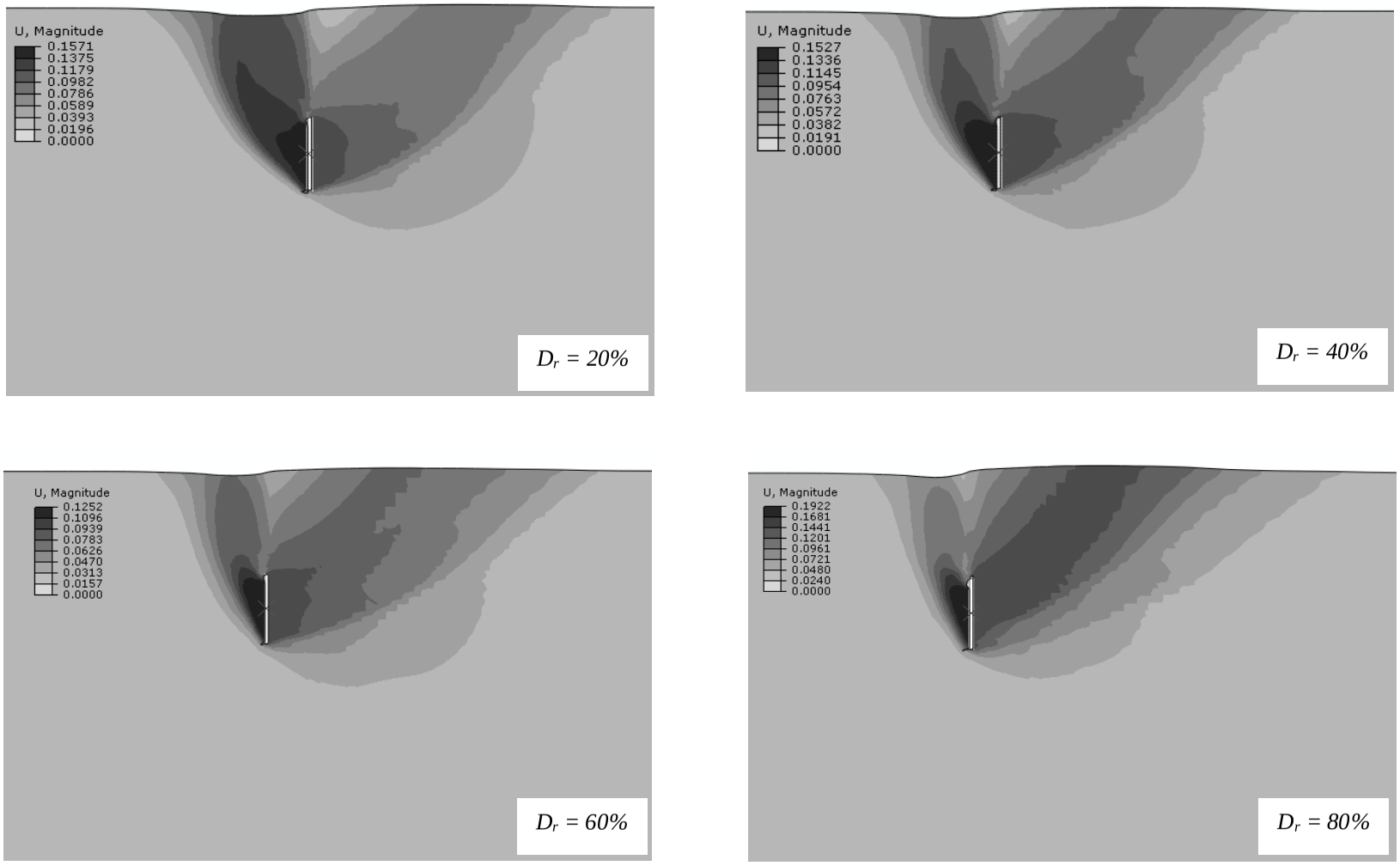

Figure 6.18 Effects of relative density on the extension of slip surfaces on the passive and active sides.

6.4.2 Intermediate anchors

For intermediate embedment depths (*e.g.*, *H/B* = 8, see Figures 6.19a and 6.19b), the development of a shallow versus deep failure mechanism depends on the relative density D_r. For instance, it can be noted that a localized failure mechanism develops in the loose sand (D_r = 30%) for inclined anchors where θ = 45º, while the influence of the free surface on the displacement pattern is still evident in dense sand (*i.e*, D_r = 80%), as shown in Figure 6.19b. It should also be noted that the plastic zone for anchors embedded in dense sand initially developed similarly to that of shallower anchors in both loose and dense sands. While the plastic zone for an anchor in loose sand is confined to the immediate vicinity of anchor, this zone extends to a height approximately three times greater than the diameter of the anchor in the pullout direction, as shown in Figure 6.19a. For relatively deep embedment depths, the effects of an active failure zone appeared to diminish, and only the passive failure zone of the soil ahead of the anchor is of a primary significance, as shown in Figure 6.19b.

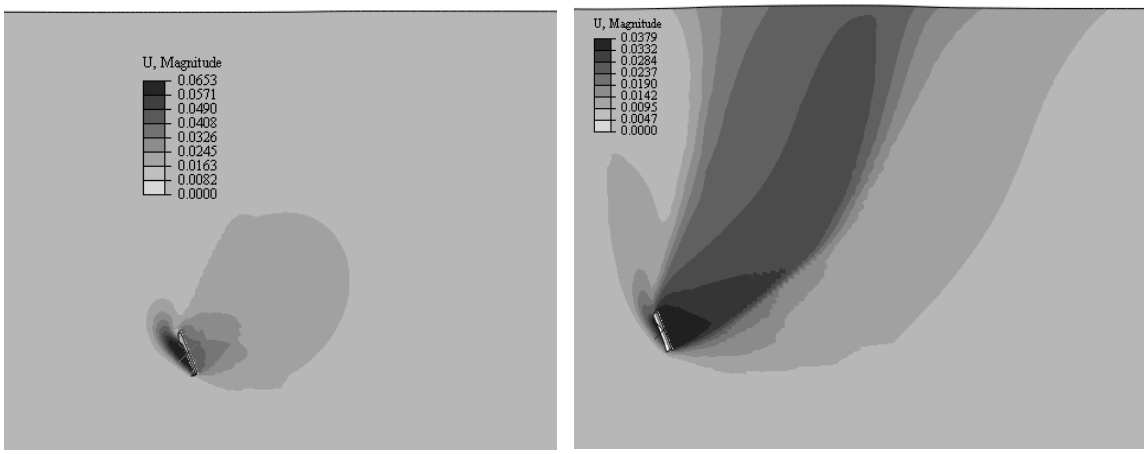

(a) Loose Sand (b) Dense Sand

Figure 6.19 Contours of the resultant displacement in loose and dense sands for intermediate anchors *H/D* = 12.

6.4.3 Deep anchors

Changes in failure behavior from general to local shear failure (i.e., a localized slip surface around the anchor) with increasing embedment depths for loose and dense sand are shown in Figure 6.20. The observed failure modes of an inclined anchor with $\theta = 45^{o}$ and embedment depth $H/B = 17$ are shown in Figure 6.20 for both loose and dense sand. As can be seen in Figure 6.20, collapse of the plate anchor in dense sand involves a wider plastic region than does loose sand. However, irrespective the soil relative density D_r, it can be seen that there was a localized zone of yield around the plate anchor.

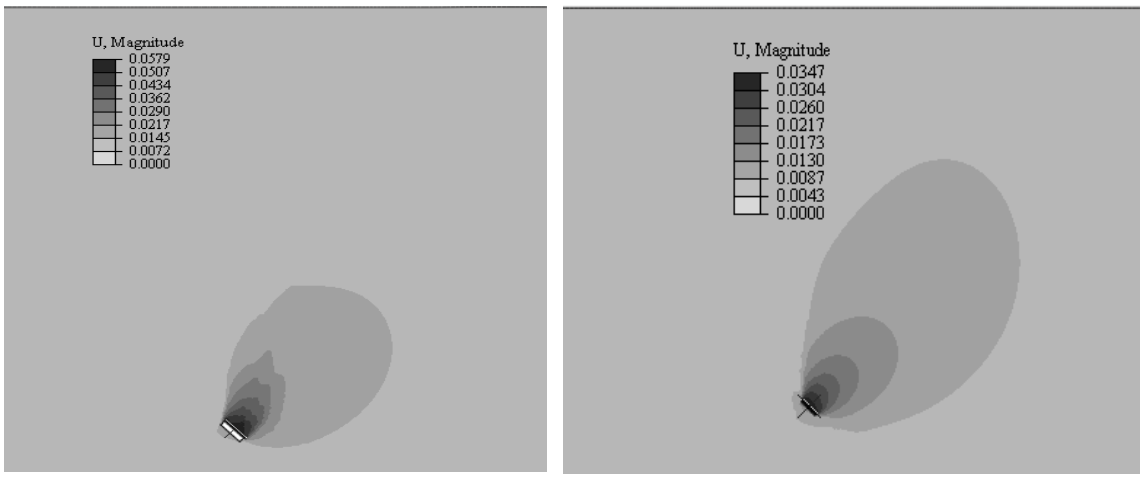

(a) Loose Sand (b) Dense Sand

Figure 6.20 Contours of resultant displacement in loose and dense sands for deep anchors H/D =17.

6.5 Comparison to prior theoretical and experimental data

The numerical results obtained from the present study were compared with published numerical, analytical, and experimental results for validation. Figure 6.21 compares the finite element solution estimates with the experimental results and upper bound solution obtained by Murray and Geddes (1989). This figure illustrates the comparison of the case of inclined anchors with $\theta = 45^{o}$, noting that ϕ and δ are 43.6 and 10.6º, respectively, where δ is the soil anchor interface friction angle.

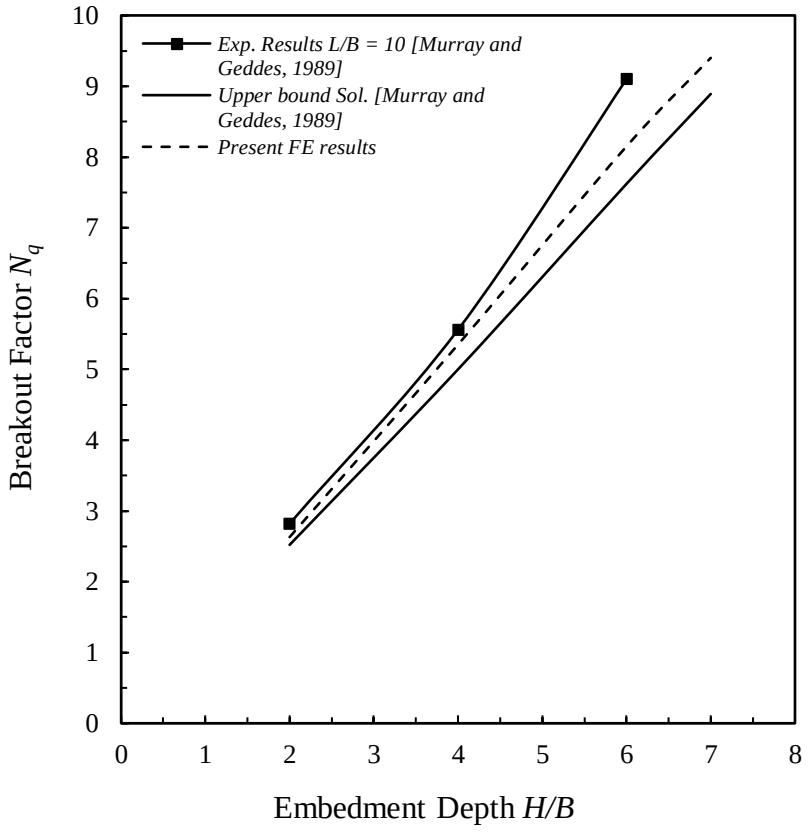

Figure 6.21 Comparison of breakout factors from the current FE study and experimental and theoretical results obtained by Murray and Geddes (1989).

Comparing numerical and experimental results can be quite complicated, due to uncertainties regarding a wide range of soil properties (*e.g.*, friction angle, dilation angle ψ, E, etc.), soil types, and the geometry of the anchor plates for which experimental results are reported (Dickin, 1988). However, the careful selection of soil parameter values allows for a close correlation with experimental results; therefore, good agreement was found when using $\psi = 12^{o}$ to 18^{o} (Murray and Geddes, 1989). The experimental observations were slightly higher than the numerical and theoretical results. While plastic limit analyses assume a rigid plastic medium, Chen (2103) showed that ultimate collapse loads are independent of the elastic response. However, if elastic effects lead to a significant geometric nonlinearity, plastic limit solutions will not necessarily match the large deformation finite element solutions.

Figure 6.22 illustrates a comparison between the present research and a finite element study performed by Rowe and Davis (1982) for cases of vertical anchors embedded in cohesionless soil with different values of friction angle ϕ'. The breakout factors increased in a nonlinear manner with increasing H/D; the greatest increase occurred with high friction angles ϕ'. However, the results of the present finite element analysis agree very well with the Rowe and Davis predictions, as shown in Figure 6.22.

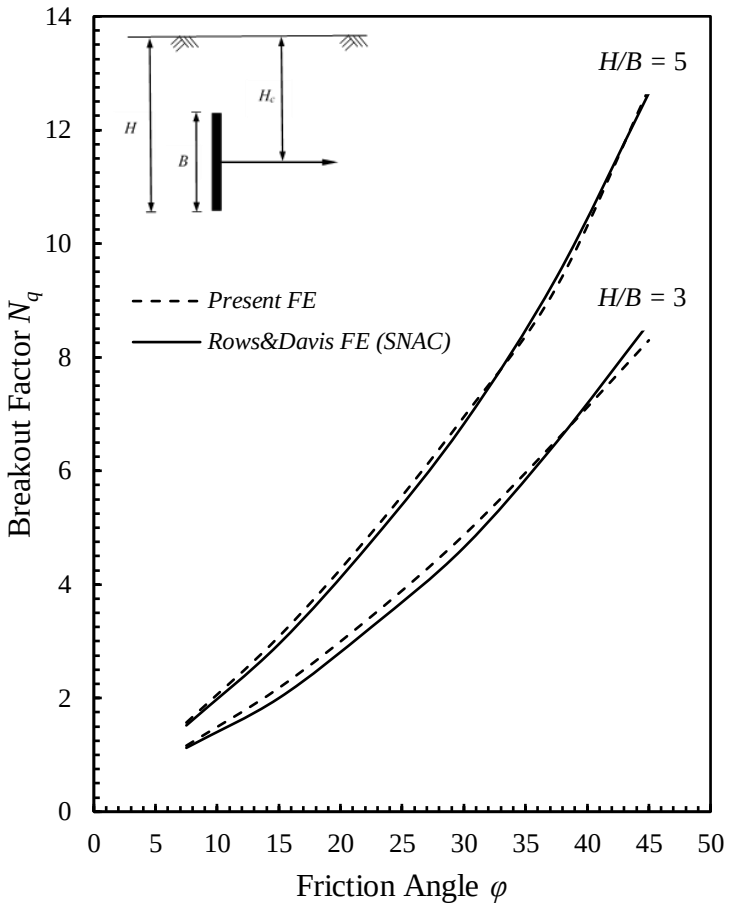

Figure 6.22 Comparison of breakout factors from the current FE study and Row and Davis (1982).

6.6 Summary

As noted above, there are very few numerical studies of inclined plate anchors embedded in cohesionless soil. The present research utilized displacement-based finite element analyses to investigate the influence of parameters such as anchor inclination (in terms of inclination factor), scale effect (i.e., *B* effect), embedment depth (i.e., *H/B*), soil relative density D_r, and anchor roughness on the overall plate anchor performance. This

section of the research presents a parametric finite element study to introduce design charts relating the breakout factor N_q to the embedment depth *H/B* and relative density D_r for different inclination angles θ and anchor widths *B*.

The predictions showed a significant sensitivity of the breakout factor N_q to the plate width *B*. Accordingly, the contribution of the scale effect (*i.e.*, the *B* effect) to the design of plate anchors in cohesionless soil should be given careful consideration, especially for vertical anchors with all embedment depth ratios. For design purposes, a relationship was proposed (Eq. 6.3) in the present research to estimate the breakout factor of an inclined anchor at any inclination angle θ between 0^o and 90^o. Also, the observations in this study confirmed the significance of the roughness of the soil anchor interface when estimating the pullout resistance of vertical anchors (*i.e.*, $\theta = 90^o$), especially for shallow embedment depths ranging from 1 to 4, while the variations of breakout factor N_q for smooth and rough anchors showed a lesser degree of sensitivity to soil roughness for inclined anchors where $\theta \leq 45^o$. It was also noted that as the angle of inclination exceeded 45^o, the active failure zone behind the anchor was significant for low relative densities (*i.e.*, loose sand), and the zone decreases as the relative density increases.

CHAPTER VII

CONCLUSIONS AND RECOMMENDATIONS

7.1 Introduction

As offshore energy and other development extend to deeper waters, conventional platforms are generally replaced by floating facilities. Increased attention is also being given to floating renewable energy facilities in water depths that are considered relatively shallow by oil-gas development standards, say greater than 60 m. Moving into deep water demands an anchoring solution for floating offshore structures. Although clay soil is the common type in the deep-water environment in which plate anchors are being used increasingly, offshore structures such as wind turbines and wave energy converters in water depths of typically less than 100m will require anchoring systems that are suitable for deployment in sands, since the seabed soils at these sites often contain sandy soil strata. As mentioned in previous chapters plate anchors provide an attractive anchorage alternative for mooring different floating facilities in a wide range of soil conditions due to their compact size, low weight, variety of installation techniques, and high efficiency. Due to the limited attention in the research literature for plate anchor performance in cohesionless soils, more reliable predictive models are needed for mooring systems to be securely designed. Few numerical studies have been conducted to assess the pullout performance of plate anchors embedded in sands and the majority of past studies has been experimentally based. Therefore, the aim of this research is to achieve a reliable numerical assessment of the performance and pullout capacity of plate anchors in cohesionless soil.

This research made some significant contributions in understanding the mechanics of plate anchors embedded in cohesionless soil as described in the following sections.

7.2 Effects of Anchor Embedment Depth and Elastic Soil Stiffness

Most previous studies of anchor performance have much performed to quantify the influence of the parameters (ϕ' and ψ) for relatively shallow levels of embedment, (typically less than 10 plate width or diameter), which is insufficiently deep to characterize the transition to deep embedment. Attention to deeply embedded plates has been very limited. Chapter IV was devoted to improve the understanding of deep plate anchor behavior in sand, characterizing the transition from shallow to deep failure mechanisms. This chapter presented a parametric study of circular, centrically loaded, horizontal plate anchors.

One of the significant findings of large deformation finite element analyses in this part of the research is the need of considering elastic soil effect (in terms of the rigidity index, I_r) in evaluating anchor performance, especially for deep anchors. The predictions showed that at shallow anchor embedment depths, rigidity index I_r has negligible influence on anchor capacity. However, the performance of deeply embedded anchors is strongly influenced by rigidity index I_r (the sensitivity to I_r is greater in denser soils), in addition to the dilation and friction angles. Since the three primary soil parameters (ϕ', ψ, and I_r) correlate well to relative density and confining stress, for design purposes and practical applications, this study developed an empirical model for predicting anchor pullout capacity as function N_q (D_r, γ', z/D). It was found that the parameters ϕ', ψ and I_r all

decrease with increasing overburden stress (Figure 4.17), implying that N_{qmax} decreases with anchor embedment, even in a soil profile having a uniform relative density (Figure 4.18a). Also, an exponential function describing the transition in the breakout factor N_q from the shallow mode (Equations 4.14 and 4.15) to its maximum value (Equation 4.9) was developed in this study. It was also found that for relative densities $D_r < 50\%$, using critical state soil parameters ($\phi' = \phi'_{crit}$ and $\psi = 0$) in the empirical model for breakout capacity greatly improves the agreement between predictions and measurements (Figure 4.19).

Two modes of failure develop in the soil mass surrounding an embedded anchor depending on soil properties and embedment depth. The failure zone for shallowly embedded anchors extends to the free surface, irrespective of soil properties. The slip surface is oriented at an angle (measured from vertical) approximately equal to the dilation angle ψ. For intermediate embedment depths, the development of a shallow versus deep failure mechanism depends on the soil properties (I_r, ϕ', and ψ). In this transitional case, localized failure mechanism develops in the loose sand, while in a very dense sand the influence of the free surface on the displacement pattern is still evident. For deep embedment depths (*e.g.* z/D = 16, Figure 4.5c and Figure 4.6c), irrespective the soil properties (I_r, ϕ', and ψ), it can be noticed a localized slip surface around the anchor.

7.3 Keying Process of Vertically Installed Plate Anchors in Sand

During keying process, both horizontal and vertical movements occur as an anchor rotates to its target orientation that is nearly perpendicular to the direction of the mooring line load. A primary evaluation of any anchor performance is pullout capacity, which is

potentially decreases as the loss of embedment increases during the orientation of the plate anchor into the direction of loading. Very few experimental data are available for plate anchor keying in sand, and to the author's knowledge, no analytical or numerical studies have been performed. The primary objective of chapter V is to fill the gap in numerical knowledge concerning the behavior of plate anchors during rotation and prediction of irrecoverable loss of embedment accompanying to that rotation. Therefore, a series of large deformation analyses were performed to investigate the response of plate anchor during the keying process in cohesionless soil.

The keying process behavior and pre- and post-pullout capacity of a vertically installed strip plate anchor embedded in uniform cohesionless soil was simulated using large deformation finite element (LDFE) analysis (*i.e.,* a RITSS technique) with various loading eccentricity ratios (*e/B*), pullout angle θ, and thickness ratio *t/B*. The anchor shank was not considered in these analyses because it was found that the including shank soil resistance increases pre pullout capacity in phases 2 and 3 by approximately 50% and post- pullout capacity in phase 4 by approximately 15% when a shank was not considered. Therefore, not considering the shank in LDFE analyses is conservative for design. As demonstrated in this study, the peak pullout capacity does not occur at the end of anchor keying process. the angle of orientation α at which the maximum pullout capacity occurs increases with increasing *e/B* ratio, ranging between 75° and 85° (Figure 5.8). The LDFE predictions revealed that as the loading eccentricity ratio *e/B* increases, the loss in anchor embedment δ_z/B during rotation decreases (see Figure 5.9). Also, once the eccentricity *e*

$\geq B$, a minimal loss in anchor embedment (*i.e.*, the highest pullout capacity) can be achieved regardless of the plate thickness.

The predictions also showed that the maximum loss in anchor embedment increased with increasing pullout angle θ (Figure 5.16) since more rotation was required to complete the anchor rotation when the higher pullout angle was applied. A linear relationship was also observed between the maximum loss in anchor embedment and anchor pullout angle θ at any *e/B* ratio, as shown in Figure 5.17. However, the numerical results from Figures (*e/B* and pullout angle θ), show that the loading eccentricity *e/B* has a much larger effect on the embedment loss than the pullout angle does.

The keying behavior of the plate anchor was determined to be essentially independent of the soil elastic stiffness *E* for shallowly embedded anchors, while it was influenced by *E* for deeply embedded anchors. Also, the predictions revealed that increasing the *t/B* ratio may increase resistance to the translational and rotational movement, due to increases in friction and bearing contact area for the anchor thickness. Therefore, it was found that the lower the anchor thickness ratio *t/B*, the higher the loss in anchor embedment δ_z/B, especially for small *e/B* ratios (Figure 5.20).

7.4 Pullout Behavior of Inclined Plate Anchor

A primary measure of anchor performance is ultimate load capacity under general conditions of loading, specifically for mooring lines oriented at arbitrary inclination angles relative to the seabed. Previous research on plate anchors has largely focused on the

horizontal or vertical breakout problems, with very limited attention directed towards obtaining a full characterization of the effects of anchor inclination angle.

For shallowly embedded anchors where free surface effects are dominant, plate orientation is likely to be particularly important. In chapter VI, LDFE analyses were undertaken to investigate the performance of strip plate anchors embedded in cohesionless soil with various inclination angles ranging from 0^o to 90^o. The effects of the anchor inclination (in terms of inclination factor F_i), scale effect (*i.e.*, the *B* effect), embedment depth (*i.e.*, *H/B*), relative density of the soil D_r, and anchor roughness were all examined. These analyses were performed for different values of the embedment depth ratio *H/B*, ranging from 1 to in some cases more than 30 anchor widths. This part of the research examined the influence of anchor width *B* on the ultimate capacity of a strip plate anchor, incorporating variations in embedment depth and relative density. It was found that the effects of anchor width *B* become more pronounced for anchors embedded in loose and dense sand, especially when the angle of inclination θ is close to the vertical. For design purposes, a relationship (Eq. 6.3) was proposed in the present research to estimate the breakout factor of an inclined anchor at any inclination angle θ between 0^o and 90^o. The observations in this study confirmed the significance of the roughness of the soil anchor interface when estimating the pullout resistance of vertical anchors (*i.e.*, $\theta = 90^o$), especially for shallow embedment depths ranging from 1 to 4, while the variations of breakout factor N_q for smooth and rough anchors showed a lesser degree of sensitivity to soil roughness for inclined anchors where $\theta \leq 45^o$ (Figure 6.12).

7.5 Recommendations and Future Work

The following points are suggested to be the most relevant to this study.

- Experimental validation is needed to confirm numerical predictions regarding the keying behavior of vertically installed plate anchors in sand subjected to different angles of mooring line load.
- The empirical equations (4.14 and 4.15) developed in chapter IV is recommended to be generalized to all anchor shapes, taking into account anchor geometry factor in addition to relative density and embedment depth.
- In the MC model, which is based on elastic-perfectly plastic adopted in this study, friction angle ϕ' and dilation angle ψ remain constant with varying plastic shear strain during analysis. This will overestimate the pullout capacity of plate anchors because MC model does not describe the softening behavior that occurs during pullout process especially in dense soil. Therefore, a constitutive model describing the process of strain softening (strength reduction) is advised for future research in estimating uplift capacity.
- More analyses for pullout behavior of square and rectangular inclined plate anchors are recommended to investigate shape effects.
- Investigation of installation disturbance effects is a worthwhile endeavor that will be considered in future studies. Also, a full study of the effects of shank resistance would require 3D modeling.

- Anchor chain generates additional frictional capacity along the length of the chain, therefore, the chain should be considered in the future analyses of the keying process.
- It is recommended to investigate the loss of embedment during the keying process and pullout behavior of inclined plate anchors in multilayered (clays and sands) soils.
- It is recommended to study group action of shallowly and deeply embedded plate anchors.

REFERENCES

ABAQUS [*Computer software*]. Providence, RI, ABAQUS Inc.

Abaqus, V. (2014). 6.14 Documentation. *Dassault Systemes Simulia Corporation*, 651.

Al Hakeem, N., and Aubeny, C. (2018). Numerical Investigation into the keying process of a plate anchor vertically installed in cohesionless soil. *Proceedings of the 37th International Conference on Ocean, Offshore& Arctic Engineering*. July 17-22, 2018, Madrid, Spain.

Al Hakeem, N., and Aubeny, C. (2019). Numerical Investigation of Uplift Behavior of Circular Plate Anchors in Uniform Sand. *Journal of Geotechnical and Geoenvironmental Engineering, ASCE,* 145 (9).

Andersen K. H. and Schjetne K. (2013) "Database of friction angles of sand and consolidation characteristics of sand, silt, and clay," *ASCE Journal Geotechnical Engineering, ASCE*, 139(7), 1140–1155.

Aubeny, Charles P. (2017). *Geomechanics of marine anchors*. Boca Raton, FL: CRC Press.

Aymone, J. L. F., Bittencourt, E., and Creus, G. J. (2001). Simulation of 3D metal-forming using an arbitrary Lagrangian–Eulerian finite element method. *Journal of Materials Processing Technology*, 110(2), 218-232.

Baker, W. H., and Konder, R. L. (1966). Pullout load capacity of a circular earth anchor buried in sand. *Highway Research Record*, (108).

Balla, A. (1961). The resistance to breaking-out of mushroom foundations for pylons. *In Proc. 5th. Int. Conf. Soil Mech. Found. Eng*. (pp. 569-576).

Barron, B.B. (2014). "An Investigation into the Keying Behavior and the Capacity of Plate Anchors in Sand." *Master of Engineering Thesis, Institute of Technology*, Sligo, 229 p.

Benson DJ (1989) An efficient, accurate and simple ALE method for nonlinear finite element programs. Comp Methods Appl Mech Eng 72:305–350.

Berezantzev, V. G., 1952. Axial Symmetrical Problem of the Limit Equilibrium Theory of Earthy Medium (*Moscow*).

Bhattacharya, P., and Kumar, J. (2014). Pullout capacity of inclined plate anchors embedded in sand. *Canadian Geotechnical Journal*, 51(11), 1365-1370.

Bolton, M. D. (1986). Strength and dilatancy of sands. *Geotechnique*, 36(1), 65-78.

Boroomand, B., and Zienkiewicz, O. C. (1997). Recovery by equilibrium in patches (REP). *International journal for numerical methods in engineering*, *40*(1), 137-164.

Brinkgreve, R. B. (2005). Selection of soil models and parameters for geotechnical engineering application. *Soil constitutive models: Evaluation, selection, and calibration*, 69-98.

Budhu, M. (2000). *Soil Mechanics and Foundations.* John Wley & Sons. Inc. New York.

Bull, John W. "Linear and Non-linear Numerical Analysis of Foundation" *Spon Press*, 2009.

Cacen, A. (2015). "MultiPolyRegress-MatlabCentral" *https://github.io./ahmetcecen/MultiPolyRegress-MatlabCentral.*

Caquot, A., and Kerisel, L. (1949). Traité mécanique des sols (*Paris*).

Carter JP, and Balaam NP. *Afena user manual 5.0*. Geotechnical Research Centre, The University of Sydney; 1995.

Chakraborty, T., and Salgado, R. (2010). Dilatancy and shear strength of sand at low confining pressures. *Journal of geotechnical and geoenvironmental engineering*, 136(3), 527-532.

Chen, Z., Tho K.K., Leung, C.F. and Chow, Y.K. (2014). "Influence of overburden pressure and soil rigidity on uplift behavior of square plate anchor in uniform clay." *Computer and Geotechnics,* 52 (2013) 71-81.

Chen, W. F. (Ed.). (2013). *Limit analysis and soil plasticity*. Elsevier.

Cheng, J. H., and Kikuchi, N. (1986). A mesh re-zoning technique for finite element simulations of metal forming processes. *International Journal for Numerical Methods in Engineering*, *23*(2), 219-228.

Cheuk, C. Y., White, D. J. and Bolton, M. D. (2007). Uplift mechanisms of pipes buried in sand. *J. Geotech. Geoenviron. Engng ASCE* 134, No. 2, 154–163.

Craig WH, Chua K. *Deep penetration of spud-can foundations on sand and clay*. Geotechnique 1990; 40(4):541–56.

Craig, R. F. (2004). *Craig's soil mechanics*. CRC press.

Das, B. M., and Seeley, G. R. (1982). Uplift capacity of pipe piles in saturated clay. *Soils and Foundations*, 22(1), 91-94.

Das, B.M. and Puri, V.K. (1989). "Holding capacity of inclined square plate anchors in clay." *Soils Found*, *29*(3): 138–144.

Das, B.M. (1990). *Earth anchors*. Amsterdam, Netherlands: Elsevier Science Publishing Company, Inc.

Davis, R. O., and Selvadurai, A. P. (2005). *Plasticity and geomechanics*. Cambridge university press.

Dickin, E. A., and Laman, M. (2007). Uplift response of strip anchors in cohesionless soil. *Advances in Engineering Software*, 38(8-9), 618-625.

Dickin, E.A. (1988). "Uplift behavior of horizontal anchor plates in sand." *Journal of Geotechnical Engineering*, 114(11): 1300-1317.

Dingle HRC, White DJ, Gaudin C. Mechanisms of pipe embedment and lateral breakout on soft clay. *Can Geotech J* 2008;45(5):636–52.

Donea, J., Antonio Huerta, J.-Ph. Ponthot and A. Rodr´ıguez-Ferran. *Encyclopedia of Computational Mechanics*, Edited by Erwin Stein, Rene de Borst and Thomas J.R. Hughes. Volume 1: Fundamentals. @ 2004 John Wiley & Sons, Ltd. ISBN: 0-470-84699-2.

Donea, J., Giuliani, S., and Halleux, J. P. (1982). An arbitrary Lagrangian-Eulerian finite element method for transient dynamic fluid-structure interactions. *Computer methods in applied mechanics and engineering*, 33(1-3), 689-723.

Downs, D. I., and Chieurzzi, R. (1966). Transmission Tower Foundations (1965 Power Division Specialty Conference, in Denver Colorado). *Journal of the Power Division*, 92(2), 91-114.

Drucker, D. C. (1954). Coulomb friction, plasticity and limit loads. *Trans. Am. Soc. Mech. Engrs* 76, 71 – 74.

Fadl M. O. (1981). "The behaviour of plate anchors in sand*." Ph.D. thesis, University of Glasgow,* Glasgow, Scotland.

Forrest, J., Taylor, R., and Brown, L (1995). *Design guide for piledriven plate anchors* (TR-2039-OCN). Port Hueneme, CA: Naval Facilities Engineering Service Center.

Gaudin, C., Tham, K. H., and Ouahsine, S. (2009). Keying of plate anchors in NC clay under inclined loading. *International Journal of Offshore and Polar Engineering*, 19(02).

Gerkus, H. S., Giampa, J. R., Senanayake, A. I., Lai, Y., Huang, Y., Flores, J. E. I., Breithaupt, B., Sivarajah, S., Bradshaw, A. S., and Gilbert R. B (2016). Preliminary development of a new concept to improve sustainability of offshore foundations. *Geo-Chicago 2016 Conference, pp. 459-469.*

Ghaly, A., and Hanna, A. (1994). Ultimate pullout resistance of single vertical anchors. *Canadian Geotechnical Journal*, 31(5), 661-672.

Ghosh, S. (1990). Finite element simulation of some extrusion processes using the arbitrary Lagrangian-Eulerian description. *Journal of Materials Shaping Technology*, 8(1), 53-64.

Ghosh, S., and Kikuchi, N. (1991). An arbitrary Lagrangian-Eulerian finite element method for large deformation analysis of elastic-viscoplastic solids. *Comput. Meth. Appl. Mech. Engng.*, 86, 127-188.

Ghosh, S., and Raju, S. (1996). R–S ADAPTED ARBITRARY LAGRANGIAN–EULERIAN FINITE ELEMENT METHOD FOR METAL-FORMING PROBLEMS WITH STRAIN LOCALIZATION. *International journal for numerical methods in engineering*, 39(19), 3247-3272.

Giampa, J. R. (2014). "Interpretation of shallow helical anchor capacity in sand." *M.S. thesis, Univ. of Rhode Island, Kingston, RI*.

Giampa, J. R., Bradshaw, A. S., and Schneider, J. A. (2016). Influence of dilation angle on drained shallow circular anchor uplift capacity. *International Journal of Geomechanics*, 17(2), 04016056.

Goldscheider, M. (1984), *True triaxial tests on dense sands. In: Constitutive relations for Soils* (Eds. G. Gudehus, F. Darve and I. Vardoulakis), Balkema, Rotterdam.

Hao D, Fu S, and Chen R. (2014). "Numerical analysis of uplift capacity of circular plate anchor in sand." *[J]. EJGE* Vol. 19, 18947-18961.

Hardin, B. O., and Black, W. L. (1966). Sand stiffness under various triaxial stresses. *Journal of Soil Mechanics & Foundations Div*, 92(ASCE# 4712 Proceeding).

Hossain MS, and Randolph MF. New mechanism-based design approach for spudcan foundations on single layer clay. *J Geotech Geoenviron Eng* 2009; 135(9):1264–1274.

Houlsby, G. T. (1991). *How the dilatancy of soils affects their behaviour* (pp. 1189-1202). Oxford: University of Oxford, Department of Engineering Science.

Hu, Y., and Randolph, M. F. (1998). A practical numerical approach for large deformation problems in soil. *International Journal for Numerical and Analytical Methods in Geomechanics*, 22(5), 327-350.

Huang, W., Shen, D., Sloan, S. W., and Yu, H. S. (2004). *"*Finite element analysis of cone penetration in cohesionless soil*." Comput. Geotech.*, 31(7), 517-528.

Ilamparuthi, K., Dickin, E. A., and Muthukrisnaiah, K. (2002). Experimental investigation of the uplift behaviour of circular plate anchors embedded in sand. *Canadian Geotechnical Journal*, 39(3), 648-664.

Janbu, N. (1963). Soil compressibility as determined by odometer and triaxial tests. *In Proc. Europ. Conf. SMFE* (Vol. 1, pp. 19-25).

Khatri, V. N., and Kumar, J. (2011). Effect of anchor width on pullout capacity of strip anchors in sand. *Canadian Geotechnical Journal*, 48(3), 511-517.

Kulhawy F. and Mayne P.W. (1990) Manual on Estimating Soil Properties for Foundation Design, Electric Power Research Institute, EPRI EL-6800, Palo Alto, California.

Kumar, J. (1999). Kinematic slices approach for uplift analysis of strip foundations. International *journal for numerical and analytical methods in geomechanics*, 23(11), 1159-1170.

Kumar, J. (2003). Uplift resistance of strip and circular anchors in a two layered sand. *Soils and Foundations*, Vol. 43, No. 1, 101 – 107, February 2003, Japanese Geotechnical Society.

Kumar, J. (2006). Uplift response of strip anchors in sand using FEM. *Iranian Journal of Science & Technology, Transaction B, Engineering*, Vol. 30, No. B4.

Laurie, C. (2017). *Wind energy facilities* (NREL/BK-6A42-67743). Golden, CO: National Renewable Energy Lab.

Lings, M. L., and Dietz, M. S. (2004). An improved direct shear apparatus for sand. *Geotechnique*, *54*(4), 245-256.

Liu, J., Liu, M., and Zhu, Z. (2011). Sand deformation around an uplift plate anchor. *Journal of Geotechnical and Geoenvironmental Engineering*, 138(6), 728-737.

Liyanapathirana, D. S. (2008). Numerical simulation of T-bar penetration in soft clay. In *GeoCongress 2008: Characterization, Monitoring, and Modeling of GeoSystems* (pp. 726-733).

Long Yu, Jun Liu, Xian-jing Kong, and Yuxia Hu. (2009). "Three dimensional numerical analysis of the keying of vertically installed plate anchors in clay." *Computers and Geotechnics,* 36 (2009), 558-567.

Lowmass, Adam C. (2006). "Installation and Keying of Follower Embedded Plate Anchors." Master of Engineering Thesis, *The University of Western Australia,* 1-6 p.

Mackay, R. B., 1966. Active and passive pressures on curved surfaces. *Sols (Paris)* 5.

Majer, J. (1955). Zur berechnung von zugfundamenten. *Osterreichische Bauzeitschrift*, 10(5), 85-90.

Menetrey, P., and Willam, K. J. (1995). Triaxial failure criterion for concrete and its generalization. *Structural Journal*, 92(3), 311-318.

Merifield, R.S., Pearce, A., Yu, H.S. and Sloan, S.W. (1999). "Stability of Anchor Plates." *Proc 8th Australia New Zealand Conference on Geomechanics*, Hobart, Australia, pp. 553-559.

Merifield, R. S., and Sloan, S. W. (2006). The ultimate pullout capacity of anchors in frictional soils. *Canadian Geotechnical Journal*, 43(8), 852-868.

Merifield, R. S., Lyamin, A. V., Sloan, S. W., and Yu, H. S. (2003). Three-dimensional lower bound solutions for stability of plate anchors in clay. *Journal of Geotechnical and Geoenvironmental Engineering*, 129(3), 243-253.

Meyerhof, G. G., and Adams, J. I. (1968). The ultimate uplift capacity of foundations. *Canadian geotechnical journal*, 5(4), 225-244.

Meyerhof, G.G. 1973. Uplift resistance of inclined anchors and piles. *Proceedings, 8th International Conference on Soil Mechanics and Foundation Engineering*, U.S.S.R., Vol. 2, pp. 167- 172.

Mors, H. (1959). The behaviour of mast foundations subjected to tensile forces. *Bautechnik*, 36(10), 367-378.

Murray, E. J., and Geddes, J. D. (1987). Uplift of anchor plates in sand. *Journal of Geotechnical Engineering*, 113(3), 202-215.

Murray, E. J., and Geddes, J. D. (1989). Resistance of passive inclined anchors in cohesionless medium. *Geotechnique,* 39(3).

NAVFAC. (2012). *Handbook for marine geotechnical engineering* (SP-2209-OCN). Port Hueneme, CA: Naval Facilities Engineering Command, Engineering Service Center.

O'Loughlin CD, Blake A, and Barron, B. (2012). "Capacity and Keying Response of Plate Anchors in Sand." *Society of Underwater Technology, Offshore Site Investigation and Geotechnics: Integrated Technologies - Present and Future, 12-14 September, London, UK,* 649–655.

O'Loughlin CD, Lowmass A, Gaudin C and Randolph MF. (2006). Physical modelling to assess keying characteristics of plate anchors. *Proceedings of the 6th International Conference of Physical Modelling in Geotechnics, Hong Kong*. 1: 659–665.

O'Loughlin, C.D., Blake, A.P., Wang, D., Gaudin, C., and Randolph, M.F. (2013). The dynamically embedded plate anchor: Results from an experimental and numerical study. In *ASME 2013 32nd International Conference on Ocean, Offshore and Arctic Engineering* (pp. V006T10A034-V006T10A034). New York, NY: American Society of Mechanical Engineers.

O'Loughlin, C.D. and Barron, B. (2012). Capacity and keying response of plate anchors in sand. *In Offshore Site Investigation and Geotechnics:* Integrated Technologies-Present and Future. Society of Underwater Technology.

Ovesen, N. K. (1981) "Centrifuge tests on the uplift capacity of anchors." *Proceedings, 10th International Conference on Soil Mechanics and Foundation Engineering*,10(1):717-722.

Pearce, A. (2000). "Experimental investigation into the pullout capacity of plate anchors in sand." *MSc thesis, University of Newcastle,* Australia.

Proudian, J. (2012). Simulating residual stress in machining; from post process measurement to pre-process predictions. *MSc. thesis, Royal Institute of Technology*.

Randolph MF, Wang D, Zhou H, Hossain MS, and Hu Y. Large deformation finite element analysis for offshore applications. *In: Proc 12th int conf of the int association for computer methods and advances in geomechanics,* IACMAG, Goa, India, 2008.

Randolph, M. F., Gaudin, C., Gourvenec, S. M., White, D. J., Boylan, N., and Cassidy, M. J. (2011). Recent advances in offshore geotechnics for deep water oil and gas developments. *Ocean Engineering*, *38*(7), 818-834.

Randolph, M. F., Jamiolkowski, M. B. and Zdravkovic, L. (2004). Load carrying capacity of foundations. Proc. *Skempton Memorial Conf., London* 1, 207–240.

Randolph, M.F. (2006). Private Communication, C.I. and Houlsby, G.T. 1991. *Analytical study of the cone penetration test in clay*. Geotechnique, Vol. 41(1), pp 17-34.

Rasulo M. P., Schneider, J.A. Newgard J. T., and Aubeny C. P. (2017). "Transition depths for deep circular anchors in saturated sand," *Society for Underwater Technology, Offshore Site Investigation & Geotechnics Committee 8th International Conference "Smarter Solutions for Future Offshore Developments," London, UK.*

Regenass, P., and Soubra, A. H. (1995). Passive resistance of strip anchors, Anchors in theory and practice. *Balkema, Rotterdam*, 117-123.

Rout, M., Pal, S. K., and Singh, S. B. (2017). Finite element modeling of hot rolling: Steady-and unsteady-state analyses. *In Computational Methods and Production Engineering* (pp. 83-124).

Rowe R. K., Davis E. H. (1982). "The behaviour of anchor plates in sand." *Geotechnique*, 32(1): 25-41.

Rowe, P. W. (1962). *The stress-dilatancy relation for static equilibrium of an assembly of particles in contact*. *Proc. R. Soc. Lond. A*, *269*(1339), 500-527.

Rowe, P. W. (1969). The relation between the shear strength of sands in triaxial compression, plane strain and direct. *Geotechnique*, *19*(1), 75-86.

Rowe, R. K., and Davis, E. H. (1982). Behaviour of anchor plates in sand. *Geotechnique,* 32(1), 25-41.

Roy K., Hawlader B., Kenny S., and Moore I. (2015). "Finite element modeling of lateral pipeline–soil interactions in dense sand." *Can. Geotech. J.*, 53: 490-504.

Saeedy, H. S. (1987). Stability of circular vertical earth anchors. *Canadian geotechnical journal*, 24(3), 452-456.

Sarac, D. Z. (1989). Uplift capacity of shallow buried anchor slabs. *International Conference of Soil Mechanics and Foundation Engineering*, 12, pp. 1213-1218.

Schanz T. and Vermeer P. A. (1996) "*Angle of friction and dilatancy of sand", Geotechnique*,46 (1): 145-151.

Schofield, A., and Wroth, P. (1968). *Critical state soil mechanics* (Vol. 310). London: McGraw-Hill.

Sheng, D., Nazem, M., and Carter, J. P. (2009). Some computational aspects for solving deep penetration problems in geomechanics. *Computational mechanics*, 44(4), 549-561.

Song Z, Hu Y, and Randolph M. F. (2008). Numerical simulation of vertical pullout of plate anchors in clay. *J Geotech Geoenviron Eng* 2008; 134(6):866–875.

Song Z, Hu Y, Wang D, and O'Loughlin CD. (2006). "Pullout capacity and rotational behavior of square anchors." *Proceedings of 6th International Conference on Physical Modelling in Geotechnics, Hong Kong* (2):1325–1331.

Song, Z., Hu, Y., O'Loughlin, C., and Randolph, M.F. (2009). "Loss in Anchor Embedment during Plate Anchor Keying in Clay." *J. Geotech. Geoenviron. Eng.*, 135 (10), 1475-1485.

Sounds and Sea Technology Engineering Solution. (2009). *Advanced anchoring and mooring study*. https://tethys.pnnl.gov/publications/advanced-anchoring-and-mooring-study.

Sun, T. K. (2013). *Numerical modeling of skin friction and penetration problems in geotechnical engineering.* HKU Theses Online (HKUTO).

Susila, E., and Hryciw, R. D. (2003). Large displacement FEM modelling of the cone penetration test (CPT) in normally consolidated sand. *International Journal for Numerical and Analytical methods in geomechanics*, 27(7), 585-602.

Taylor, D. (1948). *Fundamentals of soil mechanics*. Chapman And Hall, Limited.; New York.

Teh KL, Cassidy MJ, Leung CF, Chow YK, Randolph MF, and Quah CK. Revealing the bearing capacity mechanisms of a penetrating spudcan through sand overlying clay. *Geotechnique* 2008;58(10):793–804.

Tian Y, Gaudin C, and Cassidy MJ. Improving plate anchor design with a keying flap. *J Geotech Geoenviron Eng* 2014;140(5):04014009.

Tian, Y., Cassidy, M. J., Randolph, M. F., Wang, D., and Gaudin, C. (2014). A simple implementation of RITSS and its application in large deformation analysis. *Computers and Geotechnics*, 56, 160-167.

Trepanier, J. Y., Reggio, M., Paraschivoiu, M., and Camarero, R. (1993). Unsteady Euler solutions for arbitrarily moving bodies and boundaries. *AIAA journal*, 31(10), 1869-1876.

Vesic, A. S (1972). "Expansion of cavities in infinite soil mass." *Journal of the Soil Mechanics and Foundations Division,* 98(3): 265-290.

Vesic, A. S. (1977) "Design of pile foundations," *Synthesis of Highway Practice 42*, *Transportation Research Board*, Washington, 68p.

Vermeer, P. A., and De Borst, R. (1984). Non-associated plasticity for soils, concrete and rock. *HERON*, 29 (3), 1984.

Vermeer, P. A., and Sutjiadi, W. (1985). "The uplift resistance of shallow embedded anchors." Proc, 11th Int. *Conf. on Soil Mechanics and Foundation Engineering, San Francisco, Calif.*, Vol. 3, 1635-1638.

Walker, J., and Yu, H. S. (2006). Adaptive finite element analysis of cone penetration in clay. *Acta Geotechnica*, *1*(1), 43-57.

Wang D 1, White DJ, and Randolph MF. (2010). Large deformation finite element analysis of pipe penetration and large-amplitude lateral displacement. *Can Geotech J* 2010; 47(8):842–56.

Wang D 2, Hu Y, and Randolph M. F. (2009). Three-dimensional large deformation finite element analysis of plate anchors in uniform clay. *J Geotech Geoenviron Eng*; 136(2):355–65.

Wang D, and O'Loughlin CD. (2014). Numerical study of pull-out capacities of dynamically embedded plate anchors. *Can Geotech J*; 51(11):1263–72.

Wang, D., Hu, Y., and Randolph, M. F. (2010). Keying of rectangular plate anchors in normally consolidated clays. *Journal of Geotechnical and Geoenvironmental Engineering*, 137(12), 1244-1253.

Wang, D., Bienen, B., Nazem, M., Tian, Y., Zheng, J., Pucker, T., and Randolph, M. F. (2015). Large deformation finite element analyses in geotechnical engineering. *Computers and Geotechnics*, 65, 104-114.

Wang, D., Hu, Y., and Randolph, M.F. (2010). Keying of rectangular plate anchors in normally consolidated clays. *Journal of Geotechnical and Geoenvironmental Engineering*, 137(12), 1244-1253.

White, D. J., Cheuk, C. Y., and Bolton, M. D. (2008). The uplift resistance of pipes and plate anchors buried in sand. *Géotechnique*, 58(10), 771-779.

Willam, K. J. (1975). Constitutive model for the triaxial behaviour of concrete. *Proc. Intl. Assoc. Bridge Structl. Engrs*, 19, 1-30.

Willam, K. J., and Warnke, E. D. (1975). Constitutive Model for the Triaxial Behavior of Concrete. *Proceedings, International Association for Bridge and Structural Engineering, Vol. 19, ISMES, Bergamo, Italy*, 1–30, 1975.

Xiao, Y., Liu, H., Chen, Y., and Chu, J. (2014). Strength and dilatancy of silty sand. *Journal of Geotechnical and Geoenvironmental Engineering*, *140*(7), 06014007.

Xu, C. (2016). *Numerical modeling of object penetration in geotechnical engineering*. HKU Theses Online (HKUTO).

Young, J.J.M. (2012). Uplift capacity and displacement of helical anchors in cohesive soil.

Yu L, Hu Y, Liu J, Randolph MF, and Kong X. (2012). Numerical study of spudcan penetration in loose sand overlying clay. *Comput Geotech* 2012; 46:1–12.

Yu L, Liu J, Kong XJ, and Hu Y (2008). Three-dimensional RITSS large displacement finite element method for penetration of foundations into soil. *Comput Geotech* 2008; 35(3):372–82.

Yu, H. S. (2007). *Plasticity and geotechnics* (Vol. 13). Springer Science & Business Media.

Yu, L., Liu, J., Kong, X. J., and Hu, Y. (2009). Three-dimensional numerical analysis of the keying of vertically installed plate anchors in clay. *Computers and Geotechnics*, *36*(4), 558-567.

Yu, S.B., Hambleton, J.P., and Sloan, S.W. (2014). “Analysis of inclined strip anchors in sand based on the block set mechanism.” *In Applied Mechanics and Materials*, vol. 553, Trans Tech Publications, 422-427.

Zienkiewicz, O. C., and Taylor, R. L. (1977). *The finite element method* (Vol. 36). London: McGraw-hill.

Zienkiewicz, O. C., and Zhu, J. Z. (1992). The superconvergent patch recovery and a posteriori error estimates. Part 1: The recovery technique. *International Journal for Numerical Methods in Engineering*, 33(7), 1331-1364.

Zienkiewicz, O. C., Taylor, R. L., Nithiarasu, P., and Zhu, J. Z. (1977). *The finite element method* (Vol. 3). London: *McGraw-hill.*